CERN-THESIS-2024-032
01/04/2024

A Precise Measurement of the Lifetime of B^0_{d}-mesons, Measurement of CP-violation Parameters of B^0_{s}-mesons, the ATLAS Experiment at the LHC, and Development of Silicon Detectors for Future Particle Physics Experiments

by

Easwar Anand Narayanan

B.Sc.(Hons.), Physics, University of Delhi, 2016

M.Sc., Physics, Indian Institute of Technology Madras, 2018

DISSERTATION

Submitted in Partial Fulfillment of the

Requirements for the Degree of

Doctor of Philosophy

Physics

The University of New Mexico

Albuquerque, New Mexico

May, 2024

Dedication

This dissertation is dedicated to my family - who have lovingly supported me in all of my goals. This work is also dedicated to my wife Aiswarya who inspires me to be better.

Acknowledgments

First and foremost, I would like to express my deep gratitude to my Ph.D. advisor, Prof. Sally Seidel, for accepting me into her group, for her patient guidance, for her enthusiastic encouragement and useful critiques of this research work, and for the opportunities she has provided. I also would like to thank Maria Smizanska and Radek Novotný for the many useful conversations and guidance through out this project. I also would like to thank Benjamin Nachman, Dimitris Varouchas, and Vladimir Lyubushkin for their support. I am also thankful for the many friends and colleagues I have gained during this time.

I am grateful to the funding agencies that have allowed me to carry out this research: the U.S. Department of Energy (DOE) and the National Science Foundation (NSF). I was awarded the Chateaubriand Fellowship for 9 months by the Embassy of France and the Université Paris-Saclay which allowed me the valuable experience of working at Laboratoire de Physique des 2 Infinis Iréne Joliot-Curie (IJCLab) in Orsay, France. I am grateful to the Alexander Graham Bell Foundation for awarding me the A.G. Bell Fellowship which enhanced my research experience. I am thankful to have had the opportunity to work in the fantastic facilities provided by CERN and ATLAS.

A Precise Measurement of the Lifetime of B^0_{d}-mesons, Measurement of CP-violation Parameters of B^0_{s}-mesons, the ATLAS Experiment at the LHC, and Development of Silicon Detectors for Future Particle Physics Experiments

by

Easwar Anand Narayanan

B.Sc.(Hons.), Physics, University of Delhi, 2016

M.Sc., Physics, Indian Institute of Technology Madras, 2018

Doctor of Philosophy, Physics, University of New Mexico, 2024

Abstract

A series of connected research projects has been carried out for the purpose of seeking physics phenomena beyond the Standard Model. These consist of a precise measurement of the lifetime of a short-lived b-hadron, the B^0_{d}; preparations for measurements of CP-violating parameters in B^0_{s} decays; development of triggers that select b-hadron events; development of new instruments for improved precision in detecting fundamental particles; and monitoring and mitigating the effect of radiation on the detectors, which is inescapable in their operating environment. Datasets collected by the ATLAS detector at the Large Hadron Collider (LHC) are used for

the analyses involving the decays of b-hadrons. These analyses are supplemented by a detailed study of the evolution of the radiation effects in the current and upgraded ATLAS Pixel Detectors, using a radiation damage model and improving the model with the data collected at high luminosities. In the end, a set of comprehensive quality control tests, which include electrical and mechanical tests, has been carried out on the modules of the ATLAS Upgrade Pixel Detector.

Contents

List of Figures

List of Tables

Chapter 1

Introduction

1.1 Overview

This dissertation presents a set of related research projects focused on probing the Standard Model of elementary particles as part of a search for New Physics beyond it. To probe the Standard Model, which describes the interactions between the elementary particles, colliders where particles are accelerated before colliding with extremely high energies are needed. Similarly, complex detectors to record these collisions are required. For the projects in this dissertation, the facilities employed at the Large Hadron Collider (LHC) [1] and the ATLAS detector [2] were used. A concise overview of the Standard Model and the LHC, and a detailed overview of the ATLAS detector, are presented in this chapter.

The number of interactions that take place inside the ATLAS detector is more than a billion per second. This dissertation focuses on B-mesons, which are particles

composed of a bottom antiquark and a lighter quark[1].

For the precision measurements to constrain the Standard Model using B-mesons, data collected using the ATLAS detector from 2015 through 2018 were used. Chapter 2 presents the most precise lifetime measurement of the B^0_{d}-mesons. This measurement is a key component of the precision measurement presented in Chapter 3, which sets up the process by which the CP-violating phase in B^0_{s} decays will be determined. To select the events involving B-mesons, triggers are used to discard the irrelevant ones. Chapter 4 describes in detail the B-physics triggers, which are crucial for the B-meson analyses in Chapters 2 and 3. The ATLAS detector that is used to collect the data crucial for these precision measurements is immersed in a high radiation environment and as a result, it receives damage from the particles that provide signals of physics phenomena. To ensure reliable data-collection with the ATLAS detector, the damage it receives needs to be understood and monitored to mitigate the effects from the radiation. The precision measurements such as the measurement of the B-meson lifetimes and CP-violation parameters rely heavily on the size of the dataset collected. To further advance the precision, the current detector needs to be upgraded to increase the size of the dataset by a factor of seven. The upgraded detector will be subjected to an unprecedented amount of radiation. Chapter 5 presents the predictions of future radiation damage in the presently configured ATLAS detector and in the ATLAS upgraded detector for the High-Luminosity LHC (HL-LHC) phase. Chapter 6 presents the construction of the ATLAS upgrade detector carried out at Laboratoire de Physique des 2 Infinis Iréne Joliot-Curie (IJCLab).

[1]Unless otherwise noted, when a particle is mentioned, its antiparticle is implied as well.

1.2 The Standard Model of Elementary Particles

Particle physics deals with the constituents of matter and radiation. Many models were created to describe observed phenomena and physical laws. In the 1970s, the Standard Model (SM) of particles and their interactions was formed [3–9]. This model is in the best agreement with experimental data. The SM assumes that our world is made of 17 elementary particles and their corresponding antiparticles. The constituent particles are fermions and have half-integer spin. The field particles are bosons and have integer spin. The particles interact via four known types of force: electromagnetic, strong, weak and gravitational, of which the latter is not a part of the SM.

The SM is based on four premises:

- Its particle content includes 12 matter particles and the gauge/interaction particles of the fundamental forces.
- The fundamental forces are given by the strong and the electroweak forces.
- The local gauge symmetry group is $SU(3)_{\mathrm{C}} \times SU(2)_{\mathrm{L}} \times U(1)_{\mathrm{Y}}$.
- The Higgs mechanism generates particle masses without violating gauge invariance.

The SM has been able to explain almost all experimental results and furthermore it precisely predicted a wide variety of phenomena. With precision experiments performed at previous and current colliders, the SM has been established as a physics theory tested to the highest precision at the quantum level. However, the theory

is still far from complete. One of its flaws is that it cannot explain the dominance of matter in our visible universe. The difference between matter and antimatter is manifested in the SM through CP-violation, however the amount of CP-violation predicted in the SM is at the order 10^{-3} [10] which is not sufficient to cause the observed dominance of matter [11, 12]. Other drawbacks of the SM include the lack of inclusion of gravity and no explanation for the existence of three (and only three) generations of leptons and quarks. Astrophysical observations indicate that there is a large fraction of the matter in the universe that does not interact via the electromagnetic force (called dark matter) [13–15]; this matter is not described by the Standard Model. Astrophysical observations have also determined that there is a large amount of dark energy in the universe that is needed for explaining its evolution [16, 17]; this energy is not described by the Standard Model.

The broad scope of this thesis work is to resolve some of the problems in the Standard Model. Any precise measurements deviating from their SM prediction could indicate New Physics phenomena that are not described by the SM; these processes are Beyond Standard Model (BSM). Example BSM theories include the Minimal Supersymmetric Standard Model [18–22] and the extensions such as Minimal Flavor Violation [23, 24], Two-Higgs-Doublet Models [19], and others [25, 26].

1.3 The Large Hadron Collider

The Large Hadron Collider (LHC) [1] is the largest particle accelerator in the world. It is located in the CERN laboratory near Geneva, Switzerland. The LHC is designed as a two-ring superconducting hadron collider installed in a 26.7 km circumference

tunnel. The tunnel lies between 45 m and 170 m under the surface to suppress cosmic ray backgrounds to the experiments. It houses four major experiments - ATLAS [2], CMS [27], LHCb [28], and ALICE [29]. The LHC has successfully delivered physics data to the experiments in two runs from 2010 to 2018. The CERN accelerator complex is shown in Figure 1.1.

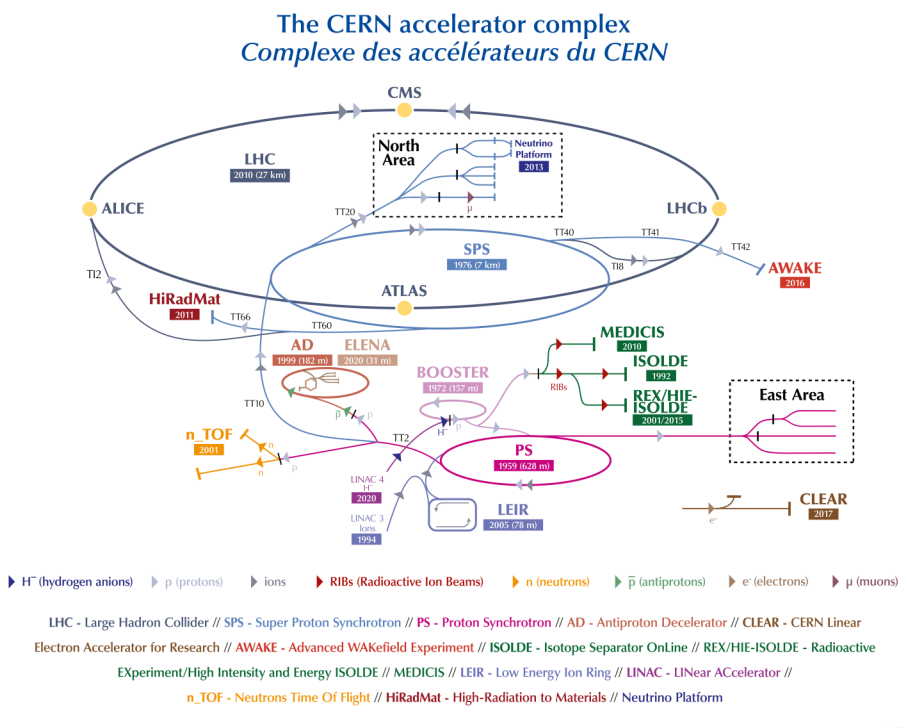

Figure 1.1: The LHC complex. The top ring is the LHC at which is installed the ATLAS Detector. The complete injection chain is depicted including all pre-accelerators. The original diagram can be found in Reference [30].

At the beginning of the acceleration chain, electrons are stripped from hydrogen atoms and the resulting protons are inserted into LINAC2. The protons are accelerated through a series of three synchotrons - the Proton Synchrotron Booster (PSB), the Proton Synchrotron (PS), and the Super Proton Synchrotron (SPS). The protons are

inserted into the two beam pipes of the LHC. The protons in each beam pipe are made to accelerate in opposite directions and are brought together (pp collisions) at four interaction points (IP) corresponding to the locations of the four experiments.

1.4 Accelerator Parameters

The most important parameters commonly used to describe accelerator performance are briefly described in this section.

- **Emittance** ϵ is the property of a particle beam that characterizes its spread in momentum-position $(p - x)$ phase space. It is used to describe a beam because unlike the physical dimensions of the beam, which vary with location in an accelerator, emittance is invariant.

- **Amplitude function** $\beta(z)$ is a beam optics quantity which is determined by the accelerator magnet configuration and powering. From the physics point of view, the most important is the value of the amplitude function at the interaction point usually referred to as β^*. The relation between $\beta(z)$ and β^* is defined as follows:

$$\beta(z) = \beta^* + \frac{z^2}{\beta^*}, \tag{1.1}$$

  where z is the distance along the nominal beam direction.

- **Crossing angle** θ_c is the angle at which two interacting bunches intersect.

1.5 Collider Parameters - Energy and Luminosity

The LHC has achieved unprecedented success in terms of center-of-mass energies achieved and in the quantity of the data collected (integrated luminosity); these are the two parameters most often cited for quantifying particle colliders [31]. The definitions of these two parameters are provided in this section.

The center-of-mass energy of two colliding particles can be computed using the energy-momentum four-vector $\mathbf{p} = (E, \overrightarrow{p})$. For one particle with mass m traveling with momentum $-\overrightarrow{p}$ (using natural units, i.e. $c = 1$):

$$\mathbf{p}^2 = E^2 - \overrightarrow{p}^2 = m^2. \tag{1.2}$$

For two colliding particles, with mass m_1 and m_2, traveling with momentum $\overrightarrow{p}_1$ and $\overrightarrow{p}_1$, the center-of-mass energy can be written as:

$$(\mathbf{p_1} + \mathbf{p_2})^2 = E_{\text{cm}}^2 = s = (E_1 + E_2)^2 - (\overrightarrow{p}_1 + \overrightarrow{p}_2)^2. \tag{1.3}$$

The term s is one of the Mandelstam variables [32, 33]. Taking the collision point to be in the laboratory frame, $\overrightarrow{p}_1 = -\overrightarrow{p}_1$, and the center-of-mass energy is:

$$\sqrt{s} = E_1 + E_2. \tag{1.4}$$

Luminosity provides the information about the number of collisions produced in a detector per second per cm^2. The luminosity is the proportionality constant between

the rate of events (or collisions) and the cross section of the event:

$$\frac{dN}{dt} = \mathcal{L}_{\sigma_{\mathrm{N}}}. \tag{1.5}$$

In e^+e^- colliders the luminosity can be determined using a process with a well defined cross section. Typically, the Bhabha scattering process ($e^+e^- \rightarrow e^+e^-$) would be used. For a hadron collider there is no corresponding process with a well known cross section. For the LHC, the parameters of the beam can be used to determine luminosity [31]. The luminosity of two Gaussian beams with identical transverse profiles (cross sections) colliding head-on is defined as:

$$\mathcal{L} = \frac{N_1 N_2 f N_b}{4\pi\sigma_x\sigma_y}, \tag{1.6}$$

where N_1 and N_2 are the numbers of protons in each of two bunches, f is the revolution frequency of protons in the collider ring, N_b is number of bunches in each beam, and $\sigma_{x,y}$ are cross sections of the Gaussian beam. Luminosity can also be expressed in terms of accelerator parameters:

$$\mathcal{L} = F\frac{N_1 N_2 f N_b \gamma}{4\pi\sqrt{\beta_x^*\epsilon_x\beta_y^*\epsilon_y}}, \tag{1.7}$$

where γ is the relativistic factor, $\epsilon_{x,y}$ is the emittance of the beam, $\beta_{x,y}$ is the amplitude function, and F is the geometrical loss factor resulting from operating with a nonzero crossing angle θ_{c}.

The luminosity in Equation 1.5 can be integrated with respect to time to give

integrated luminosity L as follows:

$$L = \int \mathcal{L} dt, \tag{1.8}$$

which is useful to characterize the size of the recorded data sample.

The first run of the LHC (LHC Run 1) occurred between the years 2010 and 2012. In 2010 and 2011, the LHC was operated at a center-of-mass energy $\sqrt{s} = 7$ TeV. In 2012, the center-of-mass energy was $\sqrt{s} = 8$ TeV. LHC Run 2 occurred during the years 2015 to 2018, and the center-of-mass energy during LHC Run 2 was $\sqrt{s} = 13$ TeV. The luminosity delivered by the LHC in Run 2 was 157 fb^{-1}. In the ATLAS experiment, several types of integrated luminosity are used:

- Delivered luminosity is the luminosity delivered by the accelerator,
- Recorded luminosity is the luminosity which is recorded by the experiment, and
- Good for Physics is the designation of the luminosity when all reconstructed physics objects are assessed to be of good data quality.

In the ATLAS experiment, the luminosity determination is carried out using van der Meer scans and dedicated luminosity detectors [34]. The overview of the accumulated luminosity in LHC Run 2 at the ATLAS detector is shown in Figure 1.2.

Run 3 began in July 2022 at $\sqrt{s} = 13.6$ TeV and is expected to end in 2025. Starting from 2029 [36], the LHC will operate at unprecedented instantaneous luminosity at $\sqrt{s} = 14$ TeV for more than 10 years and in that time, ATLAS aims for a total data set of about 4000 fb^{-1}. This era is called the High Luminosity LHC (HL-LHC).

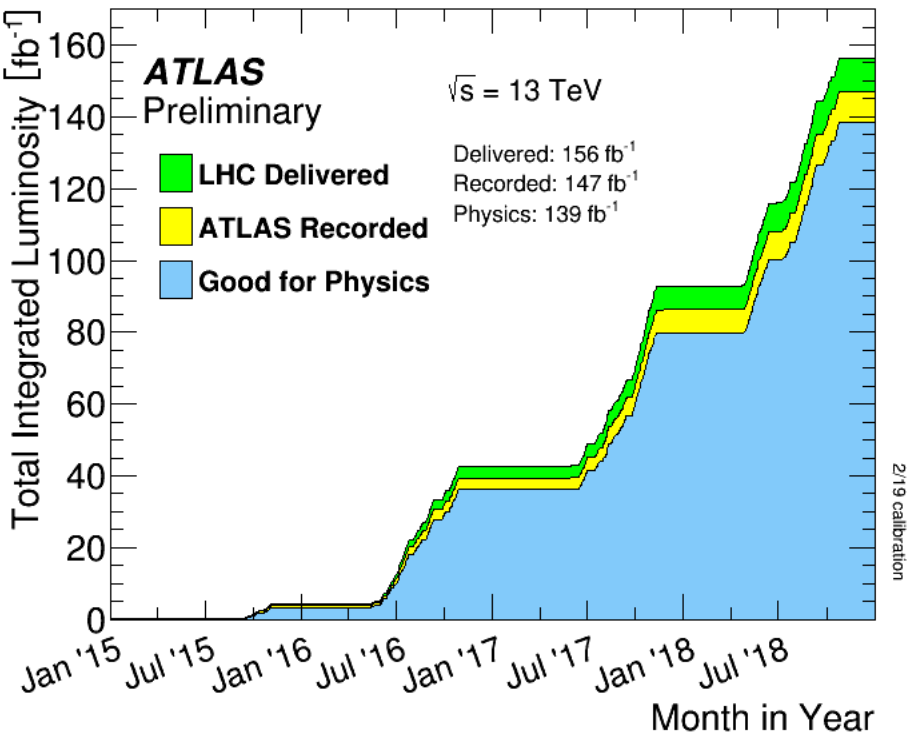

Figure 1.2: Cumulative luminosity versus date delivered to ATLAS (green), recorded by ATLAS (yellow), and certified to be good quality data (blue) during stable beams for *pp* collisions at 13 TeV centre-of-mass energy in 2015-2018 [35].

1.6 The ATLAS Experiment

The ATLAS (A Toroidal LHC ApparatuS) detector, shown in Figure 1.3, is one of the two general purpose detectors, the other being the Compact Muon Solenoid (CMS), designed to study *pp* collisions at the LHC. The main areas of research done at ATLAS are benchmark tests of the Standard Model, top quark studies, precise study of electroweak theory, SUSY (supersymmetry), Higgs studies, and searches for other new physics.

The ATLAS subdetectors cover almost the full solid angle around the collision

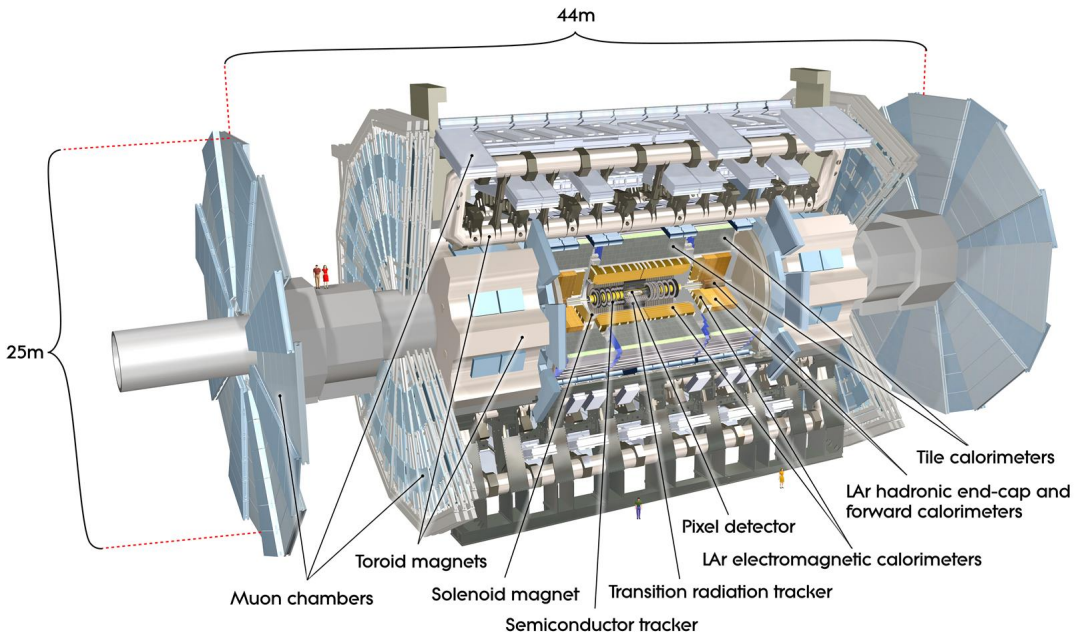

Figure 1.3: The ATLAS detector cut-away view with its subdetectors highlighted [2].

point and are symmetric in the forward-backward direction with respect to the interaction point (IP). The subdetectors can be geometrically divided into the barrel, two end caps and two forward regions. In the forward regions, there can be found the ALFA [2], LUCID [2], and ZDC [2] subdetectors which primarily provide luminosity measurements. The non-forward subdetectors are divided into three subsystems: inner detector (ID), calorimeters, and muon spectrometer (MS). The detectors are immersed in the magnetic field that bends charged particle trajectories and allows momentum measurement [29].

1.6.1 The ATLAS Coordinate System

The ATLAS coordinate system describing the detector phase space is right-handed with the $x-y$ plane perpendicular to the beam direction with the positive x-axis pointed towards the center of the LHC ring, the positive y-axis pointed upwards toward the surface of the earth and the z-axis pointed along the LHC beam line. The detector half at positive z-values is referred to as the "A-side," the other half the "C-side." The variables measured in the transverse plane are denoted with a T subscript.

The track can be measured by finding the radial dimension, r, which is the distance from the beam line, the azimuthal angle ϕ, which is the angle from the x-axis (beam axis), and the polar angle θ, which is the angle from the z-axis (beam line). Using this coordinate system, the following terms are introduced.

The pseudorapidity is defined as

$$\eta = -\ln(\tan(\theta/2). \tag{1.9}$$

The distance ΔR in the pseudorapidity-azimuthal angle space is defined as

$$\Delta R = \sqrt{\eta^2 + \phi^2}. \tag{1.10}$$

The transverse momentum, p_{T}, is defined as the component of a particle's momentum, $\mathbf{p}$, that is perpendicular to the direction of the beam line and is given by

$$p_{\mathrm{T}} = \mathbf{p} \times \sin\phi. \tag{1.11}$$

It is a useful quantity to study the properties and interactions of the particles produced in the collisions, as it reflects the dynamics of the partons inside the hadrons that collide.

1.6.2 The Magnet System

The hybrid system of four large superconducting magnets of the ATLAS detector is unique with respect to other experiments at the LHC and is necessary for the momentum measurement of charged particles. This magnet system is 22 m in diameter and 26 m in length, with a stored energy of 1.6 GJ. The magnetic system is shown in Figure 1.4.

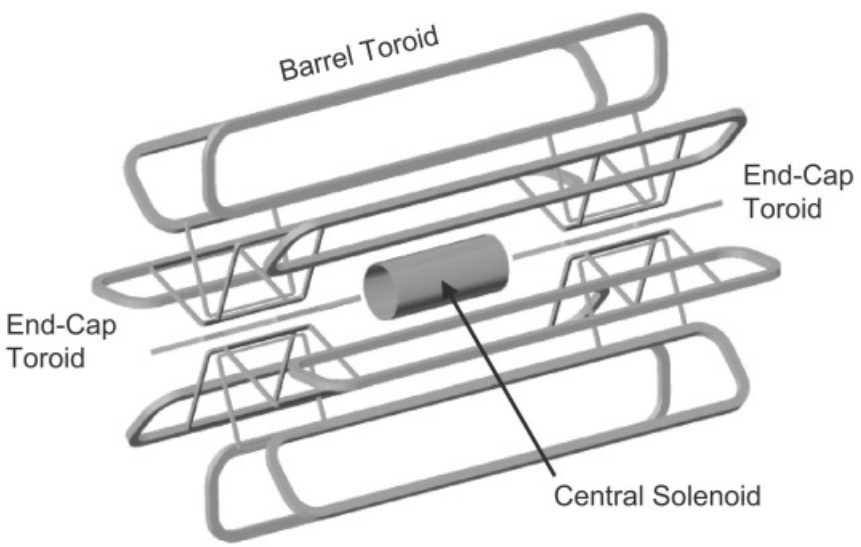

Figure 1.4: The ATLAS magnet system layout which consist of the central solenoid, barrel toroid and two end cap toroids [2].

It is made up of a central solenoid, a barrel toroid and two end cap toroids.

- The central solenoid is designed to provide a 2 T magnetic field in the central

tracking region. To achieve that, the superconducting solenoid with radius 1.247 m and length 5.283 m is used. In the nominal state, the coil is supplied with 7730 A and the whole solenoid is operated at 4.5 K using liquid helium as a coolant. To reduce the detector's material budget, the central solenoid and the electromagnetic calorimeter share a common cryostat.

- The barrel toroid, providing the magnetic field in the outer tracking region, consists of 8 flat superconducting race-track coils, each 25.3 m long and 5 m wide, grouped in a torus shape with inner bore of 9.4 m and outer diameter of 20.1 m. The nominal magnetic field for the muon detectors in the central region is 0.5 T, with peak field strength of 2.5 T in the bore. The supply current is 20.5 kA, and the operational temperature is 4.7 K.

- The end caps toroids, positioned inside the barrel toroid at both ends of the central solenoid, provide the azimuthal magnetic field across a radial span of $1.5 - 5$ m. The toroids generate the magnetic field required for optimizing the bending power in the end cap regions of the muon spectrometer system. The nominal magnetic field for the muon detectors in the end-cap region is 1.0 T, with peak field strength of 3.5 T in the bore.

1.6.3 The Inner Detector

The inner detector (ID) is designed to provide excellent momentum resolution for charged particles and both primary and secondary vertex position measurements with high precision in the pseudorapidity range of $|\eta| < 2.5$. The ID has to withstand a high-radiation environment as the innermost subsystem of the ATLAS detector.

The ID is contained within a cylindrical envelope of length 3512 mm and with a radius of 1150 mm. It is immersed in a 2 T magnetic field generated by the central superconducting solenoid. The ID consists of the Pixel detector, the Semiconductor Tracker (SCT) and the Transition Radiation Tracker (TRT).

As can be seen in Figure 1.5, the detectors are arranged as concentric cylinders around the beam axis in the barrel region. In the end cap regions, there are pixel modules located on disks perpendicular to the beam axis. All detectors are mounted on a support structure, which is made of carbon fibers to ensure good mechanical properties, thermal conduction and low material budget.

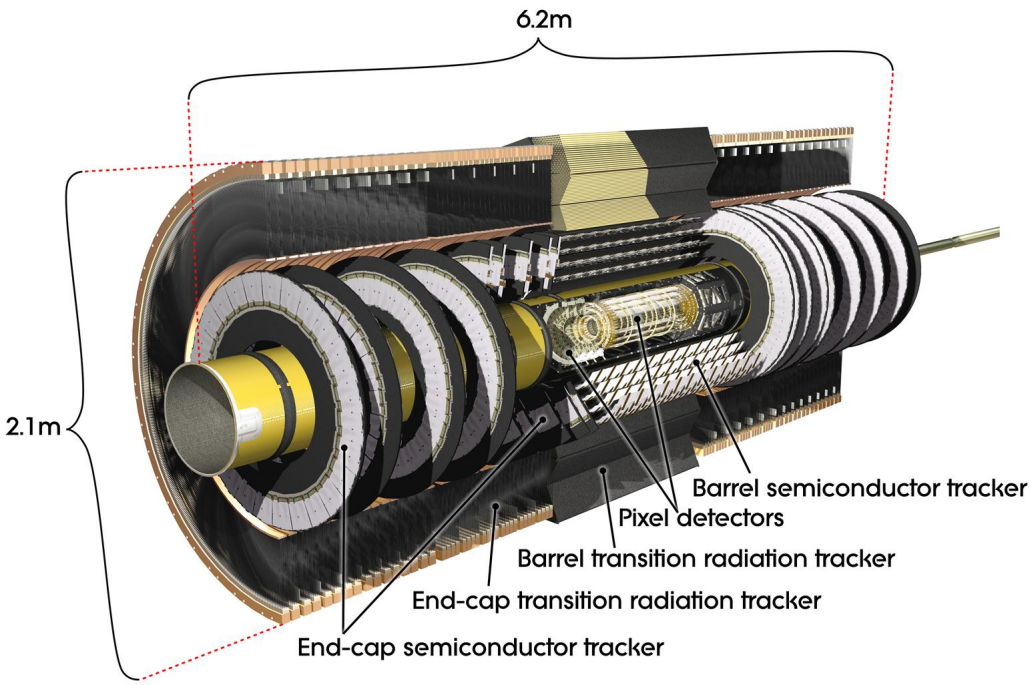

Figure 1.5: The schematic cut-away view of the ATLAS Inner Detector [2].

The **Pixel detector** is at the heart of ATLAS, closest to the interaction point of the LHC proton beams, and it contains four layers of silicon pixel modules in the

barrel region. Between LHC Run 1 and Run 2 the Insertable B-Layer was installed as the closest pixel layer to the beam line, positioned at a radius of 33.25 mm from the LHC proton beam line. Three barrel layers - B-Layer, Layer-1, and Layer-2 are positioned at a radius of 50.5 mm, 88.5 mm, and 122.5 mm, respectively from the beam line. The study presented in Chapter 5 focuses on the Pixel detector. All three barrel layers have the same dimensions along the beam line axis, $z = \pm 380$ mm, where z is measured from the interaction point, and they cover the full azimuthal angle ϕ. The disks are located at $z = \pm 495$ mm, ± 580 mm, and ± 650 mm and named Disk-1, Disk-2, and Disk-3, respectively. The modules on the disks have an inner radius of 8.88 cm and an outer radius of 14.96 cm. The four barrel layers are made up of 1736 silicon modules, and disks add an additional 288 modules. Each module includes a pixel sensor with an active surface area of (6.08×1.64) cm^2, fabricated on (252.5 ± 2.8) μm thick n-type bulk. The sensor is made by implanting highly doped p-type (p^+) and highly doped n-type (n^+) material on opposite surfaces of the bulk. These planar sensors as shown in Figure 1.6 operate with their p^+ implants on the read-out side, where the front end electronics read out the signal, and the p-n junction on the back side. In addition to planar sensors, IBL employs 3D sensors [37]. In 3D geometry, n^+ and p^+ columnar implants are in the silicon bulk. These are more radiation hard due to the smaller inter-electrode spacing as shown in Figure 1.6. The pixel detector provides approximately 80.4 million readout channels in total. Details of the pixel sensor geometry and layout can be found in References [38, 39]. The 3D sensors are proposed for future tracking upgrades as well [40].

The **Semiconductor Tracker** (**SCT**) consists of 4088 modules of silicon-strip detectors arranged in four concentric barrels and two end caps of nine disks each. It

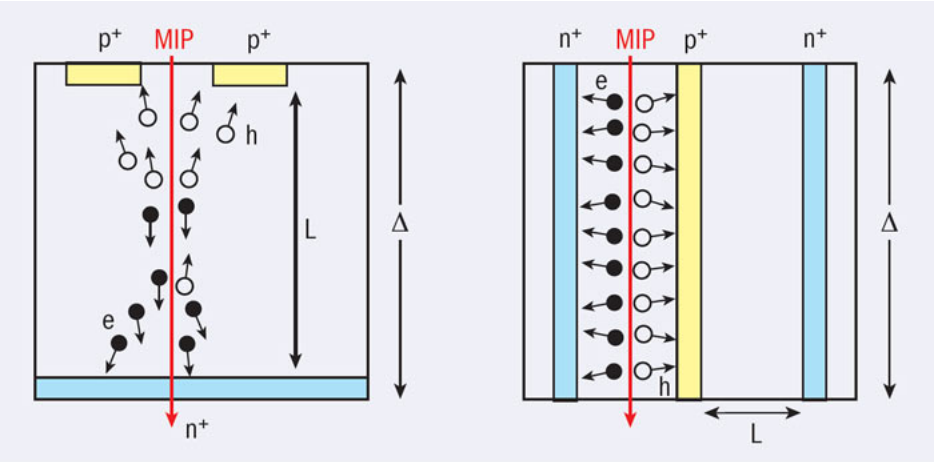

Figure 1.6: (Left) planar and (right) 3D silicon sensor geometries. These diagrams were originally published in [41].

provides typically eight strip measurements (four space-points) for particles originating from the interaction point (IP). The strips in the barrel are approximately parallel to the solenoid field and beam axis and have a constant pitch of 80 μm, while in the end caps the strip direction is radial and of variable pitch. Every two sensor modules are glued together within a hybrid module in the barrel region. On one detector layer, there are two sensor layers rotated within their hybrids by $\pm$20 mrad around the geometrical center of the sensor to measure space points in terms of r, ϕ, and $z(r)$ coordinates. The 2D spatial resolution is 17 μm in the $r - \phi$ plane and 580 μm in $z(r)$. The SCT provides between four and nine measurements per particle, with coverage up to $|\eta| < 2.5$. The sensors of the SCT are 285 μm thick and are constructed of high-resistivity n-type bulk silicon with p-type implants [42]. In total, the SCT provides approximately 6.3 million readout channels.

The **Transition Radiation Tracker** (**TRT**) is the largest of the sub-detectors in the ID. The main purpose of the TRT is to measure transition radiation of charged particles, in order to distinguish between electrons and other, heavier particles, in

the pseudorapidity range up to 2.5. The basic TRT detector elements are polyamide straw tubes with diameter 4 mm filled with a mixture of 70% Xe, 27% CO_2, and 3% O_2, and 70% Ar, 27% CO_2, and 3% O_2 in some of the tubes in which leaks were discovered during Run 2 [43]. The straw tube walls operate as cathodes, while the 30 μm thick tungsten wire plated with gold operates as the anode. The TRT is composed of 300,000 straw tubes that provide position measurements with an accuracy of approximately 130 μm in the $r - \phi$ plane in the barrel, and in the $z - \phi$ plane in the end cap. A large number of hits, typically 36 per particle, is provided, with coverage up to $|\eta| < 2.0$. The total number of readout channels of the TRT is approximately 351,000.

1.6.4 The Calorimeters

The calorimetry system is designed to provide good energy resolution for measurement of electromagnetic and hadronic showers, and it must also limit punch-through into the muon system. The calorimetry system consists of two separate calorimeters, electromagnetic and hadronic calorimeters, using different technologies suited to the widely varying requirements of the physics processes of interest, and it covers the angular region up to $|\eta| < 4.9$ [2]. An overview of the ATLAS calorimetry system is shown in Figure 1.7.

The ATLAS calorimeters are sampling calorimeters where the energy of the full shower can be inferred from the observed energy deposits. The calorimeters closest to the beam line are housed in three cryostats, one barrel and two end caps. The barrel cryostat contains the electromagnetic barrel calorimeter, whereas the two end

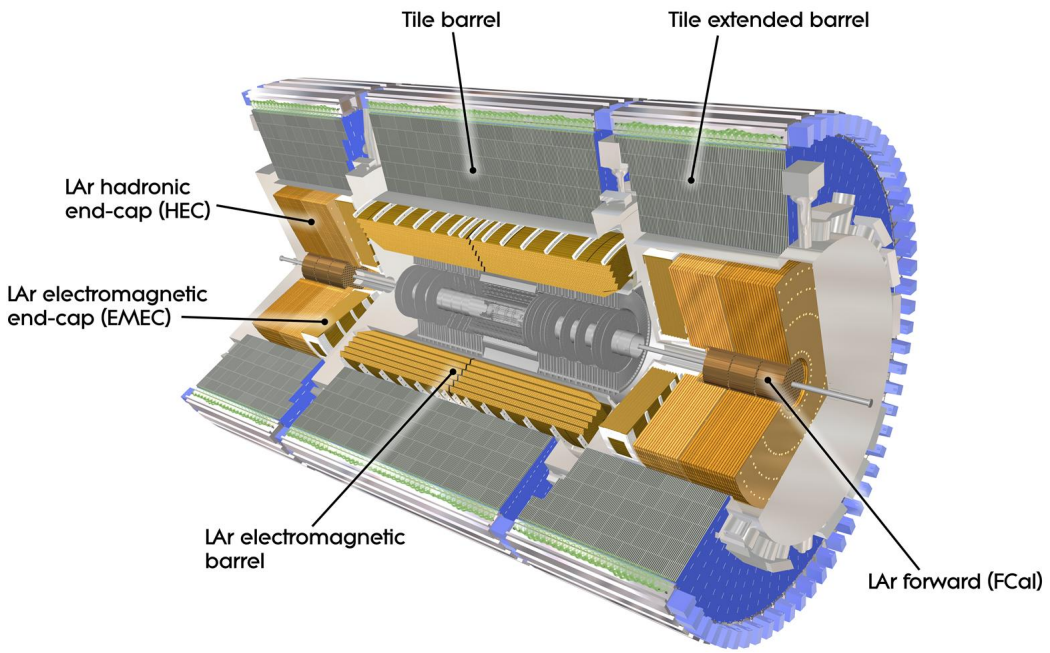

Figure 1.7: ATLAS calorimetry system cut-away view [2].

cap cryostats each contain an electromagnetic end cap calorimeter, a hadronic end cap calorimeter, and a forward calorimeter to cover the region closest to the beam. All these calorimeters use liquid argon as the active detector medium because of its intrinsically linear behaviour, its stability of response over time and its intrinsically radiation-hardness.

The energies of electrons and photons are measured by the electromagnetic (EM) barrel and end cap calorimeters. The EM has accordion shaped kapton electrodes and lead absorber plates that provides complete and symmetric ϕ coverage without azimuthal cracks. These detectors provide high granularity measurements, critical for particle identification in the range $|\eta| < 2.5$. The EM is divided into a barrel part ($|\eta| < 1.475$) and two end cap parts ($1.375 < |\eta| < 2.5$). The barrel calorimeter

consists of two identical half barrels, separated by a 4 mm gap at $z = 0$. Each end cap calorimeter is mechanically divided into two coaxial wheels: an outer wheel covering the region $1.375 < |\eta| < 2.5$, and an inner wheel covering the region $2.5 < |\eta| < 3.2$. The readout electrodes are located in the gaps between the absorbers and consist of three conductive copper layers separated by insulating polyamide sheets. The overall thickness of the EM is between 22 and 24 radiation lengths.

To ensure proper reconstruction of hadronic showers and maximal phase-space coverage, the hadronic calorimeter is divided into three parts: a tile calorimeter in the barrel, a LAr calorimeter in the end cap regions and a LAr forward calorimeter. The tile calorimeters and the LAr hadronic end cap calorimeter are designed to measure the energy of hadrons.

The tile calorimeter is placed directly outside the EM calorimeter envelope as can be seen in Figure 1.7. It consists of a barrel part covering the region $|\eta| < 1.0$ and two extended barrel parts covering the region $0.8 < |\eta| < 1.7$. The scintillator tile calorimeter (TileCal) is a sampling calorimeter using steel as the absorber and plastic scintillating tiles as the active material. Two sides of the scintillating tiles are read out by wavelength shifting fibers into two separate photomultiplier tubes. The overall thickness of the tile calorimeter in terms of interaction length is 9.7λ at $\eta = 0$.

The hadronic end cap calorimeter (HEC) is located directly behind the end cap electromagnetic calorimeter and covers the region of $1.5 < |\eta| < 3.2$. Each HEC consists of two independent wheels composed of copper LAr calorimeters of flat plate design with outer diameter of 2.03 m. The wheels closest to the interaction point are built from 25 mm parallel copper plates, while those further away use 50 mm copper plates. The copper plates are separated by 8.5 mm gaps filled with LAr, providing

the active medium for this sampling calorimeter.

The Forward Calorimeter (FCal) covers the region of $3.1 < |\eta| < 4.9$ and is designed to provide both electromagnetic and hadronic calorimetry information. The FCal consists of three modules in each end cap: the first, made of copper, is optimised for electromagnetic measurements, while the other two, made of tungsten, measure mainly the energy of hadronic interactions. The FCal modules include a metal matrix parallel to the beam axis consisting of concentric rods and tubes, where the LAr, in the gap between them, is the sensitive medium. The overall interaction length of the FCal is 10λ.

1.6.5 The Muon Spectrometer

The muon system is designed to detect muons exiting the barrel and end cap calorimeters, and to measure muon momentum in the pseudorapidity range of $|\eta| < 2.7$. It measures properties of muon tracks bent by the large superconducting air-core toroid magnets. Over the range $|\eta| < 1.4$, magnetic bending is provided by the large barrel toroid. For the region $1.6 < |\eta| < 2.7$, muon tracks are bent by two smaller end cap magnets inserted into both ends of the barrel toroid. In the region $1.4 < |\eta| < 1.6$, usually referred to as the transition region, the bending is provided by a combination of the barrel and end cap fields. In the barrel region, tracks are measured in chambers arranged in three cylindrical layers around the beam axis, while in the transition and end cap regions, the chambers are arranged in three layers perpendicular to the beam axis. Over most of the η range, a precision measurement of the track coordinates is provided by the Monitored Drift Tubes (MDTs). In the range $2 < |\eta| < 2.7$, the

Cathode Strip Chambers (CSCs), which have higher granularity, are used to withstand the demanding rate and background conditions. An essential design criterion of the muon system is the capability to trigger on muon tracks. The precision tracking chambers have therefore been complemented by a system of fast trigger chambers capable of delivering track information within a few tens of nanoseconds after the passage of a particle in the region $|\eta| < 2.4$. These are Resistive Plate Chambers (RPCs) in the barrel region ($|\eta| < 1.05$) and Thin Gap Chambers (TGCs) in the end cap ($1.05 < |\eta| < 2.4$) region. The main purpose is to provide fast track information for triggering purposes with a well-defined p_{T} threshold. A cut-away view of the muon system is shown in Figure 1.8.

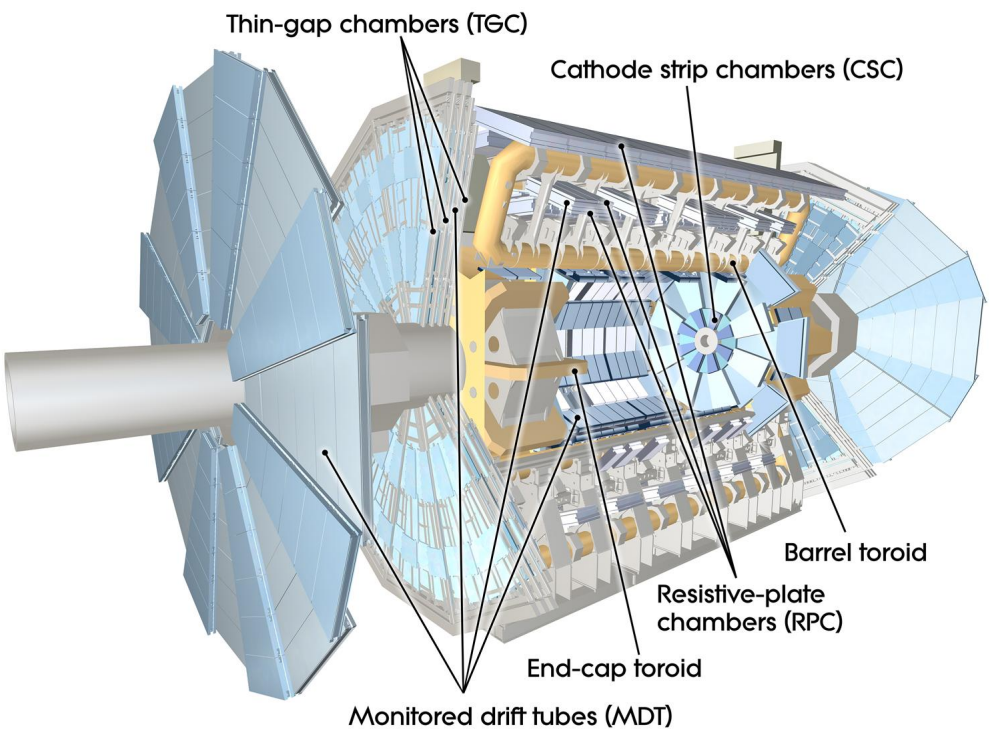

Figure 1.8: ATLAS Muon Spectrometer cut-away view [2].

Monitored Drift Tubes (MDTs): The basic detection element of the MDT

chamber is an aluminum drift tube with a diameter of 29.6 mm, pressurized with Ar/CO_2 (93/7%) gas at 3 bar. The central wire has a diameter of 50 μm and is made of a tungsten-rhenium alloy. It collects electrons created by the ionization of the gas by incoming particles. The drift tube operates at 3080 V potential difference between the wire and tube wall, producing an electric field with a maximum drift time from the wall to the wire of about 700 ns. The spatial hit resolution for each MDT tube is about $60 - 80$ μm. The MDT chambers in the barrel are arranged in three concentric cylindrical shells around the beam axis covering the region $|\eta| < 1.4$. In the end cap region, muon chambers form large wheels, perpendicular to the z-axis and covering the range $1.4 < |\eta| < 2.7$. All regular MDT chambers consist of two groups of tube layers, called multi-layers, separated by a mechanical spacer. The multi-layer consists of four tube layers in the innermost shell to enhance the pattern recognition performance, while the middle and outer shells each use only three tube layers.

Cathode Strip Chambers (CSCs): The CSCs are multi-wire proportional chambers with wires of 30 μm diameter oriented in the radial direction. The wire pitch is equal to the anode-cathode spacing of 0.25 mm. In the bending direction, the CSCs can reach a resolution of 60 μm per CSC plane. The operating voltage of 1900 V provides a maximal electron drift time lower than 40 ns, resulting in a timing resolution of about 7 ns per plane. The CSCs are used in the forward region, $2 < |\eta| < 2.7$, where the track occupancy is higher than the safe operation limit of the MDTs. The CSCs combine high spatial, time, and double track resolution with high-rate capability and low neutron sensitivity. The whole CSC system consists of two disks with eight chambers each. Each chamber contains four CSC planes,

resulting in four independent measurements in η and ϕ along each track.

Resistive Plate Chambers (RPCs): The RPC is a gaseous parallel electrode-plate detector used to provide trigger information in the barrel region. The RPC module is made of two phenolic-melaminic plastic laminate plates kept parallel to each other at a distance of 2 mm by insulating polycarbonate spacers. It is filled with a 94.7/5/0.3% mixture of $C_2H_2F_2\text{Iso} - C_4H_{10}/SF_6$ gases which combines relatively low operating voltage, non-flammability, and low cost, while providing a comfortable plateau for safe avalanche operation. The potential difference of 4.9 kV/mm between the plates allows the detector to work in avalanche mode. The signal is read out by metallic strips, which are installed on the outer side of the resistive plates. The RPCs are arranged in three concentric cylindrical layers around the beam axis covering the region $|\eta| < 1.05$. The two inner layers provide information for low momentum triggers using tracks in the range of $6 - 9$ GeV, while the outer layer measures the high momentum tracks in the range of $9 - 35$ GeV, seeding the high momentum triggers. Each RPC station is made of two detector layers and four readout strip panels, each measuring the tracks' η and ϕ coordinates.

Thin Gap Chambers (TGCs): The TGCs are multi-wire proportional chambers designed to provide two functions in the end cap muon spectrometer: the muon trigger capability and the determination of the second, azimuthal coordinate to complement the measurement by the MDTs in the bending (radial) direction. In the TGCs, the wire-to-cathode distance of 1.4 mm is smaller than the wire-to-wire distance of 1.8 mm. The cathode plates are made of FR4 (Flame Resistant 4) with a graphite coating on the inside. The gap between two plates is filled with a highly quenching gas mixture of CO_2 and n-C_5H_{12}. The nominal operation voltage is 2900 V

which provides a high electric field around the TGC wires. Together with the small wire-to-wire distance, this leads to a very good time resolution of 4 ns. The TGC detectors are mounted in two concentric rings, one in the innermost layer and the other in the middle layer. Each layer is divided into the outer ring, covering the rapidity range of $1.05 < |\eta| < 1.92$, and the inner ring, covering the rapidity range of $1.92 < |\eta| < 2.4$. The TGC units are grouped into triplet and doublet modules. The triplet module is built to cope with false coincidences from background hits, which are more likely in the end cap region than in the barrel.

1.6.6 The Forward Detectors

In addition to the main ATLAS detector systems described in the previous subsections, four smaller sets of detectors provide good coverage in the forward region. These forward detectors are placed at high pseudorapidities, and their primary objective is to measure the beam luminosity for the ATLAS detector. Furthermore, in conjunction with the main ATLAS detector, they have been used to study soft QCD and diffractive physics. All of these detectors use different techniques to detect fragments from the collisions. The location of the ATLAS forward detectors is shown in Figure 1.9.

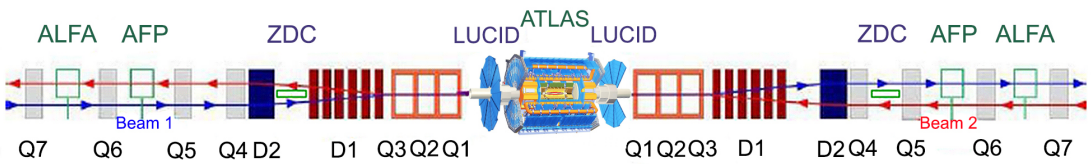

Figure 1.9: The placement of the ATLAS forward detectors with respect to the ATLAS detector [44].

Ordered according to their distance from the interaction point, the first system is a

Cherenkov detector called the LUminosity measurement using Cherenkov Integrating Detector (LUCID). The LUCID is designed to measure relative luminosity, and is located in the ATLAS cavern at ±17 m from the interaction point (IP). The second system is the Zero-Degree Calorimeter (ZDC) which is designed to detect forward neutrons in heavy-ion collisions and is located at ±140 m from the IP. This corresponds to the location where the LHC beampipe is divided into two separate pipes. The ZDC is embedded in the TAN (Target Absorber Neutral), which is located between the beampipes just after the split. The primary purpose of the ZDC is to detect forward neutrons in heavy-ion collisions. The ATLAS Forward Proton (AFP) detector is located at ±210 m from the IP and is designed to tag elastic and diffractive events. The most remote detector is the Absolute Luminosity For ATLAS (ALFA). The ALFA is designed to measure elastic proton scattering and is located at ±240 m, just before the bending magnets of the LHC arc.

Luminosity measurement using Cherenkov Integrating Detector (LUCID): The LUCID is composed of two modules located at ±17 m from the interaction point that provide a coverage $5.5 < |\eta| < 5.9$ for charged particles. The LUCID measures ATLAS luminosity using the inelastic collision products with low sensitivity to the background [45]. In Run 1, the LUCID-1 was used for the luminosity measurement; however, the increased pile-up and reduced bunch spacing in Run 2 demanded a faster and more radiation hard detector with sensors of smaller acceptance and, in general, better electrical stability. Thus for Run 2, the upgraded detector LUCID-2 was used. The LUCID-2 was installed during Long Shutdown 1 (LS 1) which was the shutdown phase between Run 1 and Run 2. It was decided to use a gasless system with 16 photomultipliers (PMs) at each arm. The PMs contain thin quartz windows

as their Cherenkov medium and a small amount of radioactive ^{207}Bi deposited on the windows for monitoring and calibration purposes. The precision of the luminosity measurement in Run 2 with the upgraded LUCID-2 detector is approximately 2% [46].

Zero Degree Calorimeter (ZDC): The ZDC provides coverage of the region $|\eta| > 8.3$ for neutral particles and is placed on two symmetric arms at ± 140 m from the interaction point. The ZDC plays an important role in the heavy ion physics program at the LHC. It is used for the centrality measurement, which is strongly correlated with the number of very forward neutrons. The ZDC is a sampling calorimeter that detects Cherenkov light produced by the highly energetic charged particles in the shower. The active element is made of quartz rods, and the light produced in the rods is detected by photomultiplier tubes. The tungsten plates are used as absorbers. The time resolution of the ZDC is about 100 ps, which is sufficient to locate the interaction point to within about 3 cm along the beam axis [47].

ATLAS Forward Proton (AFP) Spectrometer: The AFP consists of four detector stations placed symmetrically with respect to the ATLAS Interaction Point (IP), located at ± 205 m and ± 217 m. Each AFP station is inside a retractable device called a Roman pot that protects it from the LHC high vacuum with a secondary safety vacuum. Each AFP station consists of four Silicon Trackers (SiT) which provide precise position measurements. The purpose of the AFP tracking system is to measure points along the trajectory of protons that are deflected during a proton-proton interaction. Four readout chips are installed in each AFP station. The active area covered by the tracking detector is approximately 16×20 mm^2 with a pixel size of 50×250 μm^2. Detectors are tilted by 14 degrees. The resolution of a single plane is about 6 μm and 30 μm in the x and y coordinates respectively [48]. By

having two detectors on each side of the IP, one can measure not only the position of the proton with respect to the beam, but also its elevation angle. These are connected to the proton kinematics at the interaction point [49].

Absolute Luminosity for ATLAS (ALFA): The ALFA is located at ±240 m from the interaction point on both sides of ATLAS. It is designed to measure protons scattered at very small angles used for studies involving elastic and diffractive events, exclusive production, and photon-induced interactions. The whole detector is placed in Roman pots which permits the detector to reside in the primary vacuum of the LHC with only a minimal amount of insensitive material towards the beam, to avoid acceptance losses. At the beginning of the run, the ALFA detectors are in withdrawn position far from the beam and, after the beam has stabilized, the detectors are moved to within 1.5 mm of the beam. The detector is based on staggered layers of square-shaped scintillating fibers, read out by Multi-Anode Photomultiplier Tubes (MAPMTs). These fibers are made of organic scintillators with a fast decay time of 2.8 ns; however, they provide radiation hardness in the range of a few kGy. The MAPMT technology allows readout of the relatively large number of scintillating fibers [50].

1.7 ATLAS Software and Computing Tools

The core of ATLAS software consists of the Athena framework [51] with libraries for event simulation, reconstruction, visualisation, etc., and a set of tools that facilitate the writing of analysis programs developed within the framework. It contains over 2000 individual software packages and external dependencies, including over 100 software

packages including HepMC [52] and Geant4 [53]. The candidate reconstruction and event selection are done on the Athena framework producing the output data files that are then processed by an analysis program.

The analysis program can be written in C/C++ or Python utilizing CERN ROOT [54] with usage of the RooFit [55] and RooStats [56] frameworks. In general, the ROOT and Athena frameworks are well connected, but they can be used independently.

1.7.1 Athena

The Athena framework is mainly written in C++ and Python and is based on the Gaudi architecture [57]. It is used as a common framework for monitoring detector performance and conducting physics studies. It also provides functionality for the event reconstruction, event simulation, analysis tools and control for High Level Triggers (HLT).

The framework is designed to maintain strict separation between transient and persistent data. This allows individual components to be easily replaced as technologies evolve, which is essential for an experiment that will run for several decades.

One of the major upgrades in Run 3 is that of Athena whose algorithms are being optimized for multi-threaded CPUs and efficient memory usage [58].

1.7.2 ROOT

ROOT is an object-oriented analysis toolkit for data processing developed by CERN; it is available under the LGPL license. ROOT follows C++ syntax and provides a set of advanced statistical analysis and visualization tools. The ROOT framework provides containment for analysis processing and storage of analysis results in the proprietary ROOT tree structure. It also allows usage of parallel computing tools for effective processing of large data files. The analysis presented here is processed using ROOT version 6.20/06 [59]. ROOT provides the following packages:

- The **RooFit** package is a toolkit for modeling the expected distribution of events in a physics analysis. Models can be used to perform unbinned likelihood fits, produce plots, and generate "toy Monte Carlo"[2] samples for various studies. The RooFit tools are integrated into the object-oriented and interactive ROOT graphical environment. The software is primarily designed as a particle physics data analysis tool, but it could be used as a powerful tool for other types of data analysis.

- **RooStats** is used to create advanced statistical tools required for the analysis of LHC data, with emphasis on discoveries, confidence intervals, and combined measurements. The classes are built on top of the RooFit package, which provides functionality for easily creating probability models, for analysis combinations and for digital publications of the results. It is organized as a joint collaboration between ATLAS and CMS and is based on ROOT and RooFit.

[2]Toy Monte Carlo is a method based on random generators using simplified models to represent the more complex physical problem.

1.7.3 ATLAS Event Data Model

The event data model (EDM) of the ATLAS experiment ensures commonality across the detector subsystems and subgroups such as triggers, test beam reconstruction, combined event reconstruction and physics analysis. Additionally, the EDM allows the use of common software between online data processing and offline reconstruction. The EDM provides the infrastructure to ensure accessibility of data even after the data model is changed.

The EDM has undergone substantial upgrades after the first data-taking run, Run 1, even though it was very successful. One of the main problems with the EDM during Run 1 was that the event data could not be directly read by ROOT and had to be converted to a series of ROOT formats which caused an increase in the storage requirements [60]. To alleviate these problems, ATLAS converted the complex transient data model to a simpler persistent data model which could be written to ROOT directly. This new ATLAS event data model for analysis is called the xAOD (Analysis Object Data) [61]. In this model, when the RAW data are reconstructed using Athena, the output is written into the xAOD format. The final analysis dataset, incorporating n-tuples, can be created using Athena and ROOT or from xAOD by skimming[3] or slimming[4] using the derivation framework; that framework is used to create the intermediate data products from the output of reconstruction by removing and adding information while maintaining the structure of the EDM. The final component of the model is the analysis framework, which is then used by physicists to read the derived data products, apply various combined performance tools and

[3]Skimming is the removal of whole events, based on the features of the event.

[4]Slimming is the removal of variables within a given object type, uniformly across all events.

produce the final analysis n-tuple.

The physics analysis is usually performed on the final n-tuples, producing plots and applying various statistical tools to extract physics parameters. Figure 1.10 diagrams the flow of the data in the ATLAS Run 2 EDM.

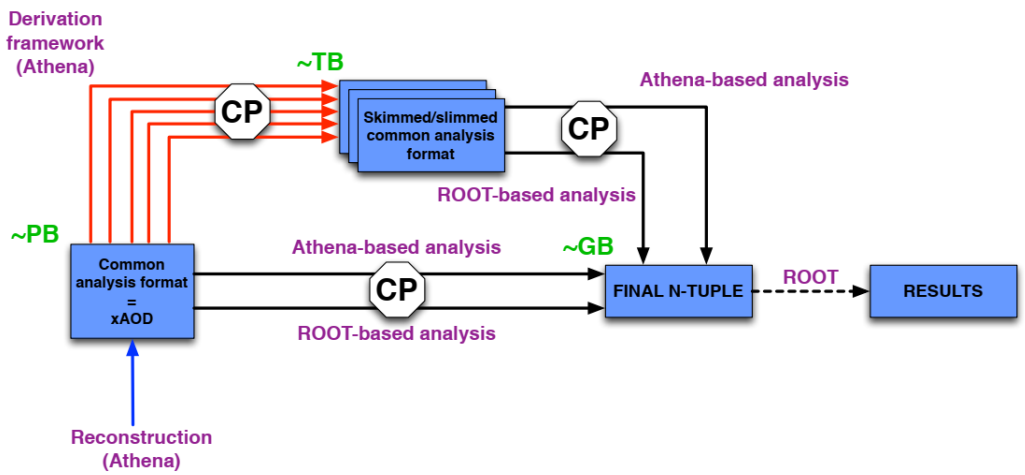

Figure 1.10: The ATLAS Run 2 analysis model consists of a new EDM (xAOD), a centralized data-reduction framework (derivation framework), and a dual-use infrastructure for applying combined performance group recommendations [61].

The BPhysics working group extensively uses the derivation framework where for each topology, a stand-alone derivation is used. This thesis covers the following decays, which share a common topology: $B_s^0 \to J/\psi(\to \mu^+\mu^-)\phi(\to K^+K^-)$, $B_d^0 \to J/\psi(\to \mu^+\mu^-)K^{*0}(\to K^\pm\pi^\mp)$, and $B^\pm \to J/\psi(\to \mu^+\mu^-)K^\pm$. These decays are covered by the BPHY5 derivation where a cascade vertex fit looks for the vertex formed by two muons originating from the J/ψ decay and one or two additional kaon tracks.

1.7.4 Monte Carlo Simulation

Monte Carlo (MC) event generators are used extensively in all the phases of a collider physics experiment. At the beginning, the generator is used for studying the physics reach of detector concepts and for designing the facilities and the detectors. The data reconstruction software is developed and optimized on the MC samples, and any upgrade or change is validated with respect to the MC simulation. The MCs are used to study the detector response to a selected signal and background processes in a physics analysis. The whole MC simulation has to proceed through a series of steps: event generation, simulation and digitization.

Event Generation

The first step of an MC simulation is the event generation. There is a variety of general and specialized event generators, but the ATLAS experiment employs two general purpose event generators: Pythia [62] and Herwig [63]. Pythia and Herwig simulate the initial parton collision described by perturbative QCD. For some studies, an additional event generator needs to be used. For B-Physics analysis, ATLAS uses a specialized version of Pythia called PythiaB [64], and in some cases the standard Pythia decay processes are replaced by EvtGen [65].

Pythia8 is the most commonly used general-purpose event generator for high-energy particle collisions. It uses a parton shower model that is based on the assumption that any $2 \to n$ process, with a complex final state, can be achieved by starting from an elementary $2 \to 2$ process. The final state is generated through a sequence of steps. In the first step, each proton in two colliding beams is characterized

by a set of parton distribution functions which define the partonic substructure of the proton. In the second step, one shower initiator parton from each beam starts a sequence of branchings, such as $q \to gg$, which builds up an initial-state shower. One incoming parton from each of the two showers enters the hard process that is described by QCD in leading order perturbation theory. After this, the generation of all subsequent activity at the partonic level follows, involving final-state radiation, multiple parton-parton interactions and the structure of beam remnants. In the final step, hadronisation of this final parton configuration is achieved, followed by the decays of unstable particles [62].

PythiaB provides an interface to Pythia dedicated to the simulation of beauty events; it also brings several functionalities for BPhysics studies [64]. It offers some advantages over standard Pythia.

- Events involving b-quarks are simulated faster in PythiaB. The events containing the b-quark are usually generated through one of the following mechanisms: flavour creation ($gg \to b\bar{b}$ and $qq \to b\bar{b}$), flavour excitation ($gb \to gb$) and gluon splitting ($g \to b\bar{b}$). However, only 1% of events are expected to contain a b and $\bar{b}$-quark in the standard Pythia simulation. In PythiaB, to speed up the process, the simulation is interrupted after the parton development to check for the presence of $b\bar{b}$ quark pairs. Only the events passing the user-defined cuts are used for the hadronisation in PythiaB.

- It offers an option to force the b-quark to decay into the channel of interest while allowing the opposite $\bar{b}$-quark to decay through any allowed channels.

- It provides an option to define b-production parameters, such as a multiple

particle interaction model, structure functions, the factorization scale or gluon probabilities.

EvtGen simulates the decays of heavy flavor particles, primarily B and D mesons. It uses spin algebra and complex decay amplitudes to generate each branch of a given full decay tree, taking into account angular and time-dependent correlations which allow for the simulation of CP-violating processes such as $B_s^0 \to J/\psi(\to \mu^+\mu^-)\phi(\to K^+K^-)$.

1.8 The Trigger System

The ATLAS experiment records about 1 kHz of physics events, out of the LHC design bunch crossing rate of 40 MHz. ATLAS employs a two-level trigger system to achieve high selection efficiency for physics events while reducing the background rate. The event selection is based on predefined physics signatures or the presence of events that are physically interesting, such as events with high p_{T}, objects with high missing transverse energy, E_{T}, that is not detected by the particle detector, but is expected to be conserved according to the laws of physics, or events with certain particles in the final state. This helps to reduce the size of the datasets that need to be analysed later. In addition, the trigger system exploits algorithms using topological information and multivariate methods to carry out the filtering for the many physics analyses pursued by the ATLAS collaboration.

The trigger system in Run 2 (2015-18) and Run 3 (2022-2025) consists of a hardware-based first level trigger (Level-1) [66] and a software-based high level trigger

(HLT) [67]. A schematic overview of the ATLAS trigger and data acquisition system is shown in Figure 1.11.

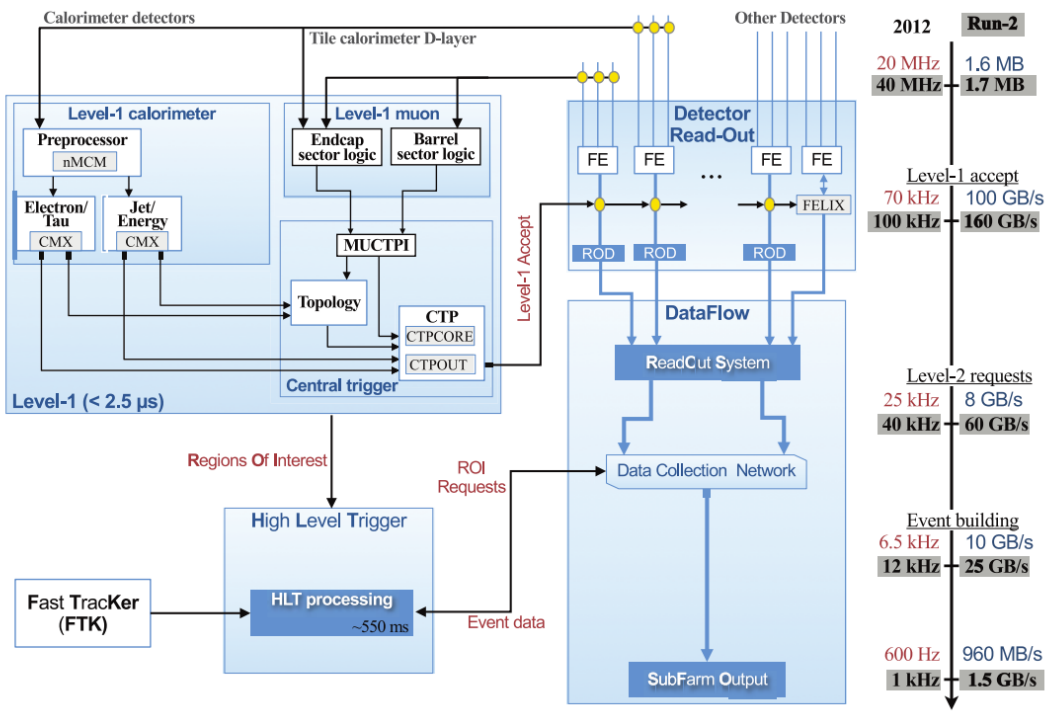

Figure 1.11: Schematic overview of the Run 2 configuration of the Trigger and DAQ system [68].

1.8.1 Level-1 (L1) Trigger

The L1 trigger is a hardware-based trigger using dedicated custom electronics to trigger on events from the calorimeter and muon detectors with a coarse granularity and lower energy/momentum resolution [69]. It accepts events at a rate up to the maximum detector read-out rate of 100 kHz, down from the bunch crossing rate of about 40 MHz, within a latency of 2.5 μs. The L1 calorimeter (L1Calo) trigger takes signals from the calorimeter detectors as input [70]. The L1 muon (L1Muon)

trigger uses hits from the RPCs in the barrel and TGCs in the end caps to determine the deviation of the hit pattern from that of a muon with infinite momentum [71]. The L1 trigger decision is formed by the Central Trigger Processor (CTP) which receives inputs from the L1Calo trigger, the L1Muon trigger through the L1Muon Central Trigger Processor Interface (MUCTPI) and the L1 topological (L1Topo) trigger [72] as well as trigger signals from several detector subsystems. The L1 trigger can select events on the basis of event-level quantities like the total energy deposited in the calorimeter, the multiplicity of objects above thresholds in, e.g., transverse momentum, or by considering topological requirements on reconstructed quantities such as invariant mass. The topological requirements are applied in the L1Topo trigger to geometric or kinematic combinations between trigger objects received from the L1Calo or L1Muon systems. For each L1-accepted event, the Front-End (FE) detector electronics read out the event data for all detectors. The data are sent first to ReadOut Drivers (RODs), performing the initial processing and formatting, and then to the ReadOut System (ROS) to buffer the data. The data from the different sub-detectors are sent from the ROS to the second stage of the trigger, the High-Level Trigger (HLT), only when requested by the HLT. In addition to performing the first selection step, the L1 triggers identify Regions-of-Interest (RoIs) in η and ϕ within the detector to be investigated at the second trigger stage. There is no tracking information extracted from the ID, because the readout system is not fast enough to acquire the required information.

1.8.2 High Level Trigger (HLT)

The second stage of the trigger, the HLT, is software-based. A typical reconstruction sequence makes use of dedicated fast trigger algorithms to provide early rejection, followed by more precise and more CPU-intensive algorithms to perform offline-like reconstruction. It uses data with full granularity within the RoI provided by the L1 and combines information from all detectors, including the ID. These algorithms are executed on a dedicated computing farm of approximately 40,000 selection applications known as Processing Units (PUs) with networking built with commercial technologies. The PUs are designed to make decisions within a few hundred milliseconds. A step in such a sequence of algorithms will typically execute one or multiple feature-extraction (FEX) algorithms requesting event-data fragments from within an RoI and terminate on a hypothesis algorithm (HypoAlg) which uses the reconstructed features to decide whether the trigger condition is satisfied or not. In some cases, information from the full detector is requested in order to reconstruct physics objects. The HLT software is largely based on the offline software Athena (Section 1.7.1). The physics recording rate of the HLT during an ATLAS data-taking run is on average 1.2 kHz with an average physics throughput to permanent storage of 1.2 GB/s. Once an event is accepted by the HLT, the Sub-Farm Output (SFO) sends the data to permanent storage for offline reconstruction and exports the data to the Tier-0 facility [73] at CERN's computing centre.

Chapter 2

Lifetimes of B^0_{d} and $B^{\pm}$ Mesons

2.1 Introduction

The measurement of the various B-meson lifetimes is of particular significance for some theoretical models. The Spectator Model, discussed in Section 2.1.1, is a basic model that expects the same lifetimes for all B-mesons. The Heavy Quark Expansion (HQE) approach, discussed in Section 2.1.2, is a sophisticated model that permits estimates of the differences in the lifetimes and their magnitudes. The lifetimes of B-mesons and their ratios allow us to examine the adequacy of the Spectator Model and the accuracy of the HQE model.

2.1.1 The Spectator Model

The Spectator Model is a simple theoretical way to look at the decays of hadrons that have a heavy quark. In this model, only the heavy quark changes in the decay, while

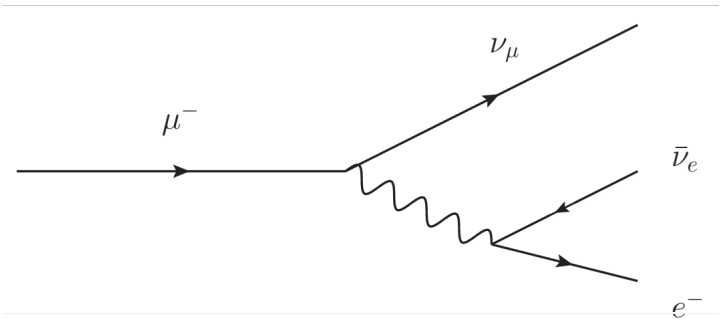

Figure 2.1: Feynman diagram for the decay of a muon.

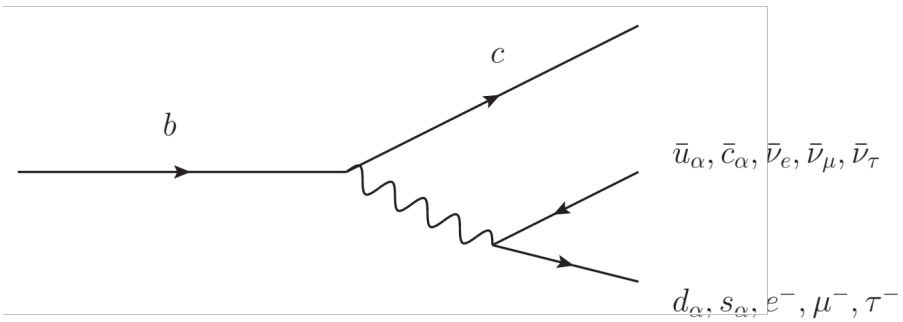

Figure 2.2: Feynman diagram for the decay of a b-quark.

the light quarks of the hadron stay the same. The model predicts that the lifetime is the same for all the hadrons that have the same heavy quark, regardless of the other quarks they contain. The heavier the quark, the more valid the approximation.

The lifetime of a B-meson can be approximated by the lifetime of a free b-quark, which is calculated from the ratio of the muon decay rate, assuming the process in Figure 2.1, to the b-quark decay rate, assuming the process in Figure 2.2.

The decay width of the muon in the first order process is given by

$$\Gamma_\mu = \frac{G_F^2}{192\pi^3} m_\mu^5, \tag{2.1}$$

where m_μ is the mass of the muon and G_F is the Fermi coupling constant given by

$$G_F = \frac{\sqrt{2}}{8}\frac{g^2}{m_W^2}. \tag{2.2}$$

The g is the weak interaction coupling constant, and m_W is the mass of the W-boson. Experiments on the lifetime of the muon have measured the value of G_F to be 1.166×10^{-5} GeV^{-2}.

The decay width of the b-quark can be estimated using Equation 2.3 with the following modifications:

- the muon mass, m_μ, is replaced with the mass of the b-quark, m_b,
- a quark to quark coupling between the b-quark and the c-quark is introduced using the square of the CKM matrix element, $|V_{cb}|^2$, and
- because the W-boson can decay into any of the three lepton generations and the two quark generations with three color variations, the decay of the b-quark has 9 decay channels that are kinematically allowed. The muon, on the other hand, only has one kinematically allowed decay channel. This results in a phase space factor of 9 for the decay of the b-quark.

Taking these into account, the decay width of the b-quark can be written as

$$\Gamma_\mu = \frac{9|V_{cb}|^2 G_F^2}{192\pi^3} m_b^5. \tag{2.3}$$

The lifetime of a b-quark in terms of the muon lifetime is given by

$$\tau_{\rm b} = \tau_{\mu} \left[\frac{m_{\mu}}{m_{\rm b}}\right]^5 \frac{1}{9|V_{\rm cb}|^2} \approx 1.3 - 1.7 \text{ ps}, \tag{2.4}$$

with $m_{\rm b} = 4.18 \pm 0.003$ GeV and $|V_{\rm cb}| = (40.8 \pm 0.14) \times 10^{-2}$ [10]. The predicted value is of the order of the observed B-meson lifetimes.

The Spectator Model predicts equal lifetimes for all b-hadron species. However, measurements reveal that there are non-negligible differences in the lifetimes of the various B-mesons, which follow the hierarchy:

$$\tau_{\rm B^{\pm}} \ > \ \tau_{B^0_{\rm d}} \approx \tau_{B^0_{\rm s}} \ > \ \tau_{B_{\rm c}}. \tag{2.5}$$

2.1.2 The Heavy Quark Expansion

One theoretical approach to the study of b hadron lifetimes is the Heavy Quark Expansion (HQE) [74–80] which is based on the operator product expansion (OPE) [81].

The HQE is a method to separate the decay amplitude into two parts: the non-perturbative, long-distance part that comes from QCD and the short-distance part that comes from electroweak interactions. In the HQE framework, the total decay width of a b-flavored hadron can be written as an expansion in powers of the inverse of the b-quark mass as follows:

$$\Gamma = \Gamma_0 \left[1 + A_2 \left(\frac{\Lambda_{\rm QCD}}{m_{\rm b}}\right)^2 + A_3 \left(\frac{\Lambda_{\rm QCD}}{m_{\rm b}}\right)^3 + ... + A_{\rm N} \left(\frac{\Lambda_{\rm QCD}}{m_{\rm b}}\right)^N\right], \tag{2.6}$$

where Γ_0 is the free b-quark decay width, as given in the spectator model, $\Lambda_{\rm QCD}$ is

the QCD scale parameter, and the A_N are computable coefficients. Equation 2.6 describes the following spectator and non-spectator effects:

- At the lowest or leading order, the decay is described by the Spectator Model, with the light spectator quark having no influence. This term is universal for all b-hadron species and there is no contribution from the $\mathcal{O}(\frac{1}{m_b})$ term.

- At order $(\frac{1}{m_b})^2$, the first correction term appears. The Fermi motion of the b-quark and from spin interactions between the light and heavy quarks is included at this level. This term is sensitive to lifetime differences between mesons and baryons. As an example, the decay rate of baryons, which have two light quarks with no net spin, is higher than that of mesons, which have one light quark with half-integer spin. As a result, the baryon lifetime is decreased by about 2% relative to the meson lifetime.

- At order $(\frac{1}{m_b})^3$, the non-spectator effects, Pauli interference and weak annihilation, arise. These effects are enhanced by a relatively large phase space factor of $16\pi^2$. This term also includes the non-perturbative matrix of four-quark operators, which has recently [82] been calculated using QCD sum rules [83, 84] formulated in Heavy Quark Effective Theory (HQET) [85]. The largest contributions to the total uncertainty on the lifetime ratio, as predicted with HQE, come from the hadronic matrix elements.

2.2 Lifetime Measurement of the B^0_{d}-meson

This dissertation focuses on the measurement of the lifetime of the B^0_{d}-meson using 140 fb^{-1} of integrated luminosity collected by the ATLAS detector at $\sqrt{s} = 13$ TeV during the period 2015-18 at the LHC. The meson is identified through a combined mass and lifetime reconstruction of the channel $J/\psi(\rightarrow \mu^+\mu^-)K^{*0}(\rightarrow K^{\pm}\pi^{\mp})$.

The predicted average decay width of the B^0_{d}-meson is $\Gamma_{\mathrm{d}} = (0.63^{+0.11}_{-0.07})$ ps^{-1} [85]. Measurements of the lifetime of the B^0_{d}-meson have been reported by a variety of experiments. The previous measurements of b-hadron lifetimes with the highest precision at the LHC have been reported by LHCb [86, 87], ATLAS [88, 89], and CMS [90].

2.3 Data-taking Conditions and Simulations

The analysis used several triggers, as the data collection spanned periods with varying instantaneous luminosity. All triggers used in this study were based on the identification of a $J/\psi \rightarrow \mu^+\mu^-$ decay, with p_{T} greater than 4 GeV, 6 GeV or 11 GeV for each muon in the dimuon pairs. Quality requirements were imposed on the data, notably on the performance of the MS, ID and calorimeter systems. The analysis used pp collision data with an integrated luminosity of 140.1 ± 1.2 fb^{-1} [91], measured by the LUCID-2 detector [46].

A Monte Carlo (MC) sample of 50M signal candidates was generated for modeling the $B^0_{\mathrm{d}} \rightarrow J/\psi K^{*0}$ decays in the ATLAS detector. The b-hadron production in pp collisions was simulated using Pythia 8.244 [92] tuned with ATLAS data. The

generation was made with the A14 set of parameter values [93] together with the CTEQ6L1 set of parton distribution functions [94]. The MC events were then passed through the full ATLAS detector simulation program based on the ATLFAST2 procedure [95] using the Geant4 package [96]. The same software that processed the detector data also was used to reconstruct the simulated events. The MC events were adjusted to match the data in terms of pile-up and trigger conditions.

2.4 Data and Event Selection

Only events that passed the trigger selections were considered. In addition, each event had to have at least one primary vertex reconstructed from four or more ID tracks, and at least one pair of oppositely charged muons reconstructed from both the MS and the ID. The muons used in the analysis were required to meet the tight[1] working point identification criteria. Since the mass resolution varies in different regions of the detector, the J/ψ candidates were split into three groups based on the pseudorapidity η of the muons. In the first subset, both muons have $|\eta| < 1.05$, where the values $\eta = \pm 1.05$ mark the boundaries of the MS barrel region. In the second subset, one muon has $1.05 < |\eta| < 2.5$ and the other muon has $|\eta| < 1.05$. The third subset contains candidates where both muons have $1.05 < |\eta| < 2.5$. The subsets are combined to use as one dataset. To get the J/ψ mass and mass resolution for these three groups, a maximum likelihood fit was applied, and the signal region was set symmetrically about the fitted mass in each case, keeping 99.7% of the J/ψ

[1]To achieve the highest muon purity, tight muon reconstruction sacrifices some efficiency and demands combined muons with hits in at least two MS stations and other criteria, as explained in Reference [97].

candidates from the fits. The $K^{*0} \to K^\pm\pi^\mp$ decay candidates were reconstructed from all tracks that were not identified as muons. Only oppositely charged tracks passing the $p_T(K^{*0}) > 3.5$ GeV, $p_T(K^\pm) > 1$ GeV, $p_T(\pi^\mp) > 0.5$ GeV, and $|\eta| < 2.5$ criteria were used, and the invariant mass of the $K^{*0} \to K^\pm\pi^\mp$ candidate was required to lie in the range 846 MeV$< m(K^\pm\pi^\mp) <$ 946 MeV.

All combinations of the selected $J/\psi \to \mu^+\mu^-$ and $K^{*0} \to K^\pm\pi^\mp$ candidates were fitted to a common vertex, forming the $B^0_d \to J/\psi K^{*0}$ candidates. The vertex fit was constrained by fixing the invariant mass of the two muon tracks to the PDG value of the J/ψ mass [10]. The $B^0_d \to J/\psi K^{*0}$ candidates that fulfill the χ^2/ndof < 3 were accepted for further analysis. The B^0_d candidate with the lowest χ^2/ndof was selected in events with more than one candidate passing the criteria. A total of 10559554 B^0_d candidates were collected within the mass range $(5.00 - 5.65)$ GeV. This range was chosen to allow enough background events in the sidebands of the mass distribution for precise determination of the properties of the background events.

The average number of interactions per bunch crossing was 31, requiring a selection of the optimal primary vertex for the B^0_d-meson production. The primary vertex (PV) positions were updated after removing any tracks involved in the B^0_d-meson reconstruction. The PV candidate with the smallest three-dimensional impact parameter[2], a_0, was used. The simulated dataset gave the fraction of B^0_d events with the wrong production vertex. The PV reconstruction resolution in the transverse plane matched the beam spot size, so the true and the selected PV were the same. In the z-direction, 6% of the vertices were incorrect - the fraction where the distance

[2]The shortest distance from each PV candidate to the line extended from the reconstructed B^0_d-meson vertex along the B^0_d momentum vector.

between the true and the selected vertex was more than 3 times the z-resolution of the PV [98]. However since the proper decay time is calculated in the transverse plane, these cases do not have any impact on the lifetime determination, as was confirmed by MC.

For each B^0_d-meson candidate the proper decay time t was determined using:

$$t = \frac{L_{xy} m_B}{p_{T_B}}, \tag{2.7}$$

where L_{xy} is the transverse decay length which is the displacement in the transverse plane of the B^0_d-meson decay vertex relative to the primary vertex, projected onto the direction of the reconstructed transverse momentum of the B^0_d-meson candidate, and m_B denotes the mass of the B^0_d-meson, taken from Reference [10]. The simulated dataset showed that using the wrong production vertex does not affect the reconstructed proper decay time.

2.5 Maximum Likelihood Fit

A two-dimensional unbinned maximum likelihood fit describing both signal and background was used to extract the lifetime of the B^0_d-meson. The model for the signal described the $B^0_d \to J/\psi K^{*0}$ decays while the background model consisted of multiple components describing:

- prompt J/ψ-mesons originating from $pp \to J/\psi X$ decays and combined with a random K^{*0} candidate in the event, and

- combinatorial background arising from the combination of a J/ψ-meson produced in another b-hadron decay, combined with a K^{*0} candidate.

The inclusion of the prompt J/ψ background in the fit ensures that no proper decay lifetime cut needs to be applied to $B^0_{\rm d}$ candidates. The maximum likelihood function to fit the mass and proper decay time simultaneously is given by

$$\begin{aligned}\ln L = \sum_{i=1}^{N} w(\tau_i) \ln[& f_{\rm sig}\mathcal{M}_{\rm sig}(m_i)\mathcal{T}_{\rm sig}(\tau_i, \sigma_{\tau_i}, p_{{\rm T}_i}) \\ & +(1-f_{\rm sig})f_{\rm prompt}\mathcal{M}_{\rm prompt}(m_i)\mathcal{T}_{\rm prompt}(\tau_i, \sigma_{\tau_i}, p_{{\rm T}_i}) \\ & +(1-f_{\rm sig})(1-f_{\rm prompt})\mathcal{M}_{\rm bkg}(m_i)\mathcal{T}_{\rm bkg}(\tau_i, \sigma_{\tau_i}, p_{{\rm T}_i})], \end{aligned} \tag{2.8}$$

where $f_{\rm sig}$ is the fraction of signal events in the total number of events, N. The mass probability density function (PDF) $\mathcal{M}_{\rm sig}$ multiplied by the time PDF $\mathcal{T}_{\rm sig}$ describes the $B^0_{\rm d} \to J/\psi K^{*0}$ events. The prompt J/ψ background is described by the mass and lifetime PDF functions $\mathcal{M}_{\rm prompt}$ and $\mathcal{T}_{\rm prompt}$. The combinatorial background is described by mass component $\mathcal{M}_{\rm bkg}$ and corresponding lifetime distribution $\mathcal{T}_{\rm bkg}$. The mass m_i, the proper decay time τ_i and its uncertainty σ_{τ_i} in $p_{\rm T}$ bins are the values measured from the data for each event i. The weight $w(\tau_i)$ is described in Section 2.7.

2.5.1 The Invariant Mass PDFs

The $B^0_{\rm d}$ signal, prompt J/ψ background and background mass shapes are described by the PDFs $\mathcal{M}_{\rm sig}$, $\mathcal{M}_{\rm prompt}$ and $\mathcal{M}_{\rm bkg}$, respectively, in the fitted mass range. The

signal PDF $\mathcal{M}_{\rm sig}$ uses the Johnson S_U-distribution [99] to describe the mass:

$$\mathcal{M}_{\rm sig}(m_i) \equiv \frac{\delta}{\lambda\sqrt{2\pi}\sqrt{1+\left(\frac{m_i-\mu}{\lambda}\right)^2}} \exp\left[-\frac{1}{2}\left(\gamma+\delta\sinh^{-1}\left(\frac{m_i-\mu}{\lambda}\right)\right)^2\right], \quad (2.9)$$

where μ, γ, δ and λ are the parameters of the Johnson S_U-distribution. The first order polynomial function describes the prompt J/ψ background mass distribution while two exponential functions describe the mass distribution of the combinatorial background as shown below:

$$\mathcal{M}_{\rm bkg}(m_i) = \frac{f_{\rm massbkg}}{\lambda_{\rm bkg1}} \exp\left(\frac{-m_i}{\lambda_{\rm bkg1}}\right) + \frac{1-f_{\rm massbkg}}{\lambda_{\rm bkg2}} \exp\left(\frac{-m_i}{\lambda_{\rm bkg2}}\right), \quad (2.10)$$

where $\lambda_{\rm bkg1}$ and $\lambda_{\rm bkg2}$ are the slopes of the exponential functions and $f_{\rm massbkg}$ is the fraction associated with the first of them. The background away from the $B^0_{\rm d}$ mass region was not modeled because it includes partially reconstructed B-mesons and kinematic reflections. Two exponential functions was adequate to approximate the background in the chosen mass region of $(5.00-5.65)$ GeV, given the available statistics.

2.5.2 The Proper Decay Time PDFs

The PDF terms describing proper decay time are composed of three terms:

$$\mathcal{T}_j(\tau_i, \sigma_{\tau_i}, p_{{\rm T}_i}) = {\rm P}_j(\tau_i|\sigma_{\tau_i}, p_{{\rm T}_i}) \cdot {\rm P}_j(\sigma_{\tau_i}, p_{{\rm T}_i}), \quad (2.11)$$

where $j \in$ (sig, prompt, bkg) stands for signal, prompt or combinatorial background, respectively. The proper decay time resolution function convolves each PDF P_j to account for the lifetime resolution:

$$R(\tau^{'} - \tau_i, \sigma_{\tau_i}) \equiv \sum_{k=1}^{3} f_{\rm res}^{(k)} \frac{1}{\sqrt{2\pi}\ S^{(k)}\ \sigma_{\tau_i}} \exp\left(\frac{-(\tau^{'} - \tau_i)^2}{2(S^{(k)}\ \sigma_{\tau_i})^2}\right). \tag{2.12}$$

The $S^{(k)}$ are the scale factors or parameters of the fit, and σ_{τ_i} is the per-candidate uncertainty on τ_i. Parameters $f_{\rm res}^{(k)}$ are the relative fractions of each Gaussian function fulfilling the normalization condition $\sum f_{\rm res}^{(k)} = 1$.

The signal proper decay time distribution of the $B^0_{\rm d}$ candidates was modeled as an exponential function,

$$\mathrm{P}_{\rm sig}(\tau_i|\sigma_{\tau_i}, p_{\mathrm{T}_i}) = E(\tau^{'}, \tau_{B_d}) \otimes R(\tau^{'} - \tau_i, \sigma_{\tau_i}), \tag{2.13}$$

where $E(\tau^{'}, \tau_{B_d}) = \frac{1}{\tau_{B_d}} \exp(-\tau^{'}/\tau_{B_d})$ for $\tau \geq 0$ with the measured $B^0_{\rm d}$ lifetime τ_{B_d}.

The resolution function R describes the proper decay time distribution of the prompt J/ψ mesons:

$$\mathrm{P}_{\rm prompt}(\tau_i|\sigma_{\tau_i}, p_{\mathrm{T}_i}) = \delta_{Dirac}(\tau^{'}) \otimes R(\tau^{'} - \tau_i, \sigma_{\tau_i}) = R(\tau_i, \sigma_{\tau_i}). \tag{2.14}$$

For the combinatorial background, the proper decay time PDF, $\mathrm{P}_{\rm bkg}$, consists of the sum of three exponential functions, each convolved with the resolution function R:

$$\mathrm{P}_{\rm bkg}(\tau_i|\sigma_{\tau_i}, p_{\mathrm{T}_i}) = \left[\sum_{j=1}^{3} b_j \prod_{k=1}^{j-1}(1 - b_k) E(\tau^{'}, \tau_{\mathrm{bkg}_j})\right] \otimes R(\tau^{'} - \tau_i, \sigma_{\tau_i}), \tag{2.15}$$

where the τ_{bkg_j} are lifetimes describing three components of the combinatorial background, and the b_j are the fitted parameters corresponding to the relative fraction of each of the three background contributions.

The probability terms $\mathrm{P}_j(\sigma_{\tau_i}, p_{\mathrm{T}_i})$ in Eq. 2.11 are two-dimensional distributions introduced to describe the difference between the signal, prompt background, and combinatorial background for the values of the per-candidate time error σ_{τ_i} and p_{T} values, respectively. To split the signal and background, the *sPlot* technique [100] was applied. The mass distribution was the discriminating variable in this data-driven procedure.

2.6 Derivation of $\Gamma_{\rm d}$ from Effective Lifetime $\tau_{\rm d}$

The ratio of the lifetimes ($\tau_{\rm d}/\tau_{\rm s}$) of the $B^0_{\rm d}$ and $B^0_{\rm s}$ mesons is calculated from the ratio of their effective lifetimes, $\Gamma_{\rm d}/\Gamma_{\rm s}$. In a $B^0 - \bar{B}^0$ system, the effective lifetime, which is the difference in the lifetimes of the light (L) and heavy (H) mass eigenstates, is related [101] to the effective decay width Γ through:

$$\tau = \frac{1}{\Gamma}\frac{1}{1-y^2}\left(\frac{1+2Ay+y^2}{1+Ay}\right), \tag{2.16}$$

where the relative width difference $y \equiv \Delta\Gamma/2\Gamma$ for the difference $\Delta\Gamma \equiv \Gamma_{\rm L} - \Gamma_{\rm H}$ between the heavy and light eigenstates. Parameter A, which depends on the common final state f of the $B^0 - \bar{B}^0$ system, is defined through the expression

$$A \equiv \frac{R^{\rm f}_{\rm H} - R^{\rm f}_{\rm L}}{R^{\rm f}_{\rm H} + R^{\rm f}_{\rm L}}, \tag{2.17}$$

where the summed decay rate of the members of the system to the final state f is

$$\langle \Gamma(B^0(t) \to f) \rangle \equiv \Gamma(B^0(t) \to f) + \Gamma(\bar{B}^0(t) \to f) = R^{\rm f}_{\rm H} e^{-\Gamma_{\rm H} t} + R^{\rm f}_{\rm L} e^{-\Gamma_{\rm L} t}. \quad (2.18)$$

The $R^{\rm f}_{\rm L}$ and $R^{\rm f}_{\rm H}$ are the helicity amplitudes. In the $B^0_{\rm d} - \bar{B}^0_{\rm d}$ system, the value of y, taken from a combination of measurements by HFLAV [102], is 0.001 ± 0.010. In the absence of CP-violation, the helicity amplitudes $R^{\rm f}_{\rm L}$ and $R^{\rm f}_{\rm H}$ can be connected [103] to the polarization amplitudes $|A_i|^2$ (where $i = 0, \|, \perp$) of the final states through the following equations:

$$R^{\rm f}_{\rm H} = |A_\perp|^2, \text{ and} \quad (2.19)$$

$$R^{\rm f}_{\rm L} = |A_\||^2 + |A_0|^2. \quad (2.20)$$

Further, the polarization amplitudes are constrained by:

$$|A_\perp|^2 + |A_\||^2 + |A_0|^2 = 1. \quad (2.21)$$

The squares of the polarization amplitudes were taken from the world average values for the $B^0_{\rm d} \to J/\psi K^{*0}$ channel [104]:

$$|A_0|^2 = 0.571 \pm 0.007, \quad (2.22)$$

$$|A_\perp|^2 = 0.211 \pm 0.008, \quad (2.23)$$

and

$$|A_\||^2 = 0.218 \pm 0.011. \quad (2.24)$$

2.6.1 Uncertainty Calculation

To obtain the uncertainty in Γ_d, Equation 2.16 is differentiated with respect to the observables to yield the following:

$$\begin{aligned}\delta\Gamma_d = &\left(-\frac{1}{\tau_d^2}\frac{1}{1-y^2}\frac{1+2Ay+y^2}{1+Ay}\right)\delta\tau_d \\ &+\left(\frac{2y}{(1-y^2)^2}\frac{1+2Ay+y^2}{1+Ay}+\frac{1}{1-y^2}\frac{2A+2y}{1+Ay}-\frac{1}{1-y^2}\frac{1+2Ay+y^2}{(1+Ay)^2}A\right)\delta y \\ &+\left(\frac{1}{\tau_d}\frac{1}{1-y^2}\left(\frac{2y}{1+Ay}-\frac{1+2Ay+y^2}{(1+Ay)^2}y\right)\right)\delta A.\end{aligned} \tag{2.25}$$

The uncertainty in A, δA, can be obtained by differentiating the following expression for A in terms of the polarization amplitudes:

$$A = \frac{R_H^f - R_L^f}{R_H^f + R_L^f} = 2|A_\perp|^2 - 1. \tag{2.26}$$

The average decay width Γ_d and the uncertainty can be calculated using Equations 2.16 and 2.25 after inserting the values of y, A and the fitted effective lifetime of the B^0_d.

2.7 Time Efficiency Corrections

Fully simulated signal MC events are used to prepare time efficiency functions to correct the data for trigger inefficiencies and inefficiencies of offline reconstruction and all types of selection cuts, applied to data. Since the triggers were different in each year, the time-efficiency functions were built separately for each year. To extract the time efficiency from MC, a histogram of the proper-decay times of the signals

passing triggers, reconstruction and selection cuts was divided by a histogram of the proper-decay times of all generated signals. In both cases, the truth value of the proper-decay time was used. The ratio of the two histograms was then fitted to an analytical function. The best results achieved used the following function:

$$p_0 \cdot [1 - p_1 \cdot (\mathrm{Erf}((t - p_3)/p_2) + 1)], \tag{2.27}$$

where Erf denotes the error function and p_0, p_1, p_2 and p_3 are parameters determined in the fit to the MC events.
In order to validate the time-efficiency function, they were first used in the fit to reconstructed MC signal proper-decay times, where each event was given a weight equal to 1/(time-efficiency) in the relevant bin of the proper-decay time.

A number of studies were performed to understand how time efficiency functions for triggers and selection cuts impact the lifetimes (see Appendix A).

2.7.1 Systematic Uncertainties

To account for any potential systematic effects due to the time efficiency fits or due to the limited MC statistics, a large number of time efficiency functions were obtained by smearing the number of MC events in the time bins used to determine the time efficiency function. In order to propagate the uncertainties of the parameters in Equation 2.27, and their correlations, the efficiency histograms were randomly resampled; and for each bin independently, the number of events obtained before any reconstruction, triggers, or selection cuts are applied (in the denominator) was varied using Poisson randomization, while the efficiency ratio was varied using binomial

randomization. Based on these alternative efficiency histograms, alternative efficiency weights were constructed. The alternative efficiency functions were then used to rerun the unbinned maximum likelihood fit on the data, to obtain lifetimes. The set of fit results was characterised by its mean value and standard deviation; these were used to estimate the systematic uncertainty. A pull plot was made from the difference between the resulting lifetime and the lifetime before the smearing of the input data. In this study, pull plots were obtained for 50 time efficiency fits which were randomly generated for each year. Further, an extra step was taken to ensure that the obtained time efficiencies are different from each other.

Time efficiencies obtained from the ratios of the number of all events in the MC after final cuts to the number of true signal events were used to fit to the lifetimes of all events in the MC. Figures 2.3, 2.4 and 2.5 show the ratios of all events to true signal events and the fitted time efficiency functions for 2015+2016, 2017 and 2018, respectively, before the smearing of the input data.

These time efficiency fits were then used in the mass-lifetime fit using the MC samples. The extracted lifetimes of B^0_d-meson are shown in Figure 2.6.

Figures 2.7, 2.8 and 2.9 show the ratios of all events to true signal events for 2015+2016, 2017 and 2018, respectively, after smearing the input data. Only one plot out of 50 plots made for each year is shown.

For each year, the lifetime obtained after the smearing of the input data was

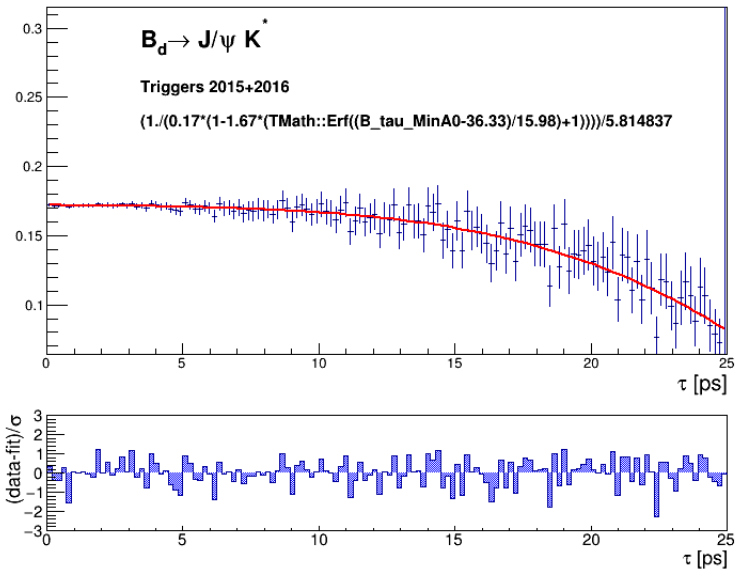

Figure 2.3: Time efficiency function for the events in the 2015+2016 MC data set.

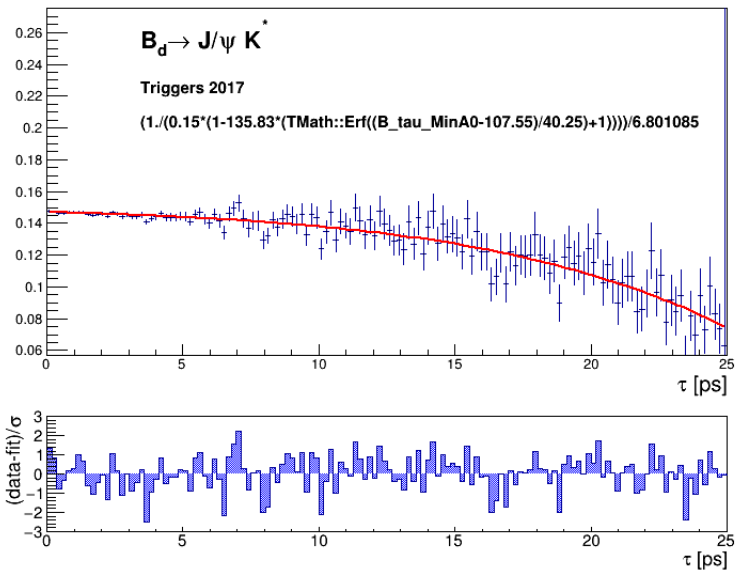

Figure 2.4: Time efficiency function for the events in the 2017 MC data set.

subtracted from the lifetime obtained before the smearing of the input data. Distributions of these differences between lifetimes before and after the smearing of the

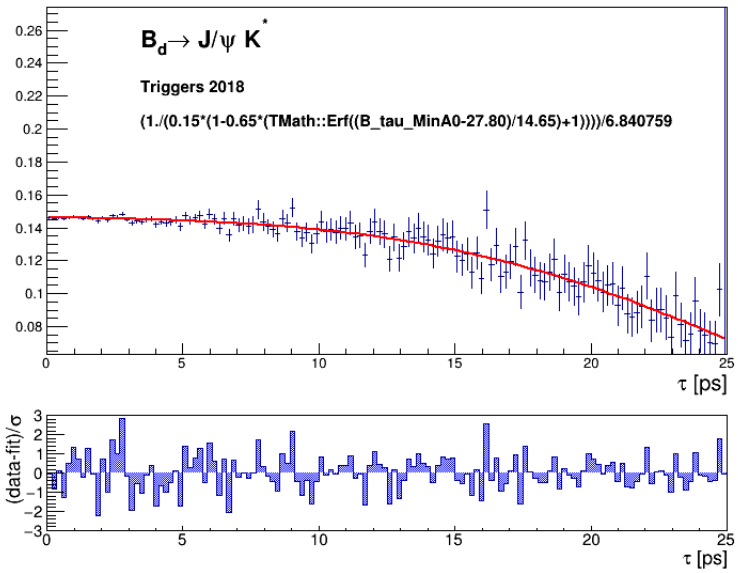

Figure 2.5: Time efficiency function for the events in the 2018 MC data set.

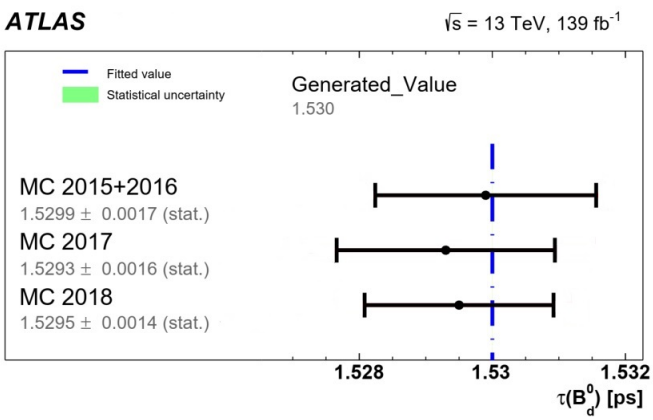

Figure 2.6: A comparison of B^0_d lifetime measurement results using the 2015+2016, 2017 and 2018 MCs.

input data using the events in the 2015+2016, 2017, and 2018 MC are shown in Figures 2.10, 2.11 and 2.12, respectively.

It can be seen from these plots that the systematic uncertainties due to time

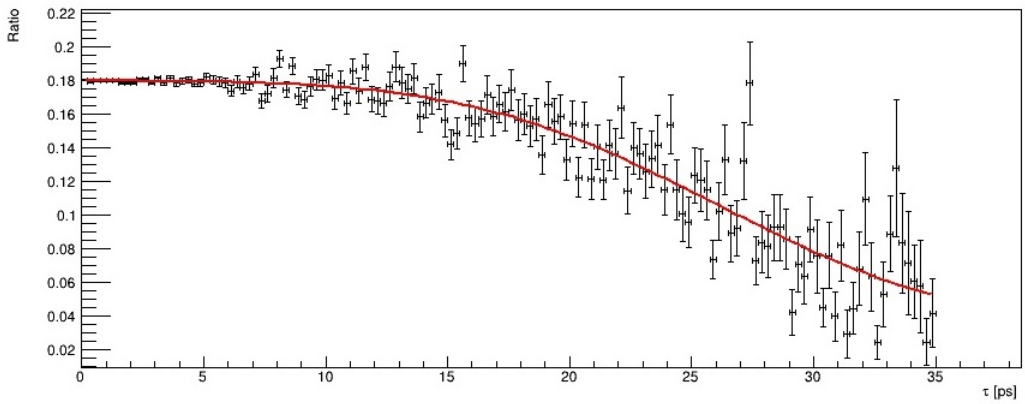

Figure 2.7: Ratios of the number of all events to the number of true signal events in the 2015+2016 MC data set after the smearing of the input data.

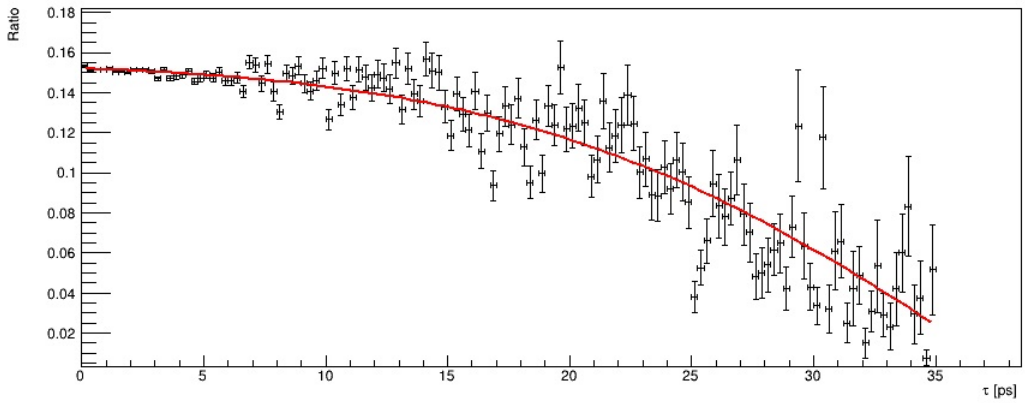

Figure 2.8: Ratios of the number of all events to the number of true signal events in 2017 the MC data set after the smearing of the input data.

efficiency fits using all events in the 2015+2016, 2017 and 2018 MC data sets are 0.0008, 0.0016 and 0.001, respectively. The extracted lifetime of the B^0_d-meson with statistical and systematic uncertainties is shown in Figure 2.13 for these three MC data sets.

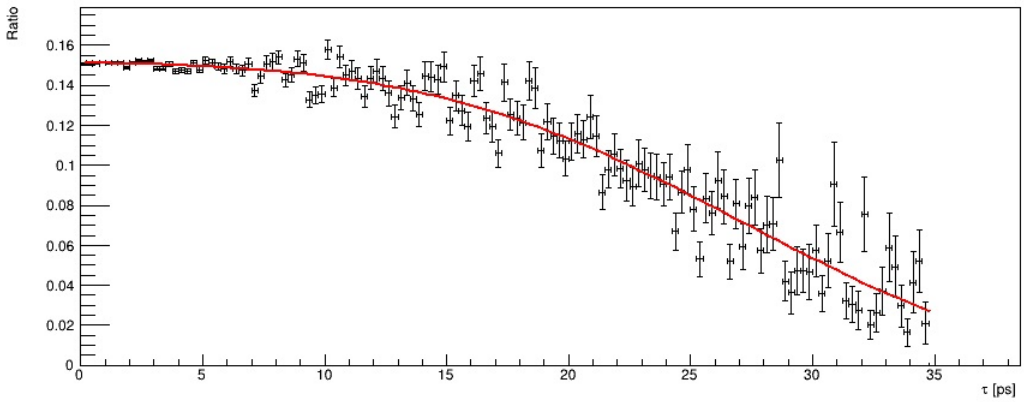

Figure 2.9: Ratios of the number of all events to the number of true signal events in the 2018 MC data set after the smearing of the input data.

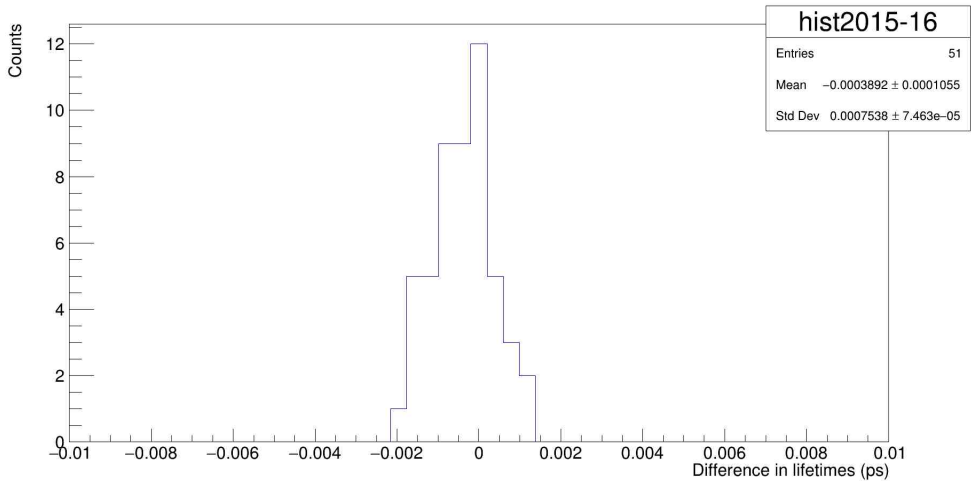

Figure 2.10: Distribution of differences between lifetimes before and after the smearing of the input data (before−after) using the events in the 2015+2016 MC data set.

2.8 Multiple Candidates and Optimal Candidate Selection

Since all B^0_d candidates are reconstructed from the $\mu^+\mu^-$ and $K^{\pm}\pi^{\mp}$ tracks, it is possible that some of the signal events contain B^0_d candidates reconstructed from

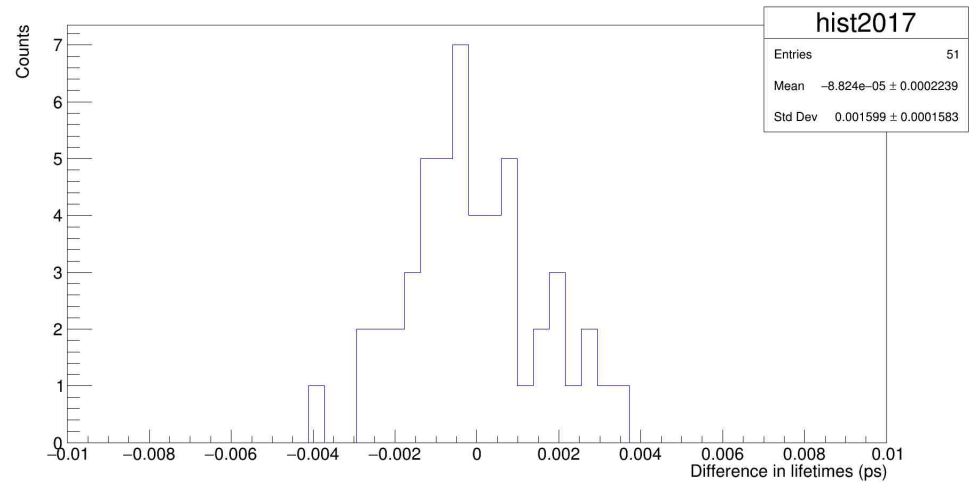

Figure 2.11: Distribution of differences between lifetimes before and after the smearing of the input data (before−after) using the events in the 2017 MC data set.

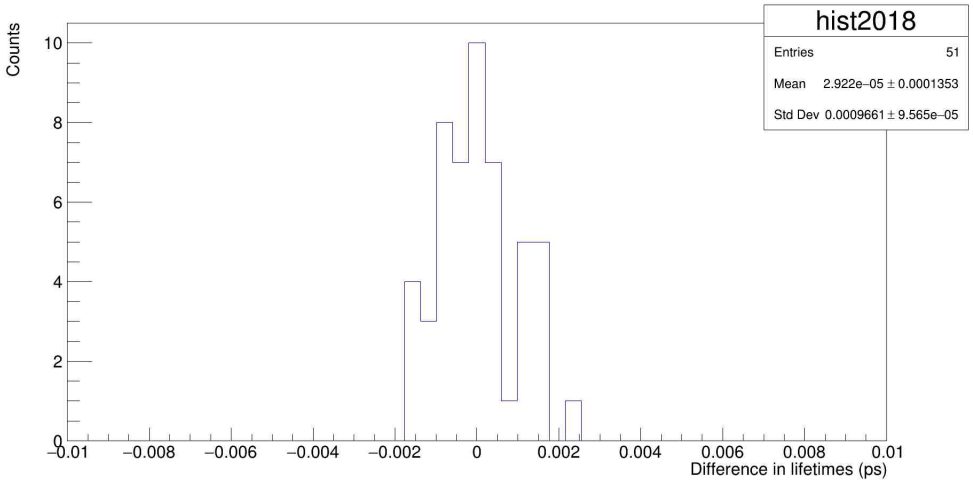

Figure 2.12: Distribution of differences between lifetimes before and after the smearing of the input data (before−after) using the events in the 2018 MC data set.

either combinations of fake tracks for the kaon and pion from the primary vertex or combinations of unrelated real tracks. Such events from fake or unrelated tracks are identified as self-background events. Since these candidates share the same J/ψ-meson, self-background events have slightly smaller lifetimes than that of the

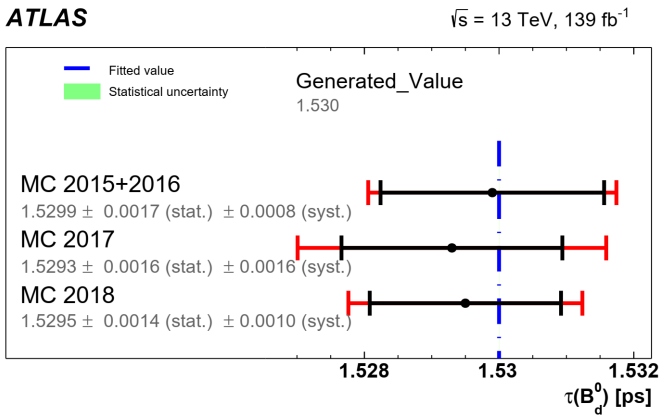

Figure 2.13: A comparison of results with statistical and systematic uncertainties using the 2015+2016, 2017 and 2018 MC data sets.

true signal events. The mass-lifetime fit does not have the necessary sensitivity to distinguish the self-background from the signal events. The self-background events, with smaller lifetimes, skew the observed lifetimes towards smaller values resulting in efficiency loss. This is mitigated by implementing stringent selection cuts.

This study was performed on MC data sets to check whether the fraction of multiple candidates is large enough to cause a non-negligible bias towards lower lifetimes, and whether the selection of candidates with the lowest χ^2 value per event is the most effective method to eliminate the self-background events. The percentages of events with multiple candidates in the data and MC data sets, after application of selection cuts, were found to be about 10% and 20%, respectively. The higher number of multiple candidates in the MC data sets was intended to study the worst case scenario. The selection cuts for the hadrons in the final states were applied to the p_{T} values and were taken from the Run 2 data characteristics as shown in Figure 2.14.

From Figure 2.14, it can be seen that the p_{T} cuts are

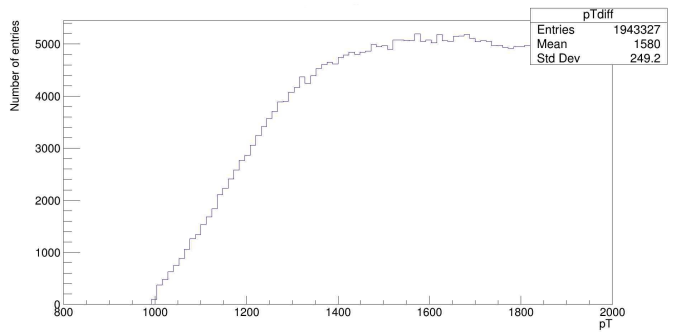

(a) $K^\pm$

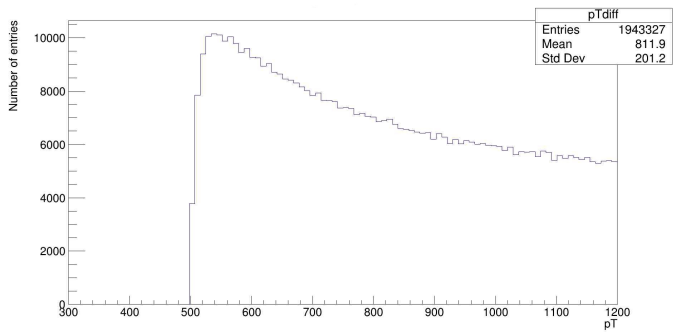

(b) $\pi^\mp$

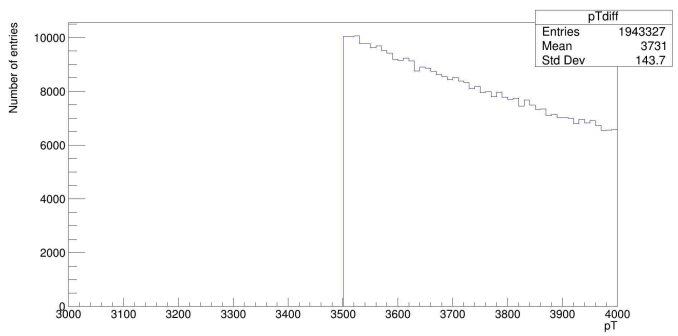

(c) K^{*0}

Figure 2.14: Number of events versus observed transverse momentum, for a)$K^\pm$, b)$\pi^\mp$, and c)K^{*0} in the Run 2 data. This information was used to choose the applied cut on p_T.

- $p_\mathrm{T}(K^\pm) > 1000$ MeV,
- $p_\mathrm{T}(\pi^\mp) > 500$ MeV, and

- $p_T(K^{*0}) > 3500$ MeV.

A normalized distribution of multiple candidates per event after application of the above selection cuts is shown in Figure 2.15.

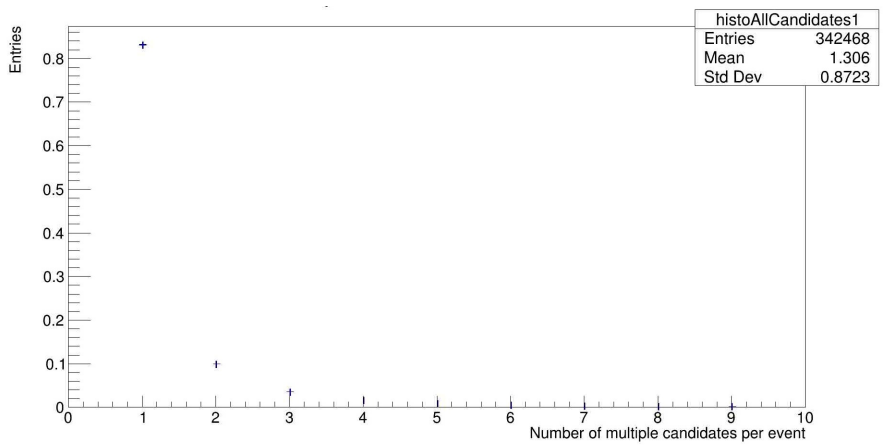

Figure 2.15: Normalized distribution of multiple candidates per event in the MC data set after application of the selection cuts.

From Figure 2.15, it can be seen that more than 80% of the events in the MC data set contain one candidate per event after application of the selection cuts. About 10% of the events contain two candidates per event, fewer than 4% contain three candidates, and so on. In Figure 2.16, the distribution of the difference between the proper decay times of the multiple candidates and that of the candidate with the lowest χ^2 value (the best χ^2 candidate), for each event in the MC data set is shown.

The following conclusions can be drawn from the distribution of proper decay time differences:

- Most of the differences are centered around zero, indicating that most of the events are single candidate solutions; and

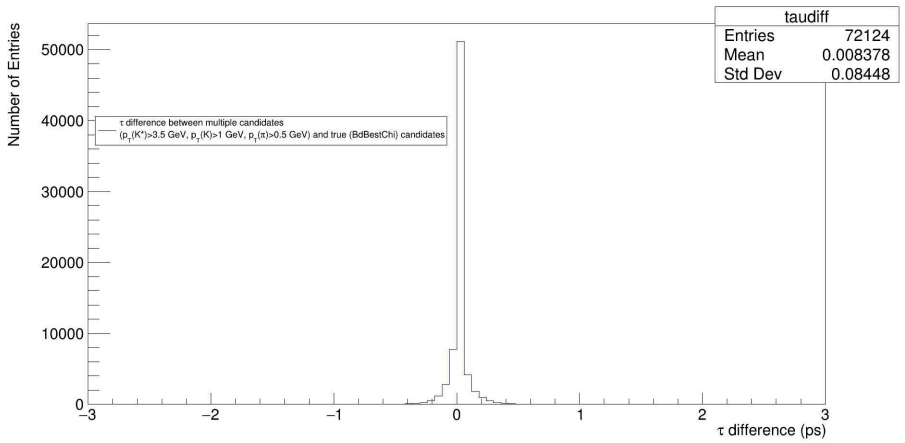

Figure 2.16: Distribution of the difference between the proper decay times in the events with the multiple candidates and that those with the candidates with the lowest χ^2 per event.

- the standard deviation is less than 1 fs indicating that multiple candidates are not a background concern in this study.

A similar observation was made for the distribution of transverse length differences between the best χ^2 candidates and the events with multiple candidates. An invariant mass distribution of the following event types was produced and is shown in Figure 2.17:

- events with a single candidate each. For multiple candidates, the candidate with the lowest χ^2 value was used. These are called "BdBestChi" or best χ^2 events;
- "best χ^2" events satisfying the condition "inclusiveTrueBd" to ensure that only events with 4 tracks are selected;
- all single candidate events and multiple candidate events, referred to as "BdAllCandidates," which satisfy the "inclusiveTrueBd" condition; and

- all events with multiple candidates in the "BdAllCandidates" set, i.e, all events with a single candidate were filtered out to study systematic and background shifts on the lifetime of B_d^0-mesons due to multiple candidate events.

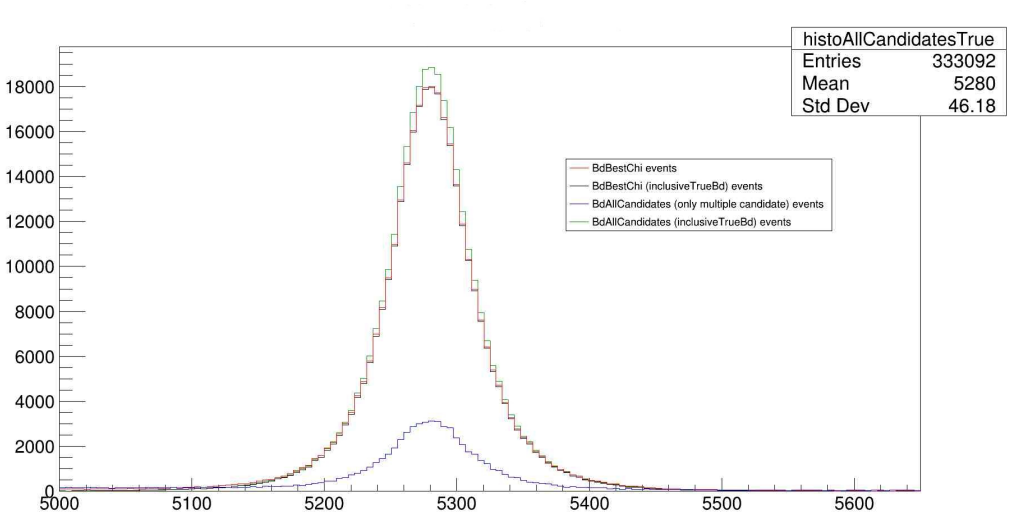

Figure 2.17: The invariant mass (MeV) distributions of the four categories of events.

The following conclusions can be drawn from the invariant mass distributions:

- the peak of the distribution of the combined set of events is centered around 5280 MeV, which is close to the mass of B_d^0-mesons compiled by the PDG, 5279.65 MeV [10];

- the number of candidates in the "BdAllCandidates" set satisfying the selection "inclusiveTrueBd" is highest, as this pool of events contains all events with single or multiple candidates per event;

- there is no difference between the number of events in the "BdBestChi" and "BdBestChi" sets satisfying the "inclusiveTrueBd" selection, implying that all

events have four tracks before imposition of this criterion; and

- the smallest contribution to the invariant mass distribution comes from the category of events with multiple candidates in the "BdAllCandidates" set. This is expected, as more than 80% of the events in Figure 2.15 were found to be single candidate events and were filtered out from this category of events.

Optimal Candidate Selection

As there is no reconstruction of K^{*0} possible due to lack of a hadronic identification in the ATLAS detector, the precision of vertex fitting is reliant on the J/ψ reconstruction. This leads to the possibility of several candidates within an event meeting the criteria for identical vertex precision. In order to check further whether, for an event having multiple candidates, the selection of a B_d^0 candidate with the lowest χ^2 value is the optimal method for candidate selection, seven sample data sets were prepared. In them, for an event with multiple candidates, a candidate is selected randomly. These were made for each year from the full Run 2 data set. Each of the seven data sets was made using a random number generator, TRandom3 class [105](which comes with ROOT toolkit) such that candidate selections in all seven data sets are different, to avoid bias. In addition to these seven samples with randomly selected candidates, a sample in which a candidate with the highest χ^2 value was selected was also made from the Run 2 data set, for each year. These samples have the candidates that satisfy the worst χ^2 selection.

Mass-Lifetime fits were performed using the following:

- samples containing the "BdBestChi" or best χ^2 events;

- samples containing randomly selected candidates from the events with multiple candidates; and
- samples containing candidates having the worst χ^2 value from the events with multiple candidates.

No time-efficiency corrections were used to address discrepancies in trigger and selection cuts, to avoid any systematic shifts in the lifetimes. Comparisons of lifetimes extracted from the above samples for 2015, 2016, 2017 and 2018 are shown in Figures 2.18, 2.19, 2.20 and 2.21, respectively.

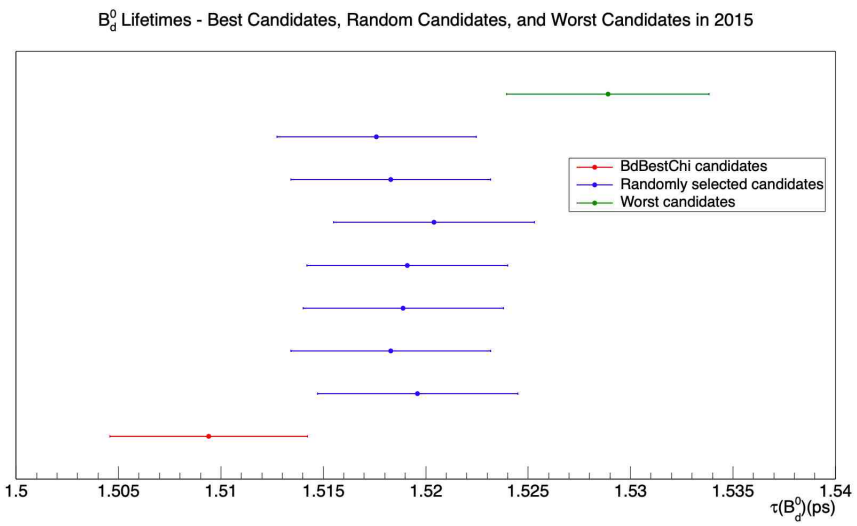

Figure 2.18: A comparison of lifetimes extracted from one sample containing the best χ^2 events, seven samples containing randomly selected candidates and one sample containing candidates with the worst χ^2 value, for the year 2015.

The following conclusions can be drawn from Figures 2.18- 2.21:

- Lifetimes extracted from events in the samples which contain candidates that

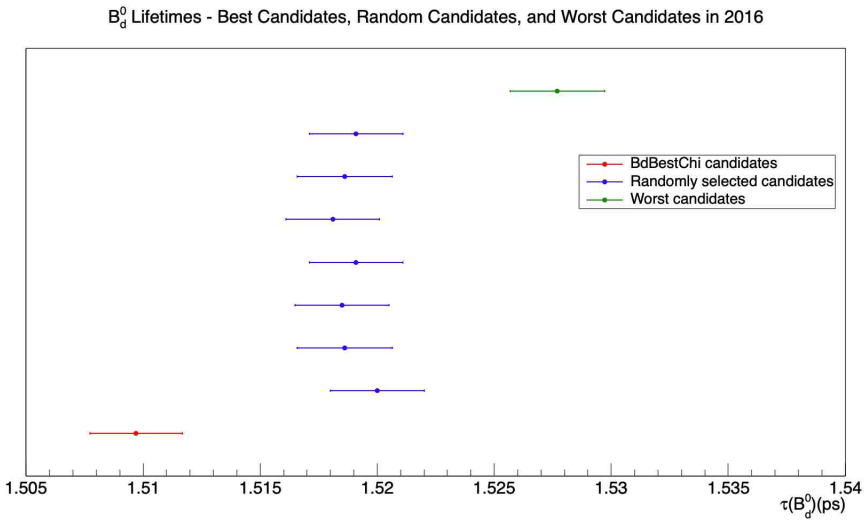

Figure 2.19: A comparison of lifetimes extracted from one sample containing the best χ^2 events, seven samples containing randomly selected candidates and one sample containing candidates with the worst χ^2 value, for the year 2016.

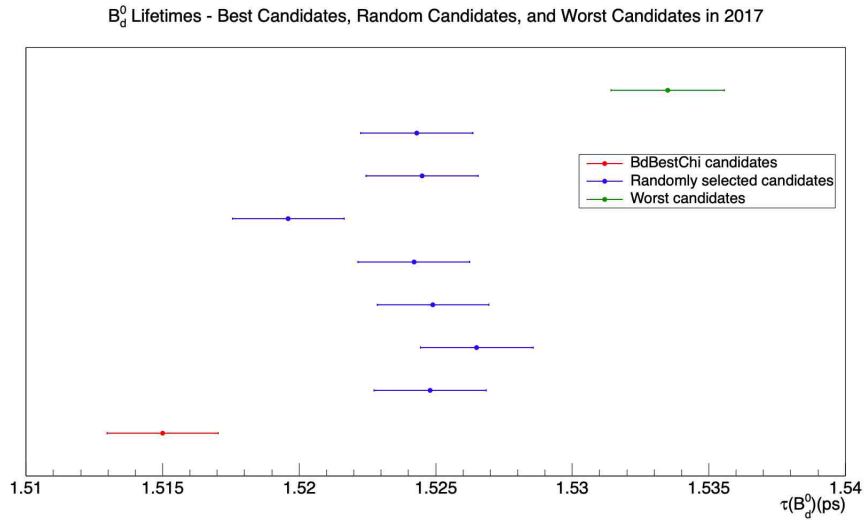

Figure 2.20: A comparison of lifetimes extracted from one sample containing the best χ^2 events, seven samples containing randomly selected candidates and one sample containing candidates with the worst χ^2 value, for the year 2017.

were randomly selected from multiple candidate events are consistent in all seven samples for all years. This is due to the fact that only about 10% of the

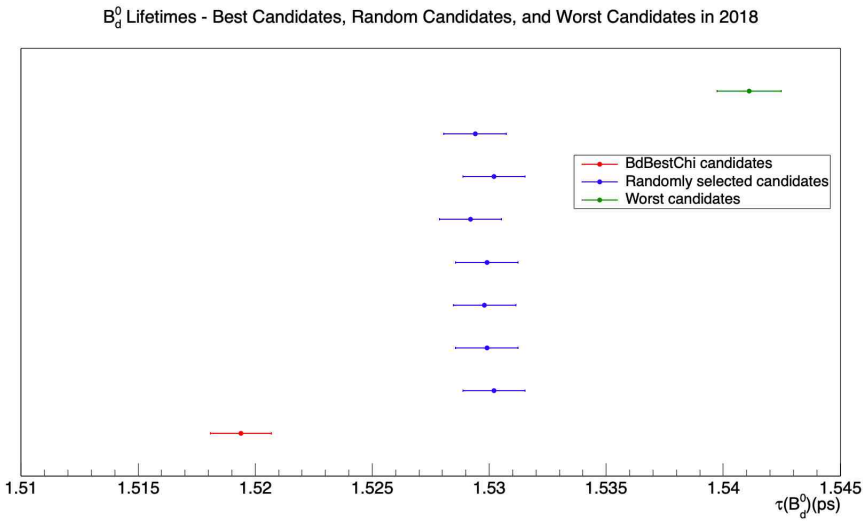

Figure 2.21: A comparison of lifetimes extracted from one sample containing the best χ^2 events, seven samples containing randomly selected candidates and one sample containing candidates with the worst χ^2 value, for the year 2018.

events have multiple candidates in the Run 2 data set, and the selection of a candidate randomly from these events does not make any significant impact on the lifetime. However, the selection of a candidate with the worst χ^2 value for all multiple candidate events makes a significant impact on the lifetime. These results were the worst, as can be seen from the plots; and

- lifetimes extracted from samples with randomly selected candidates agree with the lifetime of the B^0_d compiled by the PDG, 1.519 ± 0.004 ps [10], and the lifetimes of candidates satisfying the best χ^2 selection are within 2σ of the value compiled by the PDG for the years 2015 and 2016. This is due to the fact that this study did not use any time-efficiency corrections on trigger and selection cuts. Thus, the consistency of random selections with the PDG value for 2015 and 2016 cannot be taken as a criterion in favour of the random selection method.

The same study was repeated using MC data sets, to check if the method of selecting a candidate randomly is the less biased one, as about 20% of the events in the MC data sets contain multiple candidates. Increasing the number of events with multiple candidates improves the study of the worst case scenario. For this analysis, lifetimes were compared with the true lifetime of the generated B^0_d mesons in the MC data sets. The values of the true lifetimes for the years 2015+2016, 2017 and 2018 are shown in Figures 2.22, 2.23 and 2.24, respectively.

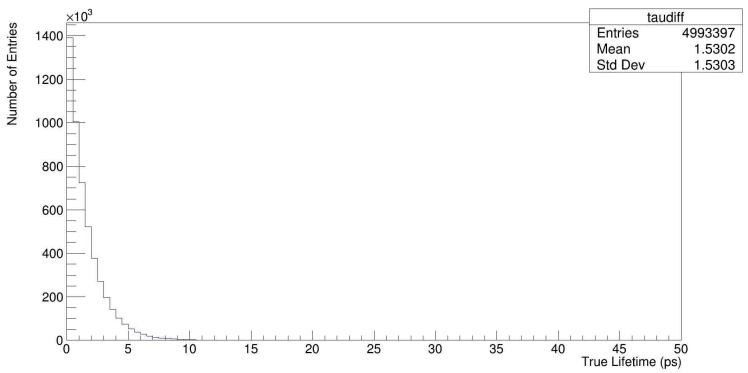

Figure 2.22: Number of events versus true lifetime of the generated B^0_d events, for the year 2015+2016, in the MC data sets.

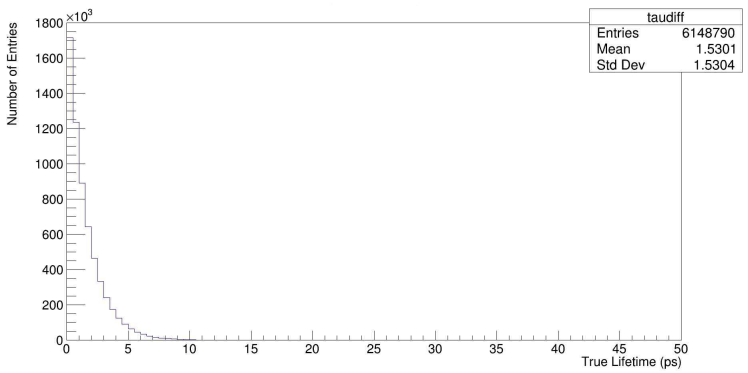

Figure 2.23: Number of events versus true lifetime of the generated B^0_d events, for the year 2017, in the MC data sets.

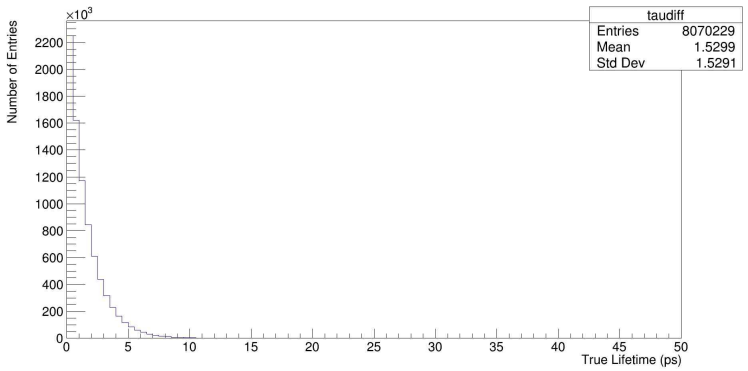

Figure 2.24: Number of events versus true lifetime of the generated B_d^0 events, for the year 2018, in the MC data sets.

The MC data sets for the years 2015 and 2016 were merged to improve low statistics. From Figures 2.22, 2.23 and 2.24, it can be seen that the mean of the true lifetimes of the generated events is 1.53 ps. Comparisons of the lifetimes of the B_d^0 candidates with the best χ^2 value, the randomly selected candidates and the candidates with the worst χ^2 value for the years 2015+2016, 2017 and 2018 are shown in Figures 2.25, 2.26 and 2.27, respectively.

The following conclusions can be drawn from Figures 2.25 - 2.27:

- Lifetimes extracted from events in the samples that contain candidates that were randomly selected from multiple-candidate events are consistent in all seven samples for all years. This is due to the fact that only about 20% of the events have multiple candidates in the MC data sets, and the selection of a candidate randomly from these events does not make any significant impact on the lifetime. However, the selection of a candidate with the worst χ^2 value for all multiple-candidate events makes a significant impact on the lifetime. These

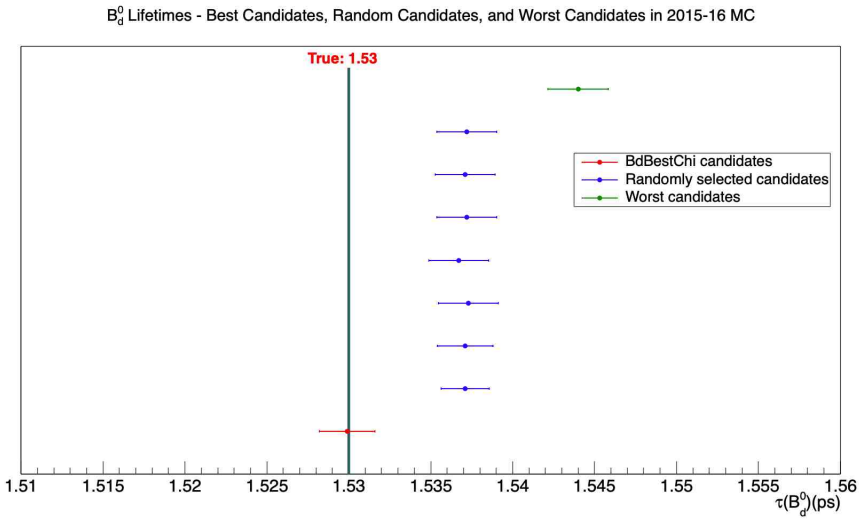

Figure 2.25: A comparison of lifetimes extracted from one sample containing the best χ^2 events, seven samples containing randomly selected candidates and one sample containing candidates with the worst χ^2 value for the years 2015+2016 MC data set.

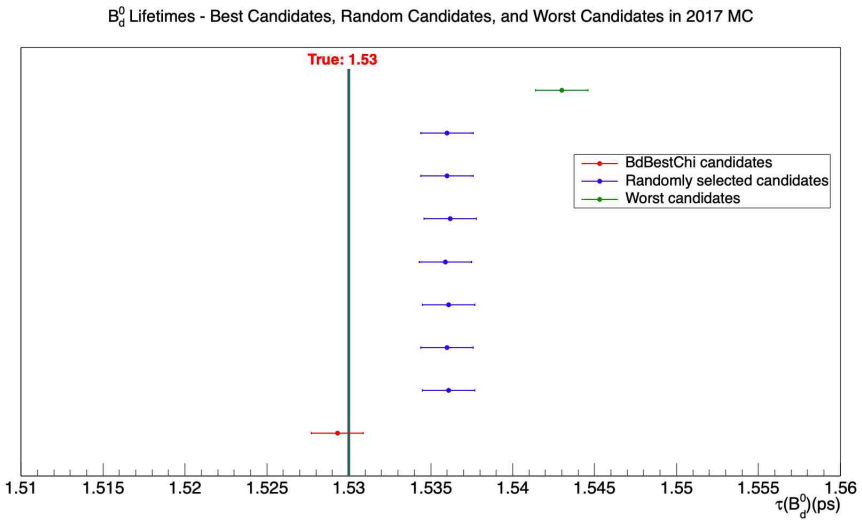

Figure 2.26: A comparison of lifetimes extracted from one sample containing the best χ^2 events, seven samples containing randomly selected candidates and one sample containing candidates with the worst χ^2 value for the year 2017 MC data set.

results were the worst, as can be seen from Figures 2.25 - 2.27; and

- for 2015+2016, 2017 and 2018, lifetimes extracted from candidates satisfying

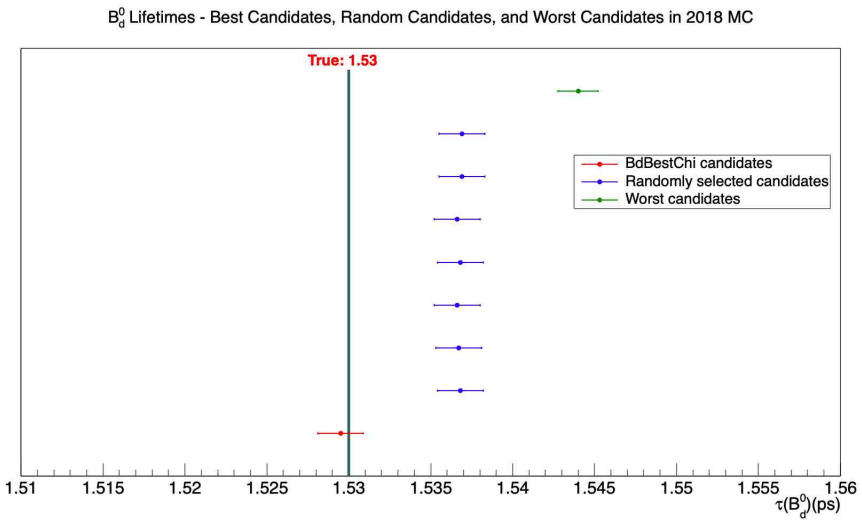

Figure 2.27: A comparison of lifetimes extracted from one sample containing the best χ^2 events, seven samples containing randomly selected candidates and one sample containing candidates with the worst χ^2 value for the year 2018 MC data set.

the best χ^2 selection agree with the mean of the true lifetimes of the generated mesons, which is 1.53 ps. It is clear from the Figures 2.18 - 2.21 for data and Figures 2.25 - 2.27 for MC that selecting the candidate with the lowest χ^2 value in an event with multiple candidates is considered the best approach for candidate selection, given that the observation remains consistent across both scenarios.

2.9 Lifetime Measurements using the Most Dominant Triggers

One of the sources of systematic uncertainty in the lifetime measurement of the B^0_d-meson using the $B^0_d \to J/\psi K^{*0}$ channel is differences that could be attributed

to events collected by different dominant triggers. This study was performed to understand the stability of the measurement under various triggers. As a first step, a list of the most dominant triggers was produced from the Run 2 data set for each year. The mass-lifetime fits were then performed on events collected by each dominant trigger after applying time-efficiency corrections. The three most dominant triggers for the years 2015, 2016, 2017, and 2018 are shown in Tables 2.1, 2.2, 2.3 and 2.4, respectively. For 2016, the trigger menu were modified later due to a miscalibration and as a result, these triggers carry a postfix "delayed" to distinguish them from the miscalibrated triggers; the data set for the year 2016 was named "2016C."

No	Trigger Name	% of the events
1	HLT_2mu4_bJpsimumu_noL2	74.35
2	HLT_2mu4_bJpsimumu	74.19
3	HLT_2mu4_bBmumuxv2	67.77

Table 2.1: Percentage of the candidate events that were selected by each of the three most dominant triggers in the Run 2 data set for the year 2015.

No	Trigger Name	% of the events
1	HLT_2mu6_bJpsimumu_delayed	38.00
2	HLT_2mu6_bBmumuxv2_delayed	36.08
3	HLT_mu6_mu4_bBmumuxv2_delayed	34.69

Table 2.2: Percentage of the candidate events that were selected by each of the three most dominant triggers in the Run 2 data set for the year 2016 (2016C.)

The following can be inferred from Tables 2.1 : 2.4:

- All three dominant triggers are dimuon triggers which is expected as the final

No	Trigger Name	% of the events
1	HLT_2mu6_bJpsimumu_L1BPH_2M9_2MU6_BPH_2DR15 _2MU6	53.09
2	HLT_2mu6_bBmumux_BpmumuKp_L1BPH_2M9_2MU6_BPH _2DR15_2MU6	46.13
3	HLT_2mu6_bBmumuxv2_L1LFV_MU6	34.46

Table 2.3: Percentage of the candidate events that were selected by each of the three most dominant triggers in the Run 2 data set for the year 2017.

No	Trigger Name	% of the events
1	HLT_2mu6_bJpsimumu_L1BPH_2M9_2MU6_BPH_2DR15 _2MU6	41.66
2	HLT_2mu6_bBmumux_BpmumuKp_L1BPH_2M9_2MU6_BPH _2DR15_2MU6	36.30
3	HLT_2mu6_bBmumuxv2_L1LFV_MU6	33.35

Table 2.4: Percentage of the candidate events that were selected by each of the three most dominant triggers in the Run 2 data set for the year 2018.

state of the $B^0_d \to J/\psi K^{*0}$ decays is a pair of oppositely charged muons, a kaon and a pion;

- for the year 2015, most of the events contained both muons with $p_T > 4$ GeV in the final states as indicated by the top three dominant triggers;
- for the year 2016, most of the events contained both muons with $p_T > 6$ GeV in the final states as indicated by the top two dominant triggers. The third dominant trigger, however, collected the dimuon events with one muon with $p_T > 6$ GeV and the other with $p_T > 4$ GeV;
- for the years 2017 and 2018, most of the events contained both muons with $p_T > 6$ GeV in the final states as indicated by the top three dominant triggers;

- for the year 2015, the first two triggers are generic triggers that collected dimuon events which satisfy the invariant mass of the J/ψ-meson, while the third trigger is a specialized dimuon trigger which collected dimuon events satisfying the invariant mass of the B^0_d-meson and also have information on hadrons in the final state;

- for the year 2016, the first dominant trigger is a generic trigger that collected dimuon events which satisfy the invariant mass of the J/ψ-meson. The second and third dominant triggers are specialized dimuon triggers which collected events satisfying the invariant mass of the B^0_d-meson and have information on hadrons in the final state; and

- for the years 2017 and 2018, the first dominant trigger is a generic trigger that collected dimuon events which satisfy the invariant mass of the J/ψ-meson. The second dominant trigger is a specialized dimuon trigger that collected events satisfying the invariant mass of the $B^\pm$-meson and have information on the K^+ as the hadronic track. This indicates that for the years 2017 and 2018, the Run 2 data set for the $B^0_d \to J/\psi K^{*0}$ events is contaminated with $B^\pm \to J/\psi K^\pm$ events. This needs to be corrected as it can cause a bias in the lifetime measurements. The third dominant trigger is a specialized dimuon trigger which collected events satisfying the invariant mass of the B^0_d-meson along with information on hadrons in the final state.

The lifetimes extracted from the third dominant trigger for the year 2015, the first three dominant triggers for the year 2016, and the first and third dominant triggers for the years 2017 and 2018 are shown in Figure 2.28. The study excluded the first

two dominant triggers from 2015, as they were generic triggers that collected dimuon events meeting the invariant mass criteria for the J/ψ-meson and yielded limited statistical significance. The second dominant trigger was ignored for the year 2017 and 2018 as it collected events which do not represent the $B^0_d \to J/\psi K^{*0}$ channel.

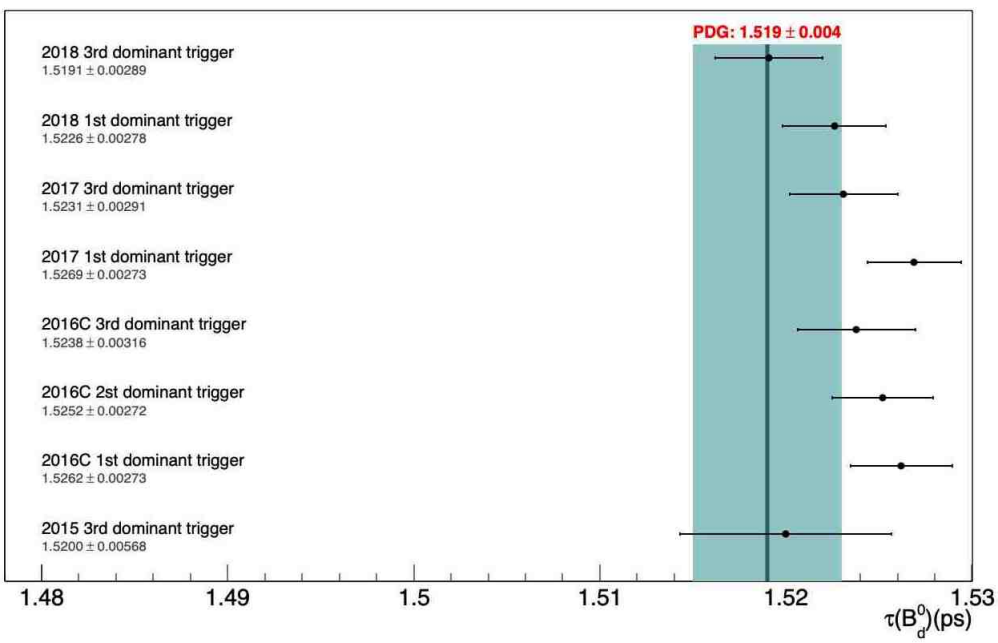

Figure 2.28: The lifetimes extracted for the events collected by each dominant trigger in the Run 2 data sets of the years 2015, 2016, 2017 and 2018.

The following conclusions can be drawn from Figure 2.28:

- The uncertainty on the lifetimes extracted from events in the year 2015 is the largest. This is expected from the low statistics of the Run 2 data set for the year 2015;
- the lifetimes extracted from the events in the years 2016 and 2017 by the first dominant trigger are within 2σ of the value compiled by the PDG [10]. This is because the first dominant trigger in the years 2016 and 2017 is a generic trigger

that collected dimuon events satisfying the invariant mass of the J/ψ-meson; and

- the lifetimes extracted from the events in the year 2018 by the first and third dominant triggers agree well with the value compiled by the PDG [10] even though the first dominant trigger is a generic trigger. This is due to the fact that the 2018 Run 2 data set had the highest statistics.

It can be concluded that the differences in the lifetimes extracted from events collected by each dominant trigger in each year are primarily due to the fact that most of the events were collected by generic triggers. These differences can be addressed by imposing more stringent selection cuts on the events.

2.10 Other Systematic Uncertainties

The B^0_d lifetime has systematic uncertainties that come from different sources, in addition to time efficiency corrections. The uncertainties were determined by comparing the nominal and modified fit outcomes and the fit biases in modified pseudo-experiments. All the systematic uncertainties are described below.

- **Momentum bias:** The B^0_d decays studied in this measurement are low momentum events. The misalignment in the ATLAS ID causes global momentum bias effects which appear as mass shifts. The tracks forming the B-vertex were refitted with the J/ψ mass constrained to the PDG value in the default fit. An alternative fit was performed to study the impact on the lifetime where the tracks forming the B-vertex were refitted without constraining the

J/ψ mass to its PDG value. Moreover, to account for the momentum-scale bias of low p_T hadrons [106], the p_T values of hadrons from the signal chain $J/\psi(\to \mu^+\mu^-)K^{*0}(\to K^\pm\pi^\mp)$ were changed. The difference in the time result relative to the default fit was considered as a systematic uncertainty.

- **Choice of mass window:** The sensitivity of the lifetime fit to the B^0_d mass window selection was estimated by studying several alternative intervals. The effects of modifying the lower and upper bounds were investigated separately. The largest difference found was symmetrized and taken as a conservative estimate for this systematic uncertainty.

- **Choice of primary vertex:** Most of the events have more than one primary vertex (PV) reconstructed. The impact parameter, a_0, is the variable that is used to identify the PV from which the B^0_d candidate originates. It is calculated as the distance between the line extrapolated from the reconstructed B^0_d-meson vertex in the direction of the B^0_d momentum vector, and each reconstructed primary vertex candidate. The PV with the smallest a_0 is chosen by default. To estimate the systematic uncertainty, an alternative approach where the PV with the highest sum of the squares of the constituent tracks' transverse momenta, $\sum p_T^2$, was used. The difference between the fitted B^0_d lifetime value using the default, and that due to the alternative PV selection, was found to be negligibly small compared to the statistical error on the fit.

- **Mass fit model:** To understand the effect of mass mismodeling on the fitted B^0_d lifetime, two approaches were considered. In the first approach, to simulate the effect of mass mismodeling, an artificial re-weighting was applied to the data. Then the fit was performed on the re-weighted data that matched the

fitted mass description in the systematic test. The difference between the results of the default fit and the alternative fit was calculated as the final systematic uncertainty. In the second approach, different mass signal models using a double-sided Crystal Ball function [107] and two single-sided Crystal Ball functions were used for alternative fits. The largest deviation from the default fit was taken as a contribution to the systematic uncertainty. Further, the polynomial function of first order with one parameter in the mass part of the model describing the prompt J/ψ background was replaced by a polynomial function of second order with two parameters. The difference of lifetime from the default fitted value was considered as the systematic uncertainty.

- **Fit model:** Some of the nuisance parameters (such as those that model the mass and lifetime background shapes) can affect the fit model, and this might cause a bias in the physics parameters measured, even when the model fits the data well. To test the stability of the results obtained from the default fit model, a set of pseudo-experiments was conducted using this model. The set of fit results was characterised by its mean value and the deviation from the default fit, and these were used to determine this systematic uncertainty.

2.11 Results

2.11.1 $B^0_{\rm d}$ lifetime result

The value of the lifetime measured using a total of 2391094 ± 4716 $B^0_{\rm d}$ signal candidates was found to be

$$\tau_{B^0_{\rm d}} = (1.5194 \pm 0.0013 \text{ (stat.)} \pm 0.0022 \text{ (syst.)}) \text{ ps}. \tag{2.28}$$

The fitted value of the lifetime extracted from $B^0_{\rm d} \to J/\psi K^{*0}$ decays agrees with the world average value [10]. Figure 2.29 shows the lifetime projections of the mass-lifetime maximum likelihood fit. The figures include the ratio of the difference between each data point and the total fit function divided by the uncertainty that includes both statistical uncertainty and fit model uncertainty.

To test the consistency, the $B^0_{\rm d} \to J/\psi K^{*0}$ lifetime value was fitted separately for each period (2015-2016, 2017 and 2018) of the recorded sample. The outcome is shown in Figure 2.30.

Determination of the $B^0_{\rm d}$ average decay width $\Gamma_{\rm d}$ and of the $\Gamma_{\rm d}/\Gamma_{\rm s}$ ratio

To extract the average decay width Γ_d from the fitted effective lifetime $\tau_{B^0_{\rm d}}$, Equations 2.16 and 2.25 were used. The value of $2y = \Delta\Gamma_d/\Gamma_d = 0.001 \pm 0.010$ was taken from the compilation of measurements by HFLAV [108]. The ratio of production rates A was calculated from the polarisation amplitudes [108]. Using the values of y,

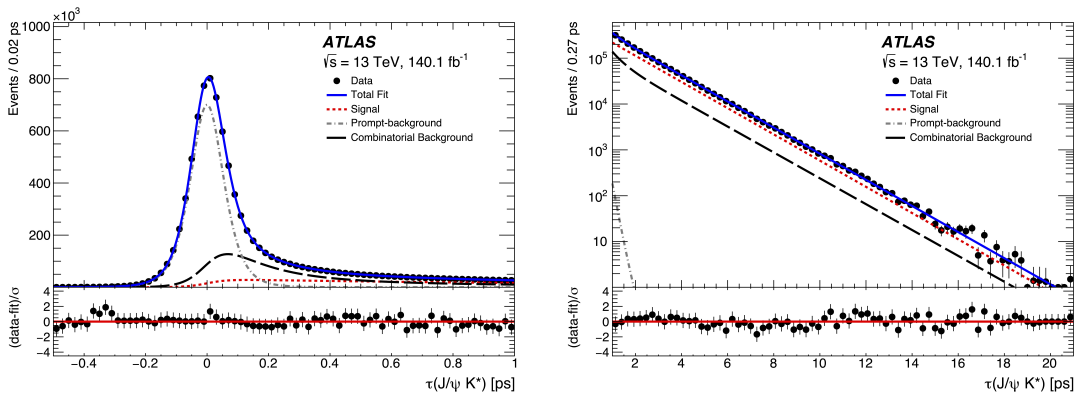

Figure 2.29: Proper decay time fit projection for the $B^0_d \to J/\psi K^{*0}$ sample shown in two different proper decay time ranges: $\tau \in (-0.5; 1)$ ps (left) and $\tau \in (1; 21)$ ps (right). The blue line and the short-dashed red line indicate the total fit and the signal, respectively. The combinatorial background and the prompt J/ψ background are shown as a long-dashed black line and a dash-dotted grey line, respectively. The difference between each data point and the total fit line, divided by the uncertainty that consists of statistical uncertainty and uncertainty from the fit model, is shown as a ratio plot below each figure.

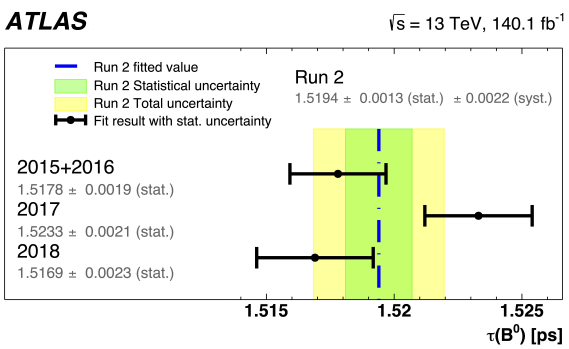

Figure 2.30: The B^0_d lifetime value for each year (2015+2016, 2017 and 2018), measured with $B^0_d \to J/\psi K^{*0}$ decays, was compared to the value from the whole sample. The lifetime result from the entire Run 2 dataset is the blue dash-dotted line, and the green and yellow boxes represent the statistical and total uncertainties, respectively. The black point and the error bar indicate the B^0_d lifetime value and the statistical uncertainty for each year.

A and the fitted B^0_d lifetime, the average decay width was calculated to be:

$$\Gamma_d = 0.6578 \pm 0.0006 \text{ (stat.)} \pm 0.0011 \text{ (sys.)} \pm 0.0038 \text{ (ext.) ps}^{-1}. \quad (2.29)$$

To differentiate the external uncertainty from this measurement's uncertainties and the external HFLAV uncertainties, the external uncertainty is given separately. The uncertainties on y and A were used to calculate the external uncertainty, which is the dominant factor in the overall uncertainty. The result agrees with the theoretical prediction [109].

The ratio of the average decay widths of the B^0_d and B^0_s mesons, Γ_d/Γ_s, is also an interesting measurement for this analysis, as Γ_d/Γ_s is predicted by the HQE [110] and Lattice QCD [109]. The average decay width Γ_s measured by the ATLAS collaboration [111] is $\Gamma_s = (0.6703 \pm 0.0014 \text{ (stat.)} \pm 0.0018 \text{ (syst.)}) \text{ ps}^{-1}$. The resulting ratio is

$$\frac{\Gamma_d}{\Gamma_s} = 0.9814 \pm 0.022 \text{ (stat.)} \pm 0.0031 \text{ (syst.)} \pm 0.0057 \text{ (ext.)}, \quad (2.30)$$

where the statistical, systematic and external uncertainties are propagated from the quantities above. The systematic errors of the two ATLAS measurements $\tau_{B^0_d}$ and Γ_s in the ratio Γ_d/Γ_s do not cancel due to a variety of reasons. Each of the decays $B^0_d \to J/\psi K^{*0}$ and $B^0_s \to J/\psi\phi$ was accepted by a dedicated trigger algorithm, with a small overlap, using a specific trigger menu in the data-taking. This does not eliminate the systematic errors of the two ATLAS measurements, $\tau_{B^0_d}$ and Γ_s. Another reason is their different background compositions which necessitate different background parametrizations, and the differences in the signal model, which is especially linked

to the double lifetime (Γ_L, Γ_H) in the B^0_s case. The only common source of systematic uncertainty, linked to the ID misalignment, was conservatively retained. There is a tension at the level of 3σ between the Γ_d/Γ_s ratio and the theory predictions [109, 110] and the experimental average [104], which stems from the tensions in Γ_s mentioned in Reference [111].

2.12 Prerequisites for Lifetime Measurements of the B^+-mesons using the Most Dominant Triggers

A lifetime measurement will be carried out for B^+-mesons using the $B^+ \to J/\psi K^+$ channel. To understand the stability of the lifetime measurements under various triggers, a list of the most dominant triggers was produced from the Run 2 data set for each year. The mass-lifetime fits were then performed on events collected by each dominant trigger after applying time-efficiency corrections. The three most dominant triggers for the years 2015, 2016, 2017, and 2018 are shown in Tables 2.5, 2.6, 2.7 and 2.8, respectively. For 2016, the trigger menu was modified later due to a miscalibration and as a result, these triggers carry a postfix "delayed" to distinguish them from the miscalibrated triggers; the data set for the year 2016 was named "2016C."

The following can be inferred from Tables 2.5 - 2.8:

No	Trigger Name	% of the events
1	HLT_2mu4_bJpsimumu_noL2	75.96
2	HLT_2mu4_bJpsimumu	73.97
3	HLT_2mu4_bBmumuxv2	72.50

Table 2.5: Percentage of the candidate events that were selected by each of the three most dominant triggers in the Run 2 data set for the year 2015.

No	Trigger Name	% of the events
1	HLT_2mu6_bBmumuxv2_delayed	49.20
2	HLT_2mu6_bJpsimumu_delayed	48.66
3	HLT_mu6_mu4_bBmumuxv2_delayed	48.64

Table 2.6: Percentage of the candidate events that were selected by each of the three most dominant triggers in the Run 2 data set for the year 2016 (2016C).

No	Trigger Name	% of the events
1	HLT_2mu6_bJpsimumu_L1BPH_2M9_2MU6_BPH_2DR15 _2MU6	52.76
2	HLT_2mu6_bBmumux_BpmumuKp_L1BPH_2M9_2MU6_BPH _2DR15_2MU6	52.33
3	HLT_2mu6_bBmumuxv2_L1LFV_MU6	38.91

Table 2.7: Percentage of the candidate events that were selected by each of the three most dominant triggers in the Run 2 data set for the year 2017.

No	Trigger Name	% of the events
1	HLT_2mu6_bJpsimumu_L1BPH_2M9_2MU6_BPH_2DR15 _2MU6	43.86
2	HLT_2mu6_bBmumux_BpmumuKp_L1BPH_2M9_2MU6_BPH _2DR15_2MU6	43.59
3	HLT_2mu6_bBmumuxv2_L1LFV_MU6	39.92

Table 2.8: Percentage of the candidate events that were selected by each of the three most dominant triggers in the Run 2 data set for the year 2018.

- All three dominant triggers are dimuon triggers which is expected as the final state of the $B^{+} \to J/\psi K^{+}$ decays is a pair of oppositely charged muons and a positively charged kaon;
- for the year 2015, most of the events contained both muons with $p_{\mathrm{T}} > 4$ GeV in the final states as indicated by the top three dominant triggers;
- for the year 2016, most of the events contained both muons with $p_{\mathrm{T}} > 6$ GeV in the final states as indicated by the top two dominant triggers. The third dominant trigger, however, collected the dimuon events with one muon with $p_{\mathrm{T}} > 6$ GeV and the other with $p_{\mathrm{T}} > 4$ GeV;
- for the years 2017 and 2018, most of the events contained both muons with $p_{\mathrm{T}} > 6$ GeV in the final states as indicated by the top three dominant triggers;
- for the year 2015, the first two triggers are generic triggers that collected dimuon events which satisfy the invariant mass of the J/ψ-meson, while the third trigger is a specialized dimuon trigger which collected dimuon events satisfying the invariant mass of the B^{+}-meson. It also has information on the positively charged kaon in the final state;
- for the year 2016, the first and third dominant triggers are specialized triggers that collected dimuon events that satisfy the invariant mass of the J/ψ-meson and have information on the positively charged kaon in the final state. The second dominant trigger is a generic dimuon trigger which collected events satisfying the invariant mass of the B^{+}-meson; and
- for the years 2017 and 2018, the first dominant trigger is a generic trigger that collected dimuon events which satisfy the invariant mass of the J/ψ-meson. The

second and third dominant triggers are specialized dimuon triggers that collected events satisfying the invariant mass of the B^+-meson and have information on the K^+ as the hadronic track.

The lifetimes extracted from the third dominant trigger for the year 2015, the first three dominant triggers for the years 2016, 2017 and 2018 are shown in Figure, respectively before and after applying time-efficiency corrections to address inefficiencies in the trigger and selection cuts, are shown in Figures 2.31and 2.32. The study excluded the first two dominant triggers from 2015, as they were generic triggers that collected dimuon events meeting the invariant mass criteria for the J/ψ-meson and yielded limited statistical significance.

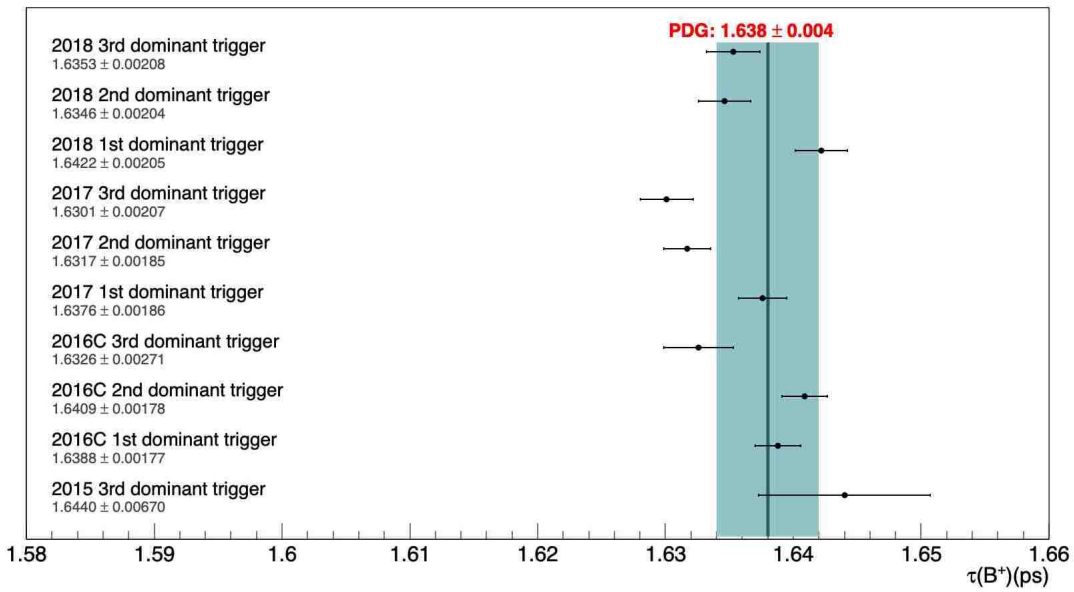

Figure 2.31: The lifetimes extracted for the events collected by each dominant trigger in the Run 2 data sets of the years 2015, 2016, 2017 and 2018, before applying time-efficiency corrections.

The following conclusions can be drawn from Figures 2.31 and 2.32:

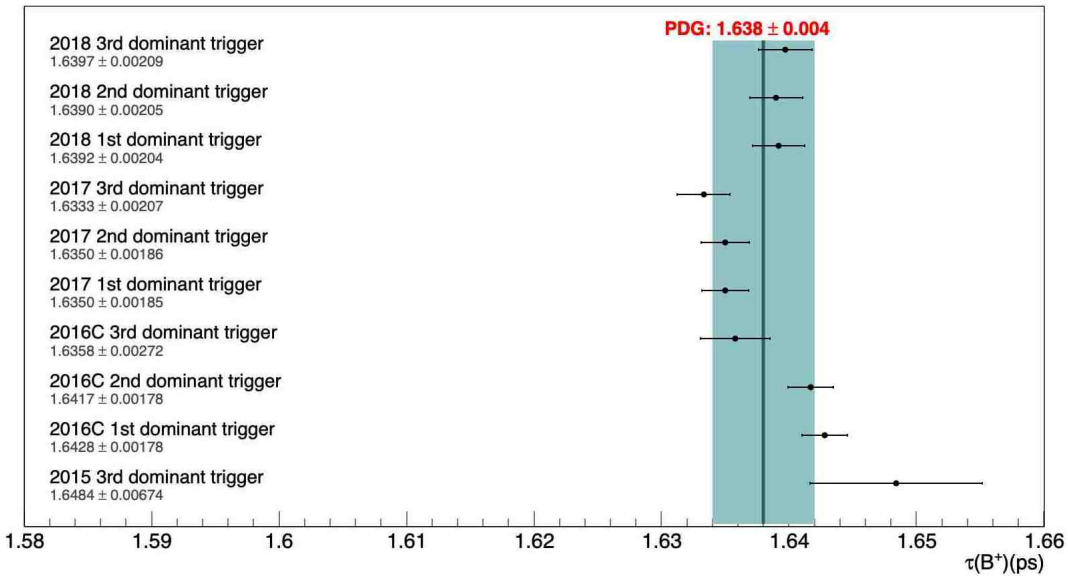

Figure 2.32: The lifetimes extracted for the events collected by each dominant trigger in the Run 2 data sets of the years 2015, 2016, 2017 and 2018, after applying time-efficiency corrections.

- The uncertainty on the lifetimes extracted from events in the year 2015 is the largest. This is expected from the low statistics of the Run 2 data set for the year 2015;

- the lifetimes extracted from the events collected by the second and third dominant triggers in the year 2017 before applying time-efficiency corrections are within 2σ of the value compiled by the PDG [10];

- after applying time-efficiency corrections, the lifetimes extracted from the events in the years 2016, 2017 and 2018 by the first three dominant triggers agree well with the value compiled by the PDG [10] even though the first dominant trigger in the years 2016, 2017 and 2018 is a generic trigger. This is due to the fact that the Run 2 data set for the years 2016, 2017, and 2018 had higher statistics compared to the year 2015 data set; and

- the effect of application of time-efficiency corrections on lifetimes for the years 2016, 2017 and 2018 is a shift of lifetimes towards the value compiled by the PDG [10]. For the year 2015, the application of time-efficiency corrections has no significant impact on the lifetimes extracted from the events collected by the first and second dominant triggers; and the lifetime extracted from the events collected by the third dominant trigger is shifted away from the value compiled by the PDG [10]. This could be due to the overall low statistics of the 2015 data set.

For all the years except 2015, the stability of lifetime measurements under various dominant triggers is excellent, and the results are consistent with the value compiled by the PDG [10]. For the years 2016, 2017 and 2018, dominant generic triggers performed well since the requirements imposed on the K^+ track in $B^+ \to J/\psi K^+$ decays were less stringent compared to those imposed on the $K^{*0}(\to K^\pm\pi^\mp)$, as K^+-mesons were reconstructed from all pairs of positively charged tracks that are not identified as muons or electrons and were assigned the mass of the K^+.

Chapter 3

CP-violation in $B_{\rm S}^0 \to J/\psi\phi$ Decays

3.1 Symmetries and Conservation Laws

An important concept in physics is that of symmetry and the conservation laws associated with it. Symmetry is manifested in an operation that leaves a system invariant, i.e., it transforms the system into a configuration that is indistinguishable from the original one. Symmetries are manifest in the equations of motion rather than in particular solutions to those equations. It is well known from Newtonian physics that a translational invariance in space is associated with the conservation of linear momentum, rotational invariance in space is linked to the conservation of angular momentum, and translational invariance in time implies the conservation of energy. Further, the gauge invariance of electrodynamics leads to the conservation of charge. In the year 1917, Emmy Noether published her famous theorem [112] relating symmetries and conservation laws which can be stated as follows:

If the Lagrangian of a system has a continuous symmetry, then there exists an associated quantity which is conserved by the system, and vice versa.

Symmetries can be continuous or discrete. The symmetries of Newtonian physics are continuous symmetries that describe continuous changes in a system. Discrete symmetries reflect discontinuous changes in a system, and some of these are of high interest in particle physics. Spatial inversion, otherwise known as parity (P), charge conjugation symmetry (C) and time inversion symmetry (T) play a crucial role in the matter-antimatter asymmetry and are discussed below.

3.1.1 Parity

Parity, P, inverts spatial coordinates of a particle in a state defined by $\psi(\vec{r})$ as follows:

$$P|\psi(\vec{r})\rangle = |\psi(-\vec{r})\rangle. \tag{3.1}$$

Acting twice with P on $\psi(-\vec{r})$ should give the original state and hence P is a unitary operator; its eigenvalues are ± 1 and label the possible parity values of the system.

Vectors that change their sign under P are called polar vectors whereas the cross product of two polar vectors under P does not change its sign and is called a pseudovector or axial vector. The dot product of two polar vectors under P does not change its sign and is called a scalar, whereas the dot product of a polar vector and a pseudovector changes sign under P and is called a pseudoscalar. These results are summarised in Table 3.1.

Scalar	$P(s) = s$
Pseudoscalar	$P(p) = -p$
Polar vector	$P(\vec{v}) = -\vec{v}$
Pseudovector	$P(\vec{a}) = \vec{a}$

Table 3.1: Scalars and vectors under parity.

According to Quantum Field Theory, the parity of a fermion must be opposite to that of its corresponding antiparticle whereas the parity of a boson is the same as that of its antiparticle. The parity of a quark is conventionally taken as positive, while that of an antiquark is taken as negative. The parity of a hadron is the product of the parities of its constituent quarks. Thus the baryon octet and decuplet have positive parity, $(+1)^3$, whereas the pseudoscalar and vector mesons have negative parity, $(-1)(+1)$. If the orbital angular momentum, l, is involved in a two-particle system with intrinsic parities P_1 and P_2, then the parity of the system is $P_1P_2(-1)^l$. The helicity H of a particle with an intrinsic spin $\vec{s}$ and momentum $\vec{p}$ is defined as

$$H = \frac{\vec{s}.\vec{p}}{|p|}. \tag{3.2}$$

It measures the sign of the component of the spin of the particle in the direction of motion. The particles with $H = +1$ have righthanded helicity whereas the particles with $H = -1$ have lefthanded helicity as shown in Figure 3.1.

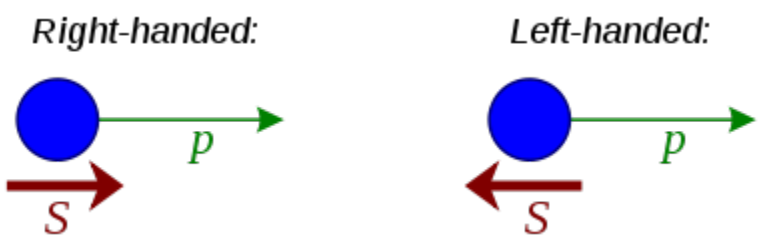

Figure 3.1: Helicity of a particle [113].

The parity transformation on a particle with a helicity H changes the sign as the intrinsic spin is a pseudovector and hence invariant. However, the chirality of a particle depends on whether it belongs to a right- or left-handed representation of the Poincaré group. For massless particles, helicity and chirality are equivalent, but for massive particles, they are distinct.

3.1.2 Charge Conjugation

Charge Conjugation, C, when applied to the wavefunction a particle, gives the corresponding antiparticle wavefunction with the sign of all quantum numbers - charge, magnetic moment, baryon number, lepton number, third component of isospin, strangeness, charm, beauty and truth - changed while mass, energy, momentum and spin remain invariant, as follows:

$$C|\psi\rangle = |\overline{\psi}\rangle, \tag{3.3}$$

where $\overline{\psi}$ represents the state of the corresponding antiparticle. Since normalization of both states requires

$$\langle\psi|\psi\rangle = \langle\overline{\psi}|\overline{\psi}\rangle = \langle\psi|C^\dagger C|\psi\rangle = \mathcal{I}, \tag{3.4}$$

where I is the identity, C is a unitary operator. Further, the operation of C on a state twice gives the same state, and hence the eigenvalues of C are ± 1. Since

$$C = C^\dagger, \tag{3.5}$$

C is a Hermitian operator that results in a physically observable quantity.

Most of the particles in nature are not eigenstates of C. Only those particles that are their own antiparticles are eigenstates of C. However, all particles are eigenstates of C^2. As an example, for a system of a fermion and its corresponding antifermion, the action of C is equivalent to particle interchange. Therefore, both orbital angular momentum l and intrinsic spin s will contribute to the eigenvalue when C acts:

$$C|\psi\overline{\psi}\rangle = (-1)^{l+s}|\psi\overline{\psi}\rangle, \tag{3.6}$$

because states of even (odd) l and s are symmetric (antisymmetric) under particle interchange.

3.1.3 Experimental Evidence for P and C Violation and CP Conservation

The Wu experiment [114], performed in 1956, tested parity conservation in weak interactions. In the experiment, the decay of ^{60}Co nuclei, with their spins aligned in a uniform magnetic field, was studied at a temperature near absolute zero to minimize thermally induced fluctuations of the spin alignment. The decay process is given by

$$^{60}_{27}\mathrm{Co} \to ^{60}_{28}\mathrm{Ni} + e^- + \overline{\nu}_e + 2\gamma. \tag{3.7}$$

If parity were conserved, then equal numbers of electrons would have been emitted in both directions, i.e., $< \vec{\sigma}.\vec{p} >= 0$ where $\vec{\sigma}$ and $\vec{p}$ are the spin and momentum of electron respectively. However, during the experiment, the majority of electrons

emitted were aligned in the direction preferentially opposite to the nuclear spin. The Wu experiment and its outcome are summarised in Figure 3.2.

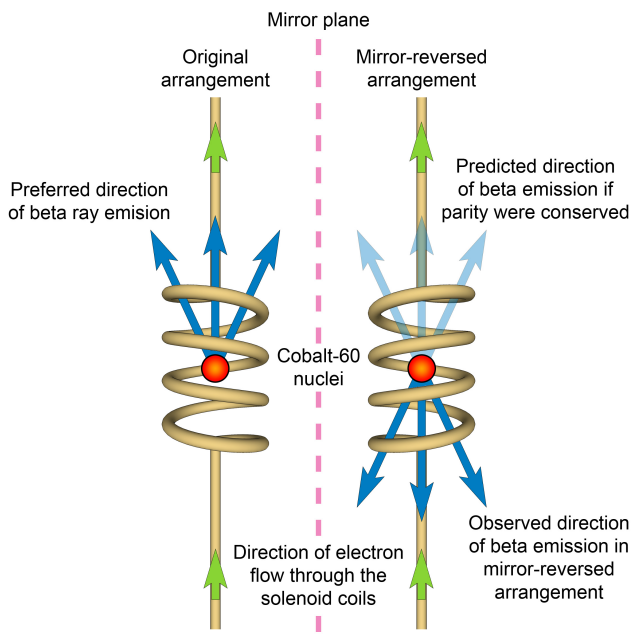

Figure 3.2: Principle behind the Wu experiment and its outcome [115].

Experimentally the intensity distribution of electrons with energy E was found to be of the form

$$I(\theta) = 1 + \alpha \frac{< \vec{\sigma}.\vec{p} >}{E}, \tag{3.8}$$

where α was found to be $+1$ for positrons and -1 for electrons.

In addition to this, the result of the Goldhaber experiment that all neutrinos are left-handed, whereas antineutrinos are right-handed, established that the violation of parity is maximal in weak interactions [116]. The violation of charge conjugation in weak interactions was established in similar studies on neutrinos.

The experimental evidence to support the violation of parity and charge conjuga-

tion symmetry in weak interactions was in the decay of pions. Since all neutrinos are left-handed while antineutrinos are right-handed, the antimuons emitted in the decay

$$\pi^+ \to \mu^+ + \nu_\mu \tag{3.9}$$

always are left-handed. In the charge conjugated version of this decay,

$$\pi^- \to \mu^- + \overline{\nu_\mu}, \tag{3.10}$$

the muons would be left-handed, but antineutrinos always right-handed. If the combination of both operations, C and P, is applied, these observations can be explained such that CP would convert right-handed muons to left-handed antimuons and *vice versa*. That CP symmetry could be used to explain why all neutrinos observed are left-handed whereas antineutrinos are right-handed as shown schematically in Figure 3.3.

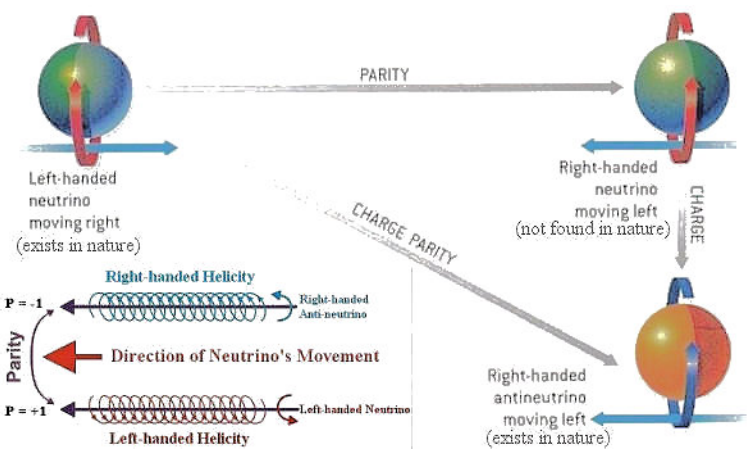

Figure 3.3: CP symmetry of neutrinos [117].

3.2 CP-violation in the Standard Model

3.2.1 CP-violation in Neutral Kaon Oscillations

It was initially believed that the combined operation CP remains invariant under weak interactions. However, even this CP symmetry was found to be broken in weak interactions. This was experimentally observed in the study of neutral kaon decays by Cronin and Fitch in 1964 [118].

The particle K^0 with strangeness $S = +1$ can oscillate into its antiparticle $\overline{K}^0$ with strangeness $S = -1$ and *vice versa* through a second-order weak interaction. Experimentally, the linear combination of K^0 and $\overline{K}^0$ is observed when the particle decays. Since kaons are pseudoscalars, the P and C operations on kaons give

$$P|K^0\rangle = -|K^0\rangle,\ P|\overline{K}^0\rangle = -|\overline{K}^0\rangle, \tag{3.11}$$

and

$$C|K^0\rangle = |\overline{K}^0\rangle,\ C|\overline{K}^0\rangle = |K^0\rangle. \tag{3.12}$$

Then, the CP operation gives

$$CP|K^0\rangle = -|\overline{K}^0\rangle,\ CP|\overline{K}^0\rangle = -|K^0\rangle. \tag{3.13}$$

Hence, the normalized CP eigenstates are

$$|K_1\rangle = \frac{1}{\sqrt{2}}(K^0 - \overline{K}^0), \tag{3.14}$$

and

$$|K_2\rangle = \frac{1}{\sqrt{2}}(K^0 + \overline{K}^0), \tag{3.15}$$

with $CP|K_1\rangle = |K_1\rangle$ and $CP|K_2\rangle = -|K_2\rangle$. The CP eigenstates can decay to 2π or 3π via the weak interactions. The possible pion final states are

- $\pi^0\pi^0$ and $\pi^+\pi^-$, where $CP = +1$, and
- $\pi^0\pi^0\pi^0$ and $\pi^+\pi^-\pi^0$, where $CP = -1$.

Hence K_1 and K_2 should decay to 2π and 3π respectively if CP is conserved during weak interactions. Experimentally, the lifetime of the K_1 and K_2 are 0.09 ns and 51.1 ns respectively [10]. The decay of K_1 to 2π is much faster and hence, a lot of 2π events could be observed near the source, and further away, only 3π events should observed. The unmistakable evidence of CP violation occurred when at large distance, 2π events were recorded indicating that the long lived K_L is some linear combination of K_1 and K_2 that is not an eigenstate of CP.

$$K_L = \frac{1}{\sqrt{1+\epsilon^2}}(K_2 + \epsilon K_1), \tag{3.16}$$

where the coefficient ϵ parameterizes nature's departure from perfect CP invariance; experimentally its magnitude is about 2.24×10^{-3} [10].

3.2.2 Quark Mixing in the Standard Model

CP-violation arises, partially, in the Standard Model of the elementary particles through a non-zero phase factor (δ) in the Cabibbo-Kobayashi-Maskawa (CKM)

matrix [119]. A 2×2 matrix was originally introduced by N. Cabibbo in 1963 to preserve the universality of weak interactions [120]. Study of the relative amplitudes of weak interactions involving $d \to u + W^-$ (where $\delta S = 0$) and $s \to u + W^-$ (where $\delta S = 1$) motivated Cabibbo to state that the d and s quark wavefunctions are not pure flavor eigenstates, but are rotated by a mixing angle θ_c. Hence, in analogy with lepton doublets, the quark doublets could be formed as

$$\begin{pmatrix} u \\ d\cos\theta_c + s\sin\theta_c \end{pmatrix}. \tag{3.17}$$

In 1970, the charm (c) quark with charge $\frac{2}{3}e$ was proposed by Glashow, Iliopoulos and Maiani to explain the suppression of flavour changing neutral currents (FCNCs); this is known as the GIM mechanism [121]. Hence, the new two quark doublets are

$$\begin{pmatrix} u \\ d' \end{pmatrix} = \begin{pmatrix} u \\ d\cos\theta_c + s\sin\theta_c \end{pmatrix} \text{ and } \begin{pmatrix} c \\ s' \end{pmatrix} = \begin{pmatrix} c \\ s\cos\theta_c - d\sin\theta_c \end{pmatrix}. \tag{3.18}$$

In 1972, a third generation of quarks was proposed by Kobayashi and Maskawa to explain the CP-violation in neutral kaon decays. With six quarks, the quark-mixing matrix can be written as follows,

$$\begin{pmatrix} d' \\ s' \\ c' \end{pmatrix} = V_{\text{CKM}} \begin{pmatrix} d \\ s \\ c \end{pmatrix}, \tag{3.19}$$

where the 3×3 unitary complex matrix is the Cabibbo-Koyashi-Maskawa (CKM) and is given by

$$V_{\rm CKM} = \begin{pmatrix} V_{\rm ud} & V_{\rm us} & V_{\rm ub} \\ V_{\rm cd} & V_{\rm cs} & V_{\rm cb} \\ V_{\rm td} & V_{\rm ts} & V_{\rm tb} \end{pmatrix}. \tag{3.20}$$

Each element $V_{\rm ij}$ represents the amplitude of one of the nine possible quark transitions from one flavor i to another j that are mediated by the $W^{\pm}$ bosons. The part of the SM Lagrangian for the Yukawa coupling of the W boson to the quark fields is defined as

$$\mathcal{L}_{\rm W} = \frac{g_{\rm W}}{\sqrt{2}} \sum_{j,k=1,2,3} [V_{\rm jk} \overline{u}_{\rm jL} \gamma^{\mu} d_{\rm kL} W_{\mu}^{+}][V_{\rm jk}^{*} \overline{d}_{\rm kL} \gamma^{\mu} u_{\rm jL} W_{\mu}^{-}], \tag{3.21}$$

where the $g_{\rm W}$ is the weak coupling constant, $u = (u, c, t)$ and $d = (d, s, b)$ are spinors that describe three quark generations and $V = V_{\rm uL}^{*} V^{\rm dL}$ is the CKM matrix.

An $N \times N$ matrix will have $N(N-1)/2$ real parameters (Euler angles) and $(N-1)(N-2)/2$ non-trivial phase angles [122]. The CKM matrix can be parameterized [123] by four independent parameters: three mixing angles $\theta_{\rm ij}$ and one complex phase δ. It is this non-zero complex phase that makes the CKM matrix a source of CP-violation within the SM. The standard choice of parametrization is

$$\begin{aligned} V_{\rm CKM} &= \begin{pmatrix} 1 & 0 & 0 \\ 0 & c_{23} & s_{23} \\ 0 & -s_{23} & c_{23} \end{pmatrix} \begin{pmatrix} c_{13} & 0 & s_{13}e^{-i\delta} \\ 0 & 1 & 0 \\ -s_{13}e^{-i\delta} & 0 & c_{13} \end{pmatrix} \begin{pmatrix} c_{12} & s_{12} & 0 \\ -s_{12} & c_{12} & 0 \\ 0 & 0 & 1 \end{pmatrix} \\ &= \begin{pmatrix} c_{12}c_{13} & s_{12}c_{13} & s_{13}e^{-i\delta} \\ -s_{12}c_{23} - c_{12}s_{23}s_{13}e^{i\delta} & c_{12}c_{23} - s_{12}s_{23}s_{13}e^{i\delta} & s_{23}c_{13} \\ s_{12}s_{23} & -c_{12}s_{23} - s_{12}c_{23}s_{13}e^{i\delta} & c_{23}c_{23} \end{pmatrix}, \end{aligned} \tag{3.22}$$

where $s_{ij} = \sin\theta_{ij}$ and $c_{ij} = \cos\theta_{ij}$. The real angles θ_{ij} can be chosen to lie in the first quadrant, so $s_{ij}, c_{ij} \geq 0$.

Experimental evidence suggests there exists a hierarchy of $s_{13} \ll s_{23} \ll s_{12} \ll 1$, and hence, the Wolfenstein parameterization [124] is chosen since it reveals this hierarchy using four conventional independent parameters as follows:

$$\begin{gathered} s_{12}^2 \equiv \lambda^2 = \frac{|V_{us}^2|}{|V_{ud}^2 + V_{us}^2|},\ s_{23}^2 \equiv A^2\lambda^4 = \frac{|V_{cb}^2|}{|V_{ud}^2 + V_{us}^2|}, \\ \text{and } s_{13}^2 e^{i\delta} \equiv A\lambda^3(\overline{\rho} + i\overline{\eta}) = -A\lambda\frac{V_{ud}V_{ub}^*}{V_{cd}V_{cb}^*}. \end{gathered} \tag{3.23}$$

The Wolfenstein parametrization allows the imaginary part to be suppressed to third order in λ, and the CKM matrix can be expanded in powers of the small parameter $\lambda \approx 0.22$. The expansion up to $\mathcal{O}(\lambda^4)$ yields the following:

$$V_{CKM} = \begin{pmatrix} 1 - \frac{\lambda^2}{2} & \lambda & A\lambda^3(\rho - i\eta) \\ \lambda & 1 - \frac{\lambda^2}{2} & A\lambda^2 \\ A\lambda^3(1 - \rho - i\eta) & -A\lambda^2 & 1 \end{pmatrix} + \mathcal{O}(\lambda^4), \tag{3.24}$$

where the independent parameters are expressed in terms of A, λ, ρ, and η. If there were no cross-generational coupling of quarks, all the parameters would be zero. Further, if $CP-$violation, which arises from the complex nature of the matrix, is allowed, the CP-violating parameter η should be non-zero. All the parameters are measured experimentally [10] and found to have non-zero values; each element of the matrix has been experimentally determined by studying the decays where the corresponding quark transition is involved [10]. For example, V_{ud} is determined by comparing nuclear β decay and μ decay rates. Experimentally the magnitudes of

diagonal elements are close to unity whereas the other matrix elements have non-zero values, the magnitudes of which are indicated in Figure 3.4.

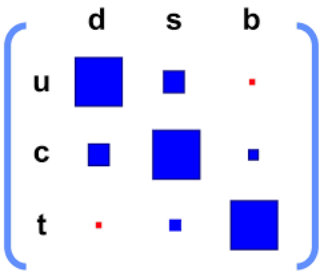

Figure 3.4: CKM matrix where magnitudes of the diagonal elements is close to unity and the area of squares shows relative magnitude [10].

3.2.3 Unitarity Triangle

The unitarity of the CKM matrix imposes $\sum_i V_{ij}V_{ik}^* = \delta_{jk}$ and $\sum_i V_{ij}V_{kj}^* = \delta_{ik}$. The six vanishing combinations that arise from the off-diagonal elements with $j \neq k$ and $\delta_{jk} = 0$ can be represented by triangles in the complex plane. The areas of all triangles are the same, half of the Jarlskog invariant (J) [125], a phase-convention-independent measure of CP-violation, defined as follows:

$$J = Im[V_{td}^* V_{tb} V_{ub}^* V_{ud}] = c_{12}c_{23}c_{21}s_{12}s_{23}s_{13}\sin\delta \simeq A^2\lambda^6\overline{\eta}. \tag{3.25}$$

The most commonly used unitarity triangle arises from the following condition:

$$V_{ud}V_{ub}^* + V_{cd}V_{cb}^* + V_{td}V_{tb}^* = 0, \tag{3.26}$$

which is then rescaled by dividing by a factor of $V_{cd}V_{cb}^*$ to get the unitary triangle as shown in Figure 3.5.

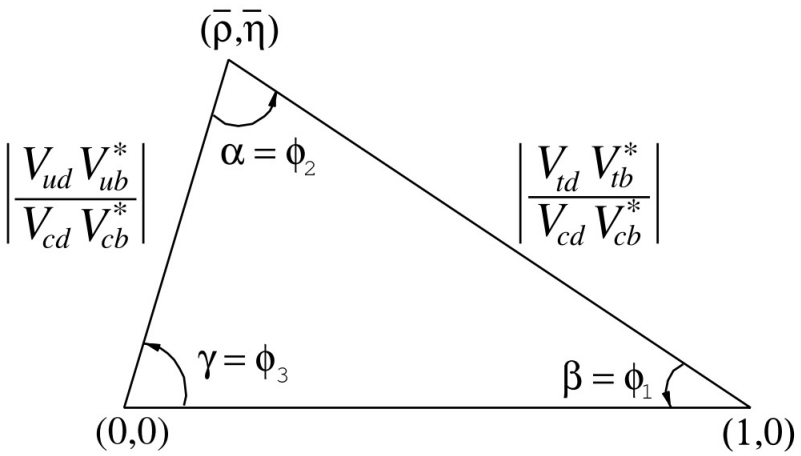

Figure 3.5: Sketch of the unitarity triangle [10].

The sides of the triangle are given by the following relations:

$$R_{\rm u} = \left|\frac{V_{\rm ud}V_{\rm ub}^*}{V_{\rm cd}V_{\rm cb}^*}\right| = \sqrt{\overline{\rho}^2 + i\overline{\eta}^2},\ R_{\rm t} = \left|\frac{V_{\rm td}V_{\rm tb}^*}{V_{\rm cd}V_{\rm cb}^*}\right| = \sqrt{(1-\overline{\rho})^2 + \overline{\eta}^2}. \tag{3.27}$$

The CP-violation parameters are associated with three angles in the triangle which are defined as follows:

$$\begin{aligned}
\alpha = \phi_2 &= \arg\left(-\frac{V_{\rm td}V_{\rm tb}^*}{V_{\rm ud}V_{\rm ub}^*}\right) = \arg\left(-\frac{1-\overline{\rho}-i\overline{\eta}}{\overline{\rho}+i\overline{\eta}}\right), \\
\beta = \phi_1 &= \arg\left(-\frac{V_{\rm cd}V_{\rm cb}^*}{V_{\rm td}V_{\rm tb}^*}\right) = \arg\left(-\frac{1}{1-\overline{\rho}-i\overline{\eta}}\right), \\
\gamma = \phi_3 &= \arg\left(-\frac{V_{\rm ud}V_{\rm ub}^*}{V_{\rm cd}V_{\rm cb}^*}\right) = \arg\left(\overline{\rho}+i\overline{\eta}\right),
\end{aligned} \tag{3.28}$$

where terms appearing on the right-hand side of these equations are of order λ^3 and hence the angles are non-trivial. The condition of non-vanishing $\overline{\eta}$ for the existence of CP-violation in the quark sector is represented as a non-flat unitarity triangle. An important goal of flavor physics is to overconstrain the CKM elements, and many measurements can be conveniently displayed and compared in the $\overline{\rho}$, $\overline{\eta}$ plane.

Figure 3.6 depicts the unitarity triangle resulting from Equation 3.26 for the latest results from the CKM fitter group [126], where the shaded 95% confidence level (CL) regions all overlap consistently around the global fit region. The sides and angles of this unitarity triangle are accessible through B_d^0 decays and hence this triangle is referred to as the "B_d^0 unitarity triangle."

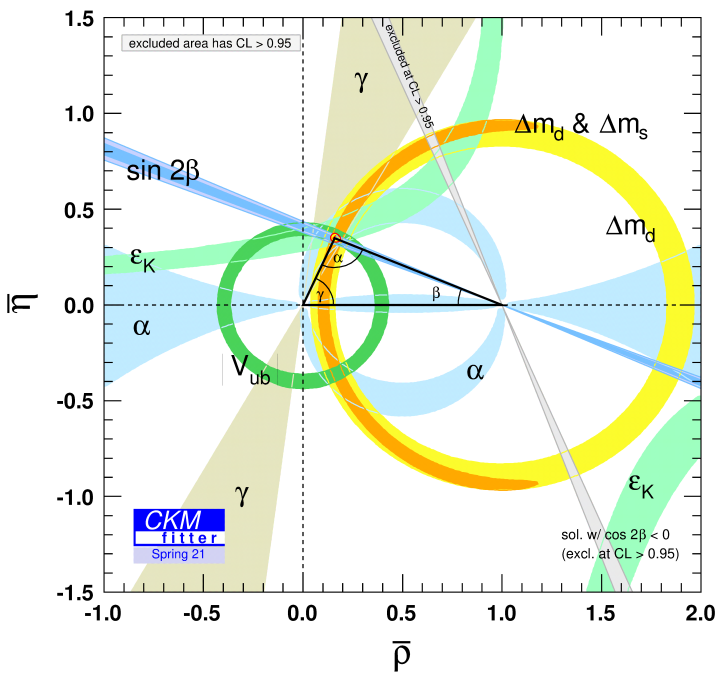

Figure 3.6: Constraints in the $\overline{\rho}$, $\overline{\eta}$ plane. The shaded areas have 95% CL [126].

V_{ub} and V_{cb} determine the length of the left side of the B_d^0 triangle. Both quantities can be accessed through semileptonic B decays. The right side of the B_d^0 triangle is determined by V_{td} and V_{tb} which can be constrained using $B_d^0 - \overline{B}_d^0$ and $B_s^0 - \overline{B}_s^0$ mixing. The angle β appears in B_d^0-meson mixing; its precise measurement, through $\sin 2\beta$, was one of the main goals of the BaBar [127] and Belle [128] experiments. The result confirmed the existence of CP-violation in the B sector for the first time. Both

experiments determined β using the "gold-plated" decay channel $B_d^0 \to J/\psi K_S^0$. The most recent combined result [102], including measurements by BaBar [127], Belle [128] and LHCb [129], is

$$\sin 2\beta = 0.695 \pm 0.0019. \tag{3.29}$$

This combination represents the most precise angular constraint entering the fit and is shown by the dark blue band in Figure 3.6.

The unitarity triangle that can be constructed from the equation

$$V_{us}V_{ub}^* + V_{cs}V_{cb}^* + V_{ts}V_{tb}^* = 0, \tag{3.30}$$

when by dividing each term by a factor of $V_{cs}V_{cb}^*$, is referred to as the "B_s^0 unitary triangle." The latest results [126] from the CKM fitter group for this triangle are shown in Figure 3.7. The angle β_s is very small and hence the triangle is very flat. It appears in B_s mixing; the current combined average value of β_s from all experiments including ATLAS [130, 131] is -0.021 ± 0.031 [102]. The SM determination of $\phi_s = 2\beta_s$ using the $B_s^0 \to J/\psi\phi$ decay channel is one of the main physics goals of the ATLAS experiment and an important topic of this thesis.

3.2.4 Phenomenology of Neutral B Meson Mixing

The B^0-meson can oscillate into its antiparticle $\overline{B}^0$ and vice versa, and this phenomenon is referred to as $B^0 - \overline{B}^0$ oscillation. This overview of the phenomenology of B-meson mixing and decay broadly follows several more detailed review articles [132–134]. The decays of neutral mesons, B_q^0, and their CP conjugates, $\overline{B}_q^0$, with $q = d, s$,

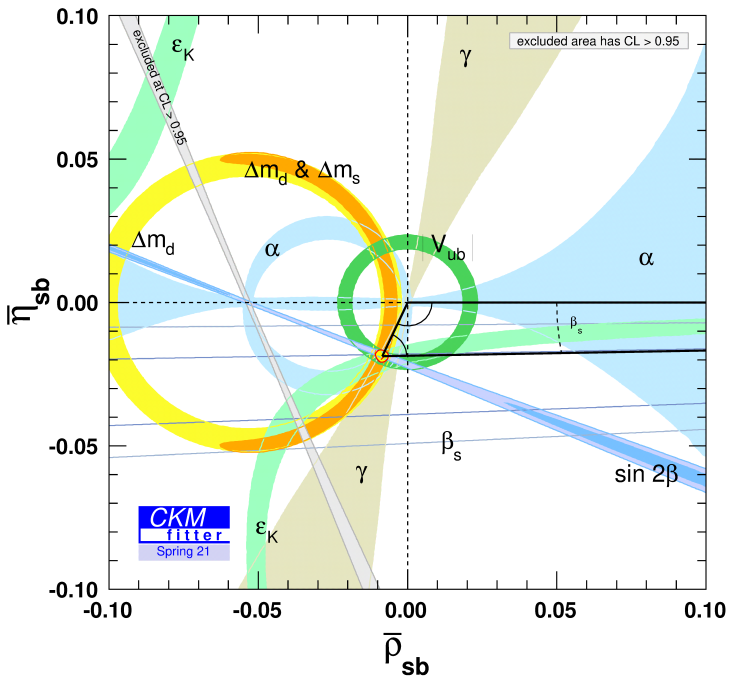

Figure 3.7: B_s^0 unitarity triangle [126].

into final states f and $\overline{f}$ can be described by the following decay amplitudes:

$$\begin{aligned} A_f &= \langle f|\mathcal{H}|B_q^0\rangle,\ \overline{A}_f = \langle f|\mathcal{H}|\overline{B}_q^0\rangle, \\ A_{\bar{f}} &= \langle \overline{f}|\mathcal{H}|B_q^0\rangle,\ \overline{A}_{\bar{f}} = \langle \bar{f}|\mathcal{H}|\overline{B}_q^0\rangle. \end{aligned} \tag{3.31}$$

The neutral B-mesons transform under the CP operation as follows:

$$CP|B_q^0\rangle = -|\overline{B}_q^0\rangle \text{ and } CP|\overline{B}_q^0\rangle = -|B_q^0\rangle, \tag{3.32}$$

where an arbitrary non-physical phase factor has been omitted. The final state, f, and its CP conjugate state, $\overline{f}$, are connected via the CP operation according to

$$CP|f\rangle = \eta_f|\overline{f}\rangle \text{ and } CP|\overline{f}\rangle = \eta_f|f\rangle \tag{3.33}$$

where $\eta_f = \pm 1$ are the phase factors appearing in the CP transformation of the states. The time development of the flavor eigenstates $|B_q^0\rangle$ and $|\overline{B}_q^0\rangle$ is given by the phenomenological Schrödinger equation as:

$$i\frac{\partial}{\partial t}\begin{pmatrix}|B_q^0\rangle \\ |\overline{B}_q^0\rangle\end{pmatrix} = \left(M - \frac{i}{2}\Gamma\right)\begin{pmatrix}|B_q^0\rangle \\ |\overline{B}_q^0\rangle\end{pmatrix} = \begin{pmatrix}M_{11} - \frac{i}{2}\Gamma_{11} & M_{12} - \frac{i}{2}\Gamma_{12} \\ M_{21} - \frac{i}{2}\Gamma_{21} & M_{22} - \frac{i}{2}\Gamma_{22}\end{pmatrix}\begin{pmatrix}|B_q^0\rangle \\ |\overline{B}_q^0\rangle\end{pmatrix}, \tag{3.34}$$

where the Hamiltonian is constructed from two hermitian matrices: mass M and decay width Γ. The mass matrix describes $B_q^0 - \overline{B}_q^0$ meson mixing. The diagonal elements M_{11} and M_{22} are the masses of the B_q^0 and $\overline{B}_q^0$ and are generated from the quark mass terms in Equation 3.21 and from the binding energy of the strong interaction. The off-diagonal terms M_{12} and M_{21} occur from the flavor changing $\Delta b = 2$ processes as shown in Figure 3.8.

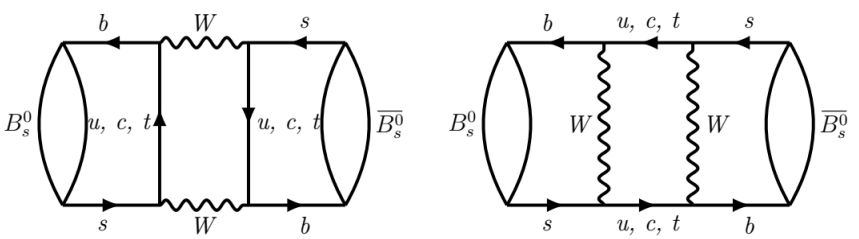

Figure 3.8: B_s^0-meson mixing in the Standard Model.

Due to the hermiticity of M and Γ, the off-diagonal elements are complex conju-

gates, $M_{21} = M_{12}^*$ and $\Gamma_{21} = \Gamma_{12}^*$. According to the CPT invariance theorem [135], $\Gamma = \Gamma_{11} = \Gamma_{22}^*$ and $M = M_{11} = M_{22}$, and then the Hamiltonian reduces to

$$i\frac{\partial}{\partial t}\begin{pmatrix} |B_{\rm q}^0\rangle \\ |\overline{B}_{\rm q}^0\rangle \end{pmatrix} = \begin{pmatrix} M - \frac{i}{2}\Gamma & M_{12} - \frac{i}{2}\Gamma_{12} \\ M_{21}^* - \frac{i}{2}\Gamma_{21}^* & M - \frac{i}{2}\Gamma \end{pmatrix}\begin{pmatrix} |B_{\rm q}^0\rangle \\ |\overline{B}_{\rm q}^0\rangle \end{pmatrix}. \tag{3.35}$$

Diagonalization of the Hamiltonian in Equation 3.35 leads to the well defined mass eigenstates, $|B_{\rm H}\rangle$ and $|B_{\rm L}\rangle$, as follows:

$$\begin{aligned} |B_{\rm H}\rangle &= p|B_{\rm q}^0\rangle + q|\overline{B}_{\rm q}^0\rangle \\ |B_{\rm L}\rangle &= p|B_{\rm q}^0\rangle - q|\overline{B}_{\rm q}^0\rangle, \end{aligned} \tag{3.36}$$

where p and q are the complex coefficients and $|p|^2 + |q|^2 = 1$. The $|B_{\rm L}\rangle$ and $|B_{\rm H}\rangle$ denote the light and heavy mass eigenstates, respectively. Time evolution of mass eigenstates is described by the following:

$$\begin{aligned} |B_{\rm L}(t)\rangle &= e^{-iM_{\rm L}t}e^{-\frac{\Gamma_{\rm L}}{2}t}|B_{\rm L}\rangle \\ |B_{\rm H}(t)\rangle &= e^{-iM_{\rm H}t}e^{-\frac{\Gamma_{\rm H}}{2}t}|B_{\rm H}\rangle, \end{aligned} \tag{3.37}$$

where $M_{\rm L}$ and $M_{\rm H}$ denote the masses and $\Gamma_{\rm L}$ and $\Gamma_{\rm H}$ the decay widths of the $|B_{\rm L}\rangle$ and $|B_{\rm H}\rangle$. The diagonalization procedure relates $M_{\rm L/H}$ and $\Gamma_{\rm L/H}$ to the elements of the Hamiltonian in Equation 3.35

$$\begin{aligned} M_{\rm L/H} - \frac{i}{2}\Gamma_{\rm L/H} &= M - \frac{i}{2}\Gamma \mp \sqrt{\left(M_{12} - \frac{i}{2}\Gamma_{12}\right)\left(M_{12}^* - \frac{i}{2}\Gamma_{12}^*\right)}, \\ &= M - \frac{i}{2}\Gamma \mp \sqrt{|M_{12}|^2 + \frac{1}{4}|\Gamma|^2 - i|M_{12}||\Gamma_{12}|\cos\phi_\Gamma - \phi_{\rm M}} \end{aligned} \tag{3.38}$$

where the phases $\phi_\Gamma = \arg(\Gamma_{12})$ and $\phi_{\rm M} = \arg(M_{12})$. The mass and decay widths of

the mass eigenstates are connected to Γ and M as follows:

$$\Gamma = \frac{\Gamma_L + \Gamma_H}{2}, \text{ and } M = \frac{M_L + M_H}{2}. \tag{3.39}$$

Then, the mass difference Δm and decay width difference $\Delta\Gamma$ can be defined as

$$\Delta m = M_H - M_L, \ \Delta\Gamma = \Gamma_H - \Gamma_L. \tag{3.40}$$

The following relations for Δm and $\Delta\Gamma$ can be derived by using Equation 3.38:

$$\Delta m^2 - \frac{1}{4}\Delta\Gamma^2 = 4|M_{12}|^2 - |\Gamma_{12}|^2, \tag{3.41}$$

$$\Delta m \Delta\Gamma = -4|M_{12}||\Gamma_{12}|\cos(\phi_\Gamma - \phi_M). \tag{3.42}$$

In both the B_d^0 and B_s^0 systems, experimental evidence [10] shows that $\Delta m \gg \Delta\Gamma$, which translates to $|M_{12}| \gg |\Gamma_{12}|$. Neglecting $\Delta\Gamma$ and $|\Gamma_{12}|^2$ in Equation 3.41 results in

$$\Delta m = |M_{12}|. \tag{3.43}$$

Inserting this into Equation 3.42 gives

$$\Delta\Gamma = -2|\Gamma_{12}|\cos(\phi_\Gamma - \phi_M). \tag{3.44}$$

The ratio of the coefficients of eigenstates is determined to be

$$\frac{q}{p} = -\sqrt{\frac{M_{12}^* - \frac{i}{2}\Gamma_{12}^*}{M_{12} - \frac{i}{2}\Gamma_{12}^*}}. \tag{3.45}$$

The above equation can be expanded in terms of $\frac{|\Gamma_{12}|}{|M_{12}|}$ for the B_d^0 and B_s^0 systems as follows:

$$\begin{aligned}\frac{q}{p} &= -\sqrt{e^{-2i\phi_M}\frac{1-\frac{i}{2}\frac{|\Gamma_{12}|}{|M_{12}|}e^{i(\phi_M-\phi_\Gamma)}}{1-\frac{i}{2}\frac{|\Gamma_{12}|}{|M_{12}|}e^{i(-\phi_M+\phi_\Gamma)}}} \\ &= -e^{i\phi_M}\left[1-\frac{1}{2}\sin\left(\phi_M-\phi_\Gamma\right)\frac{|\Gamma_{12}|}{|M_{12}|}+\mathcal{O}\left(\frac{|\Gamma_{12}|^2}{|M_{12}|^2}\right)\right].\end{aligned} \tag{3.46}$$

The time development of the $|B_q^0\rangle$ and $|\overline{B}_q^0\rangle$ is given by

$$\begin{aligned}|B_q^0(t)\rangle &= \frac{1}{2p}\left(|B_L(t)\rangle + |B_H(t)\rangle\right), \\ |\overline{B}_q^0(t)\rangle &= \frac{1}{2q}\left(|B_L(t)\rangle + |B_H(t)\rangle\right).\end{aligned} \tag{3.47}$$

Equation 3.37 can be inserted into the above equation to give

$$\begin{aligned}|B_q^0(t)\rangle &= g_+(t)|B_q^0\rangle + \frac{g}{p}g_-(t)|\overline{B}_q^0\rangle, \\ |\overline{B}_q^0(t)\rangle &= \frac{p}{q}g_-(t)|B_q^0\rangle + g_+(t)|\overline{B}_q^0\rangle,\end{aligned} \tag{3.48}$$

where $g_\pm(t)$ is given by

$$g_\pm(t) = \frac{1}{2}\left(e^{-i(M_L+\frac{\Gamma_L}{2})t} \pm e^{-i(M_H+\frac{\Gamma_H}{2})t}\right). \tag{3.49}$$

Some of the combinations using $g_\pm(t)$ are

$$\begin{aligned}|g_\pm|^2 &= \frac{1}{2}e^{-\Gamma t}\left(\cosh\frac{\Delta\Gamma}{2}t \pm \cos\Delta m t\right), \\ g_+(t)g_-^*(t) &= \frac{1}{2}e^{-\Gamma t}\left(-\sinh\frac{\Delta\Gamma}{2}t - i\sin\Delta m t\right), \\ g_+^*(t)g_-(t) &= \frac{1}{2}e^{-\Gamma t}\left(-\sinh\frac{\Delta\Gamma}{2}t + i\sin\Delta m t\right).\end{aligned} \tag{3.50}$$

It is useful to define one central quantity for CP-violation, λ_f, given by

$$\lambda_f = \frac{q}{p}\frac{\overline{A}_f}{A_f}. \tag{3.51}$$

While the phases of both $\frac{\overline{A}_f}{A_f}$ and $\frac{q}{p}$ are convention dependent, the phase of λ_f is a measurable physical quantity. The time-dependent rate for the decay of a B_q^0 to the final state f is

$$\begin{aligned}\frac{d\Gamma(B_q^0 \to f)}{dt\mathcal{N}_f} &= |\langle f|B_q^0(t)\rangle|^2 = |g_+(t)A_f + \frac{q}{p}g_-(t)\overline{A}_f|^2 \\ &= \frac{1}{2}|A_f|^2 e^{-\Gamma t}\times \\ &\left[(1+|\lambda_f|^2)\cosh\frac{\Delta\Gamma}{2}t + (1-|\lambda_f|^2)\cos\Delta m t - 2\sinh\frac{\Delta\Gamma}{2}t\mathcal{R}(\lambda_f) - 2\sin(\Delta m t)\mathcal{I}(\lambda_f)\right],\end{aligned} \tag{3.52}$$

and the rate for the $\overline{B}_q^0$ to decay to f is

$$\begin{aligned}\frac{d\Gamma(\overline{B}_q^0 \to f)}{dt\mathcal{N}_f} &= |\langle f|\overline{B}_q^0(t)\rangle|^2 = |\frac{p}{q}g_-(t)A_f + g_+(t)\overline{A}_f|^2 \\ &= \frac{1}{2}\left|\frac{p}{q}\right|^2 |A_f|^2 e^{-\Gamma t}\times \\ &\left[(1+|\lambda_f|^2)\cosh\frac{\Delta\Gamma}{2}t - (1-|\lambda_f|^2)\cos\Delta m t - 2\sinh\frac{\Delta\Gamma}{2}t\mathcal{R}(\lambda_f) + 2\sin(\Delta m t)\mathcal{I}(\lambda_f)\right],\end{aligned} \tag{3.53}$$

where $\mathcal{N}_f$ is a normalization factor. The decay rates to the CP-conjugate final state $\overline{f}$ can be obtained by making the following transformations:

$$\begin{aligned} A_f &\to A_{\overline{f}}, \\ \overline{A}_f &\to \overline{A}_{\overline{f}}, \\ \lambda_f &\to \lambda_{\overline{f}} = \frac{q}{p}\frac{\overline{A}_{\overline{f}}}{A_{\overline{f}}}. \end{aligned} \tag{3.54}$$

3.2.5 Classification of CP-violation in $B_q^0 - \overline{B}_q^0$ Mixing

Assuming the CPT invariance theorem [135], all CP-violating effects in $B_q^0 - \overline{B}_q^0$ mixing are governed by the Schrödinger Equation (Eq. 3.35) applied to meson decay and mixing. The resulting time-dependent decay rates are expressed using the decay amplitudes A_f, $A_{\bar{f}}$, $\overline{A}_f$, $\overline{A}_{\bar{f}}$, and the mixing parameters p and q. However, to arrive at non-vanishing CP-violating observables, specific conditions for the transition amplitudes and their phases need to be met. These are discussed in this section.

Strong and weak phases: There are two types of phases involved in the transition to the final state: strong and weak phases. The strong phases arise in final state interaction scattering from intermediate on-shell states, such as that through strong or electromagnetic interactions, and these interactions are CP-invariant. The strong phases are equal for two CP-conjugate states. Weak phases originate from complex couplings in Equation 3.21, and these arise in the $W^{\pm}$ couplings to the quarks via the complex CKM matrix elements. Under CP-conjugation, the weak phases change sign. Accordingly, in the course of investigation of the CKM mechanism, it is of highest interest to measure weak phases cleanly in meson decays.

It is important to note that although the existence of weak and strong phases is physically motivated, their absolute values are convention-dependent. However, relative strong and weak phases between different terms in transition amplitudes are convention-independent, and hence these can be interpreted as physically meaningful quantities. Depending on the origin and interplay of transitions that introduce weak phases, CP-violating effects can be categorized as follows:

- CP violation in the decay or direct CP violation,

- CP violation in the mixing or indirect CP violation, and
- CP violation in the interference of mixing and decay.

Direct CP-violation: In the case of meson decays, multiple amplitudes a_i, with different weak phases ϕ_i and strong phases δ_i, can contribute to the decay amplitudes. If a meson has two possible transitions with amplitudes a_1 and a_2, then the resulting decay amplitudes can be expressed as

$$\begin{aligned} A_f &= |a_1|e^{i(\delta_2+\phi_1)} + |a_2|e^{i(\delta_2+\phi_1)}, \\ \overline{A}_{\bar{f}} &= |a_1|e^{i(\delta_2-\phi_1)} + |a_2|e^{i(\delta_2-\phi_1)}. \end{aligned} \tag{3.55}$$

This implies the ratio

$$\frac{\overline{A}_{\bar{f}}}{A_f} \neq 1, \tag{3.56}$$

leading to CP-violation in the decay. This is the only type of CP-violation that can occur in charged meson systems $B^{\pm}$. Experimentally, it manifests as the difference in the decay widths of the two charge conjugated states and leads to the time-independent asymmetry of the form

$$\mathcal{A}_{CP}^{dir} = \frac{\Gamma(B^- \to f^-) - \Gamma(B^+ \to f^+)}{\Gamma(B^- \to f^-) + \Gamma(B^+ \to f^+)} = \frac{|\overline{A}_{\bar{f}}|^2 - |A_f|^2}{|\overline{A}_{\bar{f}}|^2 + |A_f|^2} = \frac{|\frac{\overline{A}_{\bar{f}}}{A_f}|^2 - 1}{|\frac{\overline{A}_{\bar{f}}}{A_f}|^2 + 1}. \tag{3.57}$$

CP-violation in mixing: The CP-violation in the $B_q^0 - \overline{B}_q^0$ meson mixing occurs when $\frac{q}{p} \neq 1$. In this case, the probability for a B_q^0 to transition into a $\overline{B}_q^0$, $\mathcal{P}(B_q^0 \to \overline{B}_q^0)$, differs from the probability for the CP-conjugate process, $\mathcal{P}(\overline{B}_q^0 \to B_q^0)$. If there is no direct CP-violation, *i.e.*, $A_f = \overline{A}_f$ and $A_{\bar{f}} = \overline{A}_f = 0$, then the resulting asymmetry

can be written as

$$\mathcal{A}_{\rm CP}^{mix} = \frac{\Gamma(\overline{B}^0_{\rm q} \to f) - \Gamma(B^0_{\rm q} \to \overline{f})}{\Gamma(\overline{B}^0_{\rm q} \to f) + \Gamma(B^0_{\rm q} \to \overline{f})} = \frac{|\frac{p}{q} g_-(t) A_{\rm f}|^2 - |\frac{q}{p} g_-(t) \overline{A}_{\overline{\rm f}}|^2}{|\frac{p}{q} g_-(t) A_{\rm f}|^2 + |\frac{q}{p} g_-(t) \overline{A}_{\overline{\rm f}}|^2} = \frac{1 - |\frac{q}{p}|^4}{1 + |\frac{q}{p}|^4}. \quad (3.58)$$

This kind of CP-violation in B-mesons can be studied using semileptonic $B^0_{\rm q} \to X l^+$ decays where a $B^0_{\rm q}$-meson mixing before decaying semileptonically can result in decays containing a l^- in the final state. This results in unequal transition probabilities, $\mathcal{P}(B^0_{\rm q} \to \overline{B}^0_{\rm q}) \neq \mathcal{P}(\overline{B}^0_{\rm q} \to B^0_{\rm q})$, leading to an asymmetry in the observed number of l^+ and l^- given by $\mathcal{A}_{CP}^{mix}$. The observed results of CP asymmetry in the mixing of $B^0_{\rm q}$-mesons are compatible with zero and are in agreement with the SM expectations [136, 137].

Mixing induced CP-violation: B-meson mixing induced CP-violation can occur when the direct decay $B^0_{\rm q} \to f$ interferes with $B^0_{\rm q} - \overline{B}^0_{\rm q}$ mixing followed by the decay $\overline{B}^0_{\rm q} \to f$ as illustrated in Figure 3.9.

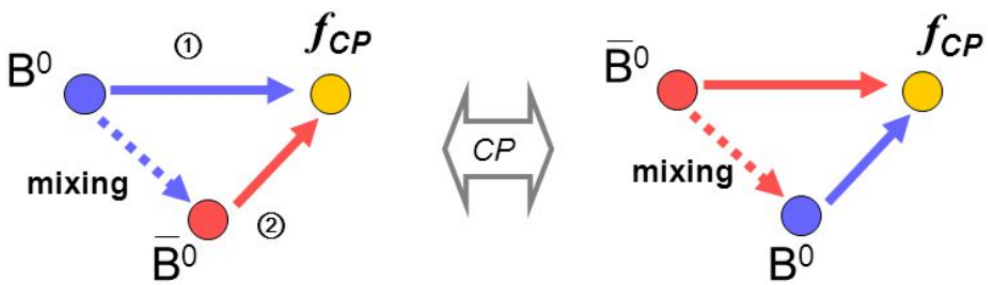

Figure 3.9: Interference between decays before and after $B^0_{\rm q} - \overline{B}^0_{\rm q}$ mixing.

If $\lambda_{\rm f}$ in Equations 3.52 and 3.53 has a non-trivial phase, *i.e.*, $\mathcal{I}(\lambda_{\rm f}) = \mathcal{I}(\frac{q}{p}\frac{\overline{A}_{\rm f}}{A_{\rm f}}) \neq 0$,

this gives rise to the following time-dependent CP asymmetry:

$$\mathcal{A}_{\rm CP}^{mix}(t) = \frac{\Gamma(\overline{B}_{\rm q}^0 \to f) - \Gamma(B_{\rm q}^0 \to \overline{f})(t)}{\Gamma(\overline{B}_{\rm q}^0 \to f) + \Gamma(B_{\rm q}^0 \to \overline{f})(t)} = \frac{(1-|\lambda_{\rm f}|^2)\cos\Delta mt - 2\sin(\Delta mt)\mathcal{I}(\lambda_{\rm f})}{(1+|\lambda_{\rm f}|^2)\cosh\frac{\Delta\Gamma}{2}t + 2\sinh\frac{\Delta\Gamma}{2}t\mathcal{R}(\lambda_{\rm f})}. \tag{3.59}$$

For $B_{\rm q}^0$ candidates, $\Delta\Gamma = 0$, and if the transition is dominated by only one amplitude, $|A_{\rm f}| = |\overline{A}_{\rm f}|$ or $\lambda_{\rm f} = 1$, then the asymmetry reduces to

$$\mathcal{A}_{\rm CP}(t) = -\sin(\Delta mt)\mathcal{I}(\lambda_{\rm f}). \tag{3.60}$$

Measurement of $\sin 2\beta$ in the $B_{\rm d}^0 \to J/\psi K_{\rm S}^0$ channel is an example of this type of CP-violation [129]. Its analogous "golden mode" in the $B_{\rm s}^0$-meson system is given by $B_{\rm s}^0 \to J/\psi\phi$, which is one of the topics of this thesis.

3.3 CP-violation in $B_{\rm s}^0 \to J/\psi\phi$

The decay of the $B_{\rm s}^0$ meson into $J/\psi \to \mu^+\mu^-$ and $\phi \to K^+K^-$ proceeds via a $\overline{b} \to \overline{c}c\overline{s}$ transition with two contributing processes: the tree level contribution ($t_{\rm f}$) and the penguin contribution ($p_{\rm f}^q$) as shown in Figure 3.10.

The total amplitude $A_{J/\psi\phi}$, including both effects, for the transition of a $B_{\rm s}^0$-meson into the final state $J/\psi\phi$ is given by

$$A_{J/\psi\phi} = V_{\rm cs}V_{\rm cb}^* t_{\rm f} + \sum_{q=u,c,t}(V_{\rm qs}V_{\rm qb}^*)p_{\rm f}^q, \tag{3.61}$$

where f denotes the given final state. The penguin amplitudes are highly suppressed,

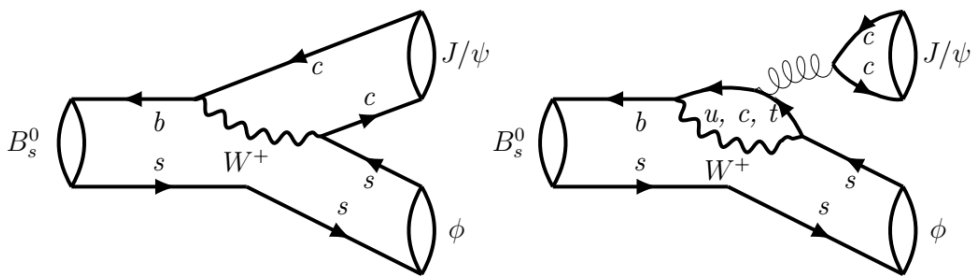

Figure 3.10: The Feynman diagrams describing contributing processes to the $B_s^0 \to J/\psi\phi$ decay. The left diagram stands for the tree level decay, while the right is the penguin diagram.

so the decay process is dominated by a single CKM amplitude. The decay amplitude A_f of $B_q^0 \to f$ can be written as

$$A_f = |A_f| e^{i(\delta_f + \phi_D)}, \tag{3.62}$$

where ϕ_D is a weak phase that enters the decay amplitude and its CP-conjugate with different signs. The δ_f is a strong phase that does not change sign under CP conjugation. The decay amplitude of $\overline{B}_q^0 \to f$ can be related to $\overline{A}_f$ using the CP condition $|f\rangle = \eta_{J/\psi}|\overline{f}\rangle$, and assuming no CP-violation in the decay, as

$$\overline{A}_f = \eta_{J/\psi}|\overline{A}_{\overline{f}}| = \eta_{J/\psi\phi}|A_f| e^{i(\delta_f - \phi_D)}, \tag{3.63}$$

where $\eta_{J/\psi\phi}$ is the CP-parity of the final state f. If the terms proportional to $V_{us}V_{ub}^*$ in the total decay amplitude $A_{J/\psi}$ are neglected, then the amplitude ratio $\frac{\overline{A}_f}{A_f}$ is given by

$$\frac{\overline{A}_f}{A_f} = -\eta_{J/\psi\phi}\frac{V_{cb}V_{cs}^*}{V_{cb}^*V_{cs}} = \eta_{J/\psi\phi}e^{2i\phi_D}, \tag{3.64}$$

where the decay phase $\phi_D = \arg(V_{cb}V_{cs}^*)$. If the B_s^0 mixes to a $\overline{B}_s^0$ before decaying to

the same final state J/ψ, then the ratio $\frac{q}{p}$ can be written as

$$\frac{q}{p} = -\frac{V_{ts}V_{tb}^*}{V_{ts}^*V_{tb}} = e^{i\phi_M}, \tag{3.65}$$

where ϕ_M is the mixing phase, given by $-2\arg(V_{ts}V_{tb}^*)$. Combining $\frac{\overline{A}_f}{A_f}$ and $\frac{q}{p}$ into λ_f gives

$$\lambda_f = \eta_{J/\psi\phi}\frac{V_{cb}V_{cs}^*V_{ts}V_{tb}^*}{V_{cb}^*V_{cs}V_{ts}^*V_{tb}} = \eta_{J/\psi\phi}e^{(2i\phi_D - i\phi_M)} = \eta_{J/\psi\phi}e^{-i\phi_s}, \tag{3.66}$$

where $\phi_s = -\arg(\eta_{J/\psi\phi}\lambda_f)$ and is the CP-violating phase that can be related to the angle β_s in the unitarity triangle in Figure 3.7 via the relation $\phi_s \simeq 2\beta_s$ with $\beta_s = \arg(-\frac{V_{ts}V_{tb}^*}{V_{cs}V_{cb}^*})$. While the mixing and decay phases depend on phase conventions and are not observable, the phase ϕ_s is a measurable physical quantity.

The angle β_s in the B_s^0 unitarity triangle is much smaller than the β_s in the B_d^0 unitarity triangle in Figure 3.5 since V_{ts} is real up to $\mathcal{O}(10^{-3})$ whereas V_{td} is already complex at $\mathcal{O}(10^{-3})$. The phase ϕ_s is very small in the SM; its recently predicted values are $(-0.03696^{+0.00072}_{-0.00082})$ rad by the CKMFitter group [126], and (-0.03700 ± 0.00104) rad by the UTfit Collaboration [138].

The B_s^0 system possesses a significant decay width difference $\Delta\Gamma_s$. The recent theoretically predicted values are (0.091 ± 0.0013) ps^{-1} [139] and (0.092 ± 0.0014) ps^{-1} [140].

If a New Physics process is involved, then different values of ϕ_s and $\Delta\Gamma_s$ should be expected. The oscillation frequency, Δm_s, is also sensitive to New Physics, but the theoretical predictions are calculated with high uncertainty. Its current predicted value is (18.3 ± 2.7) ps^{-1} [139].

3.3.1 Current Experimental Status

The phase ϕ_s and other $B_s^0 - \overline{B}_s^0$ mixing parameters have been measured in several analyses: four $B_s^0 \to J/\psi\phi$ analyses from CDF [141], D∅ [142], ATLAS [111] and CMS [143]; and four analyses from LHCb of the decay modes $B_s^0 \to J/\psi K^+K^-$ [144], $B_s^0 \to J/\psi\pi^+\pi^-$ [145], $B_s^0 \to \psi(2s)\phi$ [146] and $B_s^0 \to D_s^+D_s^-$ [146]. A combined two-dimensional fit of ϕ_s and $\Delta\Gamma_s$, without external constraints, yields two symmetric solutions related through $\phi_s \leftrightarrow \pi - \phi_s$ and $\Delta\Gamma_s \leftrightarrow -\Delta\Gamma_s$. The Heavy Flavor Combination Group (HFLAV) produced 68% confidence level (CL) contours [108] in the $(\phi_s, \Delta\Gamma_s)$ plane, showing measurements from CDF, D∅, ATLAS, CMS and LHCb and their combination, and these are shown in Figures 3.11 and 3.12 for all decay channels and for the $B_s^0 \to J/\psi\phi$ decay channel, respectively. As can be seen from the figures, the combination of results is consistent with the SM prediction, but in order to exclude any BSM physics, more precise measurements are needed.

The CL contours from the ATLAS experiment in Figures 3.11 and 3.12 are obtained from 99.7 fb^{-1} of data from Run 1 (2011-2012) [131] and part of Run 2 (2015-2017) [111]. The results are consistent with the SM predictions so far, and the precision on ϕ_s and $\Delta\Gamma_s$ is currently the best in the world achieved by using a single channel.

3.3.2 Angular Analysis

The experimental measurement of physics variables in the decay $B_s^0 \to J/\psi\phi$ uses the fact that the decay is a pseudoscalar to vector-vector transition. The J/ψ and ϕ are

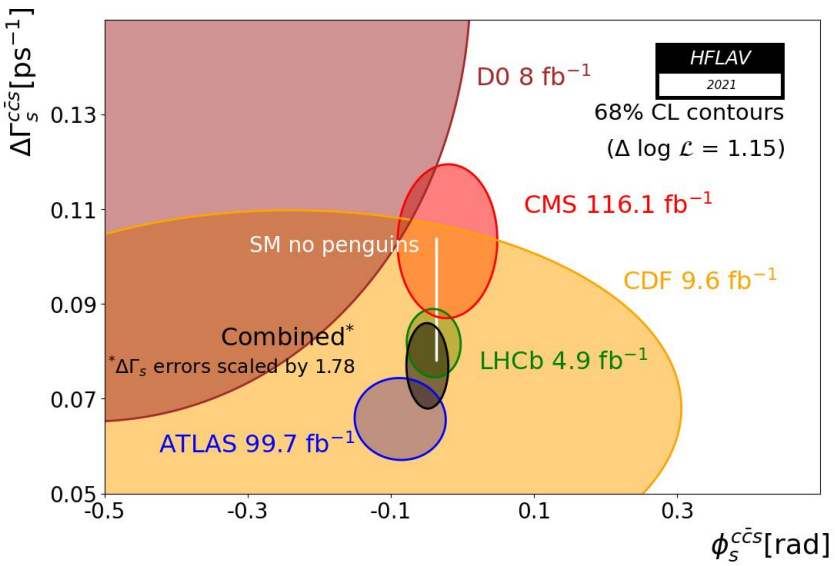

Figure 3.11: The 68% confidence level (CL) contours in the $(\phi_s, \Delta\Gamma_s)$ plane, showing individual measurements from CDF, DØ, ATLAS, CMS and LHCb and their combination for all decay channels. The thin black rectangle represents the Standard Model predictions of ϕ_s [126] and $\Delta\Gamma_s$ [139].

vector mesons: they can have an even or odd relative orbital angular momentum L in the final state ($L = 0, 1, 2$). Due to total angular momentum conservation, the final state is therefore an admixture of CP-even ($L = 0, 2$) and CP-odd ($L = 1$) states. Consequently, the decay is described by three time-dependent complex amplitudes and strong phase differences corresponding to the polarization states of the vector mesons. By defining a transversity angle basis, an angular analysis method [103, 147] is used by which the different CP-components can be separated statistically. It is described briefly in this subsection.

Two bases, helicity and transversity, are commonly used to describe the angular distribution of two vector final states, and these bases are described as follows:

- The helicity of a particle, λ, is defined as the component of the spin that is

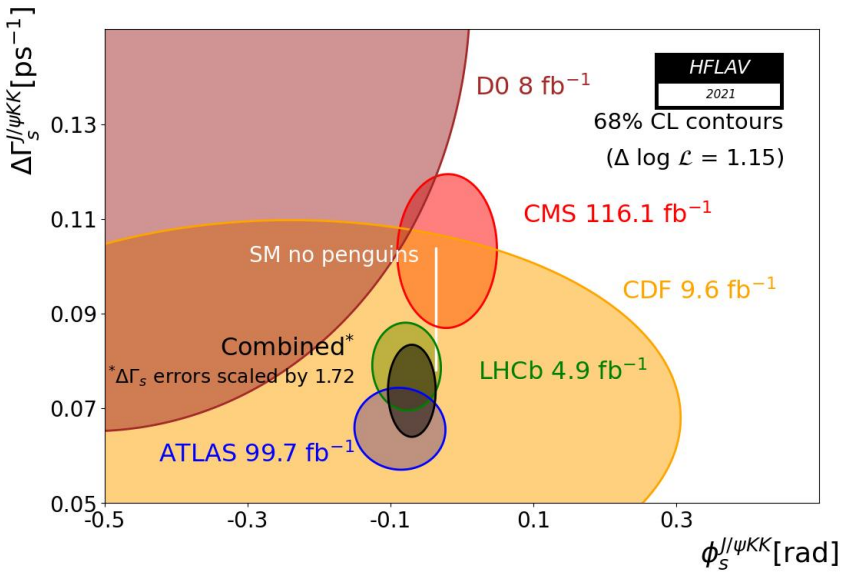

Figure 3.12: The 68% confidence level (CL) contours in the $(\phi_s, \Delta\Gamma_s)$ plane, showing individual measurements from CDF, DØ, ATLAS, CMS and LHCb and their combination for the $B_s^0 \to J/\psi\phi$ decay channel. The thin black rectangle represents the Standard Model predictions of ϕ_s [126] and $\Delta\Gamma_s$ [139].

projected along the direction of its momentum. For a vector particle its possible values are $-1, 0, 1$. The helicity basis with three helicity angles $\Omega_{\text{hel}} = (\theta_l, \theta_k, \phi_h)$ is defined in Figure 3.13. The θ_l is the angle between the positively charged lepton, l^+, and the flight direction of the opposite B_s^0 in the center-of-mass frame of the dilepton, l^+l^-. The angle θ_k is defined as the angle between the positively charged kaon, K^+, and the flight direction of the opposite B_s^0 in the center-of-mass frame of the pair of kaons, K^+K^-. The relative rotation of the two decay planes, ϕ_h, is the angle between the l^- side of the K^+K^- plane and the l^+ side of the l^+l^- plane.

Here, helicities of the final state are constrained by the orbital angular momen-

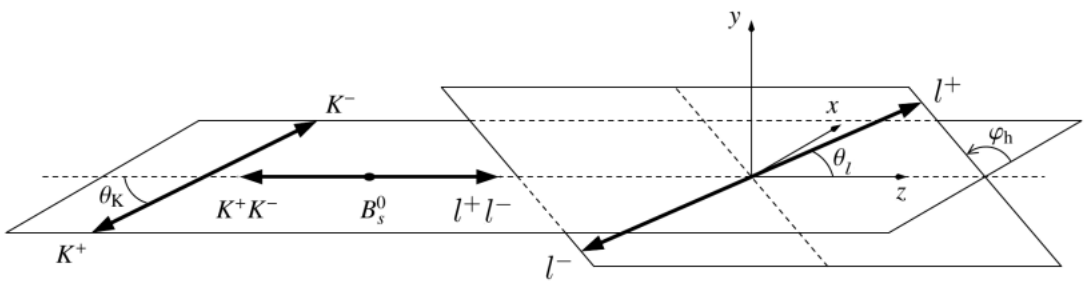

Figure 3.13: The definition of the helicity angle basis [148].

tum of the initial particle:

$$|\lambda_{J/\psi} - \lambda_\phi| = J(B_s^0). \tag{3.67}$$

Since $J(B_s^0) = 0$, the helicity of the final state particles is constrained to $\lambda_{J/\psi} = \lambda_\phi$ and thus, only three combinations are valid. The final state can be written as

$$|B_s^0\rangle = \sum_\lambda H_\lambda |f_\lambda\rangle, \tag{3.68}$$

where $\lambda = (-1, 0, 1)$ and H_λ is the helicity amplitude of the final state f_λ. However, the helicity amplitudes are not eigenstates of CP.

- In the transversity basis, the spin of one of the final states is projected onto the rest frame defined by the other final state. The decay amplitude can be decomposed into independent components, corresponding to the linear polarization states of the vector mesons in the final states. The polarization states can be longitudinal, A_0, or transverse to the direction of motion of the vector mesons. In the case of transverse polarization, the states can be parallel,

$A_\parallel$, or perpendicular, $A_\perp$, to each other. The final state can be written as

$$|B_s^0\rangle = \sum_\lambda A_\lambda |f_\lambda\rangle, \tag{3.69}$$

where $\lambda = (\parallel, \perp, 0)$.

A relationship between the transversity and helicity amplitudes exists and is given by

$$A_\parallel = \frac{H_{+1} + H_{-1}}{\sqrt{2}},\ A_\perp = \frac{H_{+1} - H_{-1}}{\sqrt{2}},\ \text{and}\ A_0 = H_0. \tag{3.70}$$

The transversity eigenstates are aligned with the CP-eigenstates, which facilitates a cleaner extraction of the physics parameters and hence, the transversity basis is preferred by experiments. This analysis is performed with the transversity basis.

The transversity basis with three transversity angles $\Omega_T = (\theta_T, \psi_T, \phi_T)$ is shown in Figure 3.14. These angles are defined in the rest frame of the final particles with the x-axis determined by the direction of the ϕ meson in the J/ψ rest frame and the $x-y$ plane defined by the K^+K^- system with $p_y(K^+) > 0$. In this coordinate system, θ_T and ϕ_T define the polar and azimuthal angles, respectively, of the μ^+ in the rest frame of the J/ψ, while ψ_T defines the angle between the momenta, $\vec{p}(K^+)$ and $\vec{p}(J/\psi)$, in the ϕ meson rest frame.

There is an associated phase $\delta_0 = \arg(A_0)$, $\delta_\parallel = \arg(A_\parallel)$ and $\delta_\perp = \arg(A_\perp)$ for each of the transversity amplitudes. The phase $\delta_0 = 0$ by convention, as only phase differences between the amplitudes appear in the differential decay rate. These parameters are used for the description of the resonant P-wave signal state; however, the primary signal can be contaminated by other processes with the same final state,

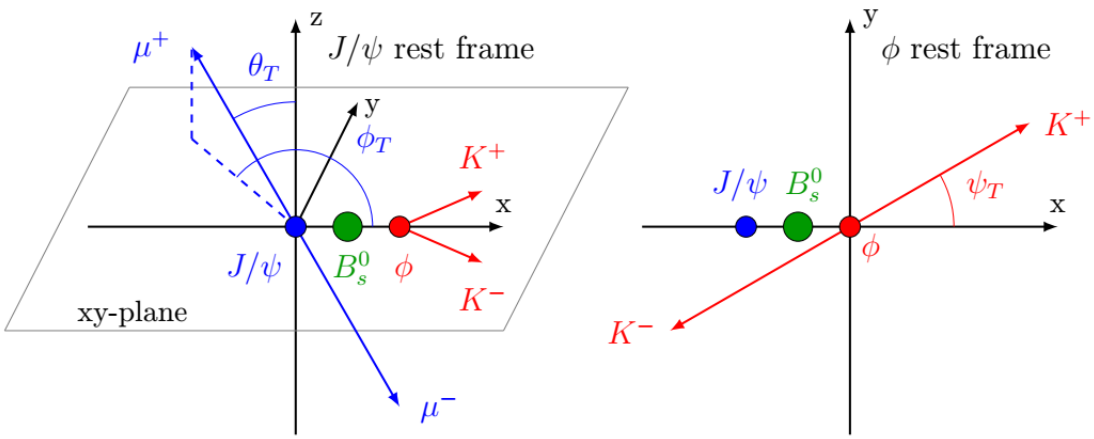

Figure 3.14: Illustration of the transversity angles between the final state particles in the $B_d^0 \to J/\psi(\mu^+\mu^-)\phi(K^+K^-)$ decay [148].

such as $B_s^0 \to J/\psi f$ where $f \to K^+K^-$, or non-resonant $B_s^0 \to J/\psi K^+K^-$. These S-wave states have to be accounted for in the final description of the decay, using their own amplitude A_S and phase δ_S.

In general, the distribution for the time t and the transversity angles $\Omega(\theta_T, \psi_T, \phi_T)$ is given by the differential decay rate

$$\frac{d^4\Gamma}{dtd\Omega} = \sum_{k=1}^{n} \mathcal{O}^{(k)}(t) g^{(k)}(\theta_T, \psi_T, \phi_T), \tag{3.71}$$

where the $\mathcal{O}^{(k)}(t)$ are the time-dependent functions corresponding to the contributions of the four different amplitudes $(A_0, A_\parallel, A_\perp, A_S)$ and their interference terms, and the $g^{(k)}(\theta_T, \psi_T, \phi_T)$ are the angular functions. The final time-dependent amplitudes, the additional S-wave terms, and the summary of angular functions are given in Appendix B.

3.4 Extraction of CP-violating Parameters from $B_s^0 \to J/\psi\phi$ Decays

The candidate events for the $B_s^0 \to J/\psi\phi$ decays were selected and reconstructed through a series of steps as outlined in the previously published paper [111]. A multidimensional unbinned maximum likelihood fit is performed to extract the physics parameters. The fit uses information about the reconstructed mass m, the measured proper decay time t, the measured mass uncertainty σ_m, the measured proper decay time uncertainty σ_t, the measured transverse momentum p_T, the per-candidate probability that the B-meson candidate was produced in a state B_s^0, $P(B|Q_x)$, and the transversity angles Ω of each $B_s^0 \to J/\psi\phi$ event. The likelihood function is composed of signal and background probability density functions (PDFs) as outlined in Reference [111]. The signal PDF includes 9 physics parameters of interest, the $CP-$violating phase, ϕ_s, the average decay width, Γ_s, the decay width difference, $\Delta\Gamma_s$, the squares of the tranversity amplitudes, A_0, $A_\parallel$, and A_S, and their strong phase differences, δ_0, $\delta_\parallel$, and δ_S.

3.5 Time Efficiency Corrections

In the analysis of $B_s^0 \to J/\psi\phi$ decays, time efficiency corrections discussed previously in Section 2.7 were used to address inefficiencies of dimuon triggers. Time efficiency corrections for the prescale triggers that select only a fraction of events to be recorded out of all possible events that would have passed the trigger requirements are shown in Figures 3.15, 3.16, 3.17 and 3.18 for the years 2015, 2016, 2017 and 2018, respectively.

For 2016, the trigger menu was modified later due to a miscalibration and as a result, these triggers carry a postfix "delayed" to distinguish them from the miscalibrated triggers; the data set for the year 2016 was named "2016B."

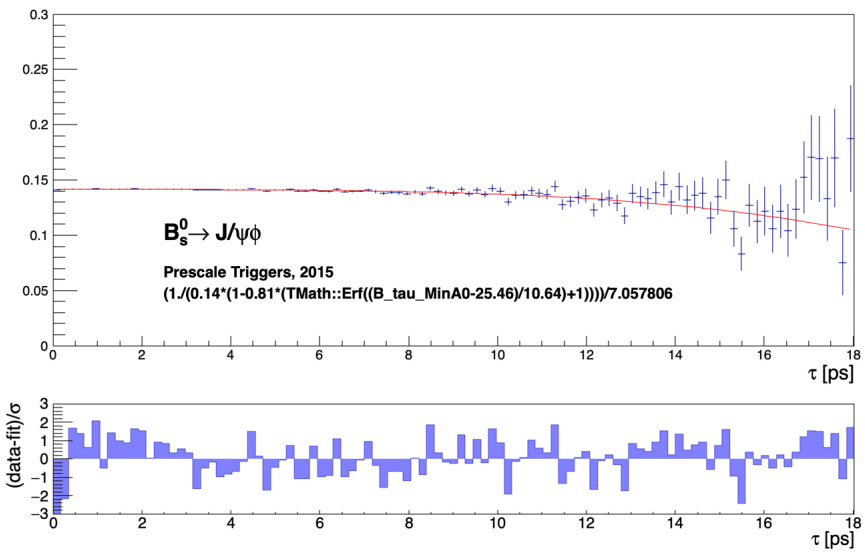

Figure 3.15: Time efficiency function for the events in the 2015 Run 2 data set.

From Figures 3.15 and 3.16, it is noticeable that the time efficiency declines after approximately 5 ps. This observation aligns with expectations since the proper decay time of the B_s^0-meson is under 2 ps. However, for data from the years 2017 and 2018 shown in Figures 3.17 and 3.18, respectively, the time efficiency decreases at a steady rate beginning at 0 ps. To understand this anomaly better, the most dominant triggers for the years 2017 and 2018 were identified. The three most dominant triggers are shown in Tables 3.2 and 3.3.

Tables 3.2 and 3.3 indicate that the triggers designed to select B_s^0 candidates,

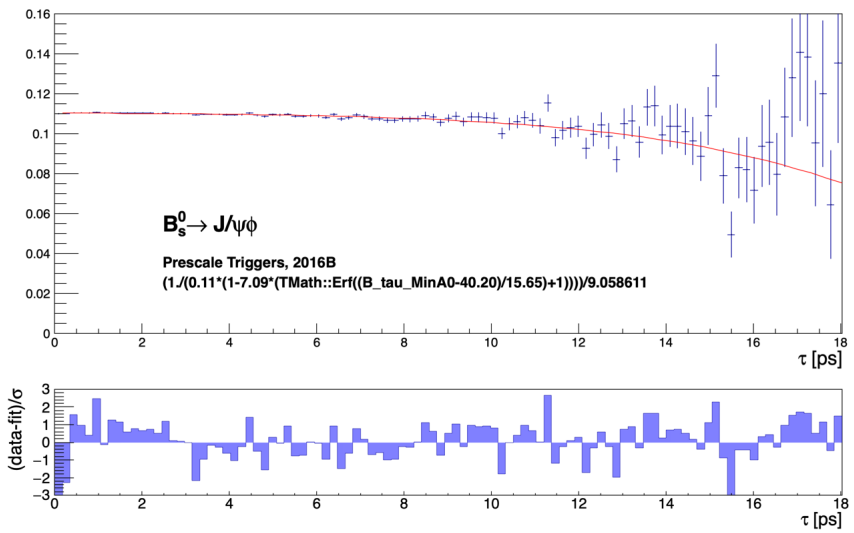

Figure 3.16: Time efficiency function for the events in the 2016B Run 2 data set.

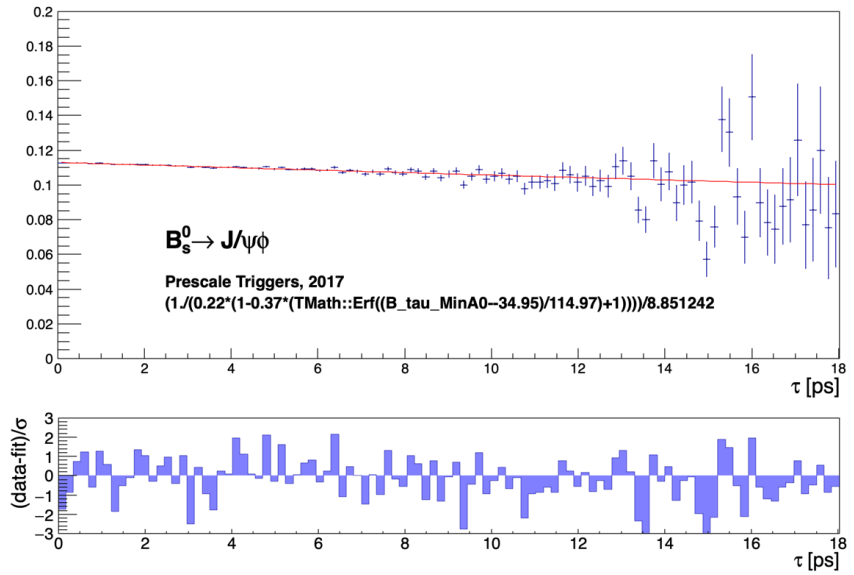

Figure 3.17: Time efficiency function for the events in the 2017 Run 2 data set.

which are reconstructed from a pair of oppositely charged muons and two additional oppositely charged tracks that satisfy the invariant mass criteria for the ϕ-meson, yielded the highest event count in the Run 2 dataset during the years 2017 and 2018.

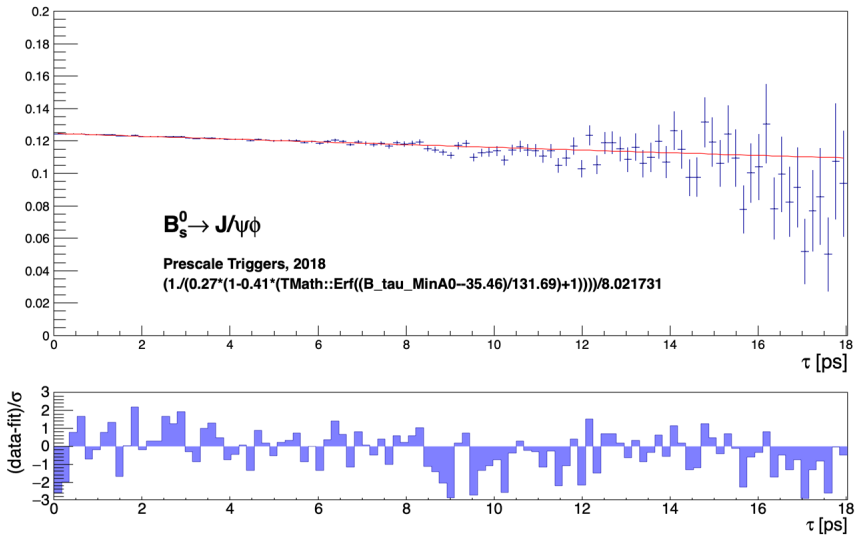

Figure 3.18: Time efficiency function for the events in the 2018 Run 2 data set.

No	Trigger Name	% of the events
1	HLT_mu6_mu4_bBmumux_BsmumuPhi_L1BPH _2M9_MU6MU4_BPH_0DR15_MU6MU4	58.37
2	HLT_2mu6_bJpsimumu_L1BPH_2M9_2MU6 _BPH_2DR15_2MU6	33.68
3	HLT_2mu6_bBmumux_BsmumuPhi_L1BPH _2M9_2MU6_BPH_2DR15_2MU6	29.08

Table 3.2: Percentage of the candidate events that were selected by each of the three most dominant triggers in the Run 2 data set for the year 2017.

These triggers are referred to as "mumuphi" triggers and were introduced in the year 2017 to facilitate the analysis using $B_s^0 \to J/\psi\phi$ decays. The time efficiency of the mumuphi trigger that collects two muons with p_T values above 4 GeV and 6 GeV is shown in Figure 3.19.

From Figure 3.19, it can be seen that the time efficiency of the most dominant trigger decreases at a rate faster than that of all triggers in year 2017 shown in

No	Trigger Name	% of the events
1	HLT_mu6_mu4_bBmumux_BsmumuPhi_L1BPH _2M9_MU6MU4_BPH_0DR15_MU6MU4	55.74
2	HLT_2mu4_bBmumux_BsmumuPhi_L1BPH _2M9_2MU4_BPH_0DR15_2MU4	37.33
3	HLT_2mu6_bJpsimumu_L1BPH_2M9_2MU6_BPH _2DR15_2MU6	30.19

Table 3.3: Percentage of the candidate events that were selected by each of the three most dominant triggers in the Run 2 data set for the year 2018.

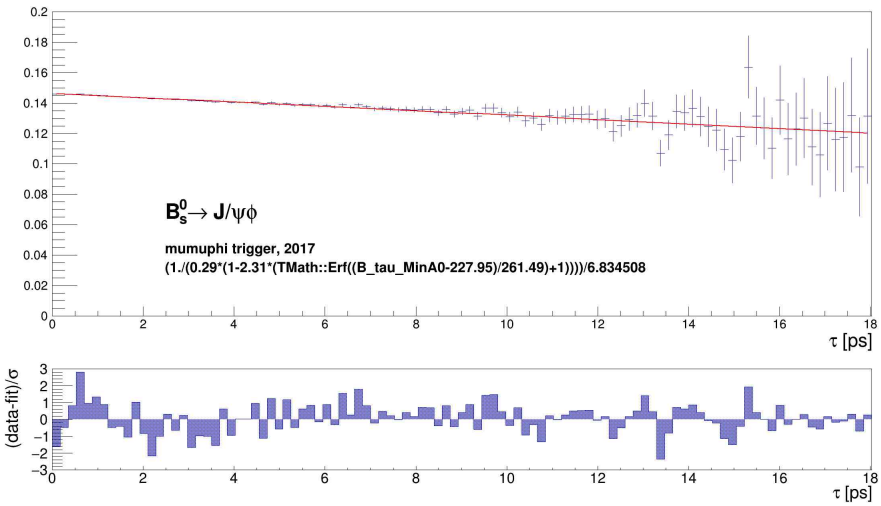

Figure 3.19: Time efficiency function for the events collected by the mumuphi trigger in the 2017 Run 2 data set.

Figure 3.17. Figure 3.20 shows the time efficiency of the triggers other than mumuphi trigger, using the events in year 2017.

From Figure 3.20, it can be observed that the time efficiency of the triggers other than the mumuphi trigger declines at a slower rate compared to that observed in Figure 3.17. However, the observed time efficiency without the mumuphi trigger still has a higher rate of decline compared to the time efficiencies for the years 2015 and

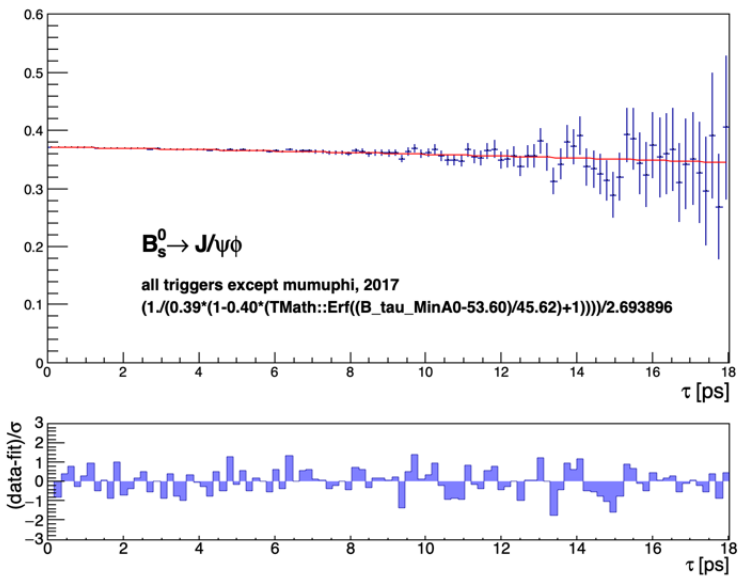

Figure 3.20: Time efficiency function for the events collected by all triggers except the mumuphi trigger in the 2017 Run 2 data set.

2016, shown in Figures 3.15 and 3.16, respectively. This is due to the fact that the study reported in Figures 3.19 and 3.19 considered only the most dominant trigger in Table 3.2; other mumuphi triggers with different p_{T} thresholds for the dimuon pair were not considered.

3.6 Impact of mumuphi Triggers on the Extraction of CP-violating Parameters

The candidates for B_s^0-mesons are reconstructed from a pair of oppositely charged muons and a pair of oppositely charged kaons. The mumuphi triggers deployed in the years 2017 and 2018 introduced a selection cut that eliminates the μ^+K^+ or μ^-K^- candidates with an angular separation, ΔR, below 0.04 radians; this value

is calculated from the pseudorapidity difference, $\Delta\eta$ of the track candidates. As a consequence, the fitted values of transversity amplitudes, A_0, $A_{\|}$, and A_S, using the full Run 2 data set (2015-18) show discrepancies compared to the fit results obtained using the partial Run 2 data set (2015-17) [111], as shown in Figures 3.21, 3.22, and 3.23, respectively.

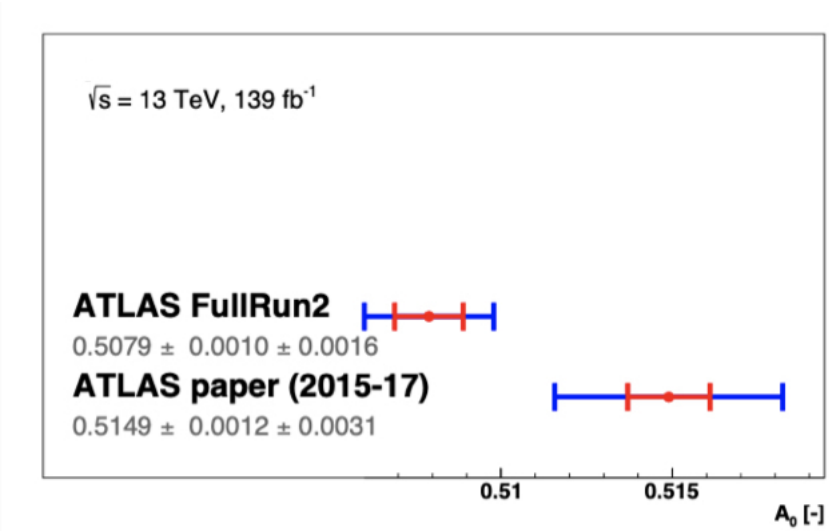

Figure 3.21: A comparison ofthe fitted transversity amplitude A_0 using the partial and full Run 2 data sets. The red bar indicates statistical uncertainty while the blue bar indicates the statistical and systematic uncertainties combined in quadrature.

However, other physics variables of interest, namely, ϕ_s and $\Delta\Gamma_s$, remain consistent in the fitted results using the partial and full Run 2 data sets, and these are shown in Figures 3.24 and 3.25, respectively.

From Figures 3.24 and 3.25, it can be seen that the statistical precision of the parameters ϕ_s and $\Delta\Gamma_s$ using the full Run 2 data set have improved by a factor of 1.3 times over the results using the partial Run 2 data set, and that they are consistent

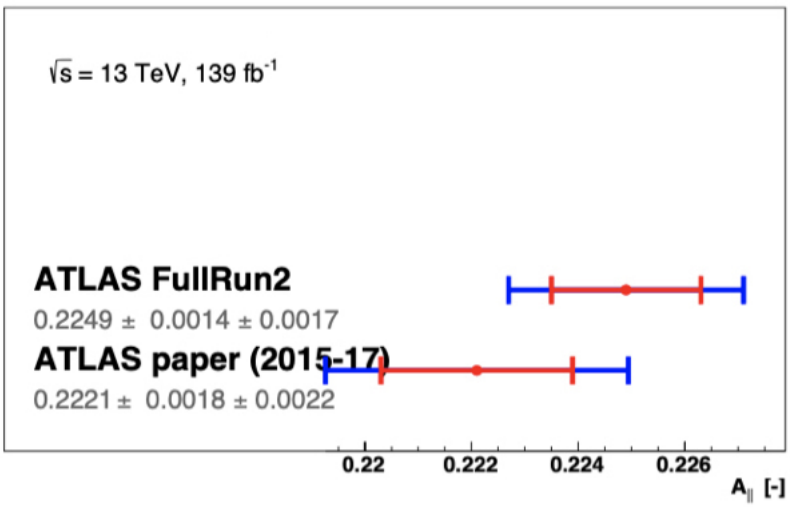

Figure 3.22: A comparison of the fitted transversity amplitude $A_{\|}$ using the partial and full Run 2 data sets. The red bar indicates statistical uncertainty while the blue bar indicates statistical and systematic uncertainties combined in quadrature.

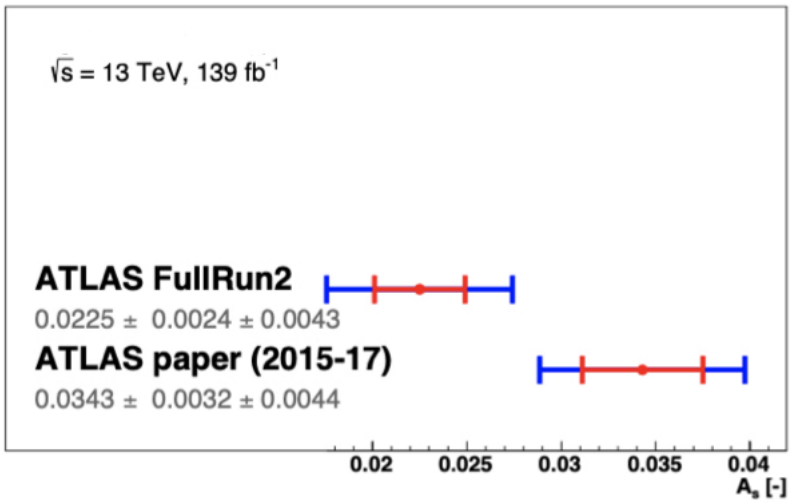

Figure 3.23: A comparison of the fitted transversity amplitude A_S using the partial and full Run 2 data sets. The red bar indicates statistical uncertainty while the blue bar indicates statistical and systematic uncertainties combined in quadrature.

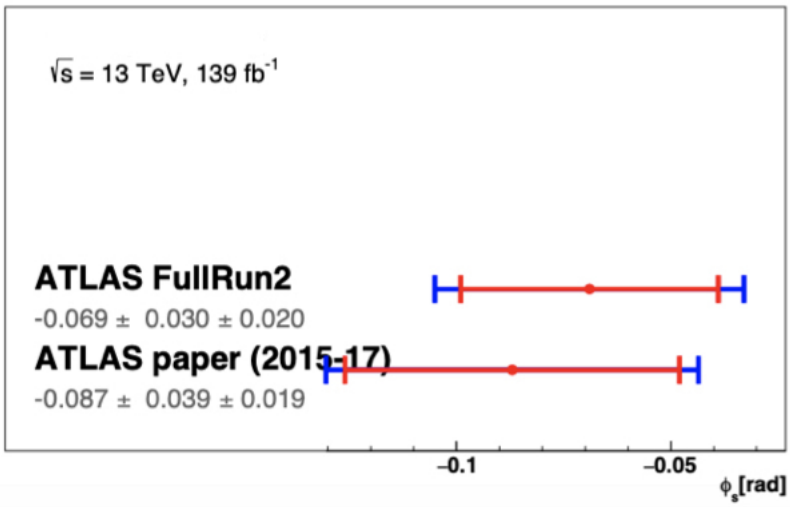

Figure 3.24: A comparison of the fitted ϕ_s using partial and full Run 2 data sets. The red bar indicates statistical uncertainty while the blue bar indicates statistical and systematic uncertainties combined in quadrature.

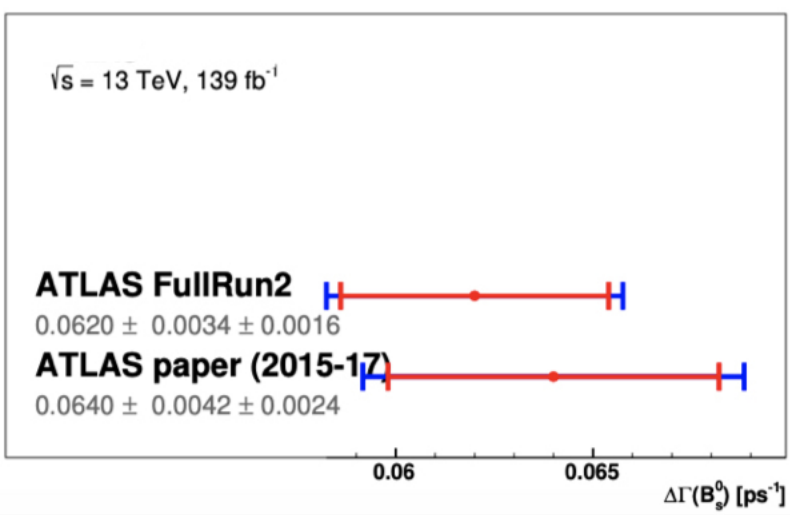

Figure 3.25: A comparison of the fitted $\Delta\Gamma_s$ using the partial and full Run 2 data sets. The red bar indicates statistical uncertainty while the blue bar indicates statistical and systematic uncertainties combined in quadrature.

with the Standard Model predictions.

3.7 Future of $B_s^0 \to J/\psi\phi$ Analysis

The most important physics parameters of the $B_s^0 \to J/\psi\phi$ decays, ϕ_s and $\Delta\Gamma_s$, achieve a statistical precision 1.3 times better than in the previously published ATLAS result [111]. It is essential to address the variations introduced by the mumuphi triggers, as the events they collected represent a substantial portion of the 2018 data. While these triggers were also active in 2017, the impact on the results is negligible due to the comparatively smaller dataset from that year. A significant effort to include the $B_s^0 \to J/\psi\phi$ decay candidates that were isolated by a flawed selection cut in ΔR is underway but is beyond the scope of this dissertation.

Chapter 4

B-Physics Triggers

4.1 Introduction

The presence of prompt muons in the final state is a distinctive signature for many physics processes studied in collisions at the LHC. These studies include measurements of properties of the Higgs boson and Standard Model processes, searches for new phenomena, and the B-physics and Light States (BLS) programme. The ATLAS muon trigger system identifies muons produced in proton–proton or heavy-ion interactions and is designed to do so with high efficiency and low muon transverse momentum (p_{T}) thresholds.

In order to be sensitive to a wide variety of final state topologies, ATLAS has developed a suite of triggers designed to select muons. A single-muon trigger with a p_{T} threshold of 26 GeV is used by many physics analyses. In addition, muon triggers in combination with electrons, τ-leptons, jets and missing transverse momentum, as

well as multi-muon triggers with lower muon p_{T} thresholds, increase the sensitivity for various physics phenomena which benefit from a lower p_{T} threshold. For the BLS programme studying beauty, quarkonia and low-mass hadrons, various low-p_{T} multi-muon triggers are used with a special configuration that allows a high trigger efficiency for non-prompt muons. This thesis uses the triggers that apply best to the BLS programme.

4.2 Trigger Validation for Dimuon HLT Triggers for Run 3

One of the major upgrades in Run 3 is that of the ATLAS software framework, Athena, whose algorithms are being optimized for multithreaded CPUs and efficient memory usage. The HLTs were modified to reflect these changes and as a result, it was essential to assure that the triggers were working prior to Run 3. A study was undertaken to understand the working of triggers that are crucial to the lifetime measurements and CP-violation studies discussed in this chapter and the next chapter, respectively.

This study was based on dimuon triggers since B-meson decays are mostly identified with a pair of oppositely-charged muons in the final state (such as in the decay $B_{\mathrm{s}}^{0} \to J/\psi\phi$ where $J/\psi \to \mu^{+}\mu^{-}$ as shown in Figure 4.1.)

The trigger validation is performed by producing the invariant mass distribution of a B-meson from a pool of MC events, using a set of dimuon triggers and applying selection criteria specific for the B-meson decay considered. Each set of dimuon

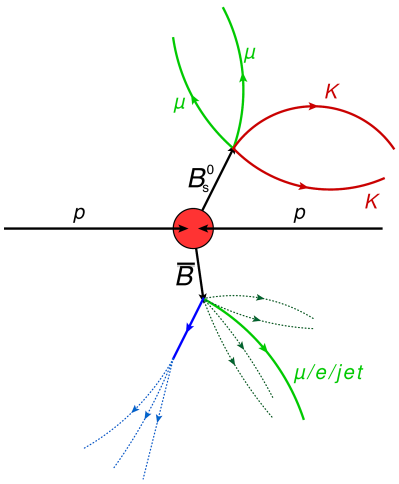

Figure 4.1: The final states of the $B_s^0 \to J/\psi\phi$ decay.

triggers is differentiated by a minimum transverse momentum p_T of the muons, and in each set, the triggers are further classified as generic or specialized triggers. The generic trigger collects dimuon events of the mass consistent with the invariant mass of the J/ψ. Each specialized trigger collects information on the hadrons in the decay recorded by the ID, in addition to information on the events satisfying the invariant mass of the J/ψ. Selection of events for each topology typically involves imposing the following requirements:

- threshold for the p_T of each muon in a dimuon pair,
- threshold for the p_T of hadron candidates,
- rejection of same-charge combinations of muons in dimuon pairs and hadronic candidate pairs,
- invariant mass requirement, and
- vertex χ^2/ndof requirement.

Trigger validation was performed for the following decay chains:

- $B_{\mathrm{s}}^{0} \to J/\psi(\to \mu^{+}\mu^{-})\phi(\to K^{+}K^{-})$,
- $B_{\mathrm{d}}^{0} \to J/\psi(\to \mu^{+}\mu^{-})K^{*0}(\to K^{\pm}\pi^{\mp})$, and
- $B^{+} \to J/\psi(\to \mu^{+}\mu^{-})K^{+}$

4.3 Trigger Validation for $B_{\mathrm{s}}^{0} \to J/\psi(\to \mu^{+}\mu^{-})\phi(\to K^{+}K^{-})$

All triggers used in this study were based on identification of a $J/\psi \to \mu^{+}\mu^{-}$ decay, with p_{T} greater than 4 GeV, 6 GeV or 11 GeV for each muon in the dimuon pair. A set of eight dimuon triggers was used to select B_{s}^{0} candidates from a MC sample of 4000 events. Four out of the eight triggers are generic triggers that collected events satisfying the invariant mass of the J/ψ, and the remaining four triggers collected events that satisfy the invariant mass of the J/ψ but also have information on the ϕ-meson in the hadronic track. All of the triggers along with their distribution in the MC sample are shown in Table 4.2. It can be observed from the table that the number of events in specialized triggers did not exceed the number of events in generic triggers for each p_{T} threshold, which is expected. As an example, HLT_2mu4_bJpsimumu_L12MU4, a generic trigger that collects events containing two muons both with $p_{\mathrm{T}} > 4$ GeV, was triggered 927 times, while HLT_2mu4_bBmumux_BsmumuPhi_L12MU4, a specialized trigger that collects events containing two muons both with $p_{\mathrm{T}} > 4$ GeV and a hadronic track that contributes to the reconstruction of the ϕ-meson, was triggered 474 times. A similar pattern was observed for other triggers.

No	Trigger Name	Counts
1	HLT_2mu4_bJpsimumu_L12MU4	927
2	HLT_2mu4_bBmumux_BsmumuPhi_L12MU4	474
3	HLT_mu6_mu4_bJpsimumu_L1MU6_2MU4	741
4	HLT_mu6_mu4_bBmumux_BsmumuPhi_L1MU6_2MU4	395
5	HLT_2mu6_bJpsimumu_L12MU6	323
6	HLT_2mu6_bBmumux_BsmumuPhi_L12MU6	185
7	HLT_mu11_mu6_bJpsimumu_L1MU11_2MU6	151
8	HLT_mu11_mu6_bBmumux_BsmumuPhi_L1MU11_2MU6	90

Table 4.1: Distribution of generic and specialized dimuon triggers in a MC sample containing 4000 events.

The candidates for the decay $\phi \to K^+K^-$ were reconstructed from all pairs of oppositely charged tracks that are not identified as muons. Candidate events for $B_s^0 \to J/\psi\phi$ decays were selected by fitting the tracks for each combination of $J/\psi \to \mu^+\mu^-$ and $\phi \to K^+K^-$ to a common vertex. The fit was also constrained by fixing the invariant mass, calculated from the two muon tracks, to the J/ψ mass. A quadruplet of tracks is accepted for further analysis if the vertex fit has $\chi^2/\text{ndof} < 3$. For the $\phi \to K^+K^-$ candidate, the invariant mass of the track pairs using a charged kaon mass hypothesis was required to fall within the interval $1.0085\ \text{GeV} < m(K^+K^-) < 1.0305\ \text{GeV}$. The 1366 candidates were found to have mass within the range $5.150 - 5.650$ GeV The invariant mass distribution of these reconstructed B_s^0 candidates is shown in Figure 4.2. The peak of the distribution of dimuon events collected by all the triggers is about 5367 MeV, which is close to the Particle Data Group (PDG) mass of the B_s^0, 5366.79 MeV [10], indicating that the triggers are working as they should.

The distribution of the 1366 candidates among triggers is shown in the Table 4.2, and the invariant mass distribution of the 1366 candidates in each trigger is shown in

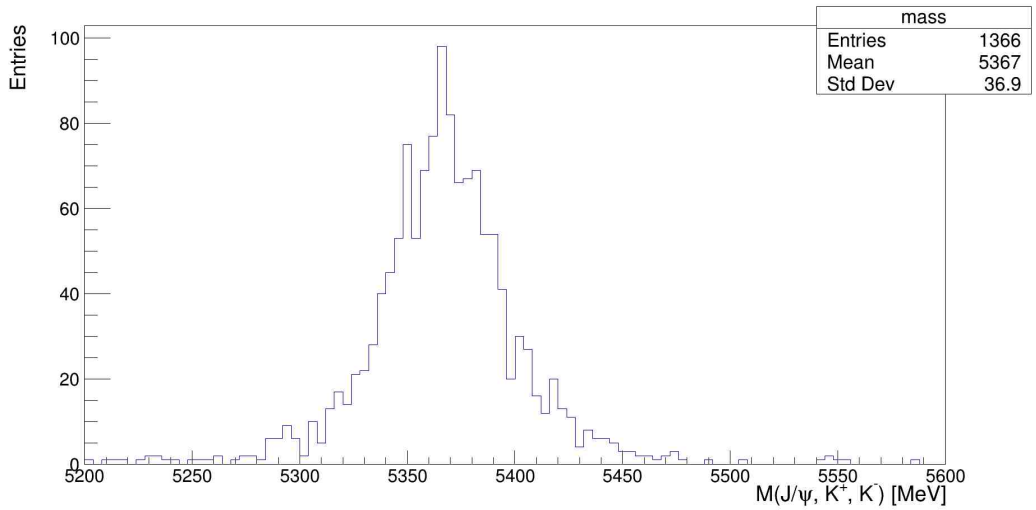

Figure 4.2: Invariant mass distribution of reconstructed B_s^0-mesons from the selected events.

Figure 4.3.

Threshold	bJpsimumu	bBmumux_BsmumuPhi	% bJpsimumu	% bBmumux_BsmumuPhi
2mu4	392	375	42.3	79.1
mu6_mu4	326	312	44.0	79.0
2mu6	160	150	49.5	81.1
mu11_mu6	79	75	52.3	83.3

Table 4.2: Distribution of triggers in the reconstructed B_s^0 candidates.

The following observations can be made about Table 4.2:

- the fraction of reconstructed B_s^0 candidates from specialized triggers for all p_T thresholds is almost twice the fraction of events from generic triggers. This is expected, as specialized triggers collect events with information on hadrons in the final state and these show higher efficiency compared to their generic counterparts. Hence, the $B_s^0 \to J/\psi\phi$ analysis benefits from specialized triggers,

- the triggers with the lowest p_{T} threshold ($p_{\mathrm{T}} > 4$ GeV) collected the most events,
- specialized triggers did not achieve 100% efficiency due to the fact that the candidates for the decay $\phi \to K^+K^-$ were reconstructed from all pairs of oppositely charged tracks that are not identified as muons and were assigned the mass of ϕ, and
- none of the triggers are biased to high or low masses.

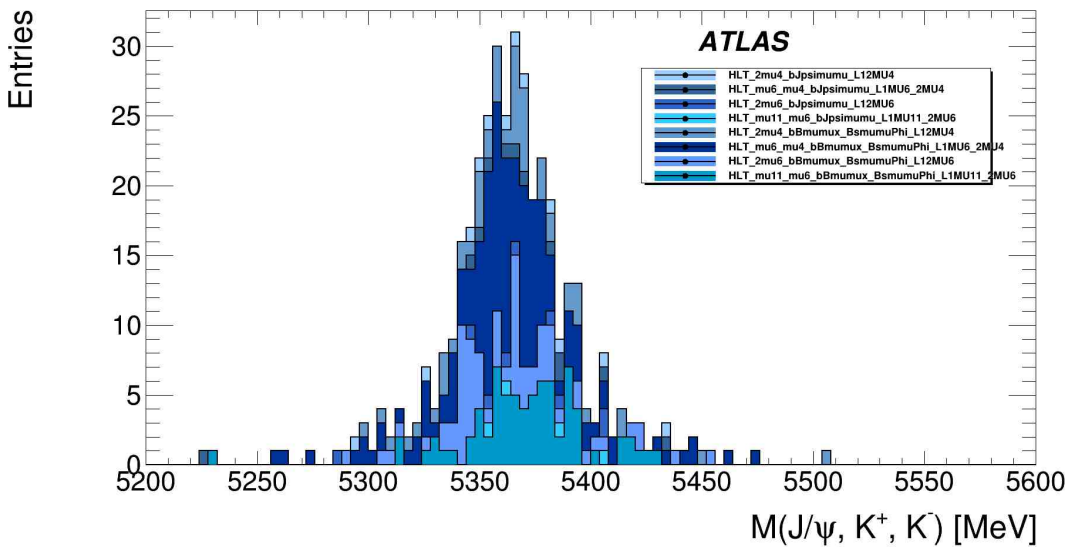

Figure 4.3: Contribution of each trigger to the invariant mass distribution of reconstructed B_{s}^0-mesons.

Dimuon triggers based on AthenaMT for $B_{\mathrm{s}}^0 \to J/\psi(\to \mu^+\mu^-)\phi(\to K^+K^-)$ are working and show good efficiency.

4.4 Trigger Validation for $B_{\mathrm{d}}^{0} \to J/\psi(\to \mu^{+}\mu^{-})K^{*0}(\to K^{+}\pi^{-})$

All triggers used in this study were based on identification of a $J/\psi \to \mu^{+}\mu^{-}$ decay, with p_{T} greater than 4 GeV, 6 GeV or 11 GeV for each muon in the dimuon pair. A set of eight dimuon triggers was used to select B_{d}^{0} candidates from a MC sample of 10,000 events. Four out of the eight triggers are generic triggers that collected events that are consistent with the invariant mass of the J/ψ, and the remaining four triggers collected events that are consistent with the invariant mass of the J/ψ and also use information on the two oppositely-charged mesons produced after the hadronic track. All triggers along with their distribution in the MC sample are shown in Table 4.3. It can be observed from Table 4.3 that the number of events in specialized triggers did not exceed the number of events in generic triggers for each p_{T} threshold, which is expected. As an example, HLT_2mu4_bJpsimumu_L12MU4, a generic trigger that collects events containing two muons both with $p_{\mathrm{T}} > 4$ GeV, was triggered 1691 times, while HLT_2mu4_bBmumux_BdmumuKst_L12MU4, a specialized trigger that collects events containing two muons both with $p_{\mathrm{T}} > 4$ GeV and a hadronic track that contributes to the reconstruction of the K^{*0}-meson, was triggered 1263 times. A similar pattern was observed for other triggers.

The candidates for the decay $B_{\mathrm{d}}^{0} \to J/\psi K^{*0}$ were required to contain at least one reconstructed primary vertex, formed from at least four ID tracks, and at least one pair of oppositely-charged muon candidates that were reconstructed using information from the MS and the ID. Since the mass resolution is different in different parts of

No	Trigger Name	Counts
1	HLT_2mu4_bJpsimumu_L12MU4	1691
2	HLT_2mu4_bBmumux_BdmumuKst_L12MU4	1263
3	HLT_mu6_mu4_bJpsimumu_L1MU6_2MU4	1385
4	HLT_mu6_mu4_bBmumux_BdmumuKst_L1MU6_2MU4	1064
5	HLT_2mu6_bJpsimumu_L12MU6	623
6	HLT_2mu6_bBmumux_BdmumuKst_L12MU6	505
7	HLT_mu11_mu6_bJpsimumu_L1MU11_2MU6	303
8	HLT_mu11_mu6_bBmumux_BdmumuKst_L1MU11_2MU6	261

Table 4.3: Distribution of generic and specialized dimuon triggers in a MC sample containing 10,000 events.

the detector, the J/ψ candidates were divided into three subsets according to the pseudorapidity, $|\eta|$, of the muons. In the first subset, both muons have $|\eta| < 1.05$ where the values $\eta = \pm 1.05$ correspond to the edges of the barrel of the MS. In the second subset, one muon has $1.05 < |\eta| < 2.5$ and the other muon has $|\eta| < 1.05$. The third subset contains candidates in which both muons have $1.05 < |\eta| < 2.5$. A J/ψ candidate and two additional oppositely-charged particles were combined to form a $B^0_{\rm d} \to J/\psi K^{*0}$ candidate. The $K^{*0} \to K^+\pi^-$ candidates were reconstructed from all tracks that were not identified as muons. One particle was assigned the mass of a positively-charged kaon, K^+, and the other the mass of a negatively charged pion, π^-. The $p_{\rm T}$ for the K^+ and π^- were ensured to be greater than 800 MeV and 400 MeV, respectively. Further, the $|\eta|$ values for both the K^+ and the π^- was required to be less than 2.5. A vertex fit of the four selected tracks was then performed by constraining the invariant mass of the two muon tracks to the nominal J/ψ mass [10]. All four tracks were constrained to originate from the same vertex. The quality of the vertex fit was ensured by the requirement $\chi^2(B^0_{\rm d})/{\rm ndof} - \chi^2(J/\psi){\rm ndof} < 16$. The invariant mass of the K^+ and π^- was required to fall within the interval 850 GeV $< m(K^+\pi^-) <$ 950 GeV. The $p_{\rm T}$ of the $K^+\pi^-$ pair was required to exceed

2 GeV and that of the B_{d}^0 candidate to exceed 10 GeV. Since particle identification of charged hadrons is not efficient in ATLAS, each pair of hadronic tracks was tested twice, with the assignments of the K^+ and π^- swapped. If both assignments satisfied the above selection criteria, the combination with the smallest deviation from the nominal K^{*0} mass [10] was chosen. The 5963 candidates were found to be within the mass range of $5.0 - 5.65$ GeV. The invariant mass distribution of these reconstructed B_{d}^0 candidates is shown in Figure 4.4. The peak of the distribution of dimuon events collected by all the triggers is about 5276 MeV, which is close to the Particle Data Group (PDG) mass of the B_{d}^0, 5279.63 MeV [10], indicating that the triggers are working as they should.

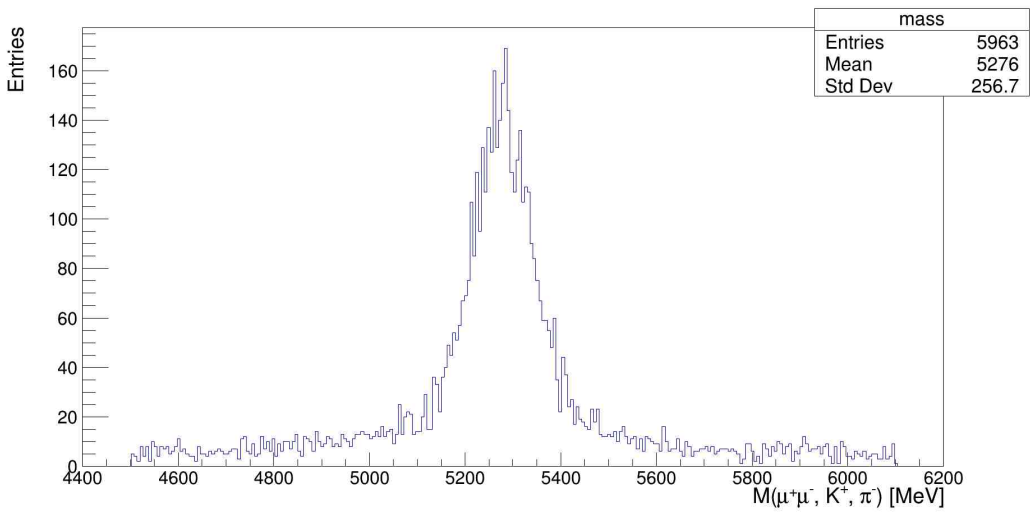

Figure 4.4: Invariant mass distribution of reconstructed B_{d}^0-mesons from the selected events.

The distribution of the 5963 candidates among triggers is shown in Table 4.4, and the invariant mass distribution of the 5963 candidates in each trigger is shown in Figure 4.5.

Threshold	bJpsimumu	bBmumux_BdmumuKst	% bJpsimumu	% bBmumux_BdmumuKst
2mu4	749	733	44.3	58.0
mu6_mu4	619	617	44.7	58.0
2mu6	282	276	45.3	54.6
mu11_mu6	146	75	52.1	56.9

Table 4.4: Distribution of triggers in the reconstructed B_{d}^{0} candidates.

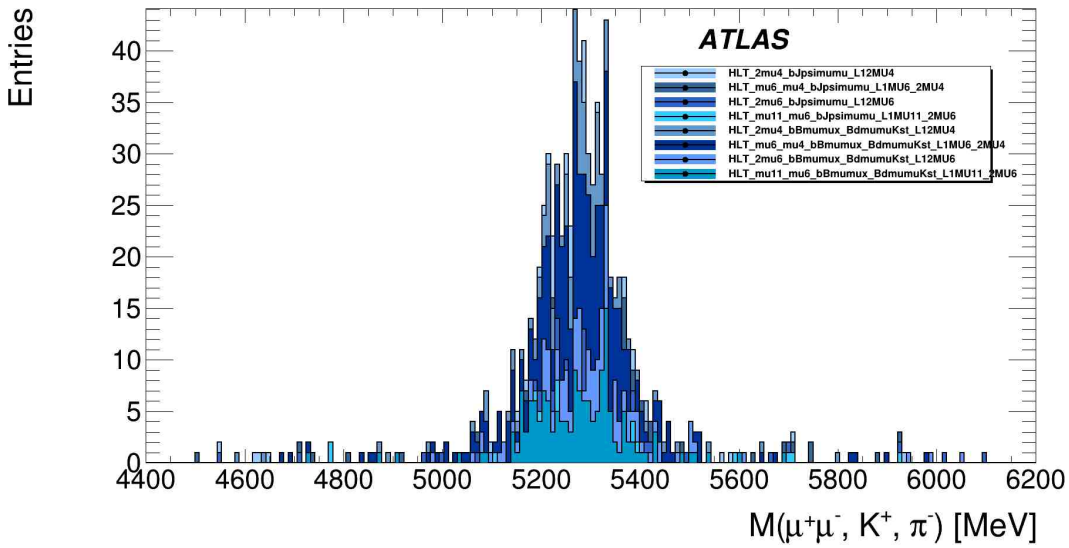

Figure 4.5: Contribution of each trigger to the invariant mass distribution of reconstructed B_{d}^{0}-mesons.

The following observations can be made from Table 4.4:

- the number of reconstructed B_{d}^{0} candidates collected by specialized triggers is only about 2% less than the number of events collected by generic triggers for all triggers except the specialized trigger with threshold mu11_mu6, which collected events with muons in the dimuon pair satisfying $p_{\mathrm{T}} > 11$ GeV and $p_{\mathrm{T}} > 6$ GeV. At least 97% of the events collected by the generic triggers were also collected by highly efficient specialized triggers. Further, more than 50%

of the events collected by specialized triggers passed the selection cuts prior to the reconstruction. This is expected, as specialized triggers collect events with information on hadrons in the final state, and these show higher efficiency than generic counterparts. Hence, the $B^0_{\rm d} \to J/\psi K^{*0}$ analysis benefits from specialized triggers:

- the triggers with the lowest $p_{\rm T}$ threshold ($p_{\rm T} > 4$ GeV) have collected the most events,
- specialized triggers did not achieve 100% efficiency due to the fact that the candidates for the decay $K^{*0} \to K^+\pi^-$ were reconstructed from all pairs of oppositely charged tracks that are not identified as muons and were assigned the masses of the K^+ and π^-, and
- none of the triggers are biased to high or low masses.

Dimuon triggers based on AthenaMT for $B^0_{\rm d} \to J/\psi(\to \mu^+\mu^-)\phi(\to K^+\pi^-)$ are working and show good efficiency.

4.5 Trigger Validation for $B^+ \to J/\psi(\to \mu^+\mu^-)K^+$

In this study, all triggers used were based on identification of a $J/\psi \to \mu^+\mu^-$ decay, with $p_{\rm T}$ greater than 4 GeV, 6 GeV or 11 GeV for each muon in the dimuon pair. A set of eight dimuon triggers was used to select B^+ candidates from a MC sample of 10,000 events. Four out of the eight triggers are generic triggers that collected events that are consistent with the invariant mass of the J/ψ, and the remaining four triggers collected events that are consistent with the invariant mass of the J/ψ and

also use information on the charged kaon associated with the hadronic track. All triggers, along with their distribution in the MC sample, are shown in Table 4.5. It can be observed from Table 4.5 that the number of events in specialized triggers did not exceed the number of events in generic triggers for each p_{T} threshold, which is expected. As an example, HLT_2mu4_bJpsimumu_L12MU4, a generic trigger that collects events containing two muons both with $p_{\mathrm{T}} > 4$ GeV, was triggered 2360 times, while HLT_2mu4_bBmumux_BpmumuKp_L12MU4, a specialized trigger that collects events containing two muons both with $p_{\mathrm{T}} > 4$ GeV and a hadronic track that contributes to the reconstruction of the K^+-meson, was triggered 1958 times. A similar pattern was observed for other triggers.

No	Trigger Name	Counts
1	HLT_2mu4_bJpsimumu_L12MU4	2360
2	HLT_2mu4_bBmumux_BpmumuKp_L12MU4	1958
3	HLT_mu6_mu4_bJpsimumu_L1MU6_2MU4	1867
4	HLT_mu6_mu4_bBmumux_BpmumuKp_L1MU6_2MU4	1577
5	HLT_2mu6_bJpsimumu_L12MU6	842
6	HLT_2mu6_bBmumux_BpmumuKp_L12MU6	724
7	HLT_mu11_mu6_bJpsimumu_L1MU11_2MU6	411
8	HLT_mu11_mu6_bBmumux_BpmumuKp_L1MU11_2MU6	358

Table 4.5: Distribution of generic and specialized dimuon triggers in a MC sample containing 10,000 events.

The candidates for $B^+ \to J/\psi K^+$ decays were identified in a series of steps. The $B^+ \to J/\psi K^+$ decay candidates were required to contain at least one reconstructed primary vertex, formed from at least three ID tracks, and at least one pair of oppositely-charged muon candidates that were reconstructed using information from the MS and the ID. Each muon candidate in the dimuon pair was required to have $p_{\mathrm{T}} > 4$ GeV and $|\eta| < 2.5$. Pairs of oppositely charged muon tracks were re-fitted to a

common vertex, and the pair was accepted if the quality of the fit met the requirement $\chi^2/\text{ndof} < 10$. Dimuon candidates with invariant mass $2.8 < m(\mu^+\mu^-) < 3.4$ GeV were retained. A J/ψ candidate and an additional positively-charged particle were combined to form a $B^+ \to J/\psi K^+$ candidate. The K^+ candidates were reconstructed from all positively-charged tracks that were not identified as electrons or muons. The track was assigned the charged-kaon mass hypothesis and combined with the dimuon candidate using a vertex fit, performed with the mass of the dimuon pair constrained to the J/ψ mass. Prompt background contributions were suppressed by a requirement on the B^+ candidate proper decay time of $\tau > 0.2$ ps. The 7448 candidates' masses were found to be within the range $4.4 - 6.2$ GeV. The invariant mass distribution of these reconstructed B^+ candidates is shown in Figure 4.6. The peak of the distribution of dimuon events collected by all the triggers is about 5283 MeV, which is close to the Particle Data Group (PDG) mass of the B^+, 5279.34 MeV [10], indicating that the triggers are working as they should.

The distribution of the 7448 candidates among triggers is shown in Table 4.6, and the invariant mass distribution of the 7448 candidates in each trigger is shown in Figure 4.7.

Threshold	bJpsimumu	bBmumux_BpmumuKp	% bJpsimumu	% bBmumux_BpmumuKp
2mu4	1512	1432	64.1	73.1
mu6_mu4	1223	1176	65.5	75.5
2mu6	582	560	69.1	77.3
mu11_mu6	295	285	71.8	79.6

Table 4.6: Distribution of triggers in the reconstructed B^+ candidates.

The following observations can be made from Table 4.6:

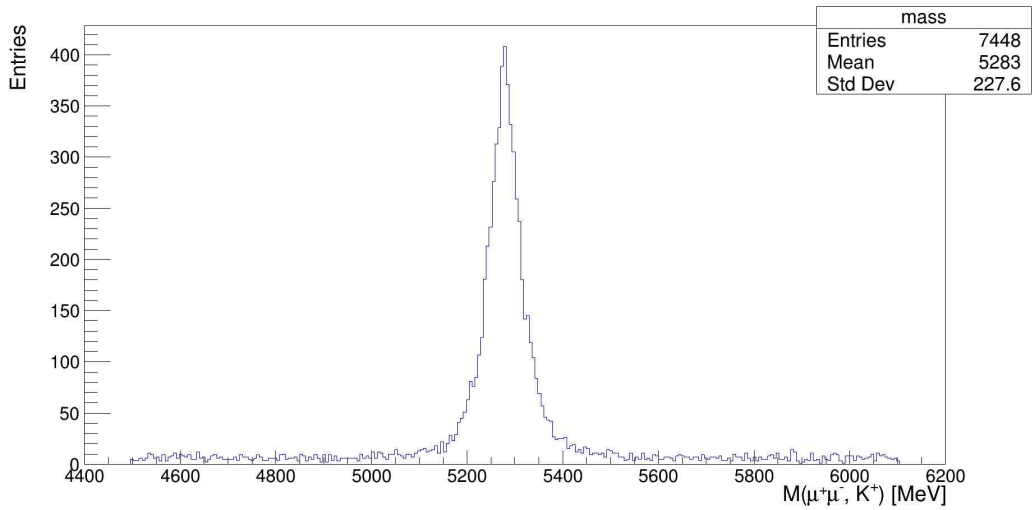

Figure 4.6: Invariant mass distribution of B^+-mesons reconstructed from the selected events.

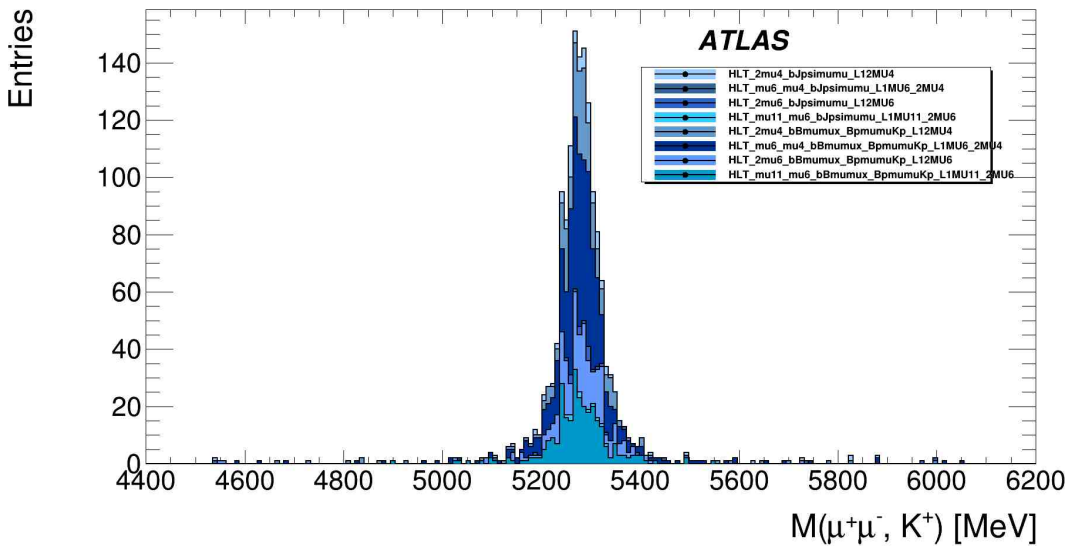

Figure 4.7: Contribution of each trigger to the invariant mass distribution of reconstructed B^+-mesons.

- more than 94% of the events collected by the generic triggers were also collected by highly efficient specialized triggers for all p_{T} thresholds. Further, more than 73% of the events collected by specialized triggers passed the selection cuts prior

to the reconstruction. This is expected, as specialized triggers collect events with information on hadrons in the final state, and these show higher efficiency than the generic counterparts. Hence, the $B^+ \to J/\psi K^+$ analysis benefits from specialized triggers:

- the triggers with the lowest p_{T} threshold ($p_{\mathrm{T}} > 4$ GeV) collected the most events,
- specialized triggers did not achieve 100% efficiency due to the fact that the candidates for the K^+-meson were reconstructed from all pairs of positively charged tracks that are not identified as muons or electrons and were assigned the mass of the K^+ and
- none of the triggers are biased to high or low masses.

Dimuon triggers based on AthenaMT for $B^+ \to J/\psi(\to \mu^+\mu^-)K^+$ are working and show good efficiency.

4.6 Addition of Dimuon Triggers to AthenaMT

Five dimuon triggers were added and configured to the Run 3 B-Physics trigger menu in the new software framework, AthenaMT, as a part of the trigger validation. They are shown in Table 4.7. These triggers were configured to collect dimuon events with one muon having $p_{\mathrm{T}} > 6$ GeV and the another muon having $p_{\mathrm{T}} > 11$ GeV; these events are taken from the events seeded to the HLT by Level-1 (L1) topological dimuon triggers that collect dimuon events satisfying $p_{\mathrm{T}} > 6$ GeV. The HLT will further reduce the rate of L1 muon triggers through several algorithms and selection

cuts applied at the HLT. This study added five triggers to the B-Physics trigger menu and applied a vertex hypothesis algorithm to each one. The algorithm selected vertices based on their invariant mass and vertex fit χ^2 values. In AthenaMT, the algorithm checks for vertices in a RoI or an event and determines their position and quality using different methods, such as track fitting or fast vertex finding. These dimuon triggers can be used for various topologies such as $J/\psi \to \mu\mu$, $B \to \mu\mu$, $\tau \to 3\mu$, and $\phi \to \mu\mu$.

No.	Trigger Name	Low Mass Cut (MeV)	Upper Mass Cut (MeV)	χ^2 Cut
1	HLT_mu11_mu6_bDimu_L1MU11_2MU6	1500	14000	0
2	HLT_mu11_mu6_bDimu2700_L1MU11_2MU6	100	2700	0
3	HLT_mu11_mu6_bBmumu_L1MU11_2MU6	4000	8000	0
4	HLT_mu11_mu6_bTau_L1MU11_2MU6	0	2700	10
5	HLT_mu11_mu6_bPhi_L1MU11_2MU6	940	1100	50

Table 4.7: Dimuon triggers that were added to AthenaMT.

Chapter 5

Leakage Current and Depletion Voltage Analysis of Silicon Tracking Detectors

5.1 Introduction to Leakage Current and Depletion Voltage Analysis

Since the ATLAS Pixel Detector lies closest to the interaction point, the radiation fields in which it is immersed in LHC Run 2 are unprecedented for a full scale particle physics detector. In order to continue to collect high quality data for future CP-violation studies with the channel $B_s^0 \to J/\psi\phi$, the impact of those radiation fields needs to be understood. As mentioned in Chapter 2, any future search for New Physics in $B_s^0 \to J/\psi\phi$ will greatly benefit from increased statistical precision

(i.e., more data), and this is anticipated in the coming decade. The radiation fields expected during Run 3 of the LHC and in the High Luminosity-LHC (HL-LHC) era will reach even higher levels than those yet observed [40]. For this, the condition of the radiation damage in the current Pixel Detector needs to be monitored in LHC Run 3, and projected to future years, to support development of radiation hard detectors for the HL-LHC.

The radiation damage of a sensor can be characterized through its leakage current and depletion voltage. The leakage current and the depletion voltage can also be used to estimate power consumption and thermal dissipation. Knowing these is critical in setting up the power supply and cooling system required for the sensor. Leakage current, or reverse current, is the current through the junction, due to thermally generated minority carriers (generation current), when reverse bias is applied. Electrons and holes drift in the reverse biased depletion zone under the influence of the electric field, giving rise to the leakage current. Depletion voltage is the bias voltage that needs to be applied to the sensor to deplete its full volume. The leakage current and the depletion voltage of the ATLAS Pixel detector can be predicted using the Hamburg Model [149], and such predictions are crucial for the safe operation of the ATLAS Pixel detector in Run 3 as well as for the development of the Inner-Tracker (ITk) Pixel System, the replacement of the ATLAS Pixel Detector for the HL-LHC era.

A linear relationship between particle fluence and leakage current applies to silicon sensors. The effective fluence, Φ_{eq}, is the number of 1 MeV neutrons applied to a sensor of surface area 1 cm^2 that cause damage equivalent to that of all particles that went through the sensor. The linear relationship between effective fluence and ΔI,

the change in leakage current at fluence Φ_{eq} relative to the value before irradiation, is given as

$$\Delta I = \alpha \cdot \Phi_{\text{eq}} \cdot V \tag{5.1}$$

where V is the depleted volume of the silicon sensor and α is the current-related damage coefficient [150] which is a function of annealing time and temperature. The leakage current and predictions are normalized to the same temperature for direct comparison. The normalization is made using the known leakage current dependence on temperature and the effective silicon band gap energy, E_{eff} [151]. The following equation converts the leakage current of a sensor measured at temperature T to that at a reference temperature T_{R}:

$$I(T_{\text{R}}) = I(T) \times R(T), \tag{5.2}$$

where

$$R(T) = (T/T_{\text{R}})^2 \cdot \exp\left[-\frac{E_{\text{eff}}}{2k_{\text{B}}}(\frac{1}{T_{\text{R}}} - \frac{1}{T})\right]. \tag{5.3}$$

E_{eff} is the effective silicon band gap energy after irradiation, also called activation energy, and k_{B} is the Boltzmann constant. T and T_{R} must be expressed in Kelvin. The value of 1.21 eV has been used for E_{eff} following a study on how this value changes under different radiation conditions [151]. This can be compared to the nominal silicon band gap energy of 1.12 eV before irradiation. It is worth noting that the temperature normalization is dependent on the choice of E_{eff}.

The depletion voltage V_{dep} of a sensor depends linearly on the doping concentration N_{eff} and the square of the thickness d of the detector (wafer thickness for a planar sensor or, approximately, electrode-to-electrode distance for a 3D sensor), and can be

written as

$$V_{\text{dep}} = \frac{\mid N_{\text{eff}} \mid d^2 q}{2\epsilon\epsilon_0}, \tag{5.4}$$

where q is the charge of the electron, ϵ is the dielectric constant, and ϵ_0 is the vacuum permittivity. The doping concentration is affected by the fluence, and the change in doping concentration ΔN_{eff} can be expressed as

$$\Delta N_{\text{eff}} = N_{\text{A}} + N_{\text{Y}} + N_{\text{C}}, \tag{5.5}$$

where

- $N_{\text{A}} = \frac{g_{\text{A}}}{k_{\text{A}}} \Phi_{\text{eq}} e^{-k_{\text{A}} t}$ reflects short-term beneficial annealing and is ignored in this study due to its negligible effect on p-type sensors [152],
- $N_{\text{Y}} = \frac{g_{\text{Y}}}{k_{\text{A}}} \Phi_{\text{eq}} (1 - e^{-k_{\text{Y}} t})$ reflects long-term reverse annealing which can be effectively frozen out below the temperature of -5^{o}C, and
- $N_{\text{C}} = N_{\text{C},0}(1 - e^{-c\Phi_{\text{eq}}}) + g_{\text{C}} \Phi_{\text{eq}}$ is the called stable damage coefficient which has no time dependence.

Here, k_{A} and k_{Y} are defined by Arrhenius equations and have a temperature dependence as follows:

$$k_{\text{i}} = k_{\text{i},0} e^{-E_{\text{i}}/k_{\text{B}}T}, \text{ i = A or Y}, \tag{5.6}$$

where $k_{\text{Y},0} = 2.4^{+1.2}_{-0.8} \times 10^{13}$ s^{-1}, $k_{\text{Y},0} = 1.5^{+3.4}_{-1.1} \times 10^{15}$ s^{-1}, $E_{\text{A}} = 1.09 \pm 0.03$ eV, and $E_{\text{Y}} = 1.33 \pm 0.03$ eV [149]. The constants g_{A}, g_{Y} and g_{C} are called introduction rates and depend on the geometry and material of the sensor and the type of radiation the sensor receives. The constant c is the donor removal constant for n-type sensors

or the acceptor removal constant for p-type sensors. $N_{C,0}$ is the number of initial acceptors that can be removed from the material with initial doping concentration $N_{eff,0}$. The leakage current and depletion voltage are predicted using the Hamburg Model by inputting the fluence simulated by FLUKA [153, 154] and GEANT4 [53, 155, 156].

5.2 Hamburg Model Predictions for the ATLAS Pixel Detector

5.2.1 Introduction

The leakage current and depletion voltage of the ATLAS Pixel detector were predicted for several thermal situations in Run 3, and these will be discussed in Section 5.2.3. Run 3 began in July 2022, and initially it was anticipated to end the data-taking in 2024 because the innermost layer, IBL, had already received a fluence of about 6×10^{24} 1 MeV neutron-equivalent per cm^2 (n_{eq}/cm^2) at the end of Run 2 in 2018. However, LHC is going to operate for one more year to allow physicists to collect more data during Run 3 than they did in the first two runs combined.

5.2.2 The Hamburg Model Predictions

The complex radiation fields in the ATLAS detector are simulated using FLUKA, a tool for modeling particle transport and interactions with matter [157, 158]. Since it is important for modeling high energy hadron cascades in the material that lead to

increased particle fluences in the detector, especially neutrons, the Inner Detector and calorimeter are modeled with high accuracy in the ATLAS FLUKA simulation framework [153]. For input to the FLUKA simulation, inelastic proton-proton interactions generated by Pythia8 [92] using the MSTW2008LO parton distribution functions [159] and the A2 tune [160] are used. All of the products of the proton-proton interactions are simulated with FLUKA. The particle and energy spectra are folded with silicon damage factors from the RD50 database [161–165] to compute the 1 MeV $n_{\mathrm{eq}}/\mathrm{cm}^2$ damage. The tabulated weights cover neutrons, protons, charged pions and electrons. The pion weights are used for charged kaons, while the proton weights are used for anti-neutrons, antiprotons, baryons and ions. Positrons are treated like electrons.

Through-going particles cause dislocations in the crystal lattice that disrupt the band structure. The displaced atom, the primary knock-on atom (PKA), becomes a silicon interstitial (Si_i) and leaves a vacancy. The recoiling PKA can strike neighboring atoms, producing clusters of bulk damage sites. These clusters can remain mobile and evolve, leading to macroscopic time-dependent effects. These displacement defects in the bulk of the Pixel sensor, initiated by hadronic species and caused by non-ionizing energy loss (NIEL), constitute the dominant radiation damage type. A compilation of damage factors due to NIEL can be found in [166] where the surface ionization is neglected in this treatment. Charged pions, the most common product of proton-proton collisions, are the largest contributor to the bulk damage for the radii covered by the Pixel Detector. Albedo neutrons originating in the outer ATLAS detectors also contribute. The resulting bulk radiation damage includes increase in the leakage current, degradation of the charge collection efficiency and change in the

doping concentration which directly affects the depletion voltage. Predictions of the 1 MeV $n_{\mathrm{eq}}/\mathrm{cm}^2$ per fb^{-1} in the ATLAS FLUKA Inner Detector geometry are shown in Figure 5.1.

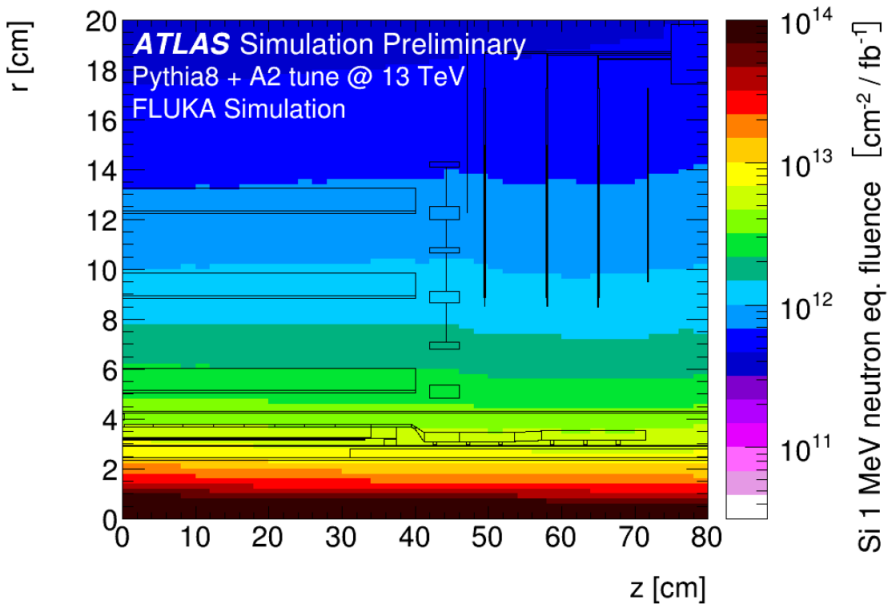

Figure 5.1: Simulated 1 MeV $n_{\mathrm{eq}}/\mathrm{cm}^2$ fluence shown as a function of the radial and longitudinal distance from the geometric center of the detector for a one-quarter slice through the ATLAS FLUKA geometry [167].

The z-dependence of the fluence, which depends on the distance from the interaction point, IP, is also accounted for in the simulation. The flux of charged particles produced at the primary collision goes as $1/r^2$. The fluence of neutrons depends on the detector geometry as these are primarily due to backscattering from the calorimeter. The simulation is used for obtaining fluence-to-luminosity conversion factors.

Figure 5.2 presents a comparison of the fluence-to-luminosity conversion factors for various subdetectors of the ATLAS Pixel Detector as a function of z. The fluence-

to-luminosity conversion factors were calculated by interpolating the Hamburg Model predictions for Run 2 and leakage current data taken during Run 2 and are compared with the predictions using Pythia, Geant4 and FLUKA for the entire silicon-based ATLAS Inner Detector [168]. The predicted values are symmetric in z by construction.

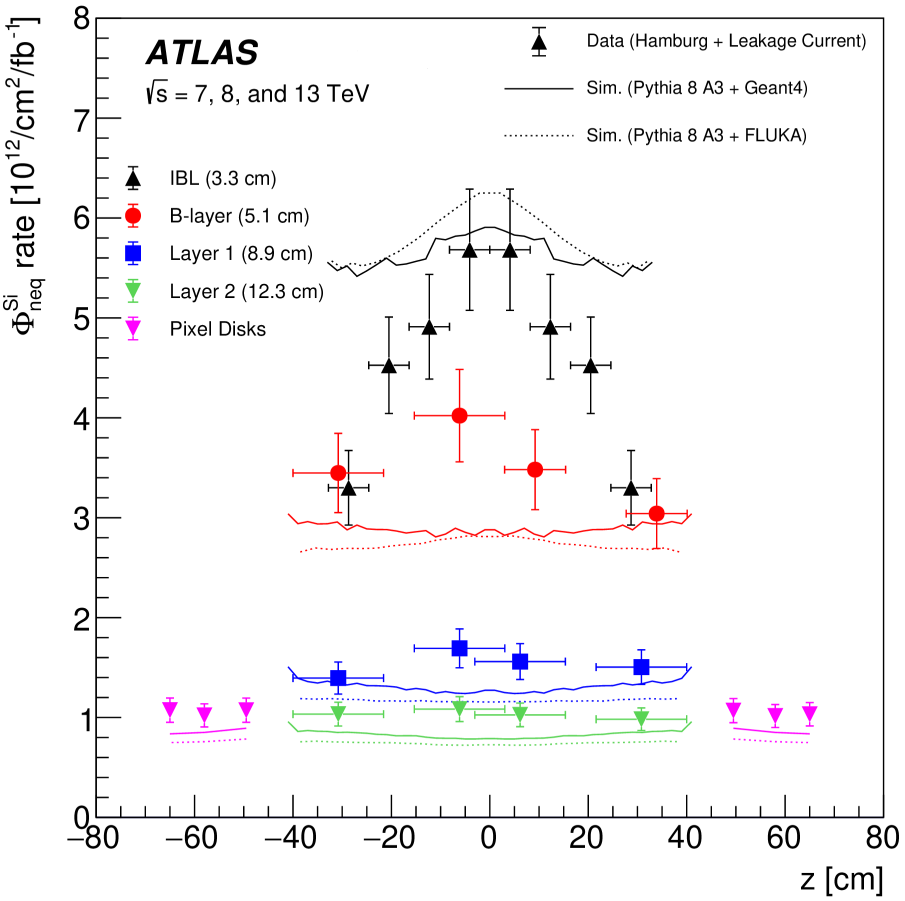

Figure 5.2: A comparison of fluence-to-luminosity conversion factors as a function of z. Distances given in parentheses behind layer names correspond to the radius of the sensors with respect to the geometric center of ATLAS [168].

Table 5.1 shows the highest fluence-to-luminosity conversion factors from FLUKA simulations (FLUKA + Pythia 8 A3 in Figure 5.2) for the IBL, B-Layer, Layer-1

and Layer-2, and these values were used for leakage current and depletion voltage predictions for the IBL, B-Layer, Layer-1 and Layer-2 in Run 3. These values correspond to the points with z-projection closest to the interaction point, IP, i.e., $z = 0$, to study the worst case scenario as the modules near the IP receive the highest fluence.

C.O.M. Energy	IBL	B-layer	Layer-1	Layer-2
7 TeV	Not Applicable	20.53	8.69	5.39
8 TeV	Not Applicable	21.73	9.11	5.67
13 TeV	62.62	28.94	12.41	7.87

Table 5.1: Fluence values simulated using the ATLAS FLUKA simulation package for three center of mass (C.O.M.) energies. Units of the values in the table are 1 MeV $n_{\text{eq}} \times 10^{11}$ cm^{-2} per fb^{-1}. The IBL was installed prior to Run 2 and has been operated only at a C.O.M. of 13 TeV.

The fluence Φ_{eq} accumulated by the ATLAS Pixel Detector, and measured in units of cm^{-2}, is proportional to the integrated luminosity, $\int Ldt$, measured in fb^{-1}. By the end of the proton-proton collision runs in 2018, the B-Layer was predicted, by Pythia8 + FLUKA, to have received an integrated fluence of $\Phi_{\text{eq}} = 5.27 \times 10^{14}$ 1 MeV n_{eq}/cm^2. The B-Layer was designed to receive a total integrated fluence of 1×10^{15} 1 MeV n_{eq}/cm^2 over the span of its lifetime. The evolution of fluence accumulation over the lifetime of the ATLAS Pixel detector, excluding the IBL, is shown in Figure 5.3.

The FLUKA simulated fluence is used as an input to the Hamburg Model [149]

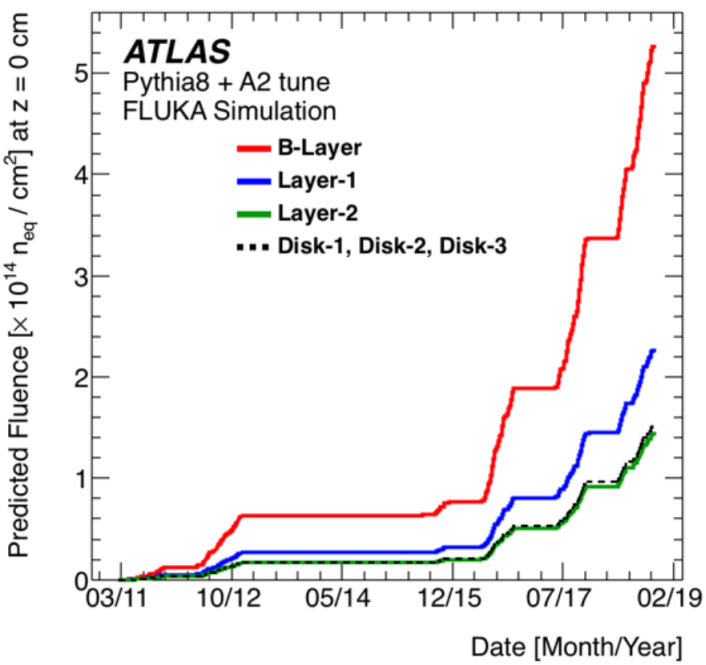

Figure 5.3: Applied fluence for the B-Layer, Layer-1, Layer-2, and the Disks, calculated by the FLUKA factors [167].

to predict the change in leakage current, ΔI_{leak}, after irradiation. This is given by:

$$\Delta I = (\Phi_{\text{eq}}/L_{\text{int}}) \times V \cdot \sum_{i=1}^{n} L_{\text{int},i} \cdot \left[\alpha_{\text{I}} \exp\left(-\sum_{j=i}^{n} \frac{t_j}{\tau(T_j)}\right) + \alpha_0^* - \beta \log\left(\sum_{j=i}^{n} \frac{\Theta(T_j) \cdot t_j}{t_0}\right)\right], \tag{5.7}$$

where $L_{\text{int},i}$ is the integrated luminosity, t_i is the time, and T_i is the temperature in period i. The first sum is over all time periods, and the two sums inside the exponential and logarithmic functions are over the interval between the irradiation in time period i and the time of the measurement. The other terms in Equation 5.7 are $t_0 = 1$ min, $V =$ depleted volume[1] (in cm^3), $\alpha_{\text{I}} = (1.23 \pm 0.06) \times 10^{-17}$ A/cm, τ follows an Arrhenius equation $\tau^{-1} = (1.2^{+5.3}_{-1.0} \times 10^{13}$ s$^{-1} \times e^{(-1.11 \pm 0.05)/k_{\text{B}}T}$ where the

[1]The fully depleted volume of the sensor module is $V = 0.25$ cm^3.

units of $k_{\mathrm{B}}T$ are eV, $\alpha^* = 7.07 \times 10^{-17}$ A/cm, and $\beta = (3.29 \pm 0.18) \times 10^{-18}$ A/cm. A small temperature dependence has been observed in the value of β [169]; for this analysis, the value at -21^{o} C, which is its lowest known value and the one closest to the operational temperature of the sensors in the detector, was used. Equation 5.7 represents the Hamburg Model as presented in [169]; under different conditions different terms will dominate. Once the simulation is complete, the predictions are scaled using Equation 5.3 to match the detector operating temperature, so they can be compared to the data.

The implementation of the Hamburg Model can be found in Reference [170]; the treatment in this analysis is identical to the treatment in the ATLAS Radiation Modeling paper [167].

The luminosity-to-conversion factor, $\Phi_{\mathrm{eq}}/L_{\mathrm{int}}$, in Equation 5.7 requires a scale factor to match the leakage current data [167]. The scale factor is determined from the constant fit to the ratio of the leakage current data and the Hamburg Model prediction. In this analysis, scale factors extracted from Run 2 data were used, and these are presented in Table 5.2. Hamburg Model predictions are made in four bins along the z-axis for each barrel layer excluding the IBL.

In Table 5.2 the bin limits are determined by the paired module powering scheme. The bin limits include the average center position of all modules in the bin. The bin limits are one centimeter more or less than the center location of the modules in the bin. The center location of the modules in the bin defines the bin.

Region	z Bin	Scale Factor
B-Layer	$-38.0 < z < -23.7$	1.31
	$-13.3.0 < z < 1.0$	1.47
	$5.7 < z < 13.3$	1.28
	$29.9 < z < 38.0$	1.15
Layer-1	$-38.0 < z < -23.7$	1.31
	$-13.3.0 < z < 1.0$	1.47
	$-1.0 < z < 13.3$	1.28
	$23.7 < z < 38.0$	1.15
Layer-2	$-38.0 < z < -23.7$	1.31
	$-13.3.0 < z < 1.0$	1.47
	$-1.0 < z < 13.3$	1.28
	$23.7 < z < 38.0$	1.15

Table 5.2: Pixel barrel layer scale factors [167].

5.2.3 Lifetime Projections

The leakage current and depletion voltage data collected in Run 2 were used to extrapolate the leakage currents and depletion voltages in the barrel layers - the IBL, B-Layer, Layer-1 and Layer 2, through Run 3 of the LHC.

B-Layer Leakage Currents and Depletion Voltages - Early Run 3 Predictions

This study was conducted before Run 3 and before the date on which it was proposed to extend Run 3 by one year. The purpose of this study was to understand if a thermal runaway situation would arise if the existing cooling system for barrel layers were modified. The main cooling system of the B-Layer, Layer-1 and Layer-2 is based on a thermosiphon, while an evaporative cooling system acts as the backup cooling system [171]. ATLAS proposed to remove three out of seven compressors of the evaporative cooling system towards the end of Run 3. This would increase

the operating temperature of the sensors if the main cooling system were to fail and, as a result, the leakage current would increase. If the applied current exceeds approximately 2 mA per module, the power supplies and services will not be able to sustain power necessary to operate the modules. This is an investigation of the expected requirement on power supply current after fluences are received in Run 3. To study the worst-case scenario, a leakage current projection was made using the Hamburg Model simulation for the B-Layer at an operating temperature of -5^{o}C since the B-Layer is the closer than Layer-1 and Layer-2 to the interaction point. This result was then compared to the results predicted for the B-layer when operated at a nominal operating temperature of -12^{o}C. Figure 5.4 shows the temperature profile that was used for the prediction.

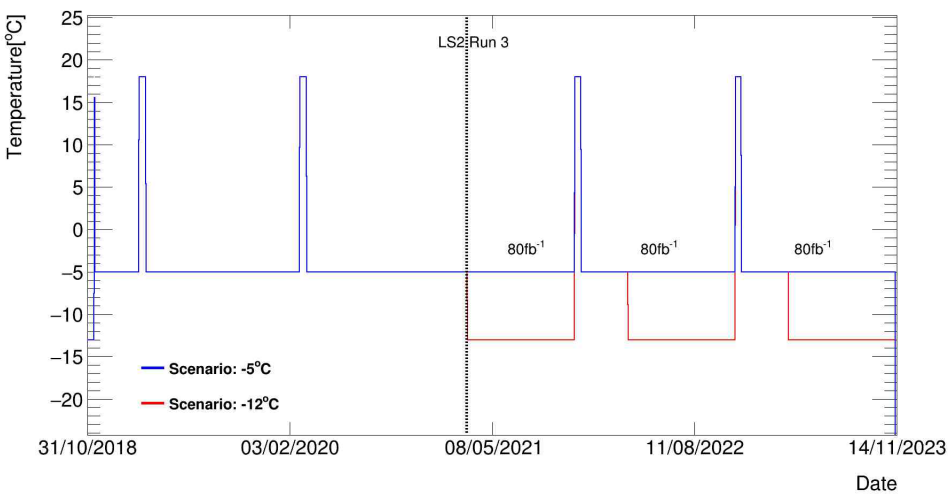

Figure 5.4: The temperature profiles used for leakage current predictions for the B-layer showing two scenarios - a scenario where the B-Layer is kept at a nominal temperature of -12^{o}C and another scenario where the B-Layer is kept at -5^{o}C if its evaporative cooling system fails.

In Figure 5.4, Long Shutdown 2 (LS2) ended in 2021 and Run 3 started in May

2021. During LS2, to permit detector maintenance, the temperature could not be maintained at the nominal level and in these situations, when the cooling system is completely switched off, the temperature of the detector came to equilibrium with the temperature of the ATLAS pit which is 18°C. The objective in LS2 was to keep these durations to a minimum; in the prediction, it was assumed that the B-Layer was kept at 18°C for four weeks. During LHC Run 3 the sensors were expected to be kept at a nominal temperature of −12°C (or −5°C if the cooling system fails during operation) and −5°C during planned technical and machine development shutdowns. An additional four weeks when the detector is kept at the temperature of the ATLAS pit (18°C) was assumed during these yearly shutdowns in LHC Run 3. The LHC was expected to deliver an additional integrated luminosity of 240 fb^{-1} during Run 3 at $\sqrt{s}$ = 13 TeV. In both scenarios, it was assumed that the ATLAS detector would collect 80 fb^{-1} of data during Run 3 in 2021, 2022 and 2023. This integrated luminosity is converted to fluence predicted with Pythia8 and FLUKA as shown in Table 5.1. The Hamburg Model projections of leakage current through Run 3 are made with these parameters and scaled with the scale factors that were extracted from Run 2 data and the Hamburg Model predictions as shown in Table 5.2. These projections are based on the Run 1 and Run 2 temperatures for the B-Layer module overlapping the interaction point (bin: $-13.3 < z < 1.0$ in Table 5.2), where the leakage current level is highest. Figure 5.5 shows a comparison of leakage current predictions for the B-Layer in two Run 3 operating scenarios - one at −12°C and the other at −5°C.

All the simulations start from 190 fb^{-1} because by the end of Run 2, the B-Layer had collected 190 fb^{-1} of data. The volume normalization in Equation 5.7 was

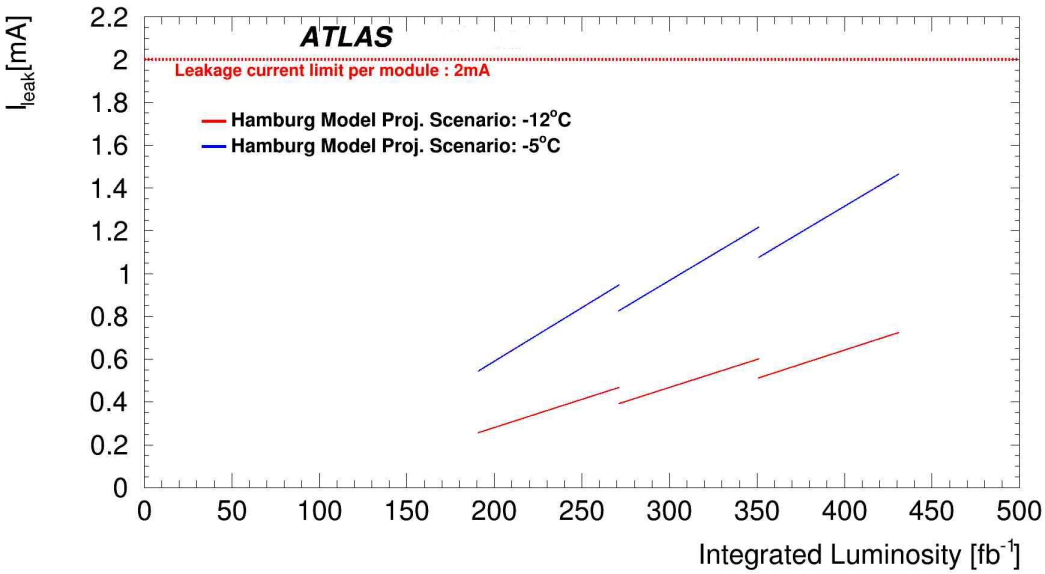

Figure 5.5: A comparison of leakage current predictions versus integrated luminosity for the B-Layer operating at -12^{o}C and -5^{o}C.

removed in order to investigate the current supplied directly by the power supply system. It can be seen that the leakage current of the B-Layer operating at -5^{o}C is higher than that of the B-Layer at -12^{o}C. However, at the end of Run 3, leakage currents at both temperatures will not exceed the leakage current limit per module which is 2 mA. The drop in leakage current due to beneficial annealing after an annual technical stop is higher if the B-Layer is operated at -5^{o}C. However, the bias voltage level required for full depletion at high temperatures increases and hence, a compromise must be made to obtain optimal functionality in Run 3. The uncertainty on the predicted leakage current is calculated from the uncertainties [167] on the inputs to the model and is summarized in Table 5.3.

The temperature offset uncertainty does not apply during periods when the power and cooling of the detector are off. The statistical uncertainty on the fluence

Scale Factor Fit	Temperature Precision - Model	Temperature Offset - Model	Total
1.6%	2.9%	10.0%	10.5%

Table 5.3: Summary of the contributing and total uncertainties for the Hamburg Model.

predictions made by Pythia8 and FLUKA is 1.0%. There are sources of uncertainty introduced to both the Hamburg Model and the predicted fluence through the silicon hardness factors [166], these are not taken into account in this analysis. The hardness factors [161–164] used here are from the RD50 database, but all of these values are without uncertainty and many are based only on simulation. Figure 5.6 shows the leakage current for the B-Layer at an operating temperature of -5^{o}C with a 10.5% uncertainty calculated from the inputs to the Hamburg Model.

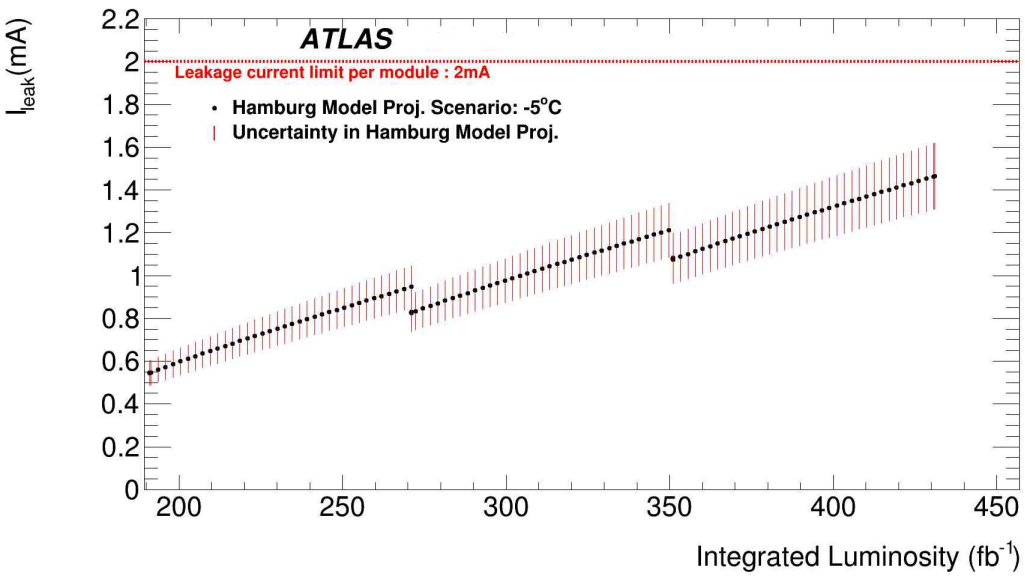

Figure 5.6: The leakage current prediction with uncertainty versus integrated luminosity for the B-Layer operating at -5^{o}C.

As we can see from Figure 5.6, the leakage current of the B-Layer at the end of

Run 3 will be 1.45 ± 0.15 mA which is under the limit of 2 mA per module. The leakage current of the B-Layer operating at a temperature of -5°C due to a cooling system with reduced efficiency would not be a major concern in Run 3.

In addition to the leakage current prediction, the depletion voltage of the B-Layer for the module overlapping the IP also needed to be studied. The depletion voltage determines the bias voltage level required for full depletion at the temperature at which the B-Layer is operated.

The Hamburg Model uses Equation 5.4 to calculate depletion voltage from the change in doping concentration, ΔN_{eff}, defined by Equation 5.5. This study used the introduction rates measured by the ROSE Collaboration [172] for beneficial annealing (N_{A}), reverse annealing (N_{Y}) and the stable damage coefficient (N_{C}):

- $g_{\text{A}} = 1.0 \times 10^{-2}$ cm^{-1},
- $g_{\text{Y}} = 1.6 \times 10^{-2}$ cm^{-1}, and
- $g_{\text{Y}} = 1.0 \times 10^{-2}$ cm^{-1}.

Figure 5.7 shows a comparison of depletion voltage predictions for the B-Layer in two operating scenarios - one at -12°C and the other at -5°C in Run 3. As we can see from the plot, the depletion voltage of the B-Layer exceeds the services limit of 600 V in both scenarios. The depletion voltage of the B-Layer if operated at -12°C would exceed the limit earlier in Run 3 compared to that of the B-Layer if operated at -5°C. The dominant uncertainty in these predictions comes from the Hamburg Model parameters and is about 20% [173]. However, these depletion voltage predictions relied on parameters based on data recorded at relatively low fluences [149]. These

predictions were used as a starting point to improve the predictions for the ATLAS Pixel detector using updated parameters extrapolated from Run 2 data which will be discussed later in this chapter.

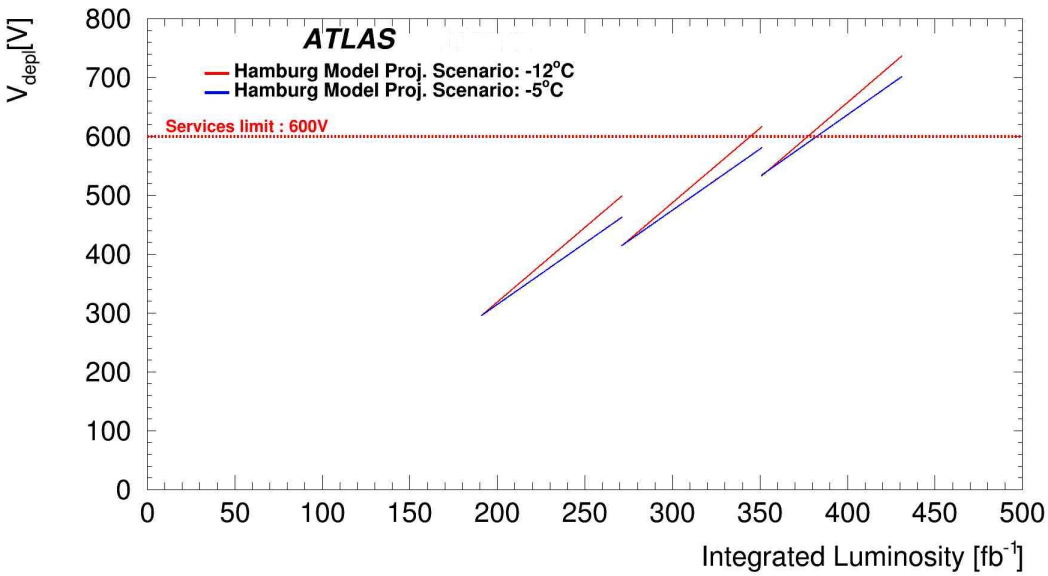

Figure 5.7: A comparison of depletion voltage predictions versus integrated luminosity for the B-Layer operating at -12°C and -5°C.

ATLAS Pixel Leakage Currents and Depletion Voltages - Run 3 Predictions

This study was conducted before Run 3 and after the date on which it was proposed to extend Run 3 by one year. The purpose of this study was to understand if the barrel layers, especially the IBL and B-Layer, can sustain radiation damage while receiving a fluence equivalent of 270 fb^{-1} in an extended Run 3 scenario. The innermost layers were highly irradiated by the end of Run 2 as the IBL and B-Layer had received fluences of about 1×10^{15} 1 MeV $n_{\text{eq}}/\text{cm}^2$ and 6×10^{14} 1 MeV $n_{\text{eq}}/\text{cm}^2$, respectively. The ATLAS detector went through several stages of maintenance

during Long Shutdown 2 (LS2) where the ATLAS Pixel detector was kept at various temperatures and hence it underwent different levels of annealing that need to be understood.

The ATLAS Pixel detector will be operated at a temperature of -12^{o}C for all layers during Run 3. Using the Hamburg Model simulation, leakage currents and depletion voltages were predicted for IBL modules with planar sensors, the B-Layer, Layer-1 and Layer-2. If the applied current exceeds approximately 2 mA per module for the B-Layer and 8 mA per two modules for the IBL [174], the power supplies and services will not be able to sustain the power necessary to operate the modules. If the depletion voltage required for full depletion exceeds the services limits of 1000 V and 600 V for the IBL and B-Layer, respectively, then the IBL and B-Layer might not be fully depleted during Run 3, causing a drop in charge collection efficiency. This is an investigation of the expected requirement on power supply current after the fluences will have been applied in each year during Run 3. Figure 5.8 shows the temperature profile that was used for the prediction of leakage currents and depletion voltages for the barrel layers.

In Figure 5.8, LS2 ends in 2022, and Run 3 starts in May 2022. During LS2, to allow detector maintenance, the cooling system was switched off and in those situations, the temperature of the detector came to equilibrium with the temperature of the ATLAS pit which is 18^{o}C. The IBL, B-Layer, Layer-1 and Layer-2 were all kept at 18^{o}C for four weeks. It was also assumed that the detector would be kept at the temperature of the ATLAS pit (18^{o}C) for around 3 days and at -5^{o}C for 3 months after each yearly run. It was assumed that the ATLAS detector would collect the following annual integrated luminosity, totalling to 270 fb^{-1} of data:

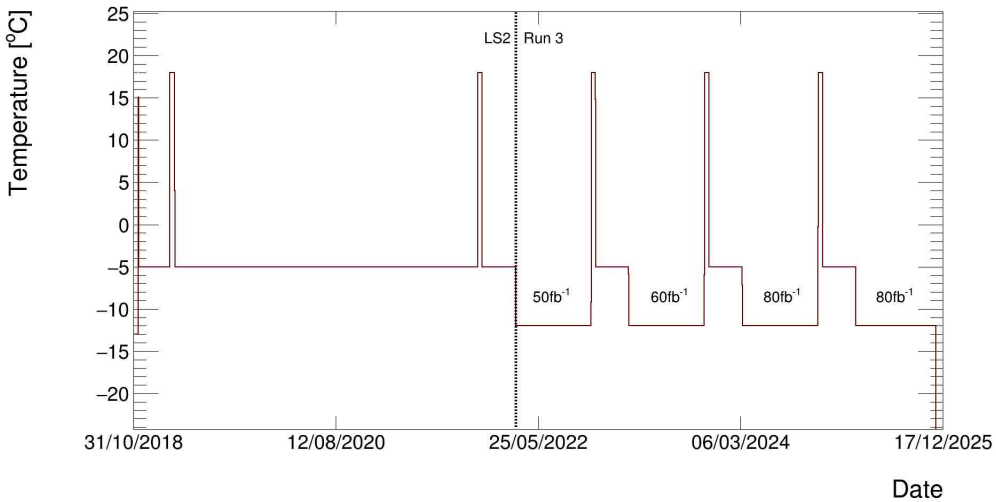

Figure 5.8: The temperature profiles used for predictions of leakage current and depletion voltage for the IBL, B-Layer, Layer-1 and Layer-2 in an extended Run 3 scenario where all layers are kept at -12^{o}C.

- 50 fb^{-1} of data in 2022,
- 60 fb^{-1} of data in 2023, and
- 80 fb^{-1} of data in 2024 and 2025.

The luminosity is converted to fluence predicted with Pythia8 and FLUKA as shown in Table 5.1. The Hamburg Model projections of leakage current through Run 3 are made with these parameters and scaled with the scale factors that were extracted from Run 2 data and the Hamburg Model predictions, as shown in Table 5.2. For the IBL, no scale factors were used to match the data. Figure 5.9 shows the leakage current prediction for the IBL operating at -12^{o}C in an extended Run 3 scenario. The leakage current was predicted for a representative sample of modules closest to the IP ($|z| < 8$ cm).

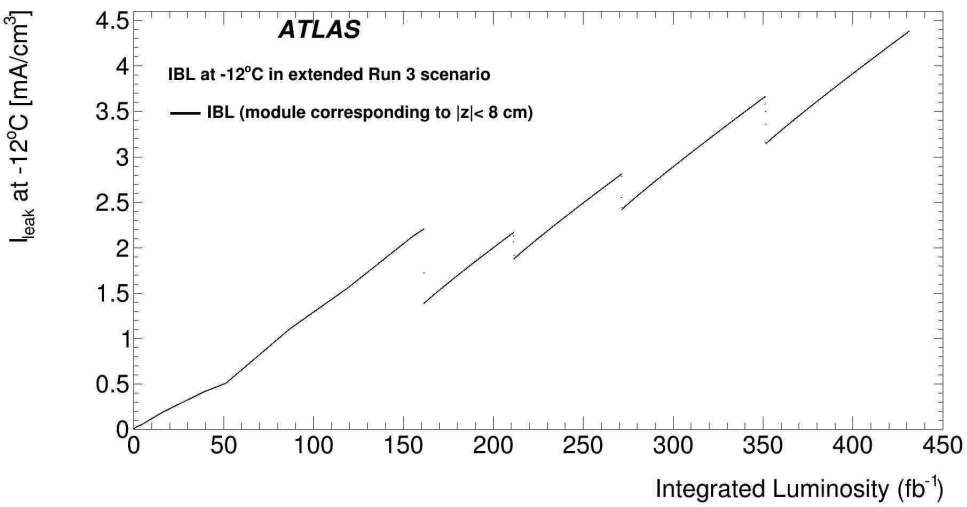

Figure 5.9: The leakage current prediction versus integrated luminosity for the IBL operating at -12°C in an extended Run 3 scenario. The leakage current was predicted for the modules closest to the IP ($|z| < 8$ cm).

In Figure 5.9, the leakage current prediction starts from 0 fb^{-1}, i.e., from the beginning of Run 1 since the leakage current depends on the duration over which the detector was irradiated and the fluence accumulated by it in previous runs. In the case of the IBL, the leakage current prediction for Run 3, which starts from 161 fb^{-1} in the plot, relied on the Run 1 and Run 2 predictions that were matched to the measured leakage currents [168]. From Figure 5.9, it can be seen that the drop in leakage current at 161 fb^{-1} after Run 2 is almost 1 mA per unit depletion volume before Run 3. This can be attributed to the fact that these modules of the IBL, which received the highest fluence and hence were highly irradiated, were kept at a temperature of -5°C during LS2, resulting in annealing of the sensors beneficially. The amount of beneficial annealing slightly increases as the fluence received by the detector rises as indicated by the drop in leakage current after yearly technical stops at 211 fb^{-1}, 271 fb^{-1} and 351 fb^{-1}. However, the reverse annealing, a dominant and

long term effect that increases with fluence, pushes the leakage current to a higher value while sensors are irradiated. The uncertainty in the leakage current prediction for the IBL is 10.4% from Table 5.3 as no scale factors were used in this simulation. The leakage current per unit depletion volume at the end of Run 3 is predicted to be 4.4 mA, and the leakage current per module[2] is 0.6 ± 0.06 mA, both of which are still within the power supply limit of 8 mA per two modules. This is expected for the sample of modules closest to the interaction point that would receive a fluence of about 3×10^{15} 1 MeV $n_{\mathrm{eq}}/\ \mathrm{cm}^2$ in its lifetime by the end of Run 3.

The leakage currents for all four representative samples of modules of the B-Layer, Layer-1 and Layer-2, outlined in Table 5.2, were predicted and are shown in Figures 5.10, 5.11 and 5.12, respectively

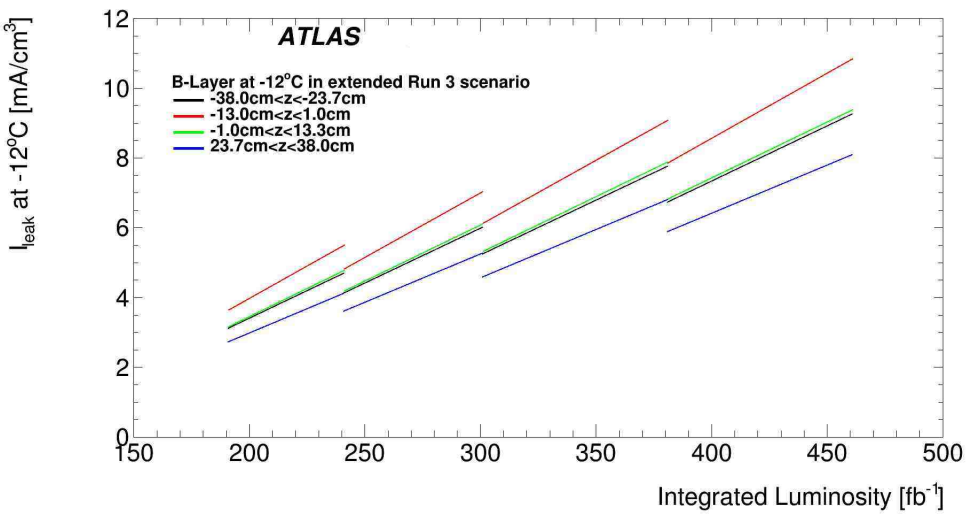

Figure 5.10: The leakage current prediction versus integrated luminosity for the B-Layer operating at -12°C in an extended Run 3 scenario. The leakage current was predicted for a representative sample of modules in z.

[2]The total area of an IBL planar sensor is 4.01×1.68 cm^2, and the thickness is 200 μm [174].

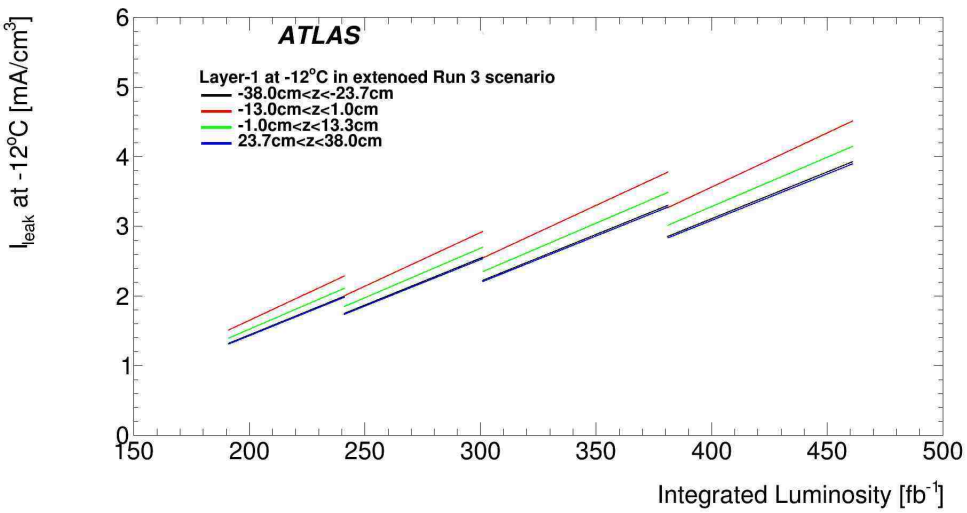

Figure 5.11: The leakage current prediction versus integrated luminosity for Layer-1 operating at -12°C in an extended Run 3 scenario. The leakage current was predicted for a representative sample of modules in z.

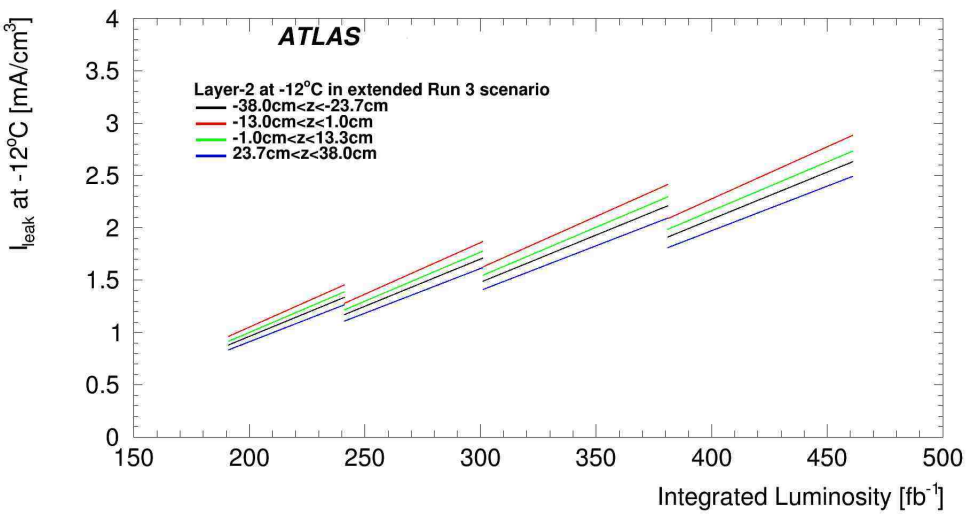

Figure 5.12: The leakage current prediction versus integrated luminosity for Layer-2 operating at -12°C in an extended Run 3 scenario. The leakage current was predicted for a representative sample of modules in z.

From Figure 5.10, it can be seen that the representative sample of modules of the B-Layer covering the beam pipe from $z = -13.3$ cm to $z = 1$ cm will have the

highest leakage current throughout Run 3, as this group of modules overlaps the interaction point, resulting in its receiving higher radiation damage. On the contrary, the modules from $z = 23.7$ cm to $z = 38.0$ cm will receive the least fluence and hence their leakage current is lower throughout Run 3. At the end of Run 3, the leakage current of the modules overlapping the interaction point will be 2.75 ± 0.29 mA which may exceed the power supply limit of 2 mA per module. From Figures 5.11 and 5.12, a similar observation can be made - the leakage current of modules overlapping the interaction point will be higher for Layer-1 and Layer-2. During Run 3, the leakage current of Layer-2 is lower than half of that of Layer-1 which is three times lower than that of the B-Layer. This is expected due to the proximity of the B-Layer to the interaction point. Further, the difference between the leakage currents across z is minimal in Layer-2, which can be attributed to the fact that all modules in Layer-2 receive similar fluences.

The modeled predictions for the B-Layer, Layer-1 and Layer-2 were directly compared with the Run 1 and Run 2 leakage current measurements [174]. The predictions were scaled up to 0^0C using Equation 5.3 to match the data. Figure 5.13 shows the Run 3 predictions of the leakage current for the B-Layer, Layer-1 and Layer-2 in z and the average of the leakage current of the B-Layer, Layer-1 and Layer-2 measured in Run 1 and Run 2.

From Figure 5.13, it can be seen that the leakage current of the B-Layer for the samples covering the beam pipe from $z = -38.0$ cm to $z = 23.7$ cm, from $z = -13.3.3$ cm to $z = 1.0$ cm, and from $z = 5.17$ cm to $z = 13.3$ cm increases steeply in Run 3, i.e., the gradient is higher. As a result, the average leakage current of the

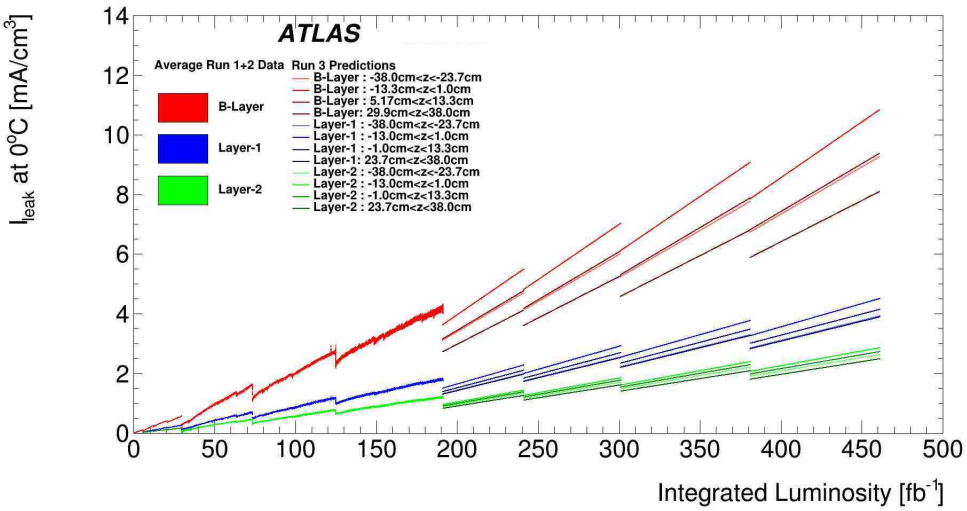

Figure 5.13: The leakage current predictions versus integrated luminosity for all representative modules in z for the B-Layer, Layer-1 and Layer-2 operating at -12°C in an extended Run 3 scenario. The predictions are compared to the average of the measured leakage currents in Run 1 and Run 2.

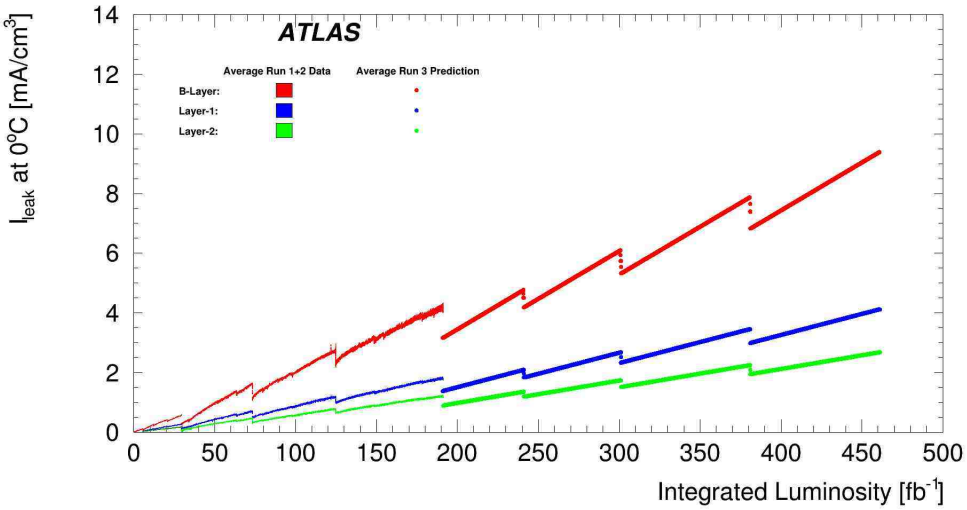

Figure 5.14: The average leakage current predictions versus integrated luminosity for the B-Layer, Layer-1 and Layer-2 operating at -12°C in an extended Run 3 scenario. The predictions are compared to the average of the measured leakage currents in Run 1 and Run 2.

B-Layer as shown in Figure 5.14 increases steeply compared to the Run 2 and Run 1 measurements. This could be attributed to the fact that since the B-Layer has been in operation since 2009, the effect of long term reverse annealing is significant.

The depletion voltages for the IBL, B-Layer, Layer-1 and Layer-2 were predicted using the Hamburg Model for an extended Run 3 scenario. The Hamburg Model parameters, N_{A}, N_{Y} and N_{C}, have been measured elsewhere [175]. The reported values vary significantly amongst different materials and particle species, and so are fit with depletion voltage data from the ATLAS pixel detector. The notion of full depletion is not well-defined for highly irradiated sensors where regions inside the sensor bulk can have very low electric field [176]. However, at moderate fluences, the depletion region is well-defined and is important for calibrating the parameters of the Hamburg Model specifically for the ATLAS Pixel detector. Using depletion voltage measurements made in Run 2 from 2015 to 2017, the Hamburg Model parameters have been adjusted for the ATLAS Pixel detector. This study used those extrapolated parameters [176] as shown in Table 5.4.

Parameter	IBL ($\times 10^{-2}$ cm^{-1})	B-Layer ($\times 10^{-2}$ cm^{-1})	Layer-1 ($\times 10^{-2}$ cm^{-1})	Layer-2 ($\times 10^{-2}$ cm^{-1})
g_{A}	0.7 ± 0.3	0.6 ± 0.2	1.4 ± 0.6	$1.4^{+1.0}_{-0.6}$
g_{Y}	$6.0^{+1.6}_{-2.3}$	$6.0^{+1.6}_{-1.3}$	$6.0^{+2.5}_{-1.9}$	6.0 ± 1.8
g_{C}	0.7 ± 0.3	$0.43^{+0.31}_{-0.21}$	0.6 ± 0.3	$0.9^{+0.7}_{-0.3}$

Table 5.4: The Hamburg Model parameters as obtained by adjusting the simulated depletion voltage to the Run 2 depletion voltage measurements made in the period from 2015 to 2017 [176].

The predicted depletion voltage for a sample of IBL modules that overlaps the interaction point ($|z| < 8$ cm) is shown in Figure 5.15.

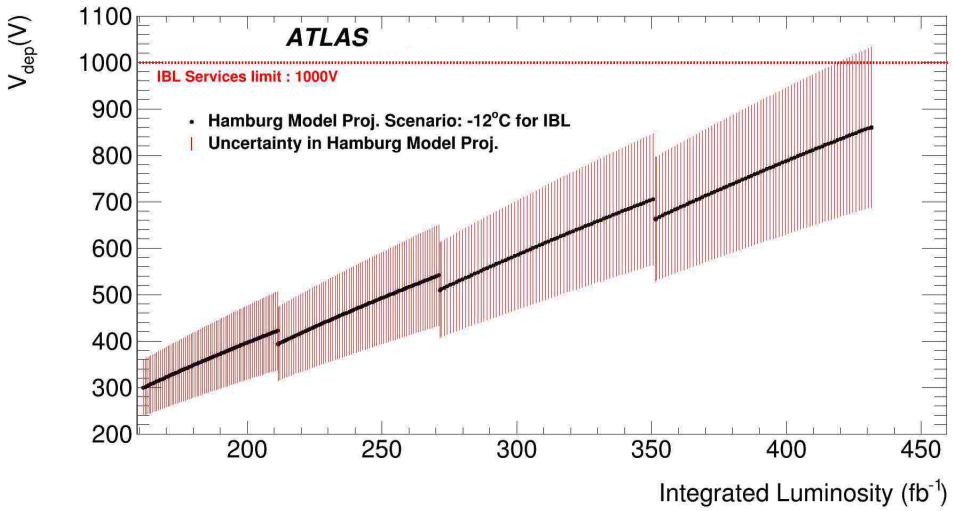

Figure 5.15: The depletion voltage prediction versus integrated luminosity for a sample of the IBL modules overlapping the interaction point and operating at -12^{o}C in an extended Run 3 scenario.

In Figure 5.15, the depletion voltage prediction includes the uncertainty that comes from the Hamburg Model parameters which is about 20% [173]. At the end of Run 3 (at 431 fb^{-1}), the depletion voltage of the IBL modules overlapping the interaction point will be 860$\pm$172 V. As can been seen in Figure 5.15, the power supply might not be able to fully deplete the IBL sensors towards the end of Run 3; but this observation should be regarded as conservative, as the Hamburg Model parameters used in this simulation were extrapolated from partial Run 2 measurements, and beneficial annealing during LS2 is not accounted for in the extrapolation of the parameters.

The depletion voltages predicted for the samples of modules in each z-region for the B-Layer, Layer-1 and Layer-2 are shown in Figure 5.16.

From Figure 5.16, it can be seen that the depletion voltage is different for each

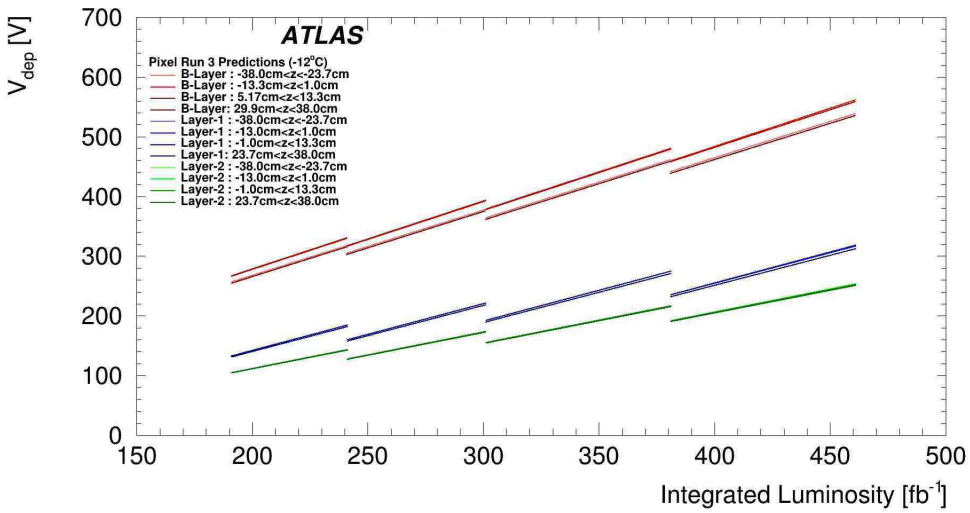

Figure 5.16: The depletion voltage predictions versus integrated luminosity for all representative modules in z for the B-Layer, Layer-1 and Layer-2 operating at -12^{o}C in an extended Run 3 scenario.

representative sample in z for each layer. The difference is larger for the B-Layer as it is closer to the IP. The fluence received by each sample in z for Layer-1 and Layer-2 is practically the same, as these are located far from the IP, resulting in similar depletion voltages for each sample in z for Layer-1 and Layer-2. Unlike leakage current predictions in which scale factors are used, the depletion voltage predictions depend solely on the fluence received and the Hamburg Model parameters, resulting in similarities observed in samples along z for each layer. Figure 5.17 shows the average of the depletion voltages of all modules in each layer.

From Figure 5.17, the average depletion voltage at the end of Run 3 will be about 560 V, 320 V and 260 V for the B-Layer, Layer-1 and Layer-2, respectively. Since the maximum bias voltage that power supplies of the B-Layer, Layer-1 and Layer-2 can provide is 600 V. the uncertainty in the depletion voltage prediction that comes from the Hamburg Model parameters (which is about 20% [173]), for the B-Layer is

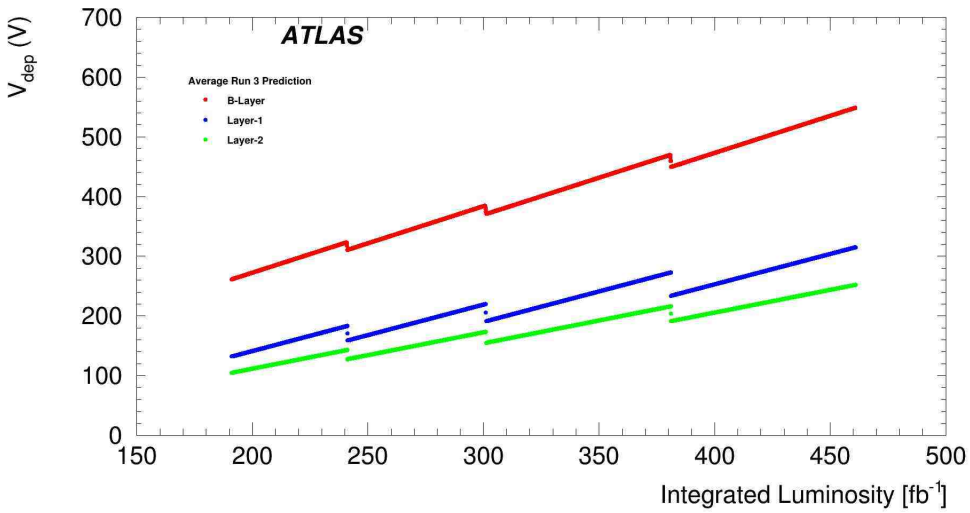

Figure 5.17: The average of depletion voltage predictions versus integrated luminosity for all representative modules in z for the B-Layer, Layer-1 and Layer-2 operating at -12^{o}C in an extended Run 3 scenario.

included and is shown in Figure 5.18.

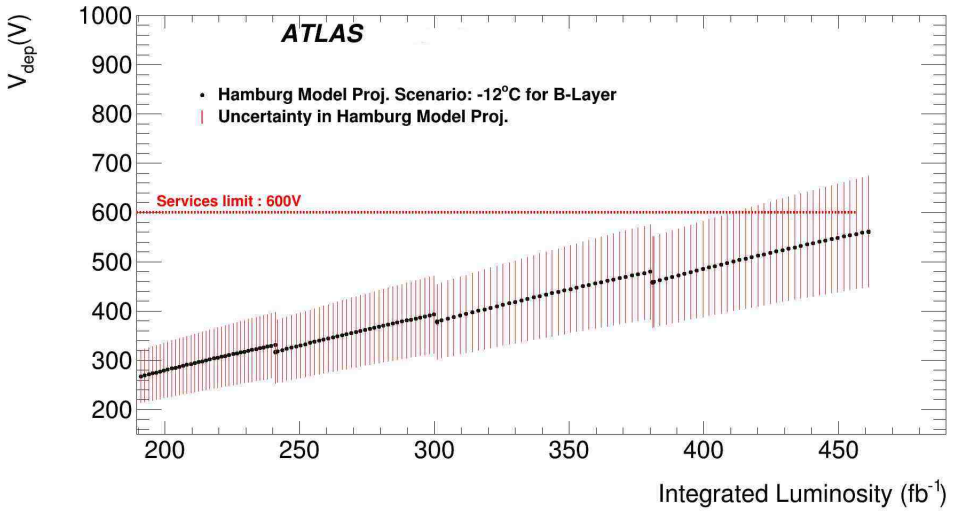

Figure 5.18: The depletion voltage prediction with uncertainty versus integrated luminosity for the B-Layer operating at -12^{o}C in an extended Run 3 scenario.

From Figure 5.18, it can be seen that the depletion voltage may exceed the services

limit of the power supply when the integrated luminosity reaches close to 440 fb^{-1} which will happen in the last year of Run 3, 2025. The depletion voltage of the B-Layer by the end of Run 3 would be 560 ± 112 V. However, this observation should be regarded as conservative, as the Hamburg Model parameters used in this simulation were extrapolated from partial Run 2 measurements, and beneficial annealing during LS2 is not accounted for in the extrapolation of the parameters.

The power consumption of the ATLAS Pixel Detector was also studied to understand the cooling requirements in the extended Run 3 scenario. The theoretical power consumption values were obtained from the product of the predicted leakage current per area, I_{leak}, as in Equation 5.7, and the predicted depletion voltage, V_{dep}, as in Equation 5.4. The predicted power consumption per sensor area versus integrated luminosity for the IBL and outer barrel layers (B-Layer, Layer-1 and Layer-2) for the modules overlapping the IP is shown in Figures 5.19 and 5.20.

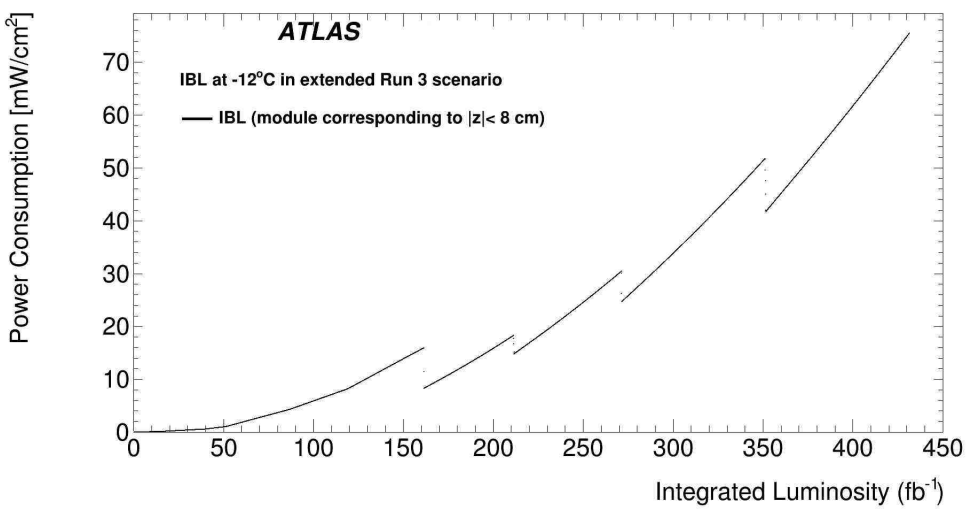

Figure 5.19: The predicted power consumption per unit sensor area versus integrated luminosity for the IBL operating at -12^{o}C in an extended Run 3 scenario.

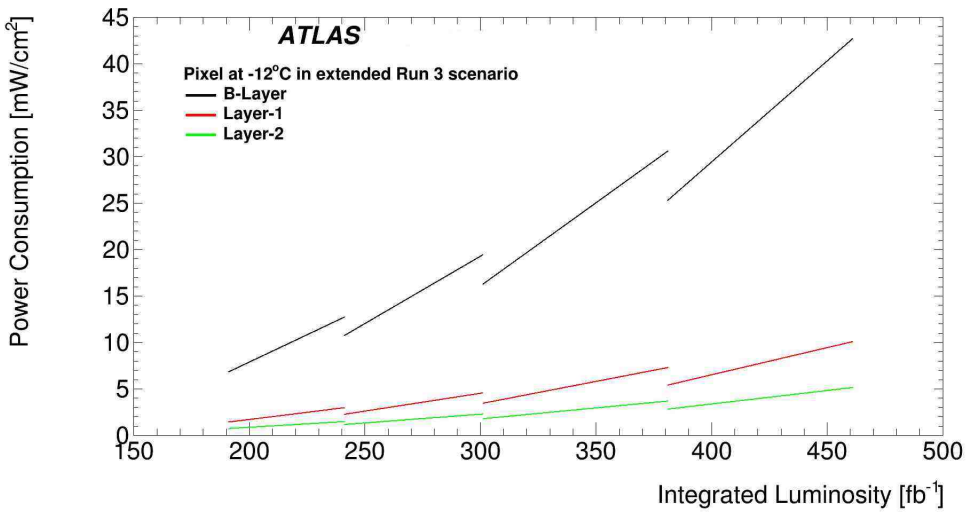

Figure 5.20: The predicted power consumption per sensor area versus integrated luminosity for the B-Layer, Layer-1 and Layer-2 operating at -12^{o}C in an extended Run 3 scenario.

It can be seen from Figure 5.19 that the power consumption per sensor area of the IBL modules overlapping the IP would be 76 mW/cm^2 at the end of Run 3. This value is much lower than the maximum sensor power, 200 mW/cm^2, arising from the IBL cooling specifications [174]. The power consumption per sensor area of the B-Layer, Layer-1 and Layer-2 at the end of Run 3 would be 43 mW/cm^2, 10 mW/cm^2 and 5 mW/cm^2, respectively and these are within the limits of their cooling specifications [2].

5.3 Extending the Range of the Depletion Voltage Model

The predictions of depletion voltage presented in the previous section relied on the temperature assumptions and introduction rates (g_{A}, g_{Y} and g_{C}) that were obtained [172, 176] by fitting the Hamburg Model to depletion voltage measurements at very low fluences. This section presents the fitting of the Hamburg Model parameters to the depletion voltages that were measured during Run 2 and Run 3.

5.3.1 $\Delta\chi^2$ Minimization and the Fitting

The χ^2 of an observable A used to calculate some parameter λ is given by

$$\chi^2(\lambda) = \frac{(A_{\mathrm{exp}} - A_{\mathrm{pred}}(\lambda))^2}{\sigma^2(A_{\mathrm{exp}})}, \tag{5.8}$$

where A_{exp} and $A_{\mathrm{pred}}(\lambda)$ are the measured and predicted values, respectively, while $\sigma(A_{\mathrm{exp}})$ is the uncertainty in the measurement of A. If there are n observables for A_n, then Equation 5.3.1 can be rewritten as

$$\chi^2(\lambda) = \sum_{i=1}^{n} \chi^2(\lambda) = \sum_{i=1}^{n} \frac{(A_{i,\mathrm{exp}} - A_{i,\mathrm{pred}}(\lambda))^2}{\sigma^2(A_{\mathrm{exp}})}, \tag{5.9}$$

where the total χ^2 is given by the sum of the χ^2 values of each observable. If this function has a minimum at a particular value of the parameter, λ_p, then the $\Delta\chi^2$ is given by

$$\Delta\chi^2 = \chi^2(\lambda) - \chi^2(\lambda_{\mathrm{p}}). \tag{5.10}$$

The parameter λ_{p} can be extracted by minimizing the function given by Equation 5.3.1. This can be used for the extraction of multiple parameters, such that the χ^2 method is a powerful way to combine various observables for the extraction of their common parameters.

Depletion voltage of a silicon sensor can experimentally be measured from fits that describes the variation of cluster charge, which is the amount of electric charge generated by a charged particle passing through it, with bias voltage applied across the electrodes of the silicon sensor, and these fitted depletion voltages are called high voltage scans.

In fitting the Hamburg Model parameters to the high voltage scans, the following expression is minimized:

$$\chi^2(g_{\mathrm{A}}, g_{\mathrm{Y}}, g_{\mathrm{C}}) = \sum_{i=1}^{N} \frac{(V_{\mathrm{dep},i,\mathrm{HV}} - V_{\mathrm{dep},i,\mathrm{pred}}(g_{\mathrm{A}}, g_{\mathrm{Y}}, g_{\mathrm{C}}))^2}{\sigma^2(V_{\mathrm{dep},i,\mathrm{HV}})}, \tag{5.11}$$

where $V_{\mathrm{dep},i,\mathrm{HV}}$ is the ith high voltage scan out of N measurements; $\sigma(V_{\mathrm{dep},i,\mathrm{HV}})$ is the uncertainty in the measurement; $V_{\mathrm{dep},i,\mathrm{pred}}(g_{\mathrm{A}}, g_{\mathrm{Y}}, g_{\mathrm{C}})$ is the predicted depletion voltage using the Hamburg Model Equation 5.4. The minimization was performed using the Minuit package [177] in the ROOT framework. The quality of the fit was gauged by the χ^2 per degree of freedom, χ^2/ndf, and the χ^2 probability. The parameters were also restricted to be positive.

Parameter	ROSE Coll. ($\times 10^{-2}$ cm^{-1})	Fitted (2015-17) ($\times 10^{-2}$ cm^{-1})	Fitted (2015-23) ($\times 10^{-2}$ cm^{-1})
g_{A}	1.0	0.7 ± 0.3	0.59 ± 0.23
g_{Y}	1.6	$6.0^{+1.6}_{-2.3}$	3.7 ± 2.9
g_{C}	1.0	0.7 ± 0.3	0.62 ± 0.06

Table 5.5: The introduction rates as obtained by fitting the Hamburg Model to the Run 2 and Run 3 depletion voltage measurements of the IBL are given in column "Fitted (2015-23)." For comparison, the introduction rates that were measured by the ROSE Collaboration [172], and the introduction rates that were measured [176] using the HV scans made during the period 2015-17, are also shown.

5.3.2 Fitted Introduction Rates from the Damages in the IBL

The Hamburg Model was fitted to 9 average high voltage (HV) scans [178] of the IBL, recorded during the period 2015-23, to extract the introduction rates for silicon sensors in the IBL. The fit used the thermal history of the IBL collected for the period 2015-23. The fitted introduction rates for the IBL as shown in Table 5.5. These introduction rates are compared to others measured at low fluences and employed in this dissertation. The χ^2/ndf and χ^2 probability were computed to be 1.48 and 0.19, respectively. Figure 5.21 shows the simulated and predicted depletion voltage of the IBL sensors, averaged over all modules, plotted against integrated luminosity using the fitted introduction rates of the Hamburg Model.

Only 9 of the 12 HV scans shown in Figure 5.21 were fitted to the Hamburg Model, because including the 3 HV scan points with the lowest uncertainty (from 40 fb^{-1} to 100 fb^{-1}) resulted in a high χ^2/ndf and a low χ^2 probability. From Table 5.5, it can be seen that the annealing parameters, g_{A} and g_{Y}, have lower values compared to

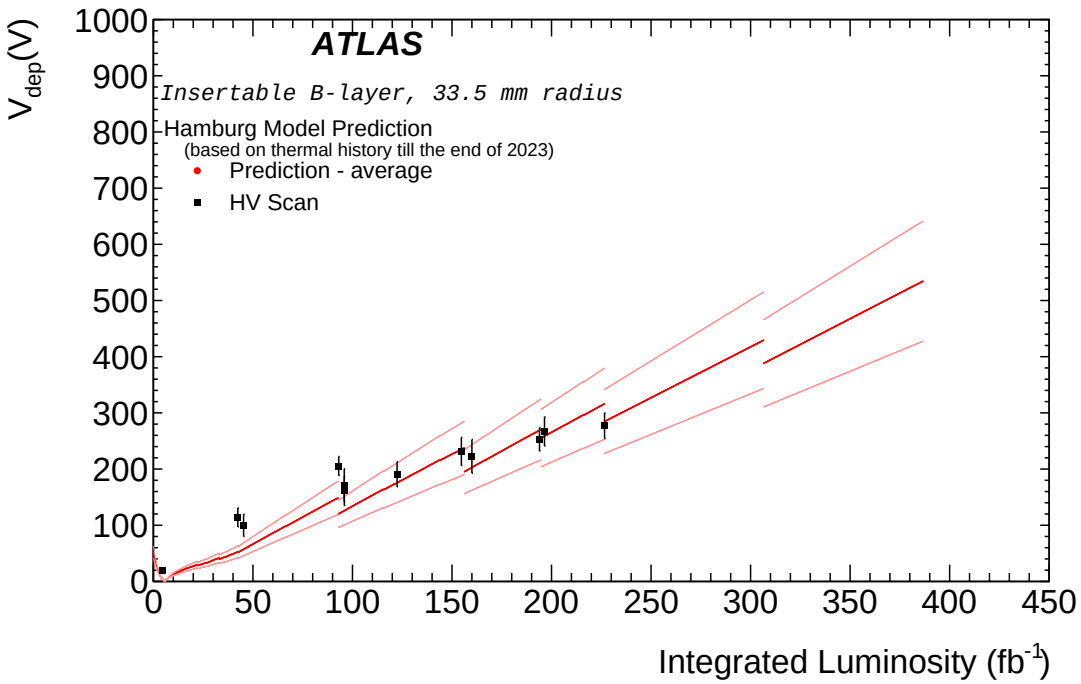

Figure 5.21: The solid red line corresponds to the simulated and predicted depletion voltages, averaged over all IBL modules, plotted against the integrated luminosity using the fitted Hamburg Model parameters. The light red lines correspond to the uncertainty on the simulations. The HV scan values are represented by black points.

the ones fitted using the 2015-17 HV scan values. Since these two parameters govern the annealing behavior in the sensors, a decrease in their values indicates that the observed annealing would be less; this is evident in Figure 5.21. This behavior can be partially explained by the fact that the duration in which the IBL modules were kept at a temperature above 0°C was short.

5.3.3 Fitted Introduction Rates from Damages in the B-Layer

The Hamburg Model was fitted to 6 high voltage (HV) scans [179] of the B-Layer, averaged over all modules. The some were recorded during the period 2015-23 to

Parameter	ROSE Coll. ($\times 10^{-2}$ cm^{-1})	Fitted (2015-17) ($\times 10^{-2}$ cm^{-1})	Fitted (2015-23) ($\times 10^{-2}$ cm^{-1})
g_{A}	1.0	0.6 ± 0.2	0.19 ± 0.4
g_{Y}	1.6	$6.0^{+1.6}_{-2.3}$	2.5 ± 2.6
g_{C}	1.0	0.43 ± 0.3	0.67 ± 0.16

Table 5.6: The introduction rates as obtained by fitting the Hamburg Model to the Run 2 and Run 3 depletion voltage measurements of the B-Layer are given in column "Fitted (2015-23)." For comparison,the introduction rates that were measured by the ROSE Collaboration [172] and the introduction rates that were measured [176] using the HV scan values made during the period 2015-17, are also shown.

extract the introduction rates for the B-Layer. The fit used the thermal history of the B-Layer collected for the period 2015-23. The fitted introduction rates for the B-Layer are shown in Table 5.6. These introduction rates are compared to others measured at low fluences and employed in this dissertation. The χ^2/ndf and χ^2 probability were computed to be 0.48 and 0.70, respectively. Figure 5.22 shows the simulated and predicted depletion voltages of the B-Layer, averaged over all modules, plotted against integrated luminosity using the fitted introduction rates of the Hamburg Model.

Only 6 of the 9 HV scans shown in Figure 5.21 were fitted by the Hamburg Model, as the fitting algorithm failed for the 3 HV scan points with the lowest uncertainty (between 70 fb^{-1} and 130 fb^{-1}). From Table 5.6, it can be seen that the annealing parameters, g_{A} and g_{Y}, have lower values compared to the ones fitted using 2015-17 data. Since these two parameters govern the annealing behavior in the sensors, a decrease in their values indicates that observed annealing would be less; this is evident in Figure 5.22. This behavior can be partially explained by the fact that the duration in which the B-Layer modules were kept at a temperature above 0°C was short. The

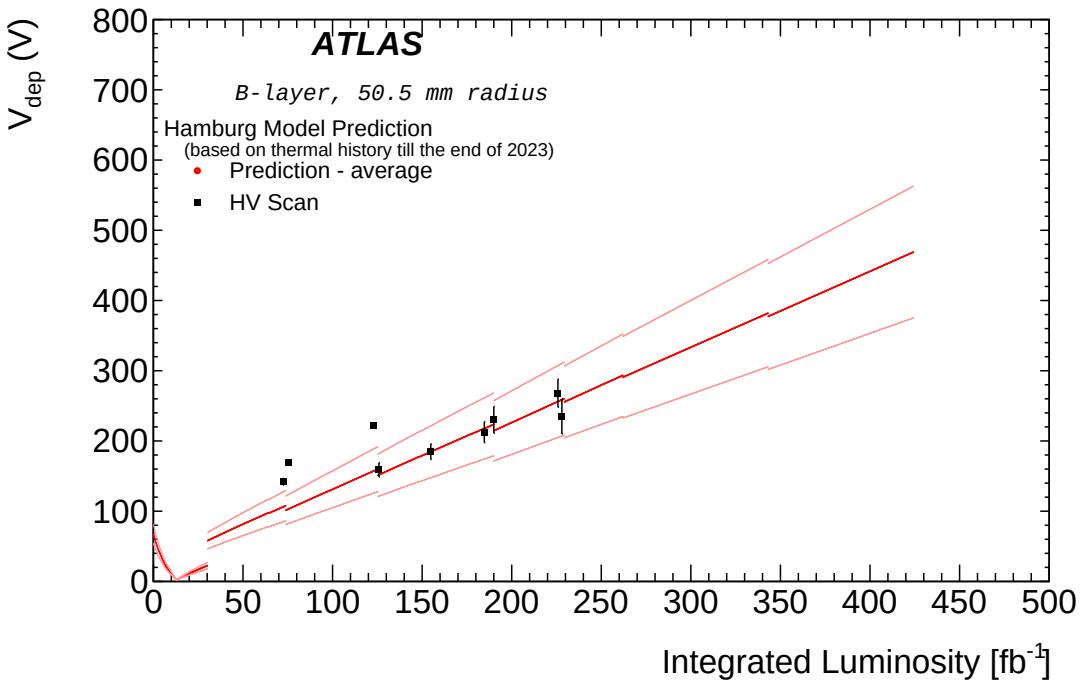

Figure 5.22: The solid red line corresponds to the simulated and predicted depletion voltages, averaged over all B-Layer modules, plotted against integrated luminosity using the fitted Hamburg Model parameters. The light red lines correspond to the uncertainty on the simulations. The HV scan values are represented by black points.

introduction rates g_A and g_Y had higher uncertainties than in the case of the IBL since only 6 HV scans were used to extract 3 parameters, which reduced the number of degrees of freedom in the fit.

5.4 Depletion Voltage Predictions for the ITk Pixel Detector

5.4.1 Introduction

The HL-LHC will operate at a peak instantaneous luminosity of 7.5×10^{34} cm^{-2}s^{-1}, which corresponds to approximately 200 inelastic proton-proton collisions per beam crossing (pile-up) [180]. It will be operational for more than ten years and in that time ATLAS aims for a total data set of about 3800 fb^{-1}. A consequence of this increased luminosity is the radiation damage requiring the tracking detectors to withstand a hadronic fluence up to 2×10^{16} 1 MeV n_{eq}/cm^2 in the Inner Tracker (ITk) Pixel system, as shown in Figure 5.23.

If the ITk will be implemented through staging, there will be situations when highly irradiated sensors of the ITk Pixel system will be kept at room temperature for long durations in the long shutdowns (LS) [36]. Depletion voltages during operation after staging would be increased. A study of depletion voltages for various staging scenarios, predicted using the Hamburg Model [149], was performed.

5.4.2 ITk Pixel and the HL-LHC

The ITk consists of a strip detector and a pixel detector. The former is composed of four layers in the barrel starting at about 400 mm from the beam axis, and six end cap disks per side. The latter is made of five barrel layers from a radius of 35 mm. In the forward region, the Pixel detector is completed by a structure of concentric

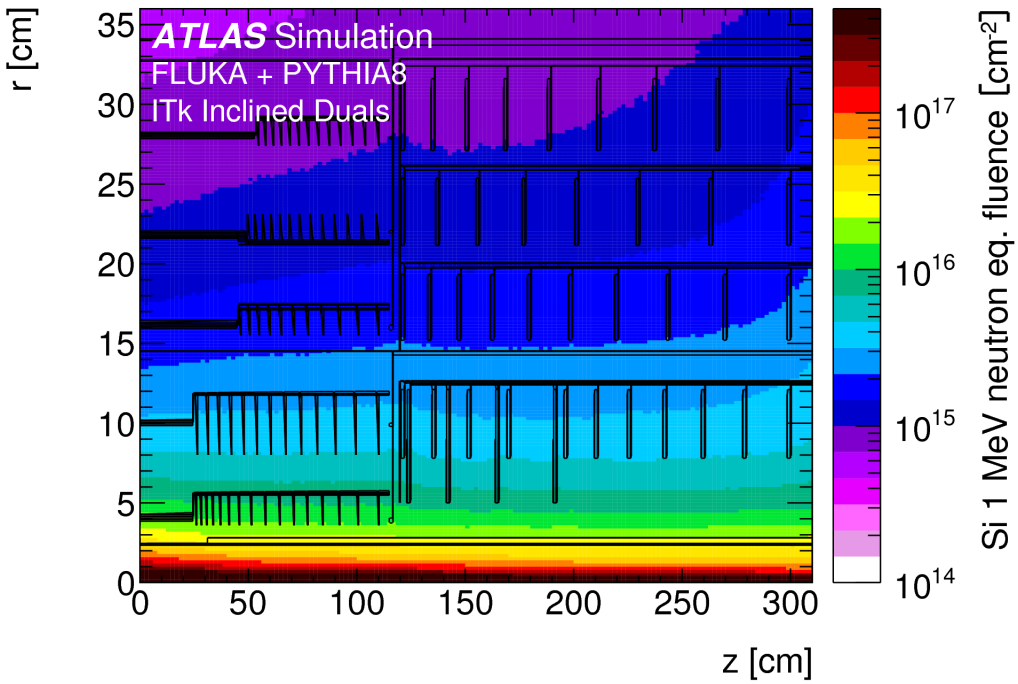

Figure 5.23: Integrated fluence distributions normalized to 4000 fb^{-1}, for the ITk Pixel detector [40].

rings arranged at different radii. Due to the very large radiation doses expected over the full HL-LHC run period, the two innermost Pixel barrel layers are designed to be replaceable and are foreseen to be exchanged after about 2000 fb^{-1}.

The Pixel system is divided into an outer system (OS) composed of three barrel layers (L2, L3, and L4) with three corresponding groups of rings (R2, R3, and R4) called outer end caps (OEC), and an inner system (IS) with two barrel layers (L0 and L1) and three groups of rings called inner end caps (IEC); there are two in correspondence with the barrel layer radii (R0 and R1) and one in between the two (R0.5). In this study, only Pixel barrel layers are considered. A schematic layout of the ITk is shown in Figure 5.24.

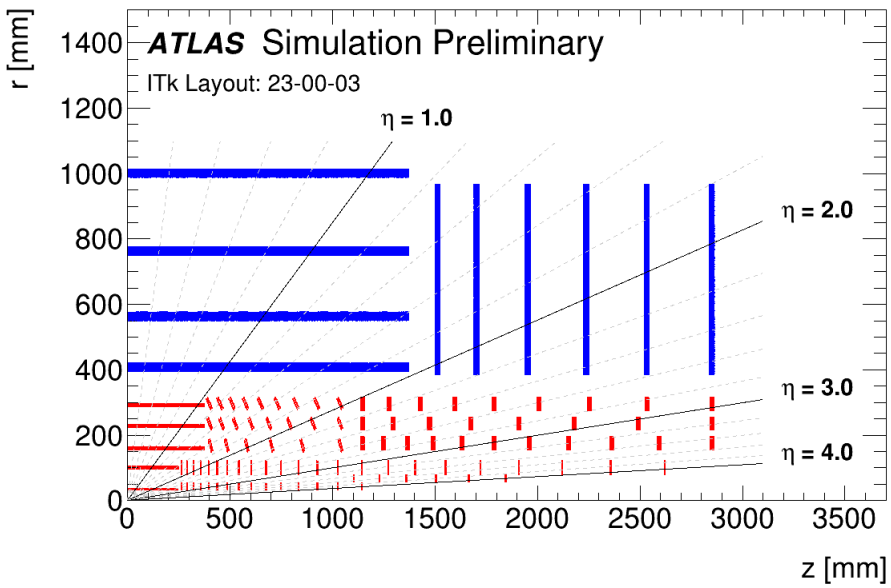

Figure 5.24: The ITk schematic layout [181].

Different sensor technologies and pixel dimensions are used in the different layers of the ITk [40]. Silicon n-in-p planar pixel sensors with an active thickness of 150 μm are employed in the outer system, while the same planar sensor technology with an active thickness of 100 μm instruments L1. Thin 3D silicon pixel sensors with electrode to electrode distance 52 μm have been chosen for the innermost layer due to the radiation hardness of this technology [182].

An integrated luminosity of 3806 fb^{-1} is to be achieved for the HL-LHC. The year-wise integrated luminosities in all runs are shown in Table 5.7.

5.4.3 The Hamburg Model Simulation and Staging Scenarios

The following Hamburg Model parameters were used in the simulation:

Run	Year	Lumi/Year (fb^{-1})	Integrated Lumi (fb^{-1})
Run 4	2027	18.5	18.5
	2028	73.8	92.3
	2029	215	307
	2030	254	561
Run 5	2032	270	831
	2033	405	1236
	2034	405	1641
Run 6	2036	385	2026
	2037	445	2471
	2038	445	2916
	2039	445	3361
	2040	445	3806

Table 5.7: Luminosity predicted to be collected in each year and run [183].

- $g_{\mathrm{Y}} = 6.0 \times 10^{-2}\mathrm{cm}^{-1}$ - obtained from fitting [184] ATLAS data on depletion voltage versus fluence, to the Hamburg Model formulas, with introduction rates as free parameters,
- $g_{\mathrm{C}} = 2.0 \times 10^{-2}\mathrm{cm}^{-1}$ - typical value [185] for p-type sensors,
- $c = 2.0 \times 10^{-13}\mathrm{cm}^{2}$ - typical value [152] for p-type sensors, and
- $N_{\mathrm{eff},0} = 2.0 \times 10^{-12}\mathrm{cm}^{-3}$ - typical value [149] for p-type sensors.

The Hamburg Model [149] predicts the depletion voltage of a sensor when it is exposed to radiation causing non-ionizing energy loss (NIEL) for a certain duration, by using the change in the doping concentration described by Equation 5.5. The model requires inputs of particle fluence in 1 MeV $n_{\mathrm{eq}}/\mathrm{cm}^2$ per fb^{-1}, the duration of the fluence application and the temperature of the sensor. The conversion factors from fluence to luminosity for ITk Pixel sensors are obtained using an interface access tool [186] utilizing FLUKA and GEANT4 and are listed in Table 5.8.

Radius r (mm)	Layer	FLUKA ($\times 10^{11}$)	GEANT4 ($\times 10^{11}$)
35	L0	53.71 (2-4)	55.00 (0-2)
100	L1	9.759 (22-24)	10.72 (24-26)
160	L2	5.074 (34-36)	6.002 (32-34)
230	L3	3.056 (36-38)	3.841 (38-40)
290	L4	2.325 (30-32)	2.935 (34-36)

Table 5.8: Conversion factors for each ITk layer using FLUKA and GEANT4. The corresponding z region in centimeters is annotated in parenthesis for each factor.

For the worst-case scenario, this study used factors obtained from GEANT4. The nominal temperature of each layer during operation is listed in Table 5.9.

Layer	Temperature (^{o}C)
L0	-24.02
L1	-12.10
L2	-15.38
L3	-15.38
L4	-15.38

Table 5.9: Nominal temperature for each layer during operation [187].

All layers will be kept at a temperature of -20^{o}C during winter shutdown. The staging involves keeping the detector inside the ATLAS pit, the underground cavern that houses the ATLAS detector, for a few days until it is brought to building SR1 at the surface, where it will be kept for a longer time for maintenance. In these situations, when the cooling is off, it is expected that the temperature of the detector will come to equilibrium with the temperature of the ATLAS pit and SR1. The temperature of the layers during the Long Shutdown varies with each staging scenario and is discussed below.

Staging of Layer-4 in Long Shutdown 4: Starting from the Long Shutdown 4, the temperature of the Outer System during the staging of Layer-4 would be as

follows:

- At ATLAS pit at 25°C for 29 week days,
- At SR1 at 20°C for 392 week days, and
- At ATLAS pit at 25°C for 33 week days.

During operation and winter shutdown, the Outer System is kept at −15.38°C and −20°C, respectively. To reflect the actual calendar time taken, the number of week days is multiplied by a factor of 7/5. This scenario is illustrated in Figure 5.25.

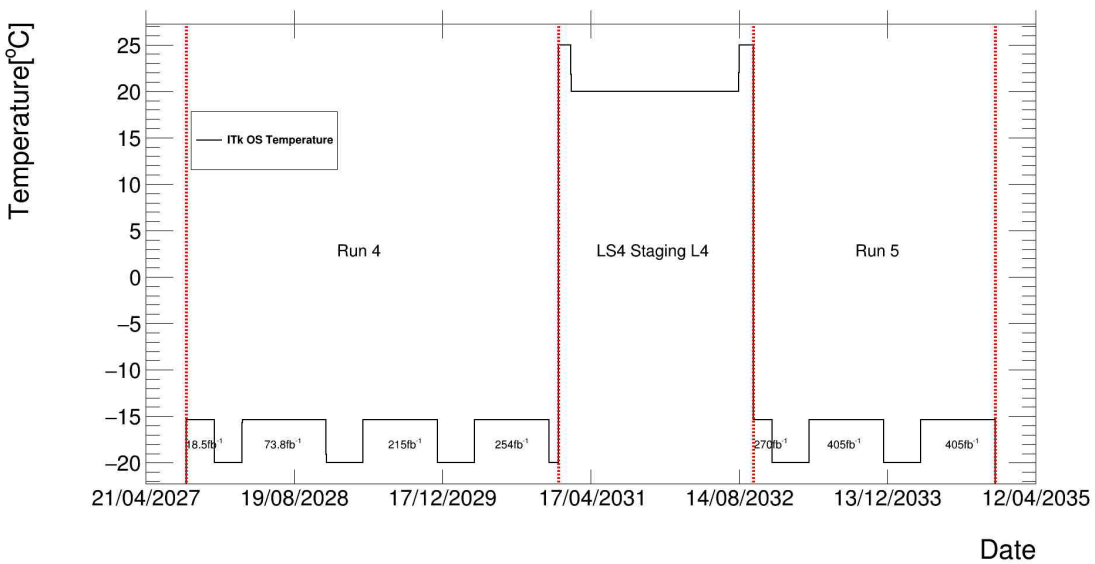

Figure 5.25: Temperature of the Outer System (OS) during Run 4, Long Shutdown 4 (LS4) with staging of Layer-4 (L4), and Run 5.

The temperature of the Inner System during the staging of Layer-4 would be as follows:

- At ATLAS pit at 25°C for 29 week days,

- At SR1 at 20°C for 16 week days,
- In a cold storage box at −20°C for 339 week days,
- At SR1 at 20°C for 37 week days, and
- At ATLAS pit at 25°C for 33 week days.

Operating temperatures for Layer-0 and Layer-1 are −24.02°C and −12.1°C, respectively. Both layers are kept at −20°C during winter shutdowns. The scenarios for Layer-0 and Layer-1 are illustrated in Figures 5.26 and 5.27, respectively.

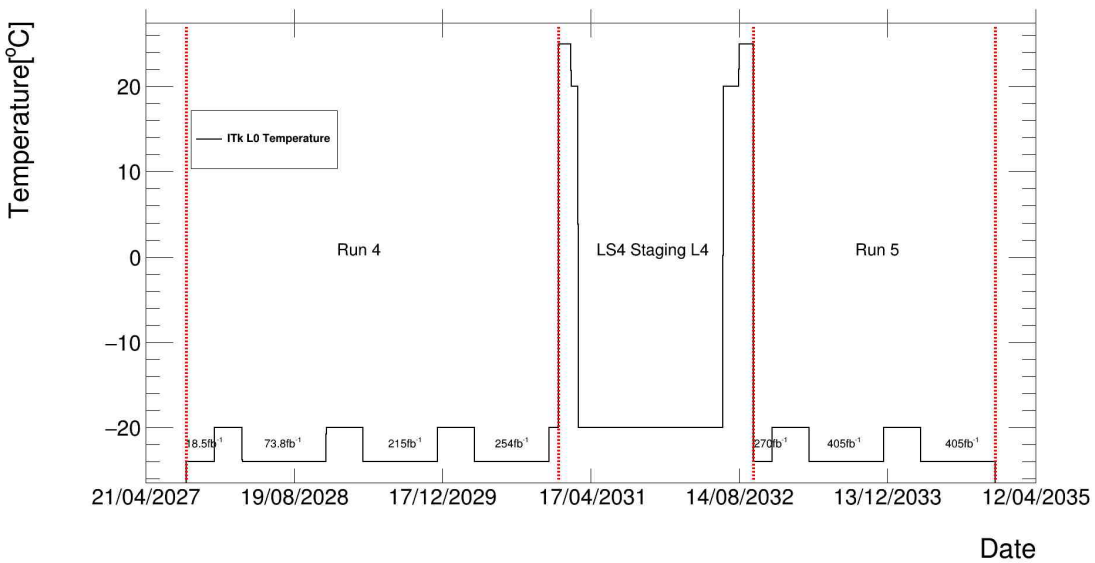

Figure 5.26: Temperature of Layer-0 (L0) during Run 4, Long Shutdown 4 (LS4) with staging of Layer-4 (L4), and Run 5.

Staging of the Outer End Caps in Long Shutdown 4: The temperature of the Outer System during the staging of the Outer End Caps would be as follows:

- At ATLAS pit at 25°C for 29 week days,

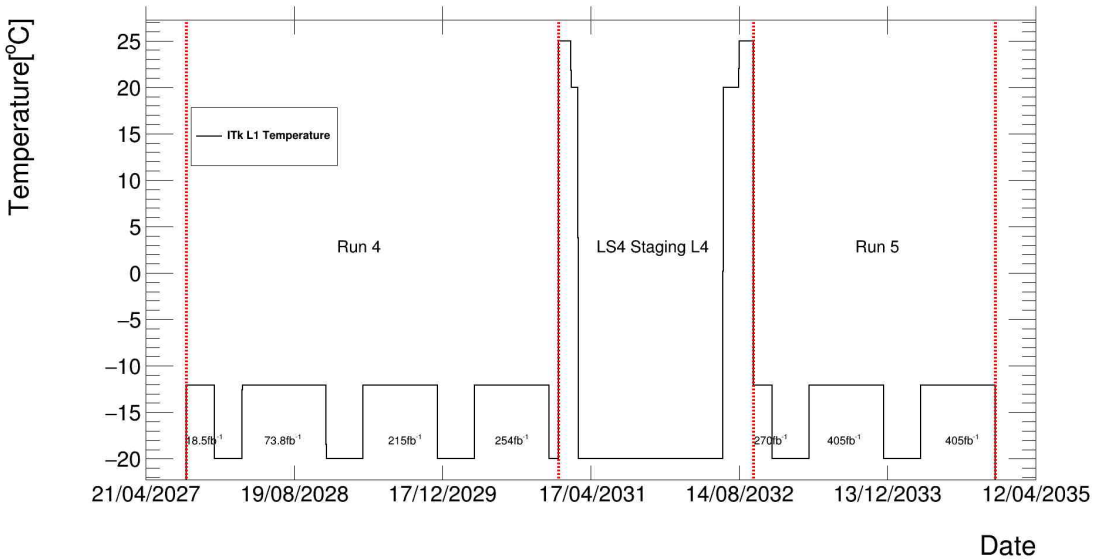

Figure 5.27: Temperature of Layer-1 (L1) during Run 4, Long Shutdown 4 (LS4) with staging of Layer-4 (L4), and Run 5.

- At SR1 at 20°C for 123 week days, and
- At ATLAS pit at 25°C for 33 week days.

During operation and winter shutdown, the Outer System is kept at −15.38°C and −20°C, respectively. This scenario is illustrated in Figure 5.28.

The temperature of the Inner System during the staging of the Outer End Caps would be as follows:

- At ATLAS pit at 25°C for 29 week days,
- At SR1 at 20°C for 16 week days,
- In a cold storage box at −20°C for 70 week days,
- At SR1 at 20°C for 37 week days, and

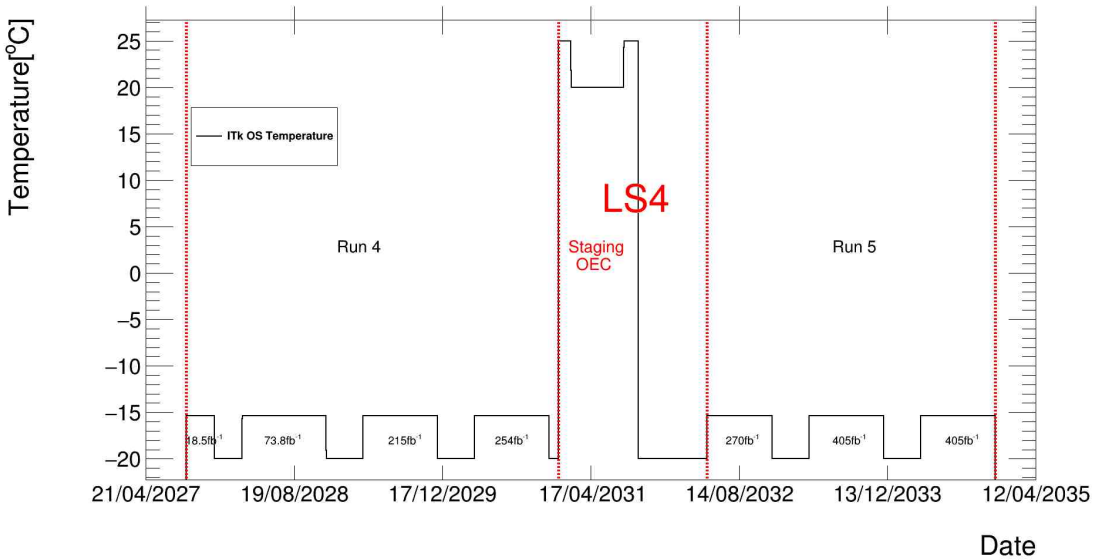

Figure 5.28: Temperature of the Outer System (OS) during Run 4, Long Shutdown 4 (LS4) with staging of the Outer End Caps (OEC), and Run 5.

- At ATLAS pit at 25°C for 33 week days.

The operating temperatures for Layer-0 and Layer-1 are −24.02°C and −12.1°C, respectively. Both layers are kept at −20°C during winter shutdowns. The scenarios for Layer-0 and Layer-1 are illustrated in Figures 5.29 and 5.30, respectively.

Staging with Scaling in Long Shutdown 4: Staging with scaling is an alternative scenario where the detector is kept at room temperature for a much longer duration. For the Outer System, the temperature would be as follows:

- At 25°C for 559 week days, and
- At −20°C subsequently until Run 5.

During operation and winter shutdown, the Outer System is kept at −15.38°C and

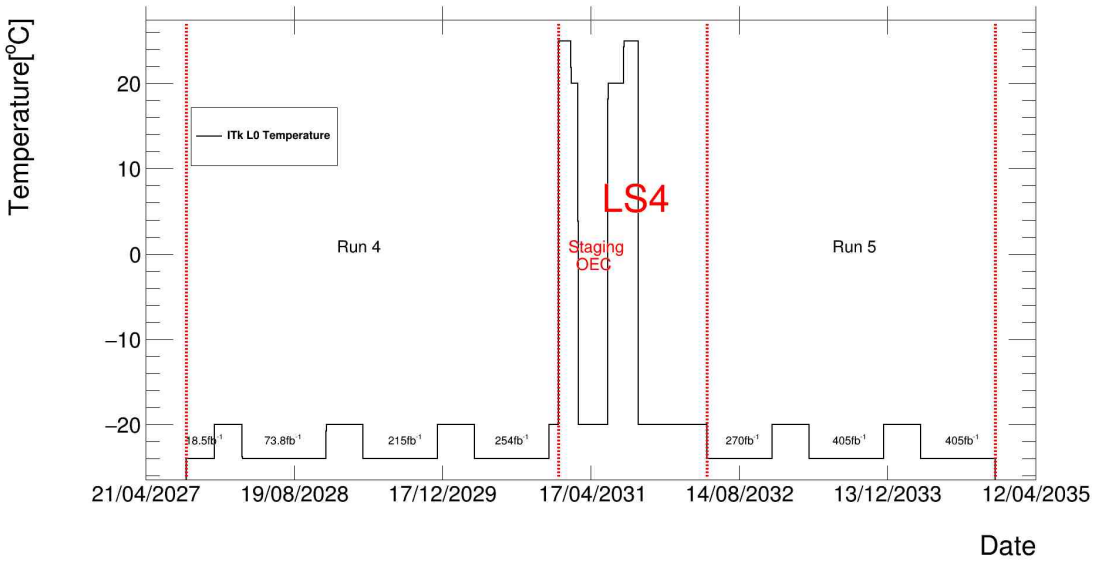

Figure 5.29: Temperature of Layer-0 (L0) during Run 4, Long Shutdown 4 (LS4) with the staging of the Outer End Caps (OEC), and Run 5.

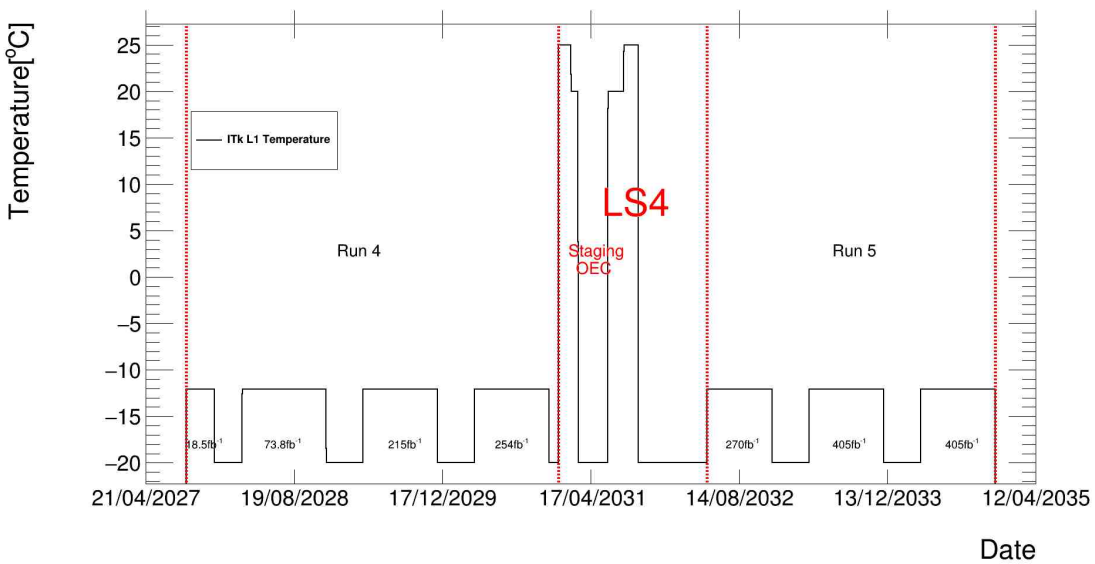

Figure 5.30: Temperature of Layer-1 (L1) during Run 4, Long Shutdown 4 (LS4) with the staging of the Outer End Caps (OEC), and Run 5.

-20°C, respectively. The scenario is illustrated in Figure 5.31.

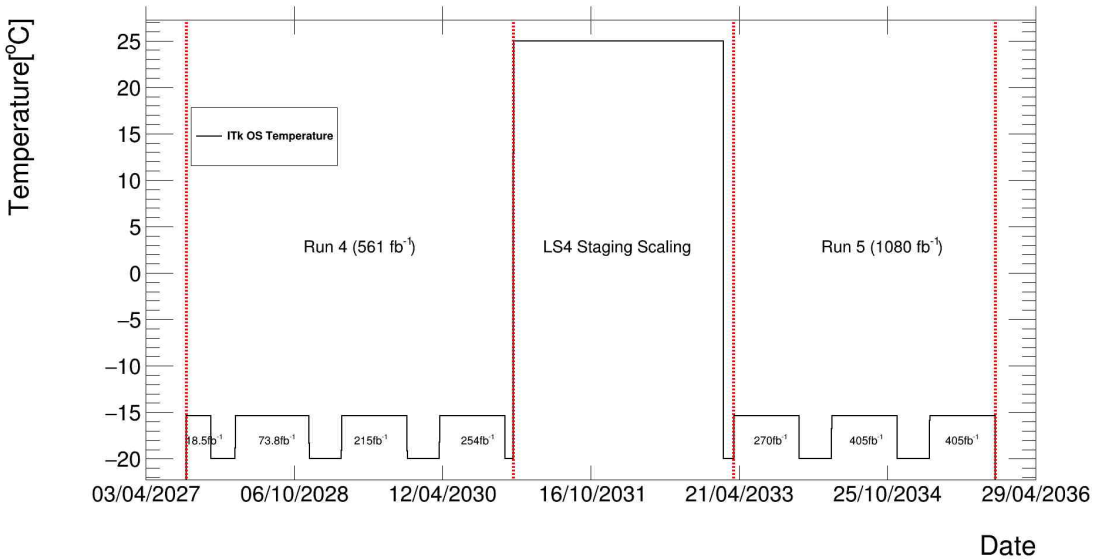

Figure 5.31: Temperature of the Outer System (OS) during Run 4, Long Shutdown 4 (LS4) with staging with scaling, and Run 5.

For the Inner System, the temperature would be as follows:

- At 25°C for 122 week days,
- At −20°C for 255 week days,
- At 25°C for 182 week days, and
- At −20°C subsequently until Run 5.

The operating temperatures for Layer-0 and Layer-1 are −24.02°C and −12.1°C, respectively. Both layers are kept at −20°C during winter shutdowns. This scenario is illustrated in Figures 5.32 and 5.33 for Layer-0 and Layer-1, respectively.

End of Lifetime Temperature Scenario with Staging of Layer-4: End of lifetime scenarios following the staging of Layer-4 in Long Shutdown 4 are studied for

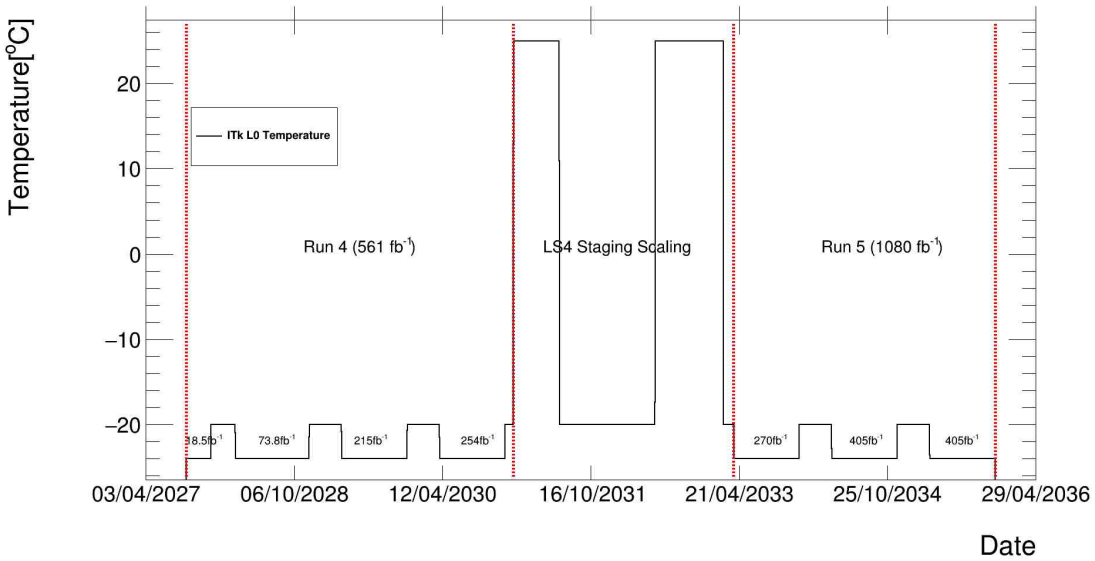

Figure 5.32: Temperature of Layer-0 (L0) during Run 4, Long Shutdown 4 (LS4) with staging with scaling, and Run 5.

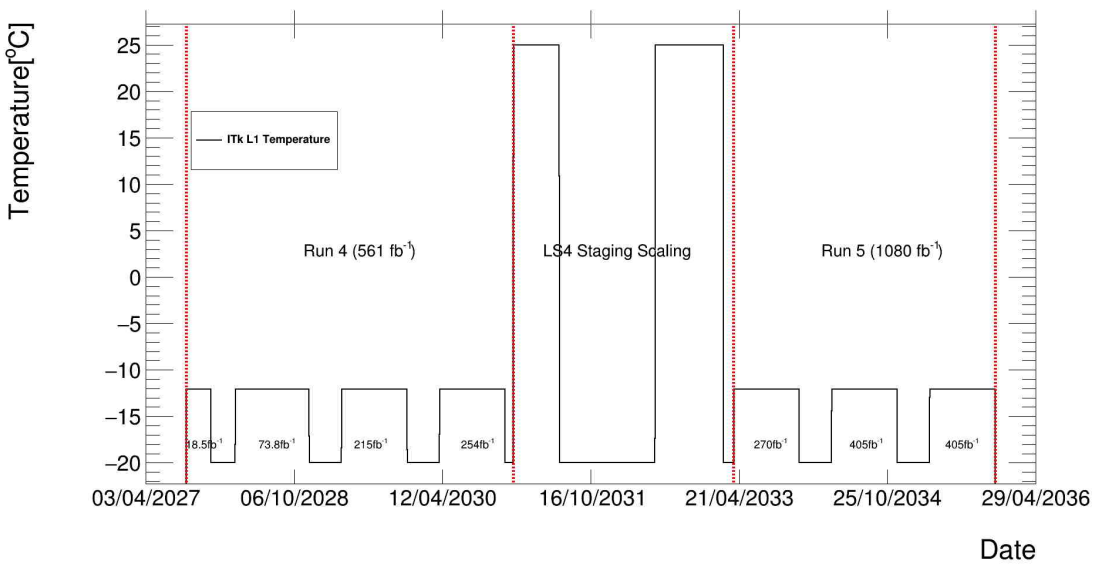

Figure 5.33: Temperature of Layer-1 (L1) during Run 4, Long Shutdown 4 (LS4) with staging with scaling, and Run 5.

two cases. In the first case, during Long Shutdown 5, the Outer System will be kept at 25°C for 6 months in order to replace the Inner System. Then, the Outer System

will go through the following sequence during the HL phase of the LHC:

- Run 4,
- Staging of Layer-4 in Long Shutdown 4,
- Run 5,
- Long Shutdown 5 (at 25°C for 6 months, at −20°C thereafter),
- Run 6.

During operation and winter shutdown, the Outer System is kept at −15.38°C and −20°C, respectively. This scenario is illustrated in Figure 5.34.

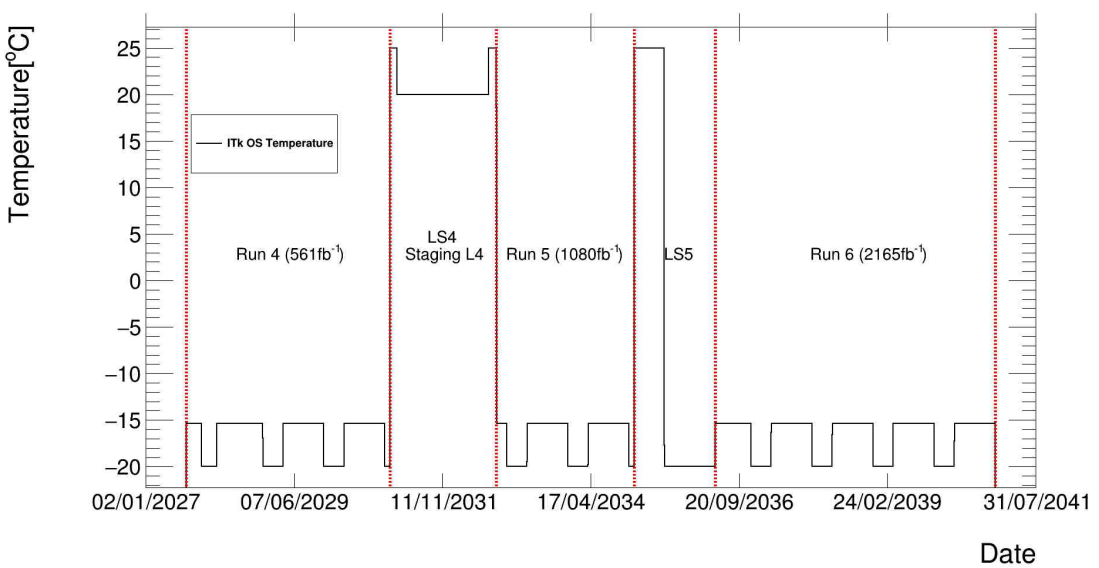

Figure 5.34: End of Lifetime temperature scenario with staging of Layer-4 (L4) during Long Shutdown 4 (LS4) - Case 1.

In the second case, the Outer System will be kept at −20°C for the entire Long Shutdown 5 as is illustrated in Figure 5.35.

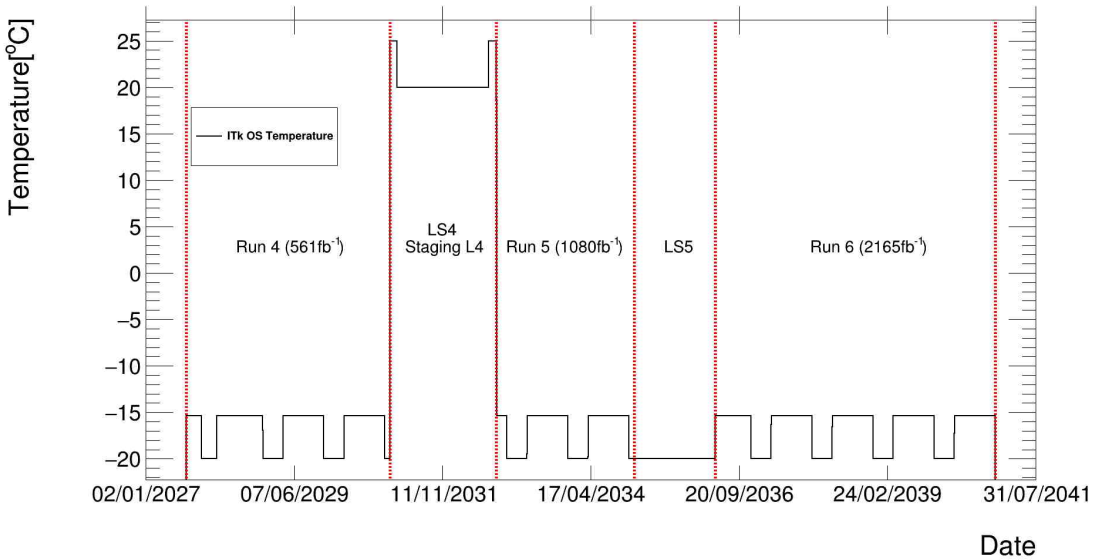

Figure 5.35: End of Lifetime Scenario with staging of Layer-4 (L4) during Long Shutdown 4 (LS4) - Case 2.

End of Lifetime Temperature Scenario with Staging of the Outer End Caps: With staging of the Outer End Caps, the Outer System will go through one of the following sequences during the HL phase of the LHC. For the first case, where it is kept at 25°C for 6 months, the sequence is:

- Run 4,
- Staging of the Outer End Caps in Long Shutdown 4,
- Run 5,
- Long Shutdown 5 (at 25°C for 6 months, at −20°C thereafter),
- Run 6.

During operation and winter shutdown, the Outer System is kept at −15.38°C and −20°C, respectively. This scenario is illustrated in Figure 5.36.

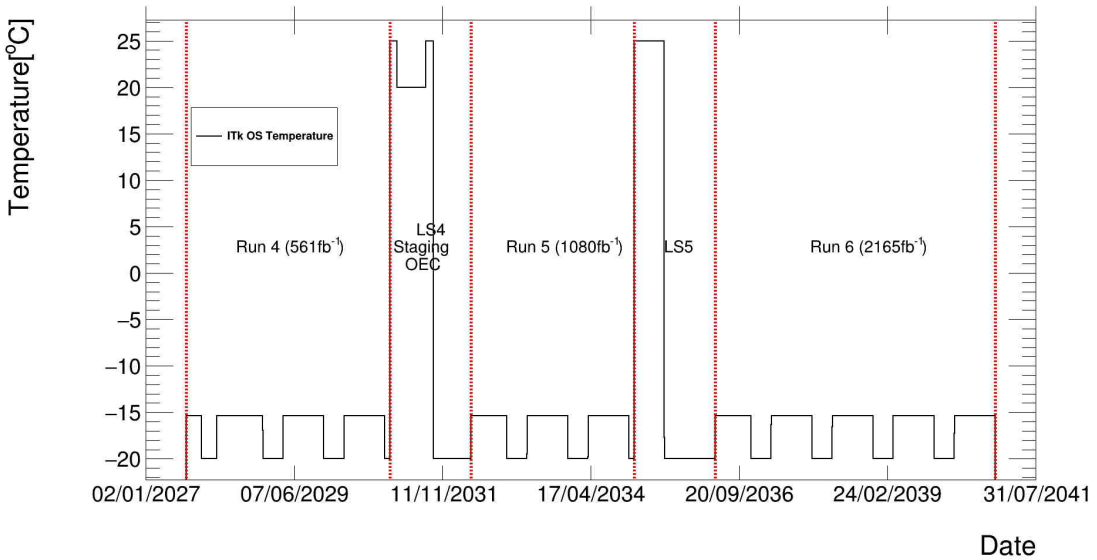

Figure 5.36: End of Lifetime temperature scenario with staging of the Outer End Caps (OEC) - Case 1.

In the second case, the Outer System will be kept at -20^{o}C for the entire Long Shutdown 5 as is illustrated in Figure 5.37.

5.4.4 Results of Simulation and Staging Recommendations

Staging of Layer-4 in Long Shutdown 4: The depletion voltage is plotted against the date for the scenario - Run 4 + Long Shutdown 4 with staging of Layer-4 + Run 5, in Figure 5.38. The horizontal segments correspond to episodes of low temperature at which the reverse annealing is frozen out.

Since Layer-2 faces the maximum radiation damage in the Outer System, and due to the long duration in which it would be kept at room temperature, its depletion voltage at the end of Run 5 is the highest. This is due to the severe reverse annealing

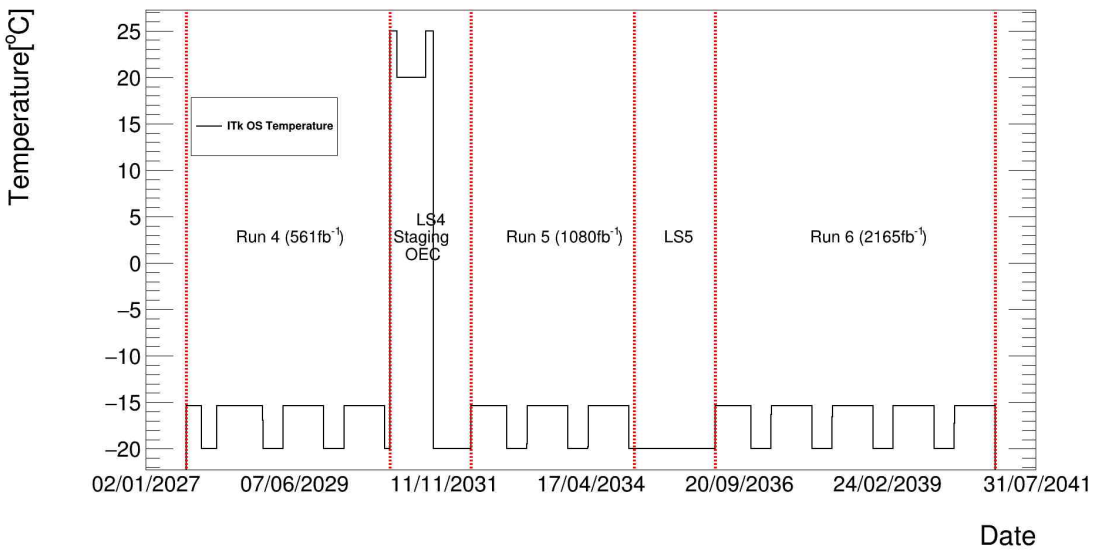

Figure 5.37: End of Lifetime temperature scenario with staging of the Outer End Caps (OEC) - Case 2.

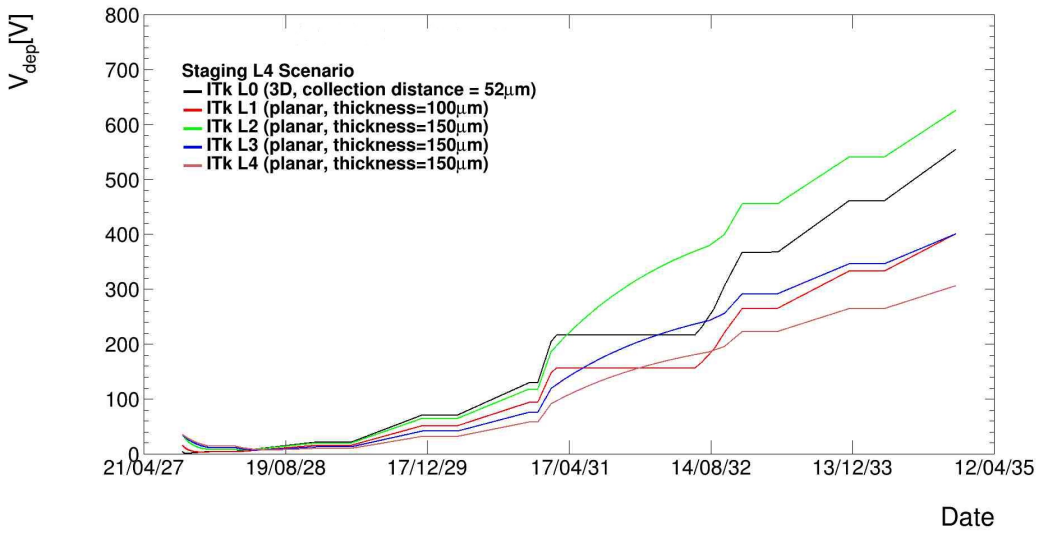

Figure 5.38: Predicted depletion voltage versus date, for staging of Layer-4 (L4) in Long Shutdown 4 (LS4).

that can be seen between the years 2031 and 2032.

Staging of the Outer End Caps in Long Shutdown 4: The depletion voltage

is plotted against the date for the scenario - Run 4 + Long Shutdown 4 with staging of the Outer End Caps + Run 5, in Figure 5.39.

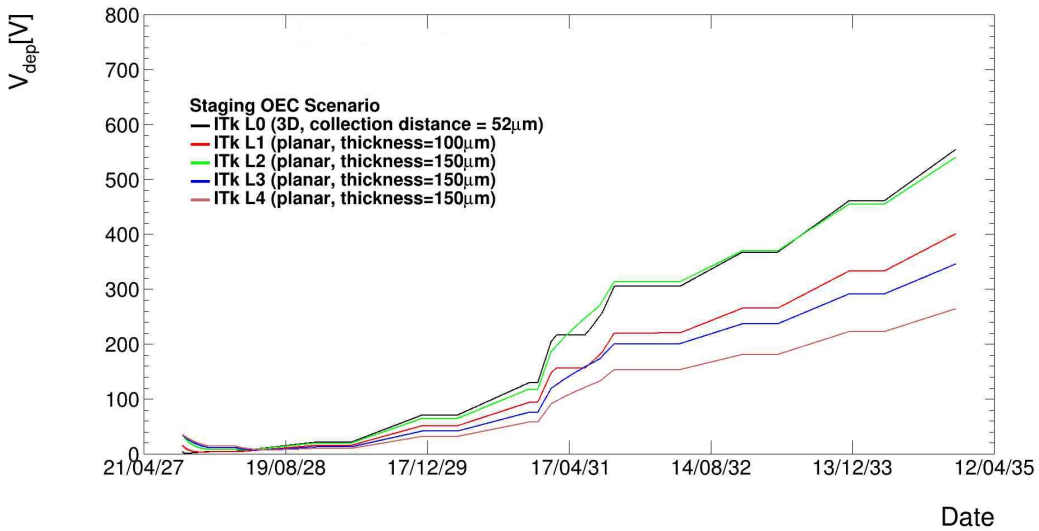

Figure 5.39: Predicted depletion voltage versus date, for staging of the Outer End Caps (OEC) in Long Shutdown 4 (LS4).

As both the Inner System and the Outer System are kept at room temperature for a shorter duration, the depletion voltages at the end of Run 5 are lower compared to those in the scenario with staging of Layer-4. This is illustrated for Layer-0 and Layer-2 as shown in Figures 5.40 and 5.41, respectively.

Staging with scaling in Long Shutdown 4: The depletion voltage is plotted against the date for the scenario - Run 4 + Long Shutdown 4 with staging with scaling + Run 5, in Figure 5.42.

It is clear that staging with scaling pushes the depletion voltage to higher values than those predicted for the other two staging scenarios, due to the much longer

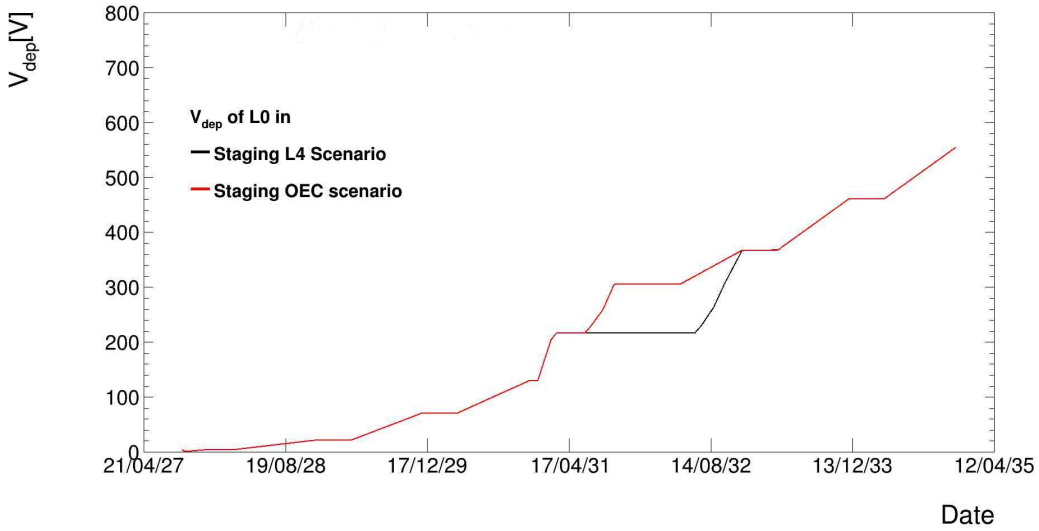

Figure 5.40: Comparison of depletion voltages of Layer-0 (L0) in response to staging Layer-4 (L4) versus the Outer End Caps.

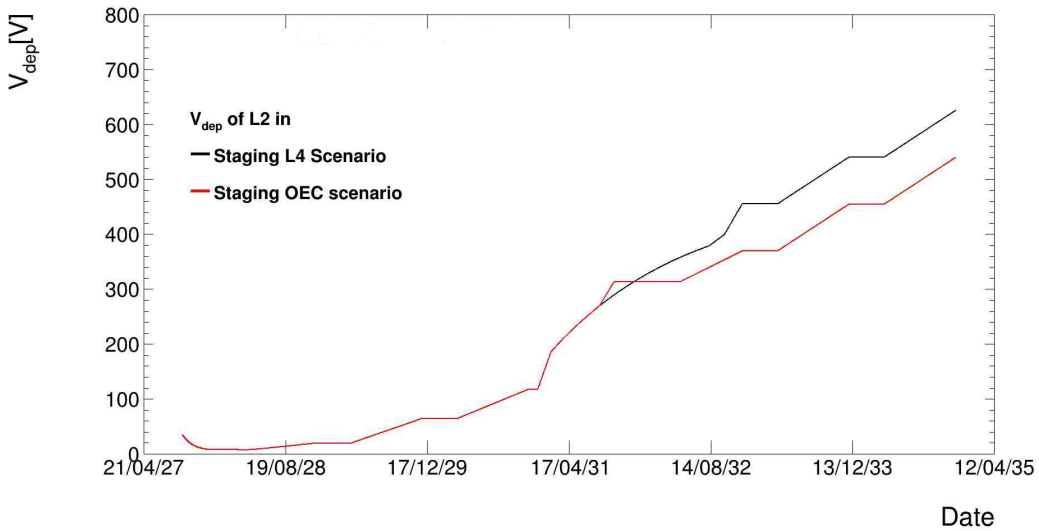

Figure 5.41: Comparison of depletion voltages of Layer-2 (L2) in response to staging Layer-4 (L4) versus the Outer End Caps.

duration in which all layers are kept at room temperature.

End of Lifetime Temperature Scenario with Staging of Layer-4: The

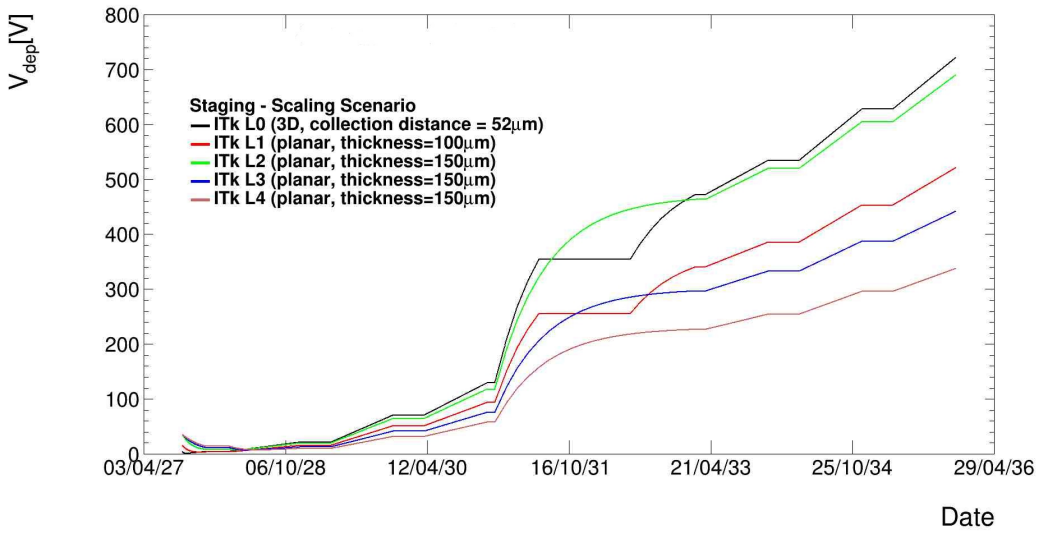

Figure 5.42: Predicted depletion voltage versus date for staging with scaling in Long Shutdown 4 (LS4).

depletion voltage is plotted against the date for the entire HL phase: Run 4 + Long Shutdown 4 with staging of Layer-4 + Run 5 + Long Shutdown 5 + Run 6 for two cases, in Figures 5.43 and 5.44.

Case 1 is the situation in which the Outer System is kept at 25°C for 6 months in Long Shutdown 5. The magnitude of reverse annealing is much higher than that during Long Shutdown 4, due to the fact that the magnitude of reverse annealing depends on the fluence received by the sensors up to that point.

If the Outer System is kept at −20°C in Long Shutdown 5, reverse annealing is effectively frozen out as indicated by the long horizontal line between the years 2035 and 2036.

End of Lifetime Scenario with Staging of the Outer End Caps: The depletion voltage is plotted against the date for the entire HL phase: Run 4 + Long

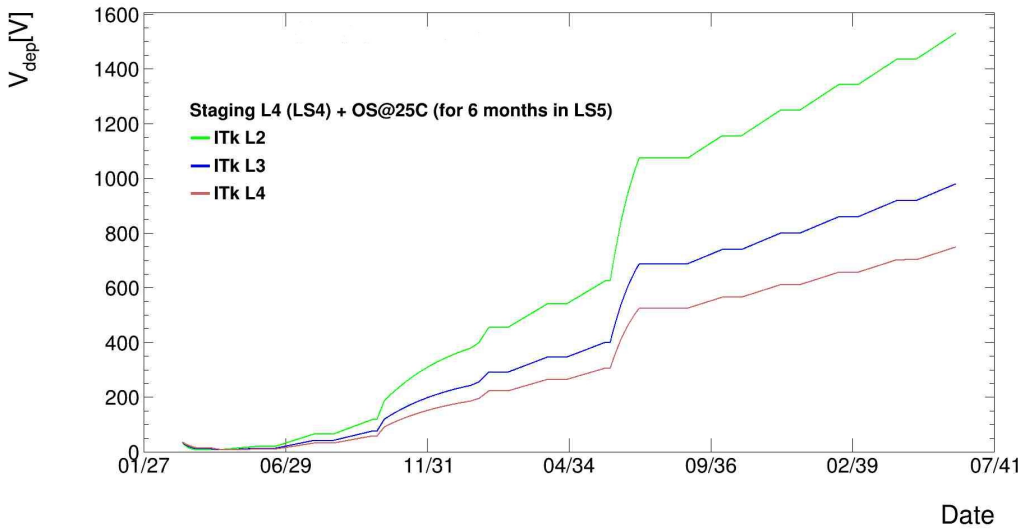

Figure 5.43: Predicted depletion voltage versus date for the Case 1 (see Figure 5.34) End of Lifetime temperature scenario with Staging of Layer-4.

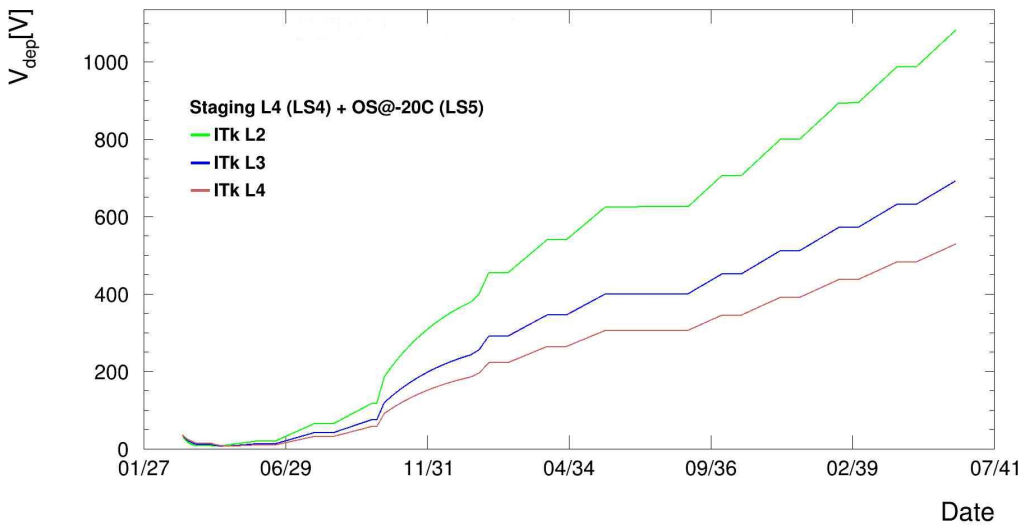

Figure 5.44: Predicted depletion voltage versus date for the Case 2 (see Figure 5.35) End of Lifetime temperature scenario with Staging of Layer-4.

Shutdown 4 with staging of the Outer End Caps + Run 5 + Long Shutdown 5 + Run 6, for two cases, in Figures 5.45 and 5.46 respectively.

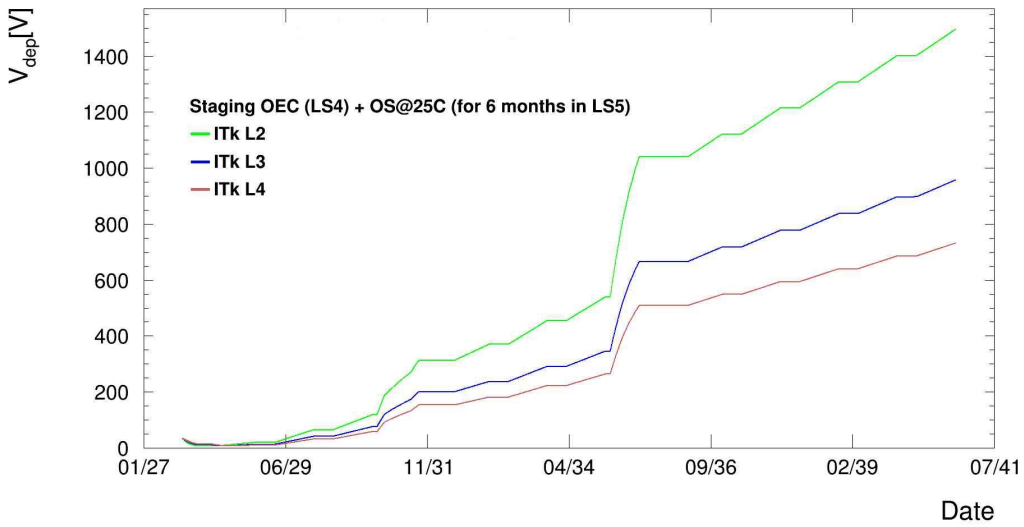

Figure 5.45: Predicted depletion voltage versus date, for the Case 1 (see Figure 5.36) End of Lifetime temperature scenario with Staging of the Outer End Caps.

Despite following the less aggressive staging scenario in Long Shutdown 4, the magnitude of reverse annealing during Long Shutdown 5 is the same as in Figure 5.43, as the sensors receive the same fluence and are kept at room temperature for the same duration in Long Shutdown 5 in both staging scenarios.

Reverse annealing is effectively frozen out if the Outer System is kept at -20^{o}C in Long Shutdown 5, leading to lower depletion voltages at the end of Run 6.

Uncertainties in the Results: The dominant uncertainty in these predictions comes from the Hamburg Model parameters and is about 20% [173]. The uncertainties in the luminosity to fluence conversion factors are about 10% [186].

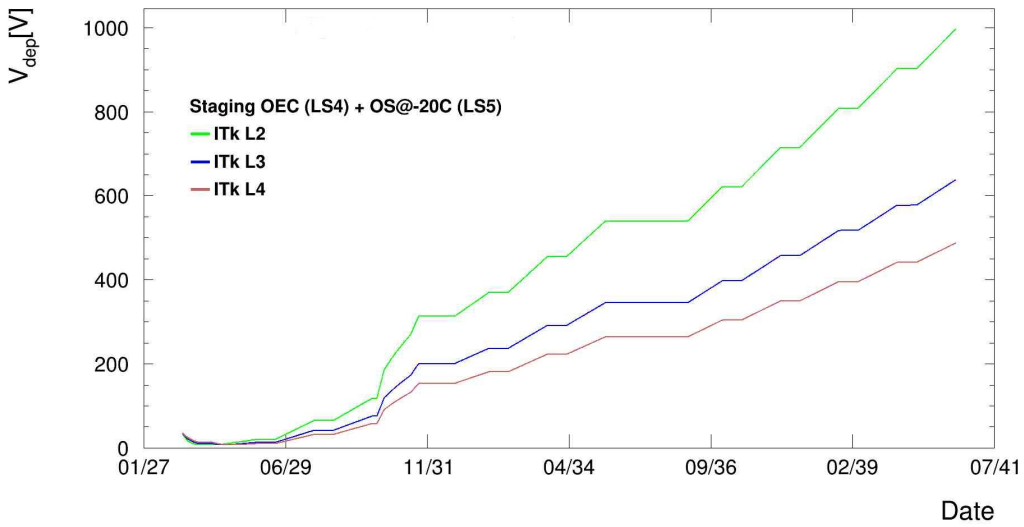

Figure 5.46: Predicted depletion voltage versus date, for the Case 2 (see Figure 5.37) End of Lifetime temperature scenario with Staging of the Outer End Caps.

5.4.5 Summary of Simulation and Staging Recommendations

Depletion voltages for various staging scenarios in Long Shutdown 4 were studied. The predicted depletion voltages and integrated fluences for each layer at the end of Run 5 are given in Table 5.10.

Layer	Fluence Received (1 MeV n_{eq} cm^{-2})	V_{dep}(V) (with Staging of Layer-4)	V_{dep}(V) (with Staging of Outer End Caps)	V_{dep}(V) (with Staging with Scaling)
L0	9.0×10^{15}	554	554	721
L1	1.8×10^{15}	400	401	521
L2	9.9×10^{14}	625	540	690
L3	6.3×10^{14}	400	345	441
L4	4.8×10^{14}	306	264	337

Table 5.10: The predicted depletion voltages and integrated fluences received at the end of Run 5 for each layer, following three staging scenarios.

The depletion voltages for the Inner System layers at the end of Run 6 following

Staging with scaling are about 30% higher compared to the other two staging scenarios. For the Outer System, the depletion voltages are lowest at the end of Run 6 following Staging of the Outer End Caps. The depletion voltages for the Outer System at the end of the High Luminosity phase of Run 6 following the Staging of Layer-4 are shown in Table 5.11.

Layer	Fluence Received (1 MeV n_{eq} cm^{-2})	V_{dep}(V) (Outer System at 25°C for 6 months in Long Shutdown 5)	V_{dep}(V) (Outer System at −20°C in Long Shutdown 5)
L2	2.3×10^{15}	1529	1081
L3	1.5×10^{15}	979	692
L4	1.1×10^{15}	748	529

Table 5.11: The predicted depletion voltages and integrated fluence received at the end of Run 6 for each layer.

The temperature at which the highly irradiated Outer System is kept during Long Shutdown 5 has a significant impact on the depletion voltages in Run 6. At the end of Run 6, there is approximately 145% increase of the depletion voltages predicted for all layers at the end of Run 5 if the Outer System is kept at 25°C for 6 months during Long Shutdown 5. If it is kept at −20°C in Long Shutdown 5, there is about 73% increase.

The depletion voltages for the Outer System at the end of the High Luminosity phase of Run 6 following the Staging of the Outer End Caps are shown in Table 5.12.

At the end of Run 6, there is an approximately 177% increase of the depletion voltage predicted in all the layers at the end of Run 5 if the Outer System is kept at 25°C for 6 months during Long Shutdown 5. If it is kept at −20°C in Long Shutdown

Layer	Fluence Received (1 MeV n_{eq} cm^{-2})	V_{dep}(V) (Outer System at 25°C for 6 months in Long Shutdown 5)	V_{dep}(V) (Outer System at −20°C in Long Shutdown 5)
L2	2.3×10^{15}	1495	996
L3	1.5×10^{15}	957	638
L4	1.1×10^{15}	731	487

Table 5.12: The predicted depletion voltages and integrated fluence received at the end of Run 6 for each layer.

5, there is about an 84% increase. To improve the accuracy of these predictions, it is recommended that the introduction rates be obtained from fits to the data from irradiated ATLAS sensors in early Run 4.

Chapter 6

Quality Assurance of the Next Generation ATLAS Detector

6.1 Introduction

The statistical precision of measurements of the CP-violating phase and associated parameters using $B_s^0 \to J/\psi\phi$ decays and lifetime measurements of B-mesons greatly improve if more data are collected. For this, the HL-LHC is planned to start operating in 2029. During its lifetime, ATLAS will collect about seven times more data than it did during the LHC's operation. The HL-LHC will achieve unprecedented levels of instantaneous and integrated luminosities. To cope with the increased data rates and fluences, ATLAS will undergo an upgrade. The ATLAS Collaboration aims to build the largest silicon detector ever made. The goal is to improve precision to deal with the expected high pileup conditions. The Inner Tracker (ITk) Pixel detector [40], which consists of five barrel layers, will replace the current ATLAS Pixel detector.

The innermost layer will be located 3.5 cm from the HL-LHC beamline. The two innermost layers will be designed to collect an integrated luminosity of 2000 fb^{-1}. As a consequence, each of these layers will receive about 10 times higher fluence than any other fully operational silicon detector ever has. The previous chapter discussed in detail how the fluence affects the leakage current and depletion voltage in the current ATLAS Pixel detector and how fluences affect the depletion voltages that will be necessary for operating the ITk Pixel sensors, for each of several installation scenarios. This work is important for the development of the new ATLAS ITk detector. The ITk construction requires strict quality assurance, because of the high radiation hardness and data throughput demands.

6.2 Construction of the ITk Pixel Detector

This research focuses on the assembly process and quality assurance of the outermost three layers - Layer-2, Layer-3 and Layer-4 - of the ITk Pixel Detector. The fundamental unit of the ITk Pixel detector is the module. An ITk Pixel module is a hybrid pixel module comprised of two parts – a passive high resistivity silicon sensor and a front-end read-out chip fabricated in CMOS technology, together called a bare module. An example bare module can be seen in the microscope image in Figure 6.1. The is combined with a flexible printed circuit, called a module flex. The RD53A prototype [188] readout chip, which was co-developed with CMS, is being used for further studies. Meanwhile, the first versions of the final readout chip ITkPixV1 are being tested to prepare for the final version ITkPixV2 [189].

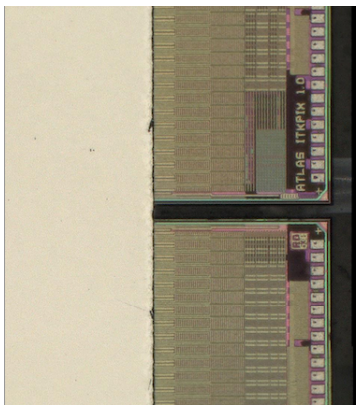

Figure 6.1: An RD53A bare module showing the edges of two read-out chips and the silicon sensor.

The silicon sensor and front-end read-out chip are joined using a high density connection technique called flip-chip bump-bonding as is shown in Figure 6.2.

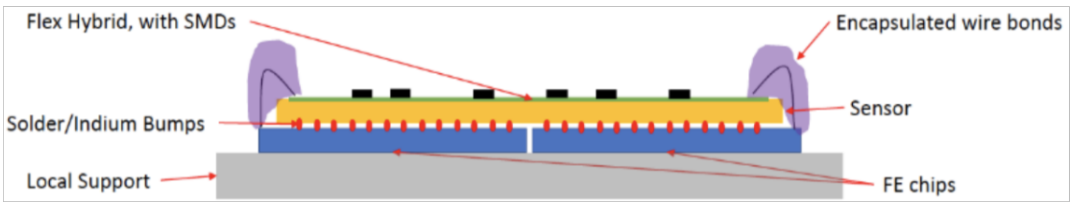

Figure 6.2: A sketch illustrating the parts of an ATLAS-ITk pixel module [190].

The sensor volume produces the signal from particles that pass through it and transmits it to the readout electronics via the bump-bond. The modules come in three types, based on how many front-end read-out chips are bump-bonded to a silicon sensor. They are: (i) quad modules with four chips, (ii) dual modules with two chips, and (iii) single chip modules. The module flex, which is attached to the back side of the sensor, connects the bare modules to the active elements for clock and command input, data output, low voltage and sensor high voltage. A schematic diagram of the assembly of an ITk Pixel quad module is shown in Figure 6.3.

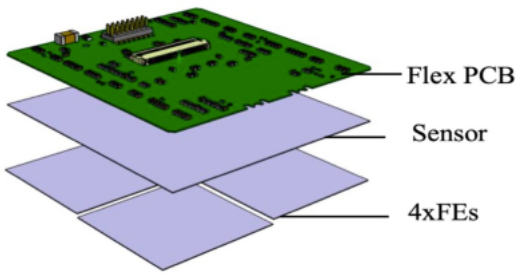

Figure 6.3: An exploded view of the schematics of an ITk quad module [191].

The module flex provides an interface between operator and detector, enabling tasks such as calibration, commissioning, and data taking through the Data Control System (DCS) network [192]. For module temperature monitoring, a temperature sensor is connected to the DCS chip which is a part of the module flex. The pixel modules will be placed on the local support which provides mechanical support, alignment, routing services and thermal management, with the back side of the front-end chips in contact with the support. This interface is part of the thermal path between the module and the cooling fluid.

Quality control and assurance were carried out at various stages of production as follows:

- Tests at wafer level: The sensors' leakage current and depletion voltage are measured before and after irradiation to test their radiation hardness. Other tests will also check their long term stability and inter-pixel capacitance and bulk resistance.

- Tests on pixel bare modules: Visual inspection and metrology of the assemblies, sensor leakage current and depletion voltage measurements, verification of front-end read-out chip functionalities and determination of bump-bond connectivity

using a probe station will be performed.

- Tests on assembled pixel modules: Module tests such as the sensor IV test using a probe station, electrical tests of chip functionality, source tests for bump-bond quality as well as thermal cycles and long-term tests at the expected operational temperature at $-25°C$ as measured on the temperature sensor on the module flex, will be performed. The most important module tests are the electrical tuning and performance tests. These consist of the fine tuning of the pixel threshold and charge response followed by noise, cross-talk and minimum threshold measurements. The results of these tests will be compared to the specifications, and performance figures of merit will be derived which will be used for the evaluation and ranking of modules. This ranking will be done in terms of the number of non-working pixels per module. Modules with a certain percentage of non-working pixels are rejected. The modules with the lowest number of non-working pixels can be selected for use in the innermost layers. If necessary, selection cuts for other detector areas can be defined to ensure that the best pixel modules will be used in the most sensitive detector areas. Entire procedures will be evaluated, improvements applied, and rejection and selection cuts will be adjusted according to the results obtained. In addition, these measurements will be used to monitor the performance of the module after it is mounted on local supports and installed in the global supports which connect the Pixel detector with the other parts of the ITk.

6.3 Metrology and Mass Measurements

6.3.1 Equipment and Precision

Since the assembly of the Pixel modules using bare modules and flexes is an extremely delicate process, the dimensions of the bare modules and flexes need to be measured prior to the assembly to ensure a precise alignment between the components in a Pixel module. In addition, since the amount of glue applied between a flex and a bare module in a Pixel module needs to be consistent and can only be extracted if the mass of individual components are measured first. For this purpose, the mass of all flexes and bare modules were measured first prior to the assembly.

The metrology measurements were done for the flex and bare modules using the Vertex-261 instrument, manufactured by Micro-Vu. The Vertex 261 [193], shown in Figure 6.4, is a table top system equipped with a high-resolution camera-based measuring system that produces fast, accurate measurements on a wide variety of parts.

For stability, the equipment is placed on a platform made of granite. The Vertex-261 instrument can take clear pictures with adjustable optical and digital zoom. It can also measure small and complex shapes with touch probes. The machine can be programmed through InSpec Metrology Software.

The first step for measuring ITk flexes, bare modules and assembled modules was to understand the machine's precision in the X, Y and Z directions. For this purpose, the Si dummy in Figure 6.5, that has the dimensions of a bare module, was used.

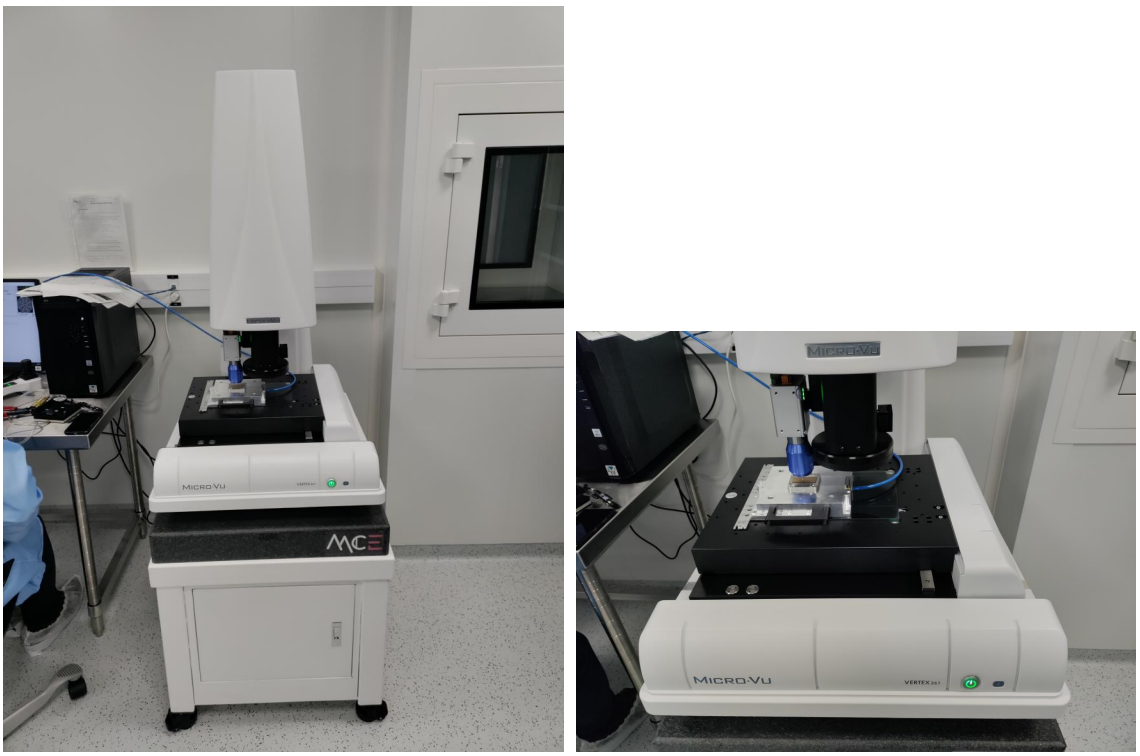

Figure 6.4: The Vertex-261 used for metrology measurements of the ITk flex, bare modules and assembled modules.

To measure the precision in the X, Y and Z directions, each dimension was measured 10 times, and the standard deviation was calculated. The precisions of the measurement along the X and Y directions are shown in Figures 6.6 and 6.7, respectively.

The machine has two options for measuring the Z direction: camera or laser, and for both options, a measurement in the Z direction was made 10 times. The precisions of the measurements along the Z direction using camera and laser are shown in Figures 6.8 and 6.9, respectively.

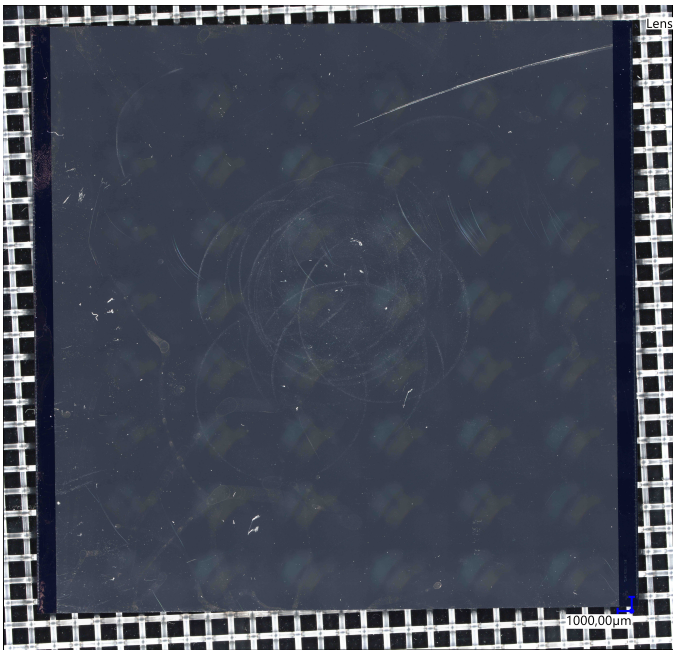

Figure 6.5: A Si dummy used for finding the precision of the metrology equipment.

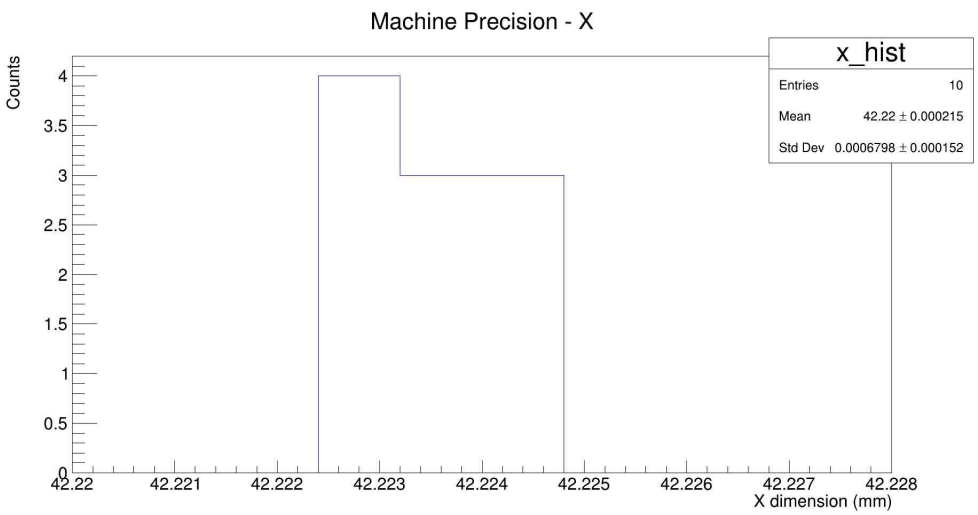

Figure 6.6: The precision of a measurement by the Vertex-261 metrology machine along the X-direction.

As can be seen from Figures 6.6 and 6.7, the precision of measurements along X and Y are 0.7 μm and 0.9 μm, respectively. As shown in Figures 6.8 and 6.9,

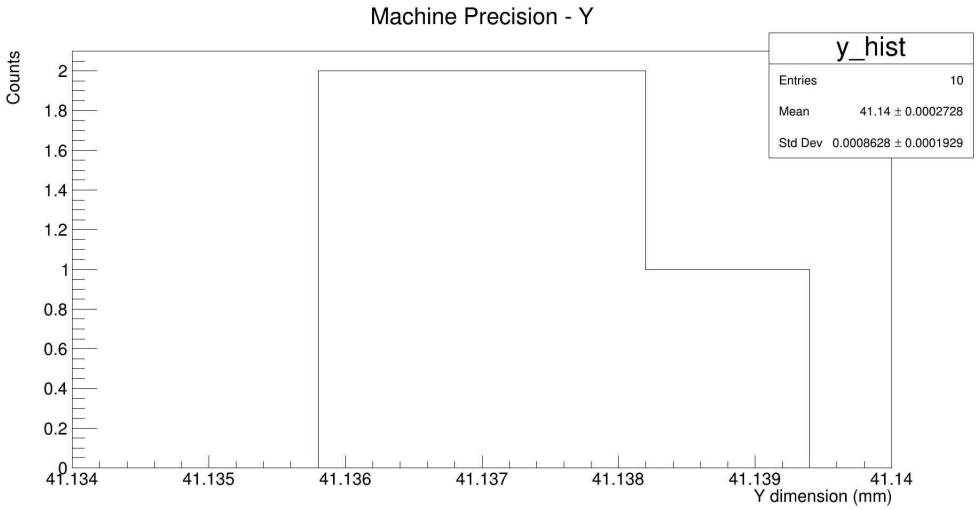

Figure 6.7: The precision of a measurement by the Vertex-261 metrology machine along the Y-direction.

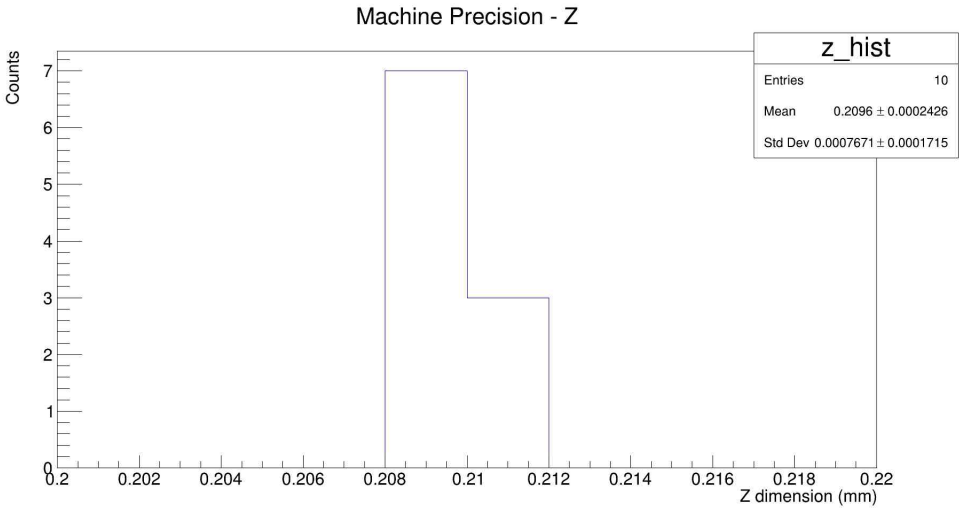

Figure 6.8: The precision of a measurement by the Vertex-261 metrology machine along the Z-direction using camera.

the precisions of the Z-measurements by camera and laser are 0.7 μm and 0.4 μm, respectively. Since the measurement using the laser offers higher precision, all the measurements for the thickness of flexes, bare modules and assembled modules were done using the laser.

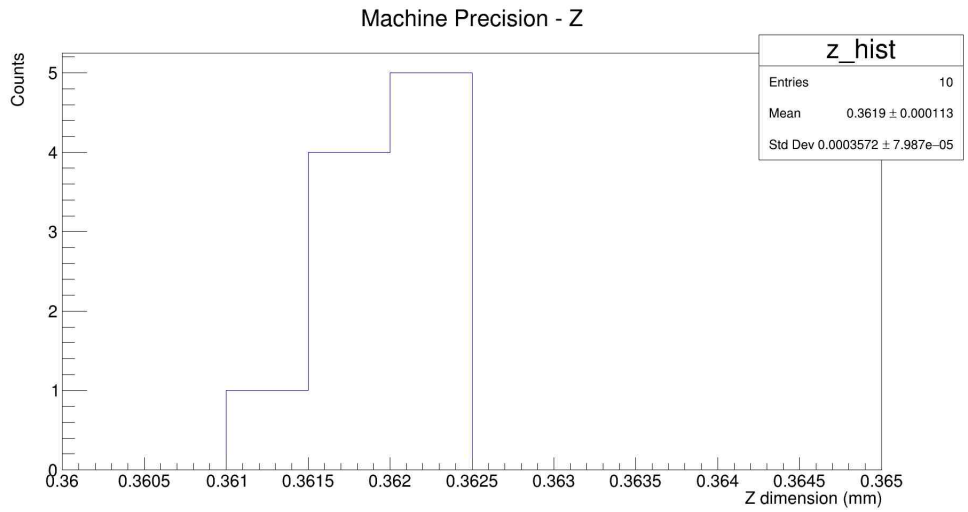

Figure 6.9: The precision of a measurement by the Vertex-261 metrology machine along the Z-direction using the laser.

For measuring the mass of the flexes, bare modules and assembled modules, a scale shown in Figure 6.10, manufactured by Steinberg Systems, SBS-LW-300A [194], was used.

To understand the precision of the scale, the Si dummy was weighed ten times, and the results were then plotted as a histogram as shown in Figure 6.11.

As can be seen from Figure 6.11, the standard deviation of all ten measurements is approximately 0.001 g which is consistent with the accuracy given in the technical specifications of this scale [194].

6.3.2 Metrology of Flexes

The loaded flex that is used for the assembly of the ITk Pixel modules is shown in Figure 6.12. The measurements were done with the flex under vacuum to immobilize

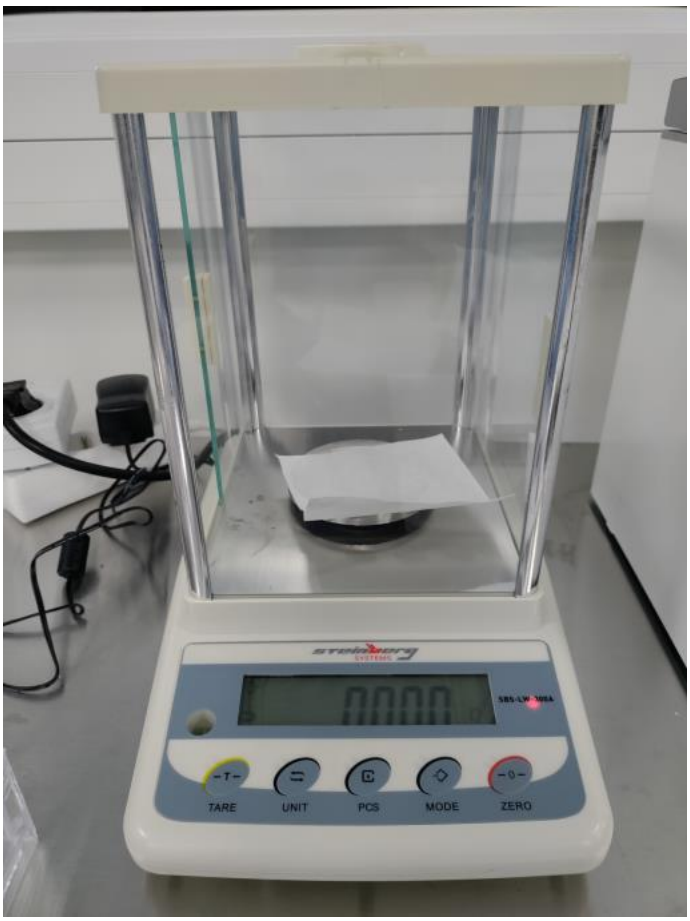

Figure 6.10: The scale used at IJCLab - SBS-LW-300A from Steinberg Systems.

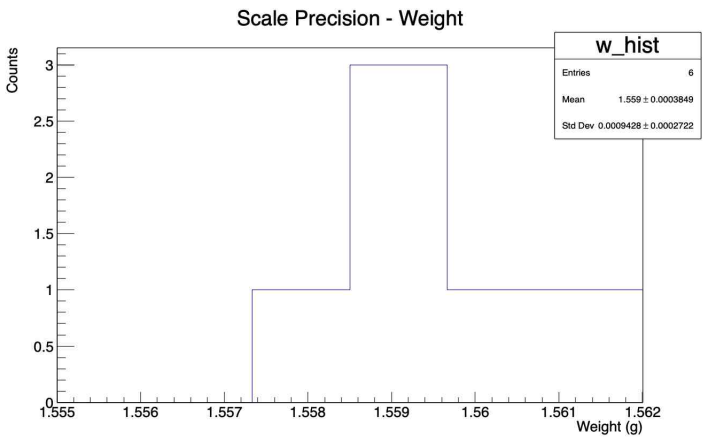

Figure 6.11: The precision of a measurement by the weighing scale.

during the measurements.

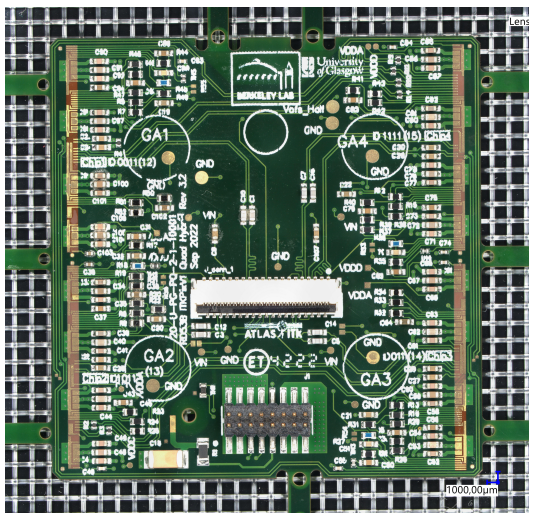

Figure 6.12: A loaded flex that is used for the ITk Pixel assembly.

Ideally, the flex should be placed on a vacuum chuck with the components facing down, as is done with the assembly tooling (vacuum chuck with cut outs). However, the vacuum chuck with cut outs was unavailable and as an intermediate solution, the flex jig/inlay of the assembly tool was used. A flex jig shown in Figure 6.13 from the previous version of the ITk Pixel assembly tool was used at IJCLab for taking metrology measurements. The flex jig was compatible with the current version of the flex, since they had similar layouts.

The following quantities were measured on the loaded flex using the Vertex-261.

- X-dimension - from one edge of the flex to the other edge in the X direction,
- Y-dimension - from one edge of the flex to the other edge in the Y direction,
- Z-dimension - thickness of the flex at the power connector excluding the pins,

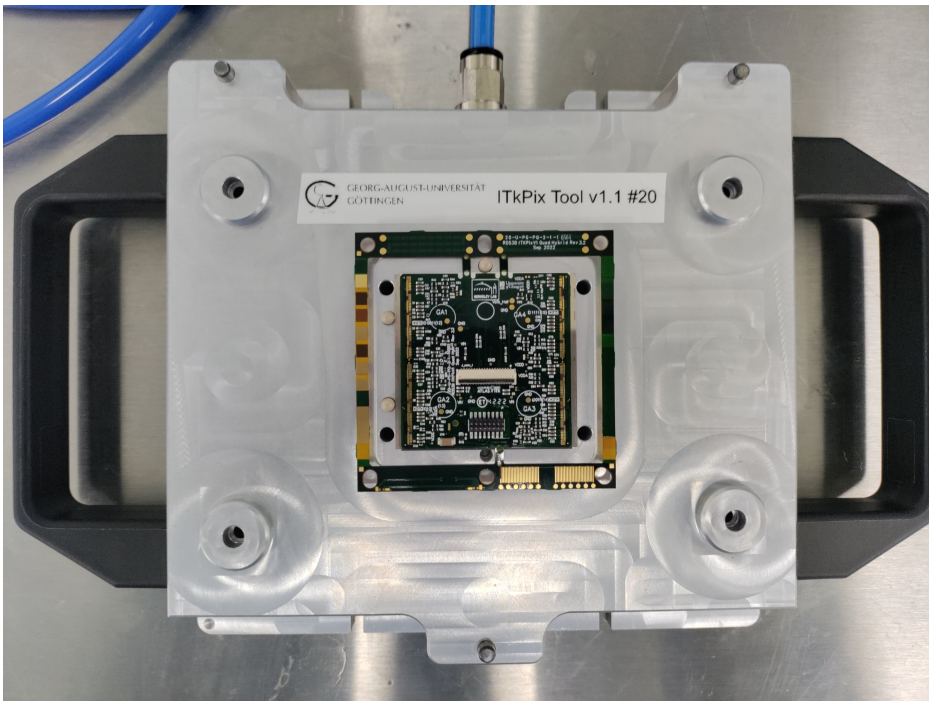

Figure 6.13: A loaded flex being held under vacuum on a flex jig prior to metrology measurements on the Vertex-261.

- Z-dimension - thickness of the flex at the HV capacitor, and
- Z-dimension - average thickness of the flex at four pickup areas (labelled on the flex as GA1, GA2, GA3 and GA4) along with the standard deviation of the measurements.

These measurements are shown in Figure 6.14.

To ensure accuracy, the Vertex-261 was programmed to measure the following quantities in these ways:

- to measure the width of the flex along the X- and Y-dimensions, parallel lines were drawn along both edges, and the average distance between them was

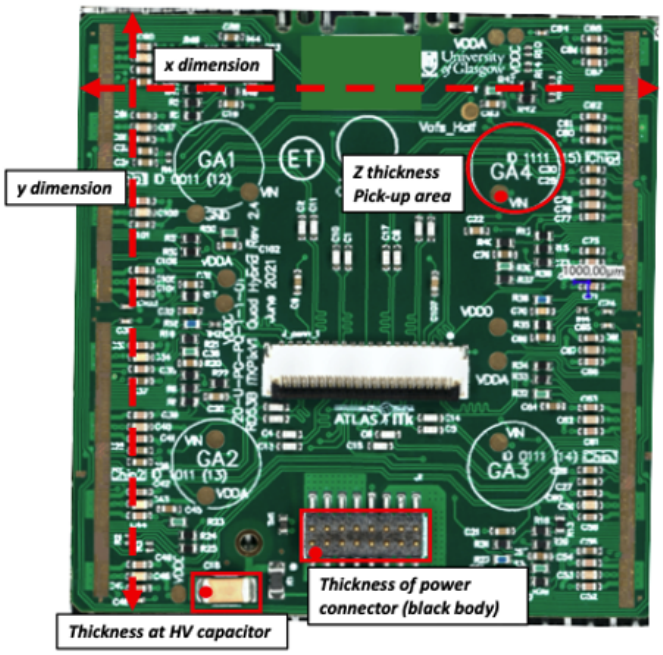

Figure 6.14: Quantities to be measured for the ITk Pixel flex using the Vertex-261.

calculated,

- the average flex height at the HV capacitor and the power connector was calculated first by taking eight measurements at each part. The height of the flex jig was measured eight times at different points, and the average of this quantity was then subtracted from the average flex height at each part. This gave the average flex thickness at the HV capacitor and the power connector, and

- the average flex thickness at the pickup areas was calculated first by taking the average of the eight height measurements made at each pickup area. The Vertex-261 then subtracted the average jig height from the average flex height. This gave the average flex thickness at the pickup areas. The standard deviation

of these average measurements was also recorded.

A total of 28 flexes were measured, and the detailed results can be found in Appendix C. The averages of the measured quantities are shown in Table C.1. Table 6.2 shows the expected range of dimensions of the ITk Pixel flex.

Mass (g)	X (mm)	Y (mm)	AVG GA thickness (mm)	STD DEV GA (mm)	AVG thickness - Power Connector (mm)	AVG thickness - HV Capacitor (mm)
1.585	39.582	40.562	0.208	0.003	1.547	1.912

Table 6.1: Average metrology and mass measurements of 28 ITk Pixel flexes.

Quantity	Expected Range (mm)
X	39.5-9.6
Y	40.5-40.7
Pickup Area Thickness	0.2-0.3
Power Connector Height	1.521-1.761
HV Capacitor Height	1.701-2.111

Table 6.2: Expected metrology values for the ITk Pixel flex.

From Tables C.1 and 6.2, it can be seen that the average quantities of all 28 samples are within specifications. However, some samples had dimensions that were out of the specifications. For example, the width along X of flex ID 0046 exceeded the specifications by 500 μm.

6.3.3 Metrology of Silicon Dummies and Bare Modules

The metrology measurements of silicon (Si) dummies and bare modules were performed using the Vertex-261 instrument. The Si dummies are used to develop and test the

assembly and wire bonding procedures that will be used to build the final detector; they have similar dimensions to the bare module. Figure 6.5 shows a sample Si dummy used for the assembly. Figure 6.15 shows a sample bare module used for the assembly.

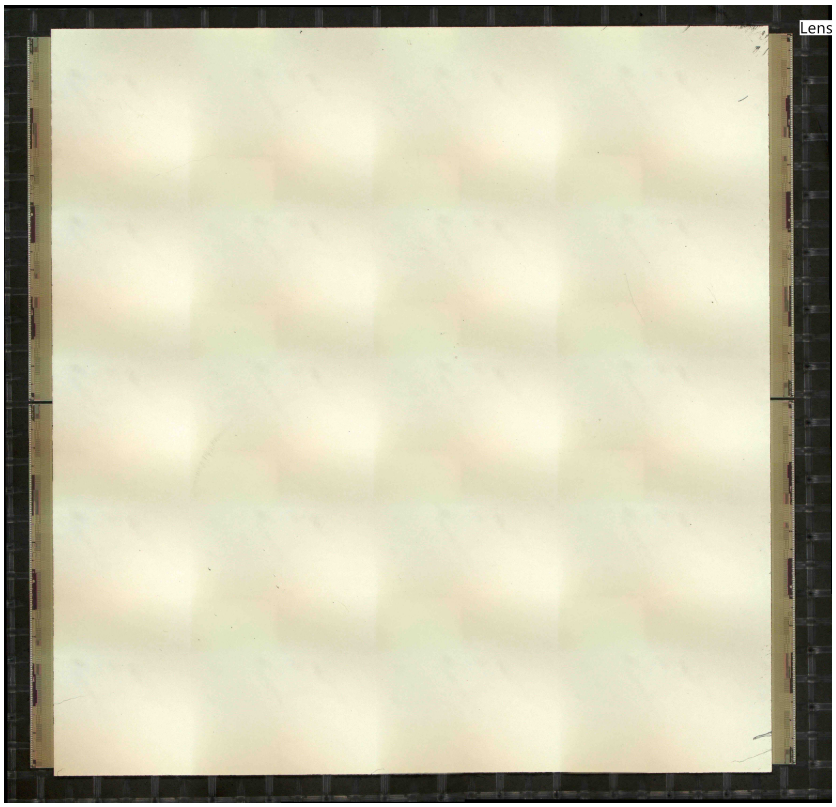

Figure 6.15: A bare module that is used for the ITk Pixel assembly.

The measurements were done with the Si dummy and bare module under vacuum to immobilize it during the measurements, and for this purpose, the module jig of the assembly tool was used as is shown in Figure 6.16.

The following quantities were measured on the Si dummies and bare modules using the Vertex-261.

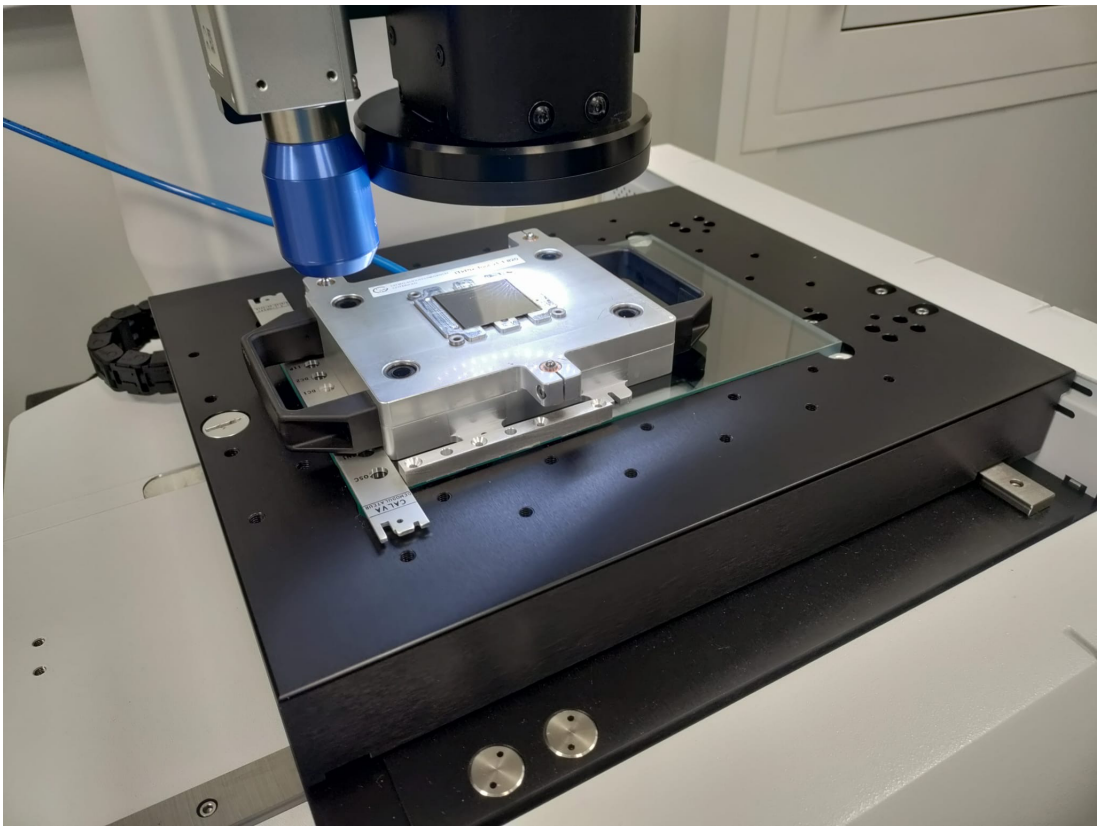

Figure 6.16: A Si dummy that is used for the ITk Pixel assembly, held under vacuum on the Vertex-261 instrument.

- X-dimension - from one edge of the Si dummy to the other edge in the X direction. For a bare module, the distance between the two front end (FE) chips measured from their outer edges in the X direction and the distance between the two edges of the sensor in the X direction,

- Y-dimension - from one edge of the Si dummy to the other edge in the Y direction. For a bare module, the distance between the two FE chips measured from their outer edges in the Y direction and the distance between the two edges of the sensor in the Y direction,

- Z-dimension - average thickness of the Si dummy at the edges where the wire

bond pads are located,

- Z-dimension - average thickness of the FE chips on the bare module,
- Z-dimension - average thickness of the bare module. This corresponds to the combined thickness of the sensor, FE chips and wire bonds in between them,
- X-dimension - distance of the fiducial markers (F1, F2, F3 and F4) on the Si dummy and bare module from the nearest edge in the X direction,
- Y-dimension - distance of the fiducial markers on each FE chip (F1, F2, F3 and F4) of the Si dummy and bare module from the outer edge in the Y direction, and
- the distance between two fiducial markers on the Si dummy and bare module.

These measurements for the Si dummy and bare module are illustrated in Figure 6.17 and Figure 6.18.

An illustrative diagram for measuring the distance of a fiducial marker from the nearest edge in the X and Y directions on the Si dummy and bare module is shown in Figure 6.19.

To ensure accuracy, the Vertex-261 was programmed to measure the following quantities in these ways:

- To measure the width of the Si dummy/bare module along the X and Y-dimensions, parallel lines were drawn along both edges, and the average distance between them was calculated.

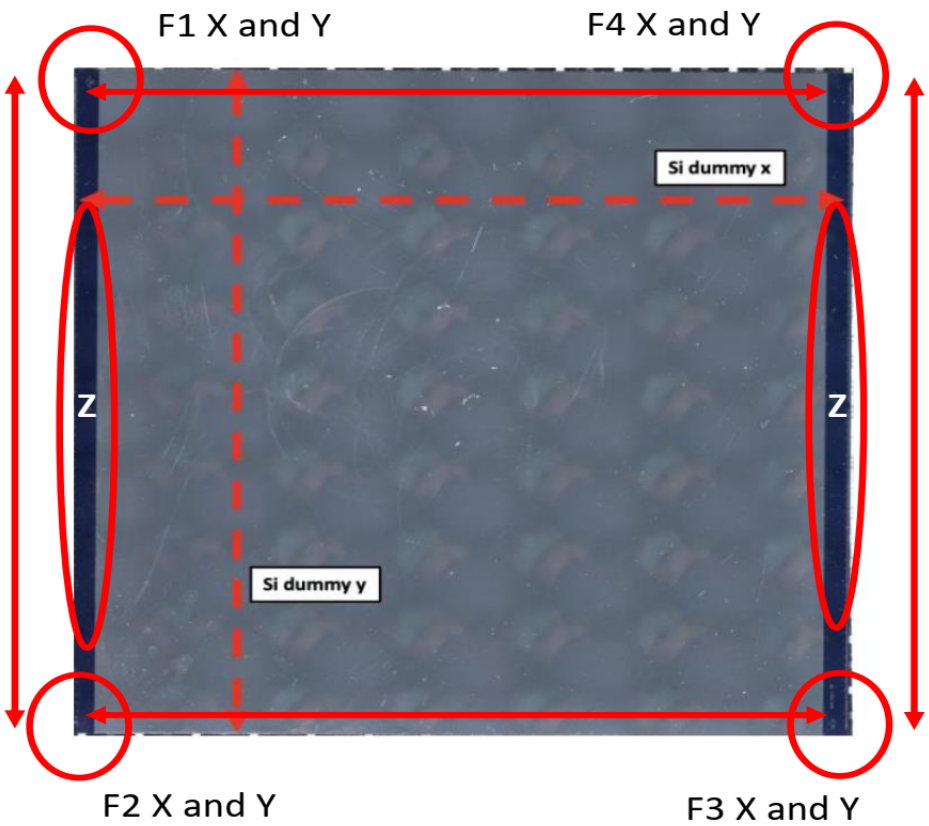

Figure 6.17: Quantities to be measured for the ITk Pixel Si dummy using the Vertex-261.

- The average Si dummy height at two edges was calculated first by taking five measurements at each edge. The height of the flex jig was measured eight times at different points, and the average of this quantity was then subtracted from the average Si dummy height. This gave the average Si dummy thickness at the edge where the wire bond pads are located.

- The distance between the outer edges of the sensor and the FE chips of the bare module on both edges was calculated by drawing parallel lines along both edges and calculating the average distance between them.

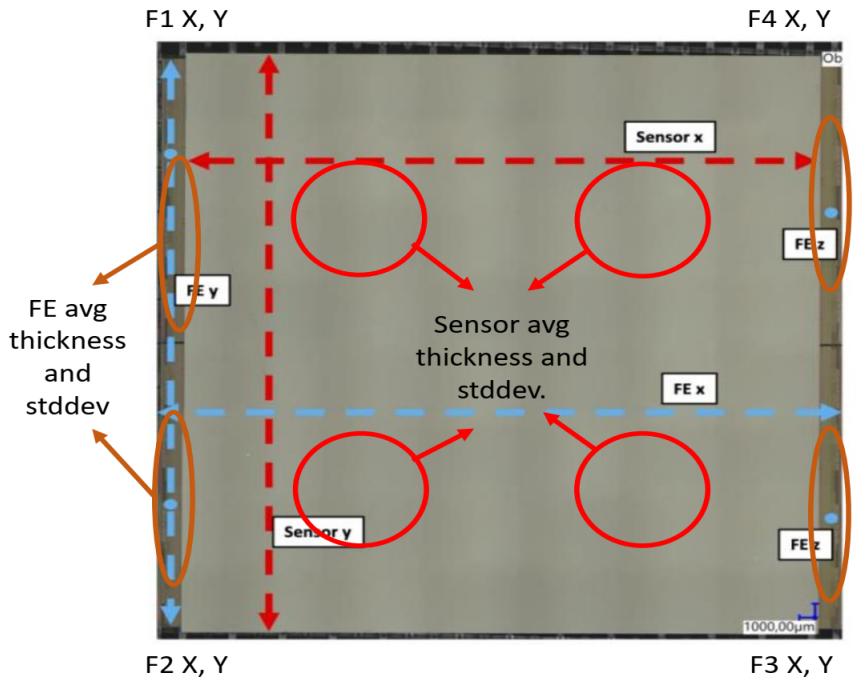

Figure 6.18: Quantities to be measured for the ITk Pixel bare module using the Vertex-261.

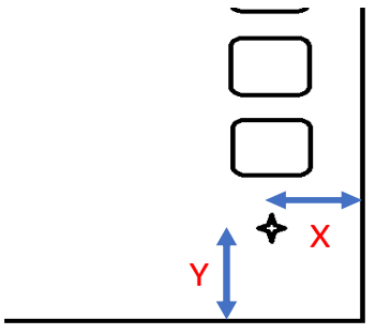

Figure 6.19: A diagram that illustrates the measurements that use the fiducial marker on the ITk Pixel Si dummy/bare module.

- The average height of the four FE chips on the bare module was obtained by measuring the height five times at each FE chip. The height of the flex jig was measured eight times at different points on the jig, and the average value was computed. This value was subtracted from the average height of the four FE

chips. This resulted in the average thickness of the FE chips.

- The average bare module height was calculated first by taking ten height measurements of the bare module in the sensor area. The height of the flex jig was measured eight times at different points, and the average of this quantity was then subtracted from the average bare module height measured at the sensor area. This gave the average bare module thickness.

- The distance in the X and Y directions of a fiducial marker from the outer edge was calculated by detecting the edges and fiducial markers. A similar procedure was used for the distance between two fiducial markers.

A total of 3 Si dummies were measured, and the averages of the widths in the X and Y directions and thickness in the Z direction along with their expected ranges are shown in Table 6.3.

Quantity	Average Value (mm)	Expected Value (mm)
X	42.19	42.19 ± 0.5
Y	41.14	41.1 ± 0.5
Z - thickness	0.315	0.300 ± 0.015

Table 6.3: Measured and expected metrology values for the ITk Pixel Si dummy.

As can be understood from the Table 6.3, the measured quantities are within the specifications. The average mass of all 15 bare modules was measured to be 1.243 g. The metrology measurements for the fiducial markers are shown in Table 6.4.

From Table 6.4, it can be seen that the distance between two fiducial markers along the same edge of the Si dummy is consistent across all 3 samples. The distance between fiducial markers F1 and F2 and the distance between fiducial markers F3

Quantity	Sample 1 - Values (mm)	Sample 2 - Values (mm)	Sample 3 - Values (mm)
Distance between F1 and F2	40.098	40.100	40.096
Distance between F2 and F3	42.039	42.041	42.041
Distance between F3 and F4	40.097	40.098	40.097
Distance between F4 and F1	42.038	42.037	42.036
X distance of F1 from the nearest edge	0.080	0.071	0.069
Y distance of F1 from the nearest edge	0.547	0.527	0.535
X distance of F2 from the nearest edge	0.077	0.066	0.068
Y distance of F2 from the nearest edge	0.509	0.512	0.509
X distance of F3 from the nearest edge	0.120	0.135	0.134
Y distance of F3 from the nearest edge	0.510	0.513	0.513
X distance of F4 from the nearest edge	0.126	0.134	0.138
Y distance of F4 from the nearest edge	0.531	0.531	0.526

Table 6.4: Measured metrology values for the fiducial markers on the ITk Pixel Si dummy.

and F4 are measured in the Y-direction, so they are smaller than the Y-dimension of the Si dummy. Likewise, the distance between fiducial markers F2 and F3 and the distance between fiducial markers F4 and F1 are measured in the X-direction, so they are smaller than the X-dimension of the Si dummy.

The expected values of the X and Y distances of the fiducial markers relative to the outer edge of the FE chips and Si dummies are shown in Figure 6.20.

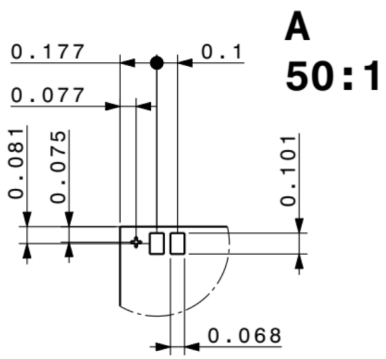

Figure 6.20: Measurements of the fiducial marker and wire bond pad positions relative to the outer edge of the FE chips and Si dummies. The expected values are the same for all bare modules and Si dummies.

From Figure 6.20 and Table 6.4, it can be noted that the positions of the fiducial markers relative to the outer edge are not all within the specifications for all three Si dummies. Further, the fiducial markers on one edge of the Si dummy are much closer to the edge than the fiducial markers on the opposite edge. The uneven placement of the fiducial markers and wire bond pads may pose a challenge for wirebonding the connections from the flex to the FE chips after the flex and bare modules are glued together. Figure 6.21 illustrates the asymmetry of the fiducial markers on the opposite edges of a Si dummy.

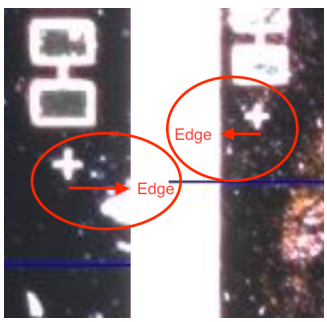

Figure 6.21: The uneven placement of the fiducial markers on opposite edges of the Si dummy.

A total of 15 bare modules were measured, and the averages of the widths in the X and Y directions and thickness in the Z direction along with their expected range are shown in Table 6.5. The expected ranges for most of the quantities in Table 6.5 are shown in Figure 6.22.

Quantity	Average Value (mm)
Sensor X	39.530
Sensor Y	41.152
Chip to chip X	42.222
Chip to chip Y	40.320
FE to sensor - left	1.344
FE to sensor - right	1.348
FE chip thickness	0.163
STDDEV - FE chip thickness	0.005
Bare module thickness	0.329
STDDEV - bare module thickness	0.001

Table 6.5: Measured values for the ITk Pixel bare modules.

As can be seen from Figure 6.22, the sensor dimensions and the chip to chip dimensions in the X and Y directions in Table 6.5 agree with the specifications. The thickness specifications of 325 ± 15 μm and 160 ± 15 μm are met by the FE chips and the bare modules, respectively. The bare module thickness measurement has a much lower standard deviation than the FE thickness measurement, even though the Vertex-261 instrument was programmed to use the laser for both thickness measurements. This could be attributed to the fact that the sensor area is bigger than the FE chip area when the bare module is placed on the Vertex-261 instrument with the sensor facing up to avoid scratches and enable metrology measurements. The average mass of all 15 bare modules was measured to be 1.248 g. The metrology

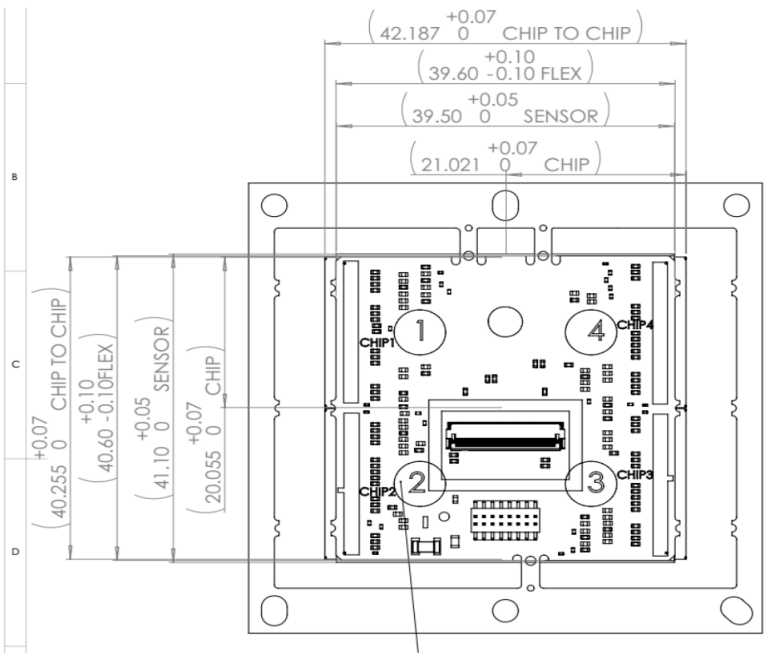

Figure 6.22: The expected ranges for the dimensions of the ITk Pixel bare module [195].

measurements for the fiducial marks are shown in Table 6.6.

The distance between fiducial markers F1 and F2 and the distance between fiducial markers F3 and F4 are measured in the Y-direction, so they are smaller than the chip to chip distance in the Y-direction. Similarly, the distance between fiducial markers F2 and F3 and the distance between fiducial markers F4 and F1 are measured in the X-direction, so they are smaller than the chip to chip distance in the X direction.

However, it can be noted that the positions of the fiducial markers relative to the outer edge are not all within the specifications in Figure 6.20 for all 15 bare modules. This could be attributed to the fact that the fiducial markers on the FE chips of all 15 bare modules were below the resolution of the camera of the Vertex-261 instrument.

Quantity	Average Value (mm)
Distance between F1 and F2	40.079
Distance between F2 and F3	42.029
Distance between F3 and F4	40.074
Distance between F4 and F1	42.000
X distance of F1 from the nearest edge	0.098
Y distance of F1 from the nearest edge	0.113
X distance of F2 from the nearest edge	0.102
Y distance of F2 from the nearest edge	0.112
X distance of F3 from the nearest edge	0.090
Y distance of F3 from the nearest edge	0.127
X distance of F4 from the nearest edge	0.116
Y distance of F4 from the nearest edge	0.116

Table 6.6: Measured metrology values for the fiducial marks on the ITk Pixel bare module.

6.4 Leakage Current Measurements

6.4.1 Equipment

The leakage current measurements on the bare modules were made using the WL-350 semi-automatic probe-station [196] manufactured by Signatone Corporation. The WL-350 probe-station can handle 300 mm wafers and perform reliable and accurate

radio frequency (RF)/direct current (DC)/capacitance-voltage (CV) and high-power thermal test measurements. The equipment has a local enclosure or Faraday cage that is a high performance environmental chamber and provides a light-tight environment for low noise and low capacitance measurements. The chuck used in this probe-station is controlled by an air cooled C300 Low Temp System [197] manufactured by ATT Systems. The C300 can be used to control temperature of the chuck from -60^{o} C to $+300^{o}$ C and to monitor the environmental humidity. In order to keep the air inside the Faraday cage dry, a continuous input of medical grade dry air is supplied to the system. The probe-station can be configured to use up to three needles simultaneously.

A 4200A-SCS Parameter Analyzer [198] semiconductor characterization system (SCS) manufactured by Keithley Instruments is connected to the probe-station. The 4200A-SCS has a modular and customizable design that offers flexibility to choose from different measurement modules, such as source measure units (SMUs), capacitance-voltage units (CVUs), and pulse generators. At IJCLab, the 4200A-SCS is configured to use two 4200 SMUs [198] for sensor IV measurements with bias voltage ranging from -200 V to $+200$ V and one 4210 CVU [199] for sensor CV measurements in the frequency range of 1 kHz to 10 MHz. A Keithley 4200A-CVIV Multi-Switch [198] is also connected to the probe-station; it allows switching between current-voltage (IV) and CV measurements without changing the cables or connections to the device under test (DUT). Another dedicated sourcemeter 2636B [200] from Keithley Instruments is also connected to the probe-station. The probe-station and associated equipment connected to it are shown in Figure 6.23.

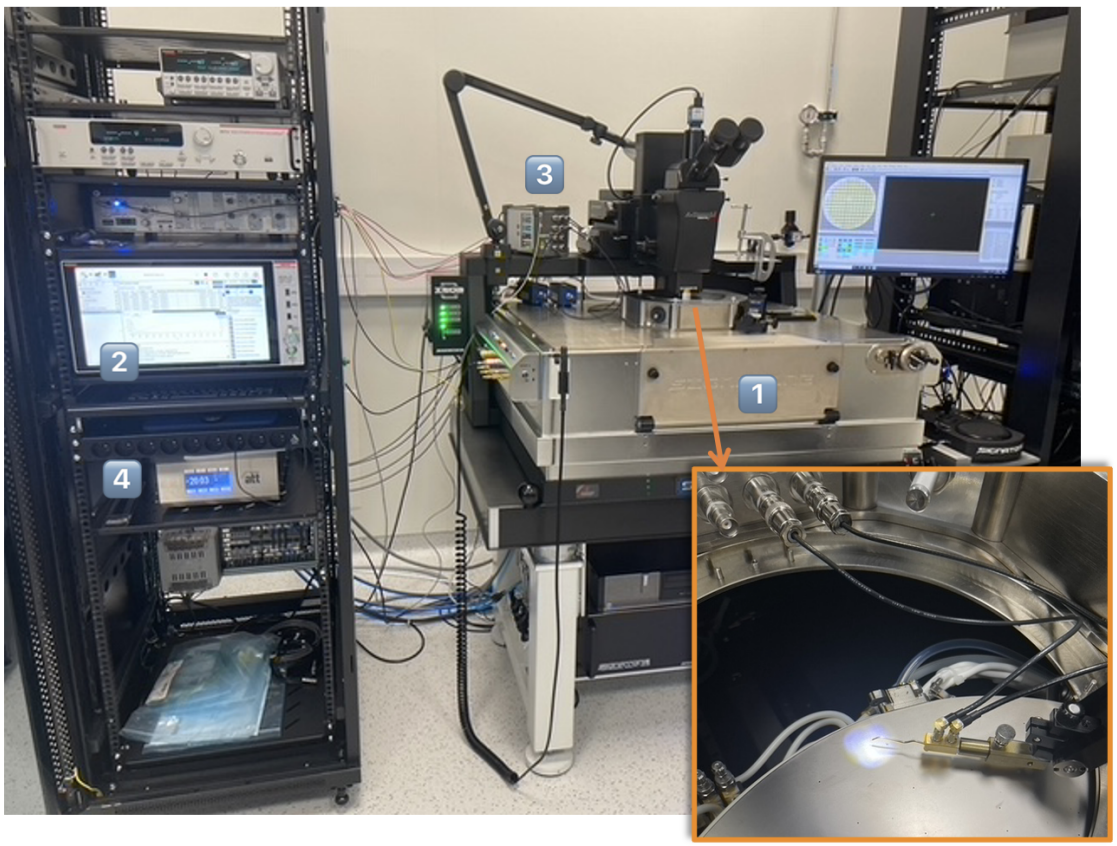

Figure 6.23: The setup used to measure electrical characteristics of the ITk Pixel sensors at IJCLab - (1) Signatone WL-350 probe-station, (2) Keithley 4200A-SCS Parameter Analyzer, (3) Keithley 4200A-CVIV Multiswitch and (4) ATT Low Temp System C300. In the insert, the probe or needle and chuck used are shown.

6.4.2 The IV Measurement on Bare Modules

The leakage current was measured for the unirradiated ITk Pixel quad bare modules using the probe-station. The following steps were taken to perform an IV scan for the samples:

- The bare module was placed on the probe-station chuck with the sensor on the bottom and FEs on top.

- Only one probe was used. This probe was made to touch the probe pad for ground either in between two FE chips or at the corner of the sensor as shown in Figure 6.24.

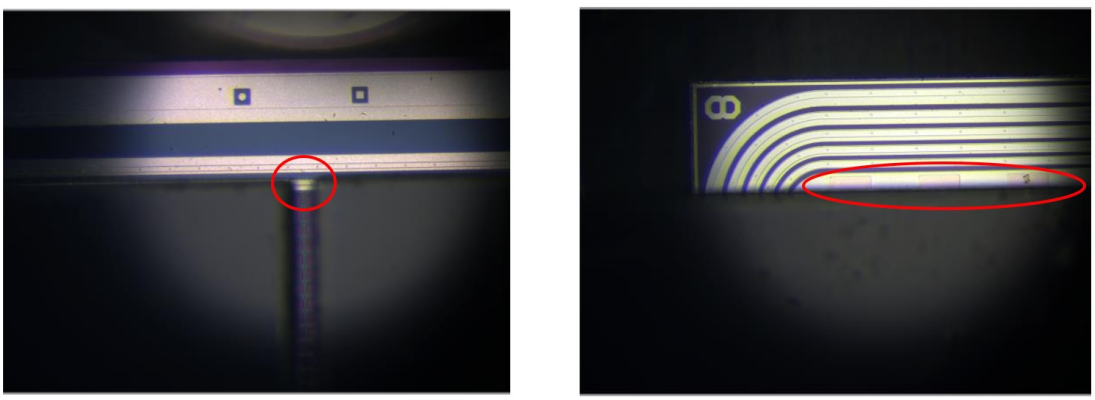

(a) In between two FE chips. (b) At the corner of the sensor.

Figure 6.24: The position of the ground probe pads used for the ITk Pixel bare module IV measurements.

- The chuck was connected to the HV. The biasing rails, to which probes were connected, were connected to ground.
- The temperature of the chuck and the clean room was set to 20° C, so that the results could be compared to previous tests.
- The relative humidity (RH) was measured from the dew temperature of the chuck and was ensured to be less than 50% to avoid condensation.
- The IV scan was performed by applying a voltage from 0 V to −200 V in steps of −5 V to the back side of the sensor of the ITk Pixel quad bare module via the chuck.
- An average of ten measurements was taken.

- A delay of two seconds after changing the bias voltage was used to attain stability in the leakage current measurements.

The leakage current for a total of two batches - April and May 2023, each containing 9 bare modules with unirradiated sensors, was measured and was compared to the results of their IV scan made at sensor level, prior to the assembly of the bare module. The leakage current measurements of the bare modules of the April and May 2023 batches are shown in Figures 6.25 and 6.26, respectively.

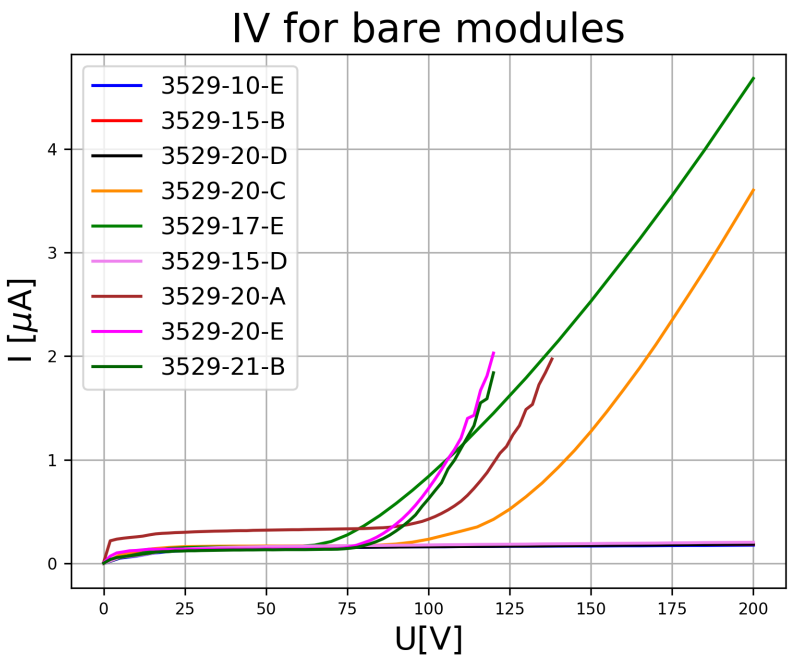

Figure 6.25: The leakage current measurements versus applied bias voltage of nine bare modules in the April 2023 batch.

From Figures 6.25 and 6.26, the following observations can be made:

- Eight out of eighteen bare modules show an early breakdown voltage below 125 V.

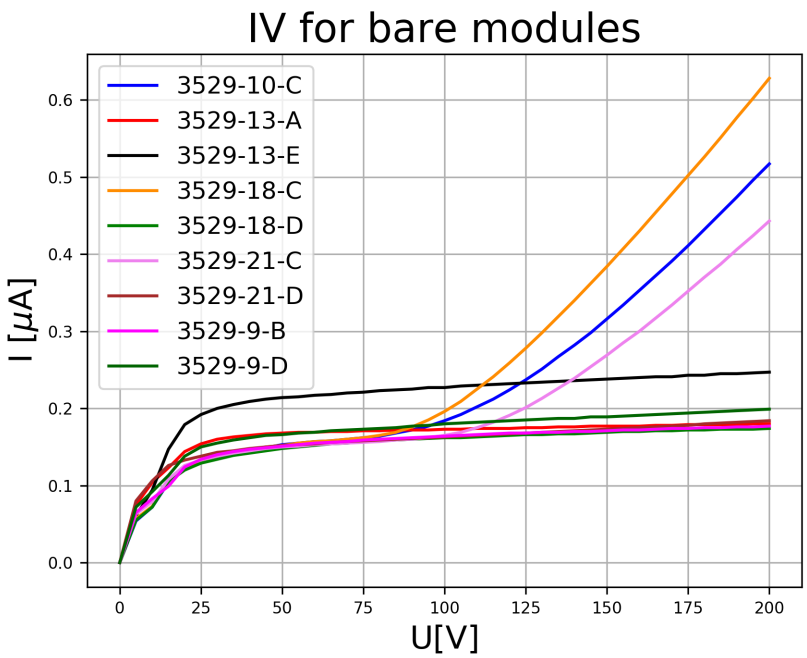

Figure 6.26: The leakage current measurements versus applied bias voltage of nine bare modules in the May 2023 batch.

- One bare module, 3529-17-E, in Figure 6.25 has a breakdown voltage below 75 V. The leakage current at the breakdown voltage is 0.276 μA.

- The bare module 3529-13-E shows higher leakage current (over 0.2 μA) from the beginning of the measurement among working modules despite the fact that all modules were unirradiated and all had their leakage current measured at 20^{o} C.

These IV measurements made at the bare module level are then compared to the IV measurements at the sensor level. Figure 6.27 provides an example.

As can be seen from Figure 6.27, the leakage current measured at the sensor level is approximately 450% higher than that measured at the bare module level.

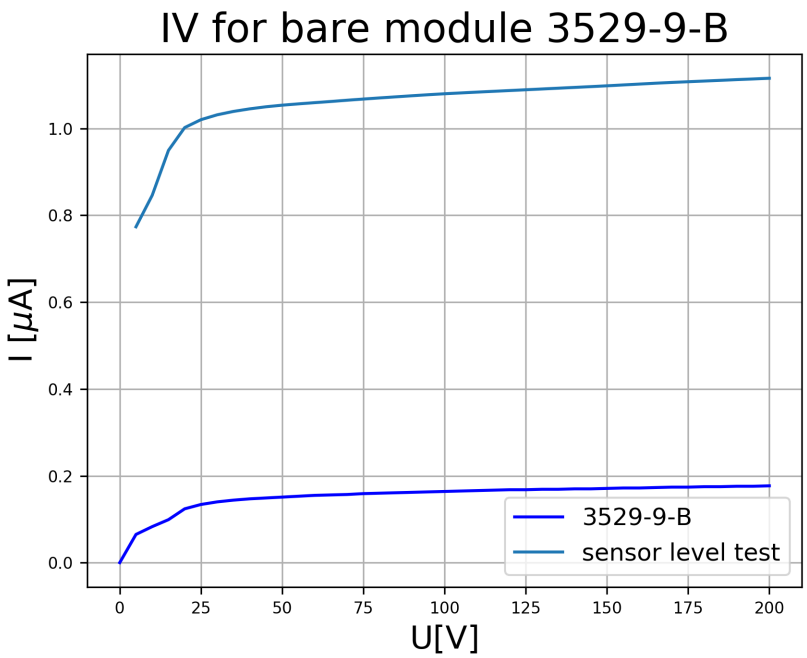

Figure 6.27: A comparison of leakage current measured versus applied bias voltage both at the bare module level and sensor level for a "good" bare module.

This behavior was observed on all modules. Among the failed bare modules in Figures 6.25 and 6.26, all except one did not show early breakdown at the sensor level test. Figure 6.28 shows an example of a bare module that passed the IV test at the sensor level but failed at the bare module level.

The early breakdown of bare module 3529-20-C shown in Figure 6.28 could be attributed to the fact that the bare module was exposed to a higher temperature after assembly, during ground transportation. This is suggested because the bare module did not have any visible damage when inspected. Figure 6.29 shows the bare module that showed an early breakdown both at the sensor and bare module level IV tests.

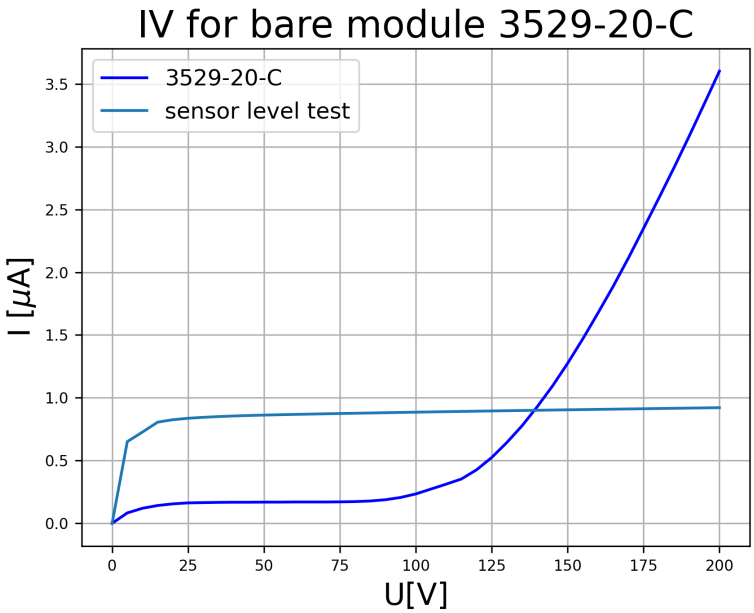

Figure 6.28: A comparison of leakage current measured versus applied bias voltage both at the bare module level and at the sensor level for a bare module that failed the IV test at the bare module level.

From Figure 6.29, it is not clear that the bare module 3529-10-C showed the breakdown at the bare module due to a higher scale of leakage current observed at the sensor level. However, from Figure 6.26, the same bare module 3529-10-C had an early breakdown at the bare module level IV test, indicating this particular bare module failed at both tests.

6.5 ITk Pixel Module Assembly

After measurements of the dimensions and masses of the flexes and bare modules, inspection of them visually, and acquisition of the IV characteristics of the bare modules, the components are assembled into ITk Pixel modules. This section describes

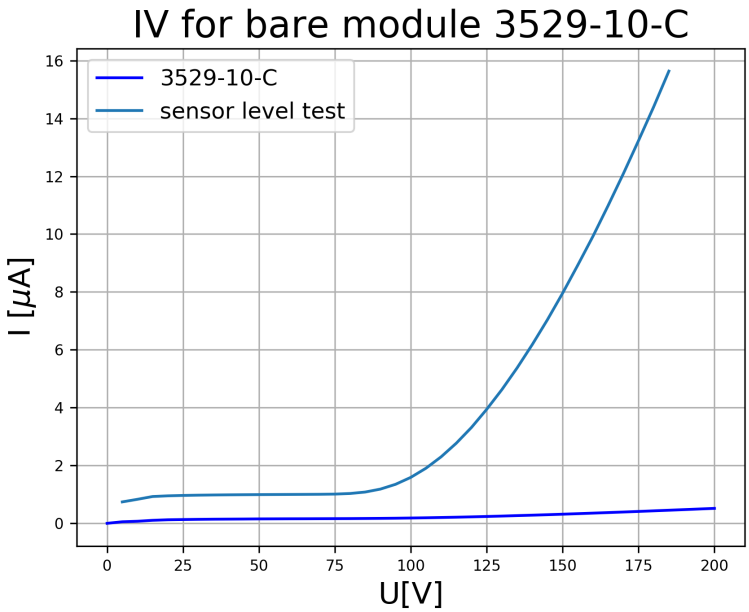

Figure 6.29: A comparison of leakage current measured versus applied bias voltage both at the bare module level and at the sensor level for a bare module. This particular bare module failed both at the bare module and sensor level IV tests.

the assembly process that was performed at IJCLab to make an ITk Pixel module. The tooling for the assembly process, and the flex-to-bare-module attachment for quad modules has been developed for the whole ITk Pixel collaboration.

6.5.1 Equipment

The main set of tools used for assembly consisted of the following:

- a bare module jig that includes a dial gauge
- a flex jig
- a flex loading block

- mating screws
- a stencil tool
- a stencil frame
- a spatula

Some of the tools are shown in Figure 6.30. With dowel pin alignment on the bare module jig, the correct positioning of the components relative to each other is assured, allowing the operator to place them on top of each other with 50 μm precision.

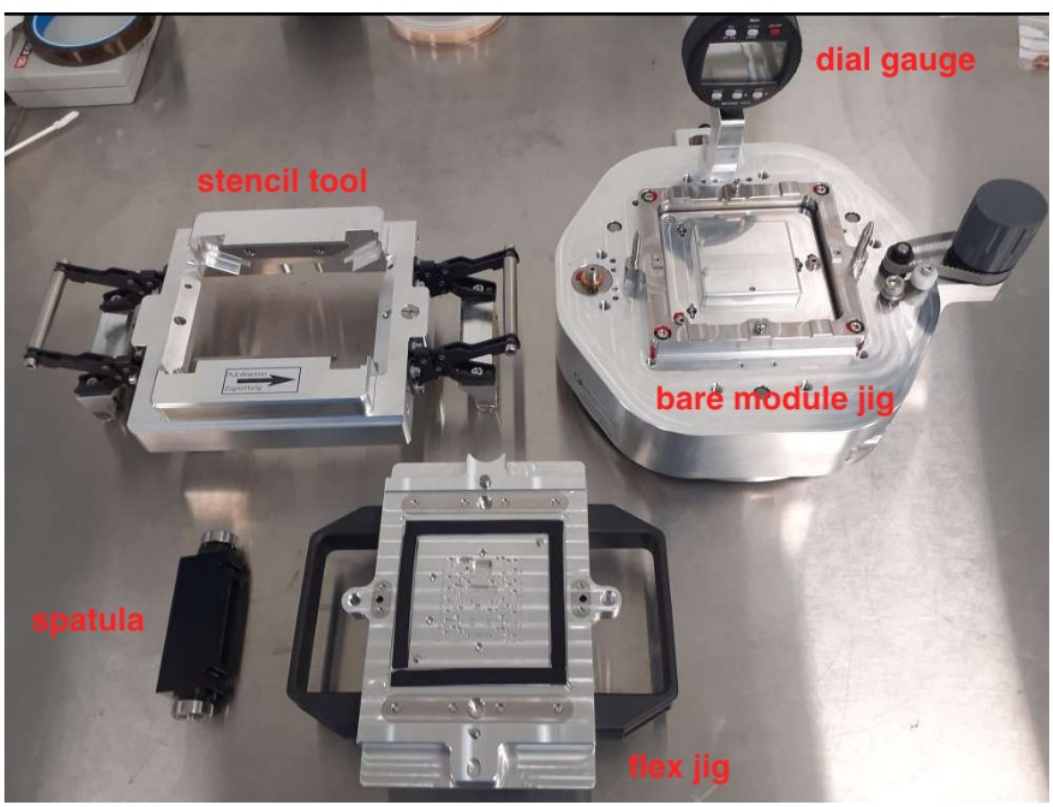

Figure 6.30: The set of module gluing tools used at IJCLab.

The bare module jig and flex jig are connected to a vacuum pump to immobilize

the bare module and flex. The global pressure was set to 95 kPa. Half of it was applied to each jig as shown in Figure 6.31.

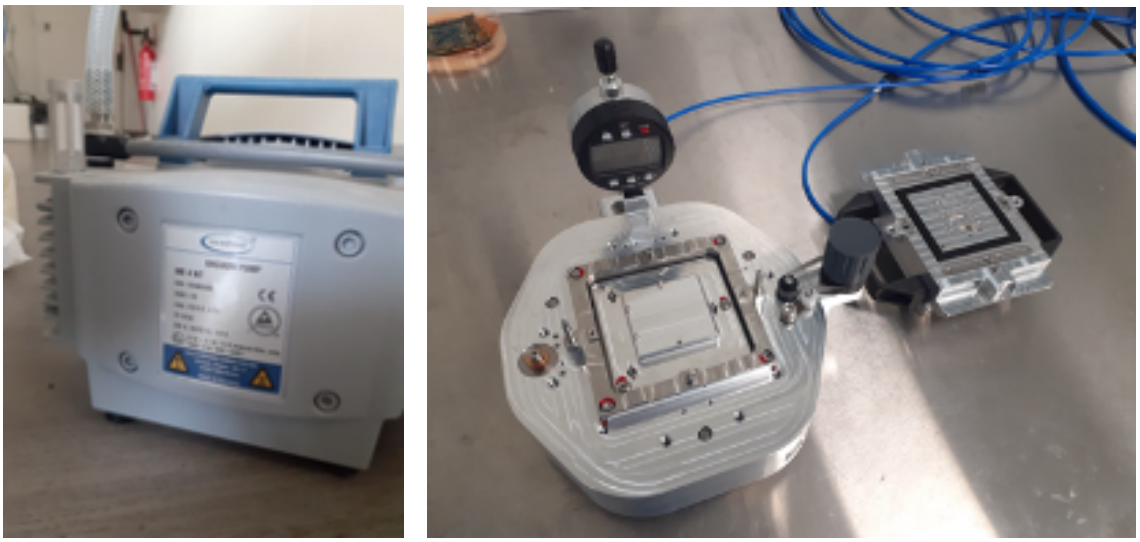

(a) Vacuum pump (b) Each jig is connected to the vacuum pump via a hose.

Figure 6.31: The vacuum pump applying pressure of approximately 47.5 kPa to each jig via a hose.

Adjusting Glue Thickness: The dial gauge on the bare module jig needed to be calibrated as the first step. The platform on which the bare module is placed, the bare module plate, is movable in the vertical direction via a knob and an inner fine thread on the jig. When closing the jigs with the flex placed on the flex jig and the bare module on the bare module jig, the height of the glue between flex and bare module can be controlled by adjusting the dial gauge before applying the glue. For the ITk Pixel module assembly, the gap was set to 40 ± 15 μm as shown in Figure 6.32, and this value is defined such that the module envelope fits in the limited space in the pixel detector layers [191].

Figure 6.32: Typical calibration reading on the dial gauge for the thickness of the glue layer between the flex and the module.

6.5.2 ITk Pixel Module Assembly

The module assembly was performed using the common tools described in Section 6.5.1 in the following order:

- The calibration of the dial gauge for glue layer thickness was performed using the module and the flex that were to be glued together.

- The stencil tool, which comprised a stencil frame and stencil sheet, was fixed on top of the flex jig with the flex held under vacuum as shown in Figure 6.33.

- The adhesive used in the assembly process must have high thermal conductivity and low viscosity so that it can be applied as a thin layer, and radiation hardness. For this reason, Araldite 2011, a two-component epoxy paste adhesive, was used. The Araldite requires a resin to curing agent volume ratio of one to one when mixed. The Araldite adhesive container is loaded into a caulking gun

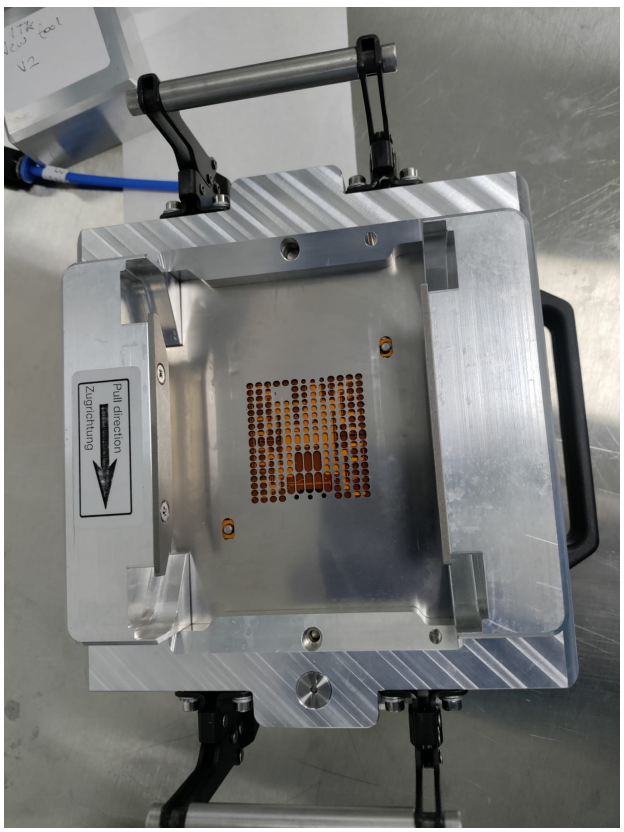

Figure 6.33: With the stencil tool, which comprises a stencil frame and stencil sheet, a predefined amount of glue can be spread on the flex before the tooling is closed for attachment and curing.

that applies pressure to the two parts of the adhesive container simultaneously, and the two components of the Araldite adhesive are deposited directly into a disposable cup. The Araldite 2011 adhesive container loaded into the caulking gun and the disposable cup are shown in Figure 6.34.

The adhesive mixing was done using a centrifugal planetary mixer as shown in Figure 6.35 where the two-component epoxy is mixed in a container that is rotated about two axes simultaneously for 50 seconds. The centrifugal mixing can disperse the particles, droplets, and bubbles in the adhesive and also remove

Figure 6.34: The caulking gun loaded with the Araldite 2011 adhesive container, and the disposable cup into which the glue mix was deposited.

air bubbles by bringing them to the surface or breaking them as shown in Figure 6.36.

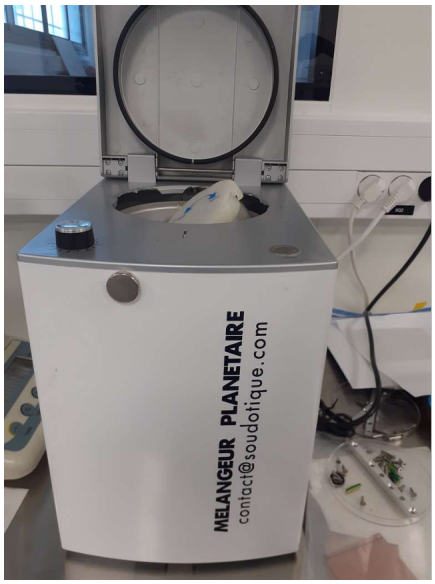

Figure 6.35: The centrifugal planetary mixer used at IJCLab to mix two components of the Araldite 2011 adhesive.

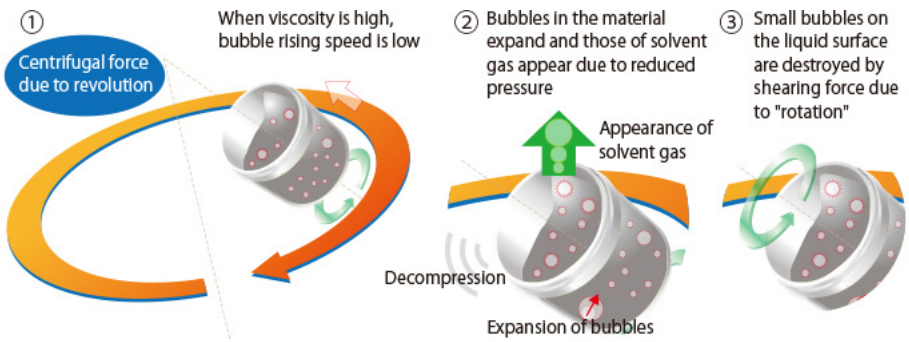

Figure 6.36: The concept behind the mixing of the Araldite using a centrifugal planetary mixer [201].

- Application of the glue with the spatula on the stencil sheet was performed as shown in Figure 6.37. The resulting glue pattern can be seen in Figure 6.38.

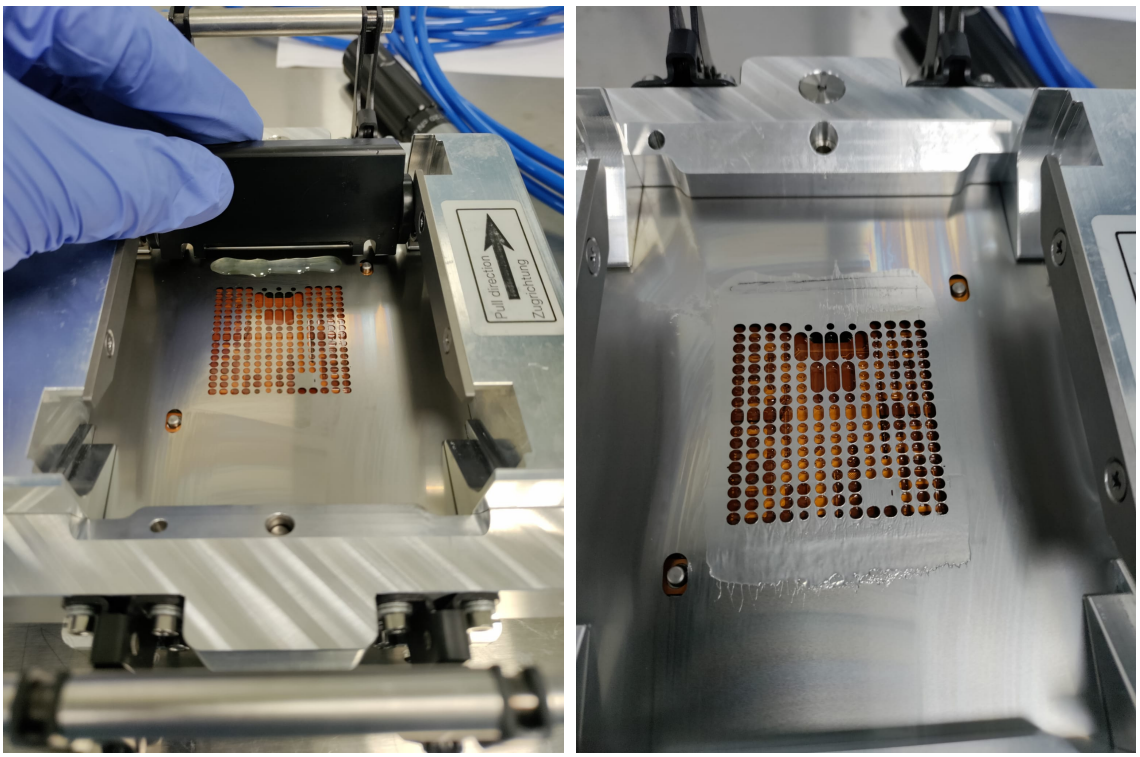

Figure 6.37: Application of the glue with the spatula on the stencil sheet with the flex below it.

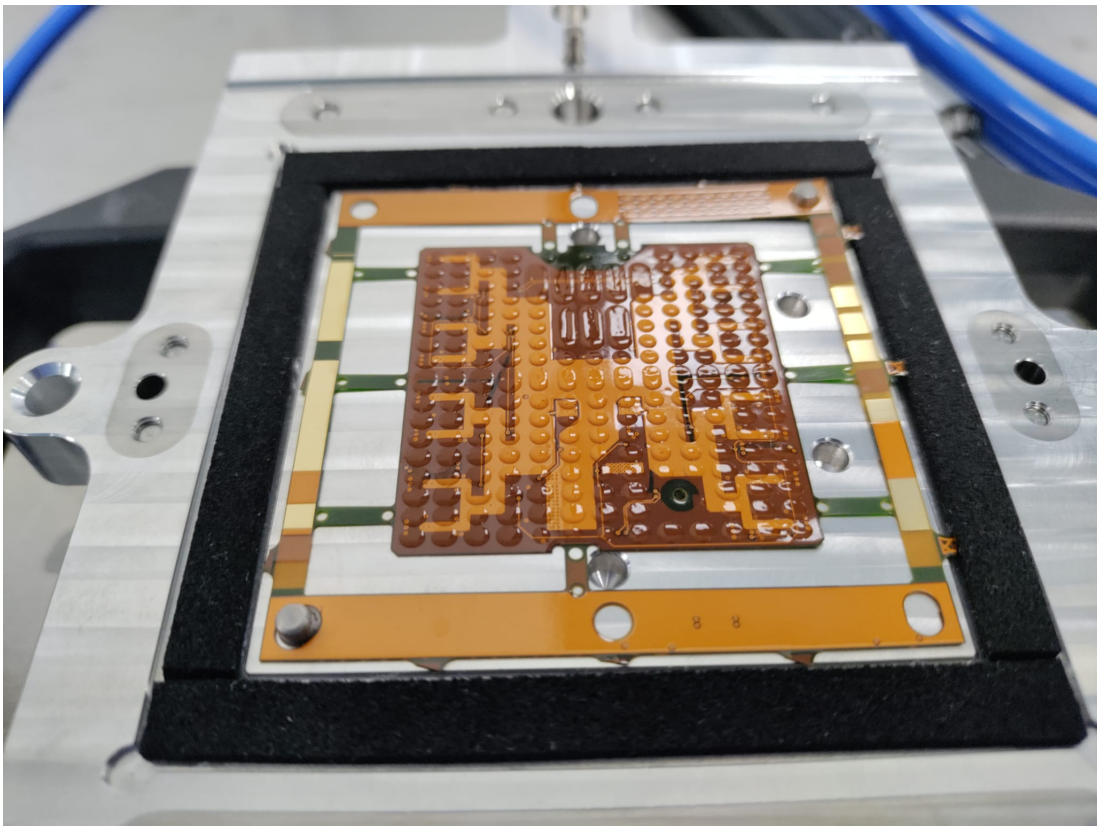

Figure 6.38: The optimized gluing pattern on the ITk Pixel flex.

The gluing pattern is optimized to provide full glue coverage with the glue thick enough to allow proper wire bonding and further handling of the module. Higher glue viscosity can lead to reduced glue coverage. This can result in delamination after the thermal cycling that happens during normal detector operation, due to cooling failures as well as planned cool and warm times of the detector modules.

- The flex jig was then placed on top of the bare module jig and the former was fastened with screws. Using the knob and dial gauge, the gap between the flex and the bare module was brought down to 40 μm. The assembly was then left untouched with the vacuum pump switched on for eight hours in order to allow

the glue to cure.

Initial Testing With Glass Dummies: In order to predict the glue coverage after curing, the assembly was performed on glass dummies and unpopulated flexes. One such sample is shown in Figure 6.39.

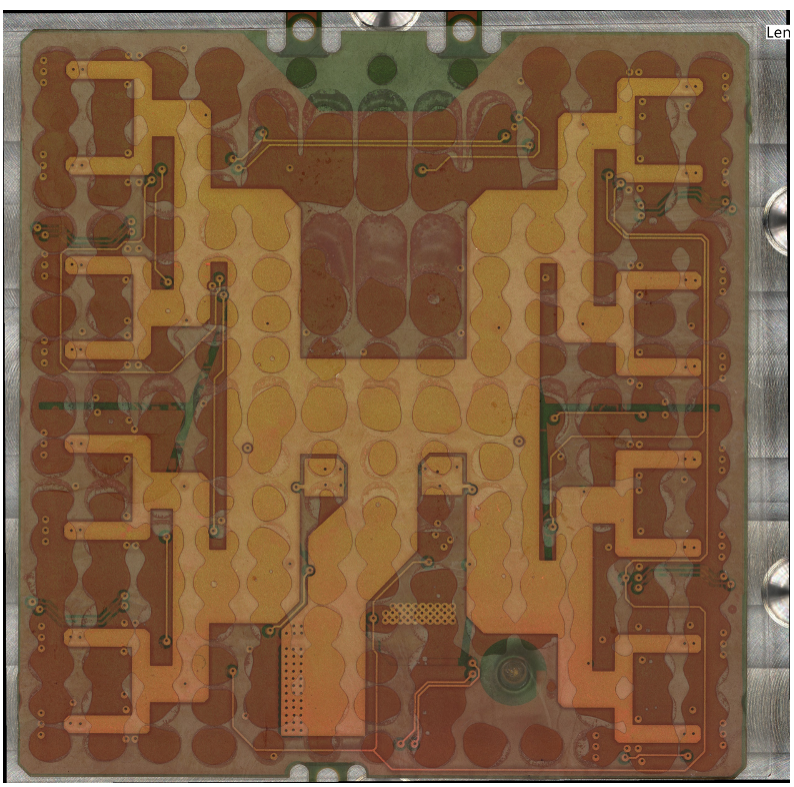

Figure 6.39: An assembled dummy module using a glass dummy in place of a bare module and an unpopulated flex in place of a flex with components on it.

In the assembled dummy modules, glue coverage was found to be continuous on the periphery but the glue was not applied uniformly across the surface. The amount deposited was found to be consistent, between 70 and 80 mg. However, glue seepage through the HV hole was observed in most of the dummy modules as shown in Figure 6.40. Since a wire bond has to go through the HV hole when real

components are used, this observed glue seepage was a major concern.

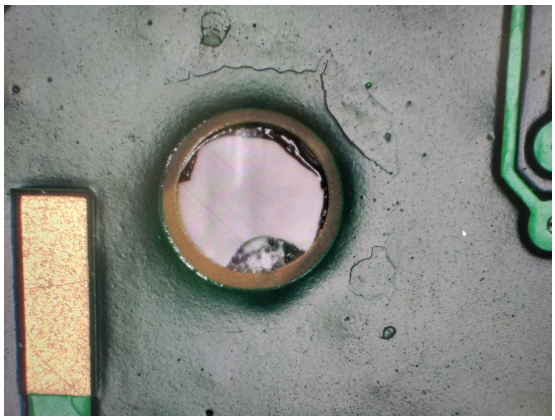

Figure 6.40: The hardened adhesive that seeped through the HV hole of the flex in the dummy module, seen under a microscope.

The following modifications in the assembly were made to ensure that the glue is compressed evenly everywhere and that no glue seeps out through the HV hole:

- the glue layer thickness achieved via the knob and inner fine thread on the bare module jig was changed from 40 μm to 30 μm.
- A piece of Kapton tape having an area of approximately 2.5×2.5 mm^2 and a thickness of 25 μm was used to cover the HV hole during the gluing process as shown in Figure 6.41.

6.5.3 Metrology and Mass Measurements of the Assembled Modules

The metrology measurements of assembled modules using silicon (Si) dummies and bare modules were performed using the Vertex-261 instrument for the following

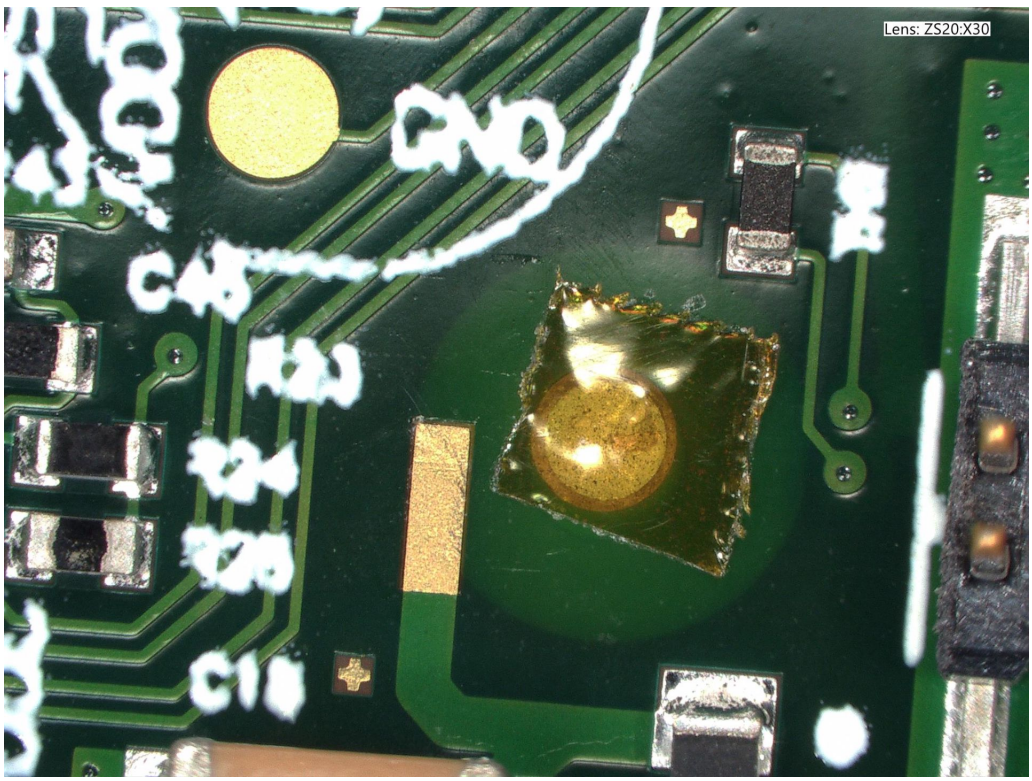

Figure 6.41: The HV hole masked by a piece of Kapton tape to prevent glue seepage through it, seen under a microscope.

quantities with the assembled module under vacuum:

- Z-dimension - thickness of the assembled module at the power connector on the flex excluding the pins,
- Z-dimension - thickness of the assembled module at the HV capacitor on the flex,
- Z-dimension - average thickness of the flex at four pickup areas on the flex (labelled as GA1, GA2, GA3 and GA4),
- Z-dimension - difference between the highest and lowest of the thickness measurements at four pickup areas,

- Z-dimension - glue thickness at four pickup areas obtained by subtracting the thickness measurements of the bare module and flex from the thickness measurements of the assembled module, and
- alignment measurements - the X and Y distances between the fiducial markers on the flex and FE chip on the bare module or Si dummy. The fiducial markers are located on the top left and bottom right corners of the assembled module as shown in Figure 6.42.

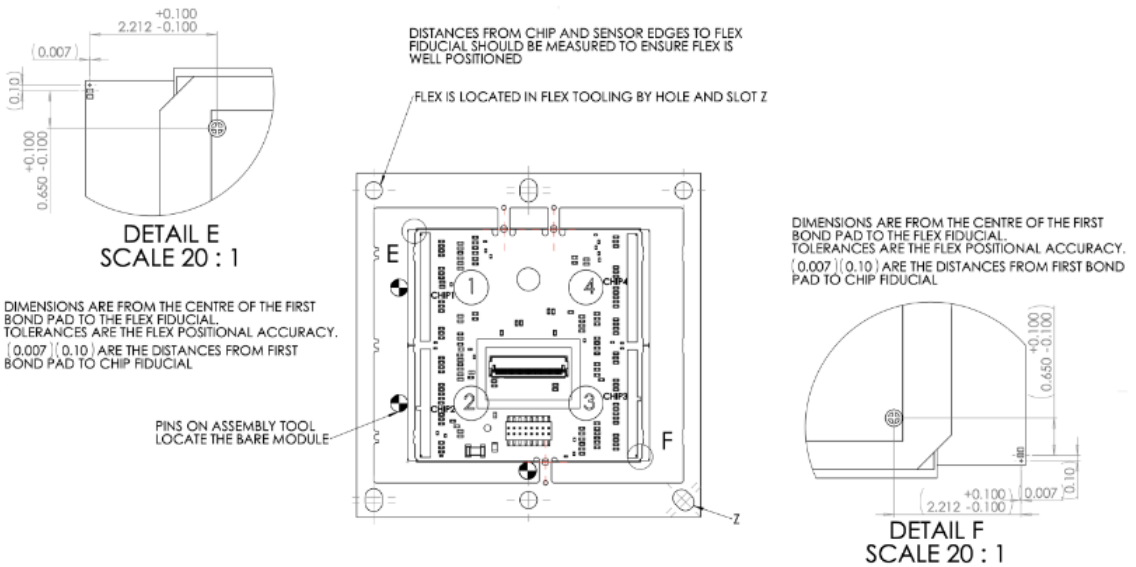

Figure 6.42: The nominal distances in the X and Y directions between the fiducial markers on the chip and on the flex are shown. The fiducial markers are located on the top left and bottom right corners of the assembled module [195].

The Vertex-261 was programmed to measure the quantities mentioned above as follows:

- the average assembled module height at the HV capacitor and the power connector on the flex was calculated first by taking eight measurements at each

part. The height of the flex jig was measured eight times at different points, and the average of these quantities was then subtracted from the average assembled module height at each part. This gave the average assembled module thickness at the HV capacitor and the power connector on the flex, and

- the average assembled module thickness at the pickup areas was calculated first by taking the average of the eight height measurements made at each pickup area. The Vertex-261 then subtracted the average jig height from the average assembled module height. This gave the average assembled module thickness at the pickup areas.

- The distance in the X and Y directions of a fiducial marker on the flex from that on the FE chip was calculated by detecting the fiducial markers on the flex and FE chip.

A total of 6 ITk Pixel modules were assembled using Si dummy modules. The averages of the thickness of the assembled modules at the power connector and HV capacitor were measured to be 1.923 mm and 2.254 mm, respectively. The average thickness measurements of the assembled modules at four pickup areas - GA1, GA2, GA3 and GA4 were found to be 0.568 mm, 0.565 mm, 0.567 mm and 0.567, respectively, showing excellent consistency in all samples. The average glue layer thickness of all 6 Si dummy assembled modules was found to be 41.3 μm. The minimum and maximum thicknesses of the glue layer measured from all samples were 39 μm and 46.5 μm, respectively, which is within the precision guaranteed by the dial gauge on the gluing tool, 40 ± 15 μm. The average glue mass of all samples was 74.6 mg, and the minimum and maximum reported glue masses were 65 mg and 84 mg, respectively.

The X and Y distances between the fiducial markers on the flex and Si dummy of all 6 assembled dummy modules are shown in Table 6.7.

Sample Number	Top X (mm)	Top Y (mm)	Bottom X (mm)	Bottom Y (mm)
1	2.120	0.618	2.447	0.753
2	2.108	0.619	2.456	0.760
3	2.111	0.504	2.542	0.753
4	2.214	0.718	2.306	0.673
5	2.130	0.658	2.372	0.769
6	2.128	0.657	2.366	0.788

Table 6.7: The X and Y distances between fiducial markers on the flex and Si dummy of the assembled dummy modules.

From Figure 6.42, the expected values of the X and Y distances between fiducial markers on the top right and bottom left corners of an ITk Pixel module are 2.212 ± 0.100 mm and 0.650 ± 0.100 mm, respectively. From Table 6.7, it can be seen that the X distance between the fiducial markers on the bottom left corner of five ITk Pixel Si dummy modules is out of specification while that of the top right corner fiducial markers is within specification. A similar pattern was observed for the Y distance between fiducial markers. This large discrepancy cannot be explained by the uneven placement of fiducial markers on the Si dummy that was observed during the metrology of the Si dummies and reported in Section 6.3.3; it is possible that the Vertex-261 failed to identify the exact location of the fiducial markers.

A total of 9 ITk Pixel modules were assembled using bare modules and loaded flexes. The averages of the thickness of the assembled modules at the power connector and HV capacitor were measured to be 1.911 mm and 2.333 mm, respectively. The average thickness measurements of the assembled modules at four pickup areas - GA1,

GA2, GA3 and GA4 were found to be 0.576 mm, 0.569 mm, 0.577 mm and 0.573, respectively, showing excellent consistency in all 9 samples. The average thickness of the glue layer of all nine assembled modules was found to be 36.5 μm. The minimum and maximum thicknesses of the glue layer measured on all samples were 31.25 μm and 46.5 μm, respectively, which is within the precision guaranteed by the dial gauge on the gluing tool, 40 ± 15 μm. The average glue mass of all samples was 74.9 mg, and the minimum and maximum reported glue masses were 72 mg and 78 mg, respectively.

The X and Y distances between the fiducial markers on the flex and bare module of all 9 ITk Pixel modules are shown in Table 6.8.

Sample Number	Top X (mm)	Top Y (mm)	Bottom X (mm)	Bottom Y (mm)
ParisPreProd10	2.166	0.550	2.383	0.836
ParisPreProd11	2.160	0.691	2.217	0.823
ParisPreProd12	2.130	0.737	2.277	0.763
ParisPreProd13	2.185	0.659	2.240	0.819
ParisPreProd14	1.705	0.938	2.129	1.157
ParisPreProd15	2.201	0.901	2.100	0.690
ParisPreProd16	2.223	0.813	2.143	0.715
ParisPreProd17	2.204	0.758	2.212	0.731
ParisPreProd18	2.114	0.786	2.284	0.676

Table 6.8: The X and Y distances between fiducial markers on the flex and bare module of the ITk Pixel modules.

From Table 6.8, it can be seen that none of the samples met specifications. One sample, ParisPreProd14, had a serious misalignment in which the flex was rotated counterclockwise with respect to the bare module due to an error in the gluing process as shown in Figure 6.43.

The X distances between the fiducial markers on the top right corner of all ITk

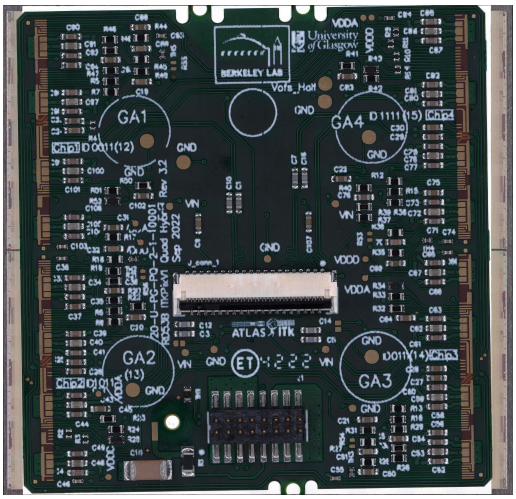

Figure 6.43: The sample, ParisPreProd14, that suffered a serious misalignment. As a result, this sample could not be wirebonded.

Pixel modules except ParisPreProd14 agree with specifications. The X distances between the fiducial markers on the bottom left corner of all ITk Pixel modules except ParisPreProd10 were within specifications. However, the results of Y distance measurements of the fiducial markers on both corners were inconclusive as all of them had Y distances between fiducial markers on both corners exceeding the specifications. The samples ParisPreProd17 and ParisPreProd18 had relatively better alignment compared to other samples as these had Y distance measurements close to the specifications. Figure 6.44 illustrates the excellent alignment between the bare module and the flex in the ParisPreProd18 sample.

The observed misalignment in all samples could be attributed to the fact that the fiducial markers on the FE chips of all ITk Pixel modules were below the resolution of the camera of the Vertex-261 instrument. One way to improve the detection of fiducial markers by the Vertex-261 is by improving lighting in the clean room.

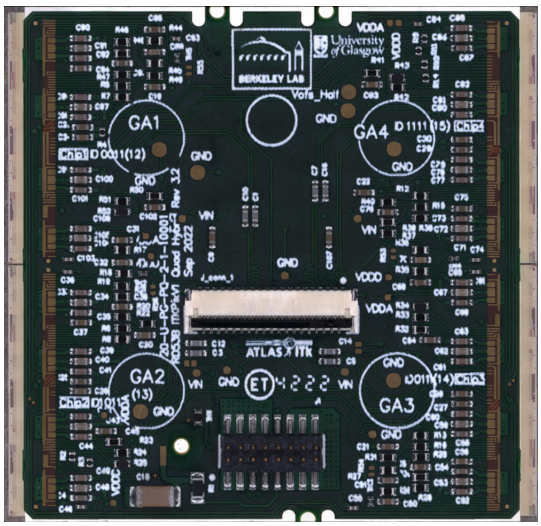

Figure 6.44: The bare module and flex on ParisPreProd18 had good alignment because the fiducial positions of this module were close to the specifcations.

6.6 ITk Pixel Module Flatness Measurements

As part of the QA/QC on the ITk Pixel modules, it needs to be demonstrated that they meet the flatness specification of 50 ± 25 μm (between peak and valley) [202] across the four FE chips when the module is held on the pickup points. The tool used for this purpose consists of two main parts - the pickup base, which is used to locate the sample and hold it under vacuum, and the pickup body as shown in Figure 6.45.

The pickup body has four suction cups that draw the surface of the flex onto mating surfaces on the tool. To use the tooling to inspect a sample, the following steps were taken:

- the sample was located on the pickup base using the 3 dowel pins, and the vacuum was switched on as shown in Figure 6.46;

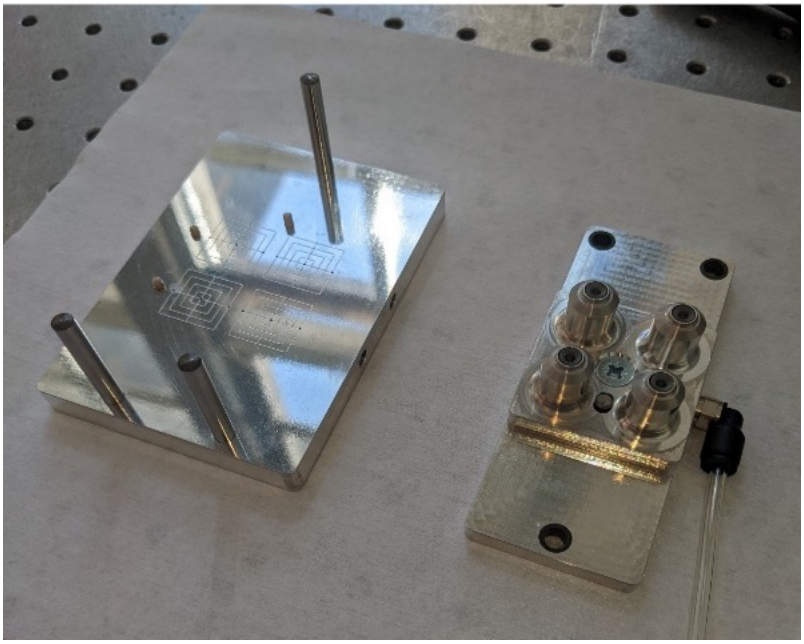

Figure 6.45: The pickup tool and base plate to locate the module.

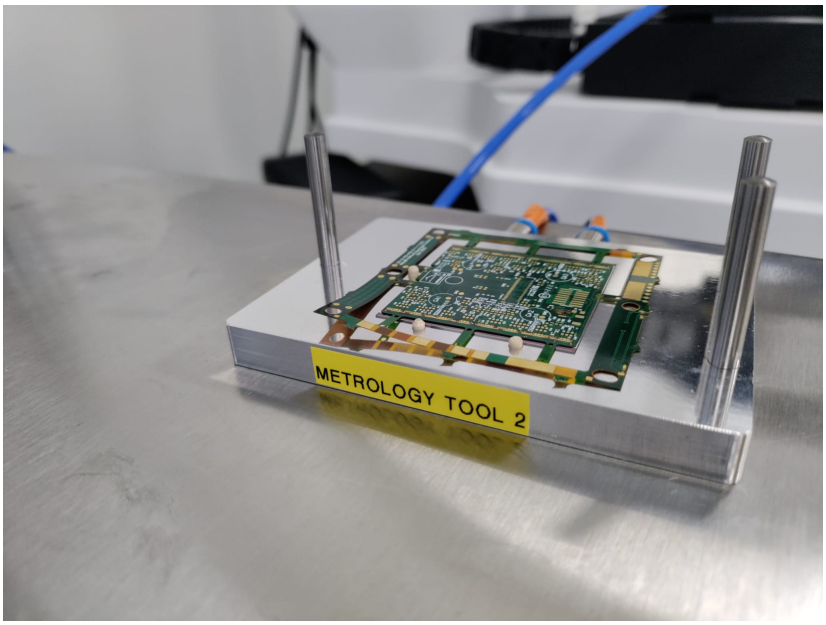

Figure 6.46: The sample, an assembled Si dummy module, was located on the pickup base using the 3 dowel pins.

- the pickup body was aligned with the 3 dowels and placed on the sample. Then, the vacuum for the pickup body and the base was turned on and off, respectively, as shown in Figure 6.47; and

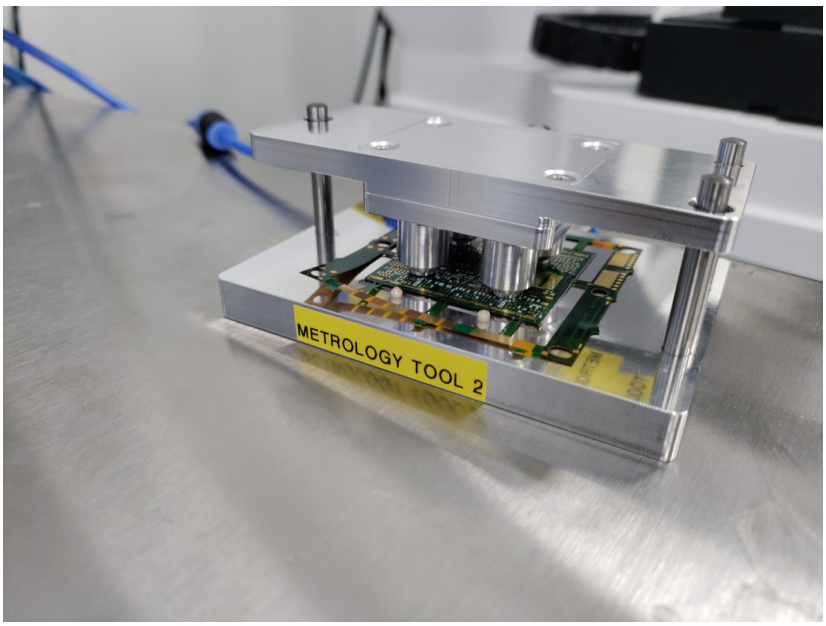

Figure 6.47: The pickup body was positioned on the 3 dowels of the pickup base.

- the pickup body was then lifted and turned over to show the bottom surface of the FE chips as shown in Figure 6.48;

- the pickup body was clamped to the stage of the Vertex-261 to avoid movements while taking flatness measurements, as shown in Figure 6.49.

The flatness measurements were first done using assembled Si dummy modules. Since the Vertex-261 machine cannot measure the surface profile by scanning the valley and peak, an alternative approach was used to measure the flatness of the assembled modules. By using the laser, the height of each point in a grid of points on the surface

Figure 6.48: The pickup body was flipped over to reveal the bottom surface of the chips.

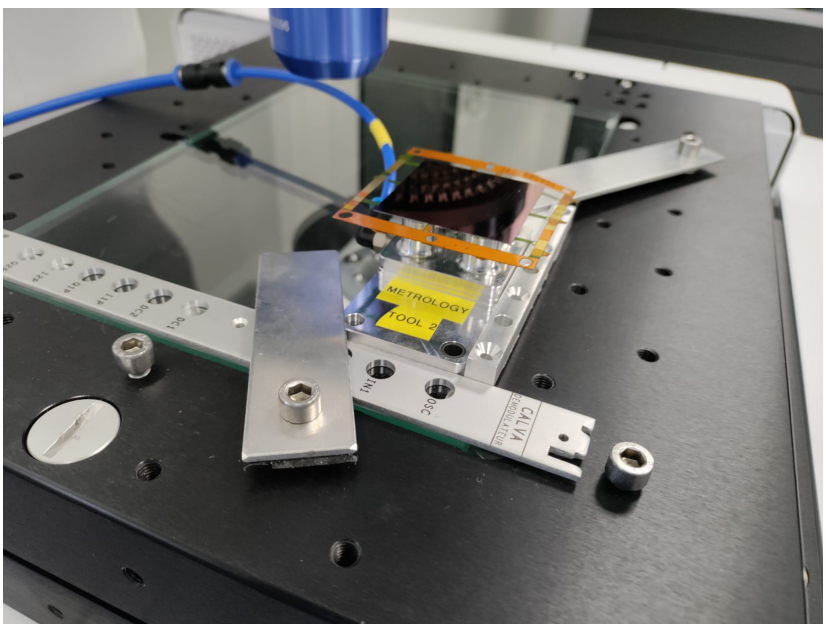

Figure 6.49: The pickup body clamped to the stage of the Vertex-261 to allow flatness measurements of the assembled Si dummy module.

was measured. The number of points was set to approximately 1730 with a 1 mm gap between each point. The height of each point in the grid was then read by a script written in Python to create a surface profile as shown in Figure 6.50.

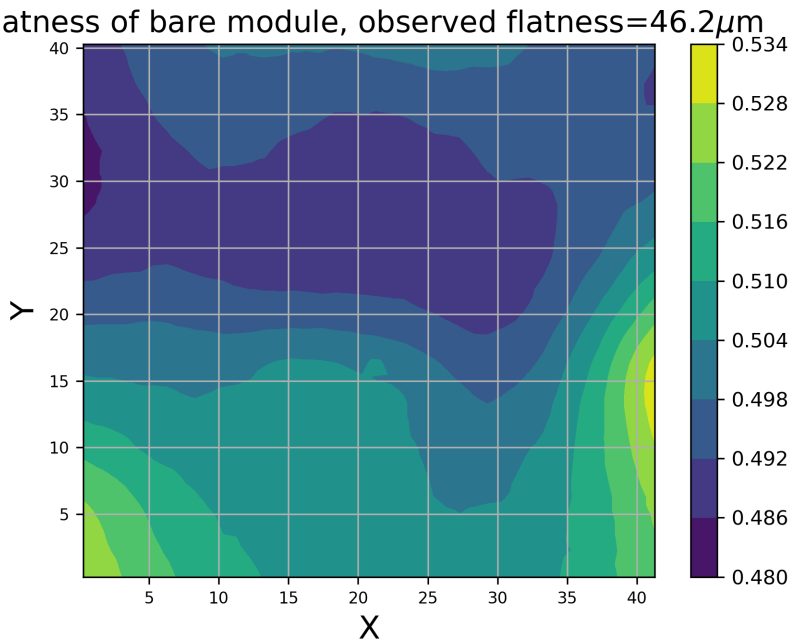

Figure 6.50: The surface profile of the assembled Si dummy module. The dimensions, X and Y, and Z are in units of mm.

As can be seen from Figure 6.50, the observed flatness which is the difference between peak and valley for this particular assembled Si module is 46.2 μm which is within the specifications. The glue distribution in this module can also be understood from Figure 6.50. On the left and right edges of the assembled module, there are areas where the height of the module is above 52.8 μm, and these areas indicate that the gap between the flex and Si dummy is significant and could pose difficulty in performing wirebonding on these areas.

A similar procedure was performed to extract the flatness of the ITk Pixel

assembled module. Since the flatness of an ITk Pixel module needs to be extracted from the four FE chips, the gap between each pair of FE chips needed to be excluded from the measurements by the Vertex-261 instrument. Instead of using a large grid of 1730 points that covers all FE chips, the Vertex-261 used a small grid of 400 points on each FE chip as shown in Figure 6.51, and it measured their height.

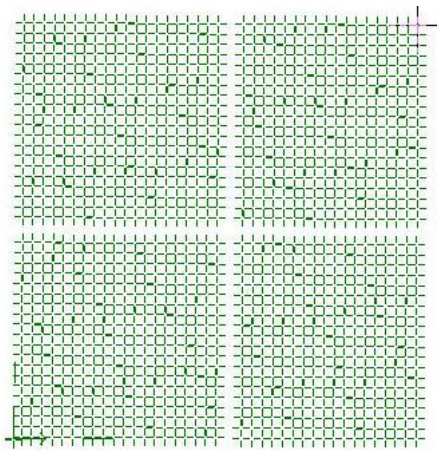

Figure 6.51: A small grid of 400 points on each FE chip on the ITk Pixel module whose flatness was to be measured by the Vertex-261 instrument.

The height of each point in the grid on the ITk Pixel module was used to create a surface profile using Python as shown in Figure 6.52.

From Figure 6.52, the observed flatness of the ITk Pixel module is 33.6 μm which is within the specifications.

6.7 Visual Inspection of the ITk Pixel Modules

The bare module, Si dummy, and flex were examined under a microscope for defects before the gluing process began. The same was done for the assembled module after

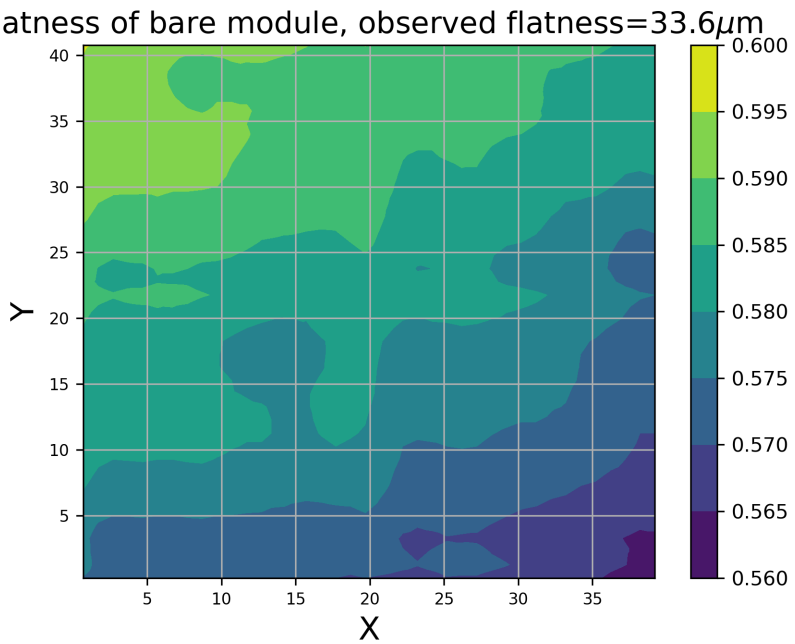

Figure 6.52: The surface profile of the ITk Pixel module. The dimensions, X and Y, and Z are in units of mm.

the gluing process. The visual inspections of all components and assembled modules were done using the VHX-7000 instrument manufactured by Keyence [203].

6.7.1 Equipment Description

The VHX-7000 instrument shown in Figure 6.53 is a digital microscope system that has a camera with a resolution of 8 million pixels (MP) that can capture images with high clarity and detail, making it comparable to a scanning electron microscope (SEM).

The magnification of the VHX-7000 instrument can be changed from 20x to 6000x with a motorized turret, without any manual intervention or focus adjustment. The

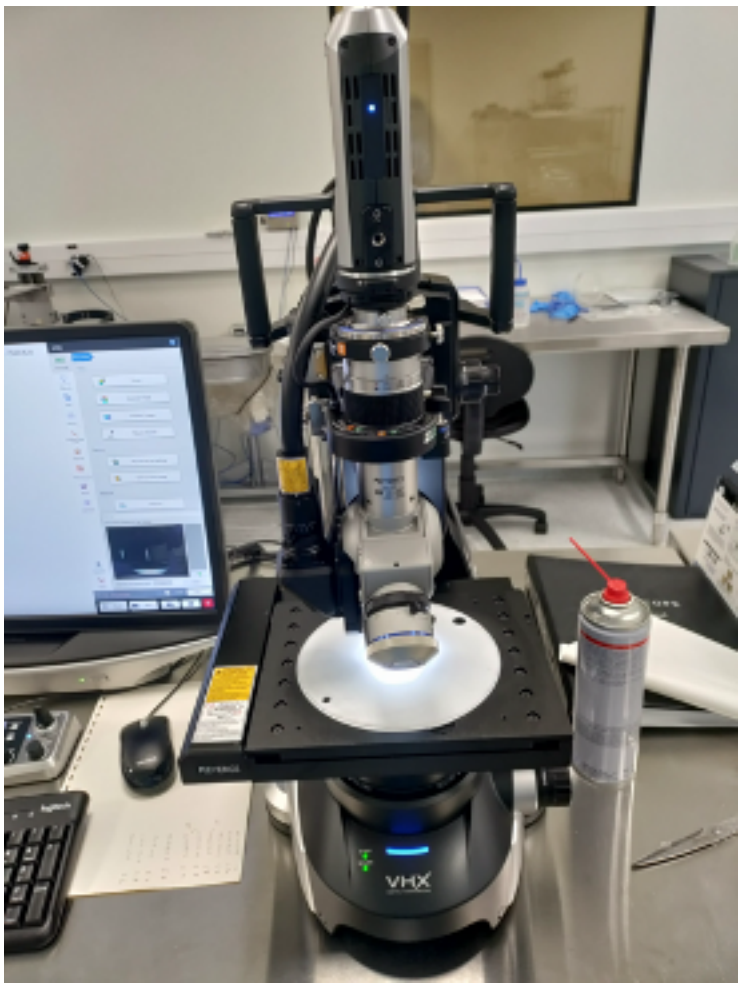

Figure 6.53: The digital microscope from the VHX-7000 series manufactured by Keyence, used for visual inspection of the ITk Pixel modules at IJCLab.

images are shown in full color and high definition on a 27-inch LCD monitor connected to it, which has a wide viewing angle and brightness and contrast settings that can be adjusted.

6.7.2 Visual Inspection of the Bare Modules and Si Dummies

All bare modules and Si dummies were inspected, and some of the defects observed were the following:

- dicing defects on the surface or edges of the sensor die that occurred during the process of cutting the wafer into individual die as shown in Figure 6.54. These dicing defects can cause chipping, cracking, or contamination of the sensor die, which can affect the electrical, optical, or mechanical properties of the sensor. The sensor can have a smaller active area or a lower resolution because of these defects, which can degrade the performance of the sensor. The sensor can have a higher leakage current or a higher noise level due to these defects, which can lower the sensitivity or the reliability of the sensor,

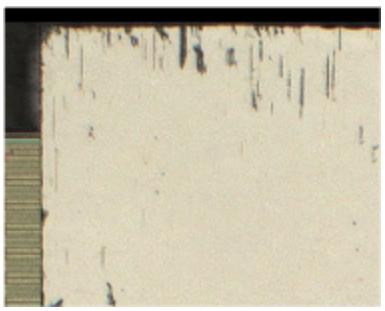

Figure 6.54: The chipped sensor of an ITk Pixel bare module observed under the VHX-7000 microscope.

- tooling marks on the sensors: marks or impressions that are left on the surface of a sensor by a handling tool as shown in Figure 6.55,

- dot-like contamination on the sensors due to dust, dirt, oil, water, chemicals, or manufacturing errors as shown in Figure 6.57. The dot-like contamination

Figure 6.55: Several tooling marks on an ITk Pixel bare module observed under the VHX-7000 microscope.

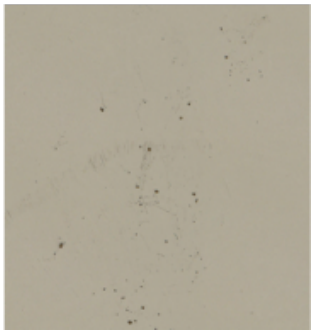

Figure 6.56: The dot-like contamination on the sensor of an ITk Pixel bare module observed under the VHX-7000 microscope.

on the sensors can alter the electrical properties of the sensor, such as the capacitance, resistance, and leakage current, and affect the signal generation or amplification,

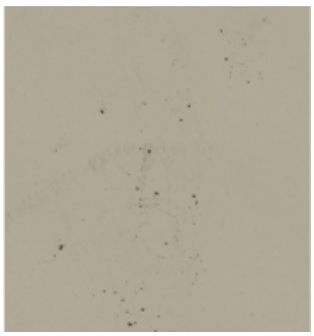

Figure 6.57: The dot-like contamination on the sensor of an ITk Pixel bare module observed under the VHX-7000 microscope.

- irregular dicing or chipping of the FE-chips as shown in Figure 6.58. The irregular dicing can cause faulty connections with the flex, and since the FE chips are responsible for processing and transmitting the signals from the sensors to the readout electronics, this can result in signal loss, distortion or noise. These defects can alter the shape or the size of the FE chips, which can affect the alignment or the placement of the bare module on the flex, and

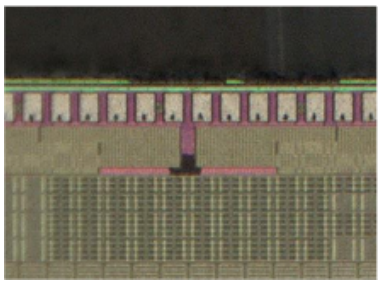

Figure 6.58: The irregular dicing of a FE chip of an ITk Pixel bare module observed under the VHX-7000 microscope.

- contamination of wirebond pads on the FE chips as shown in Figure 6.59. This defect can reduce the quality or the strength of the bond between the wire and the pad and hence can affect the electrical characteristics of the ITk Pixel module.

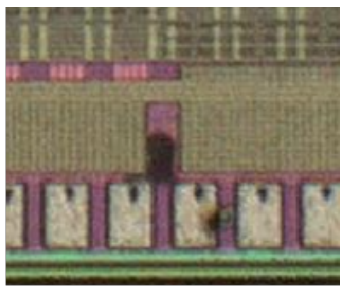

Figure 6.59: The contamination of wirebond pads on a FE-chip of an ITk Pixel bare module observed under the VHX-7000 microscope.

6.7.3 Visual Inspection of the Flexes

All flexes were inspected, and the most common defects observed were the following:

- an exposed copper trace on the flexes due to a missing protective layer or solder mask as shown in Figure 6.60. The exposed copper traces are vulnerable to corrosion, oxidation, and contamination, which can degrade the performance of the ITk Pixel module,

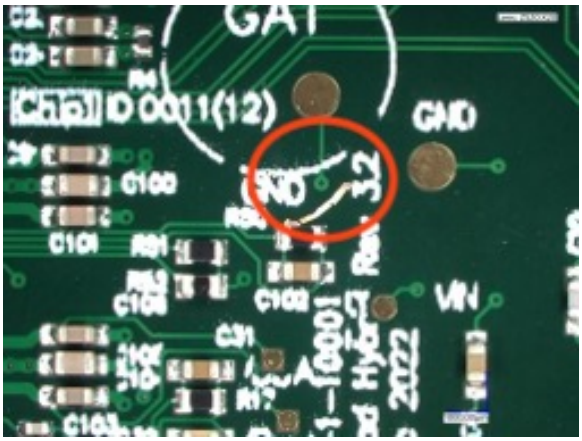

Figure 6.60: The exposed copper trace on the flex observed under the VHX-7000 microscope.

- contamination or scratches on the wirebond pads on the flexes as shown in Figure 6.61. This defect can reduce the quality or the strength of the wirebond, and

- material or particle contamination due to foreign objects such as dust that can settle on the surface or between the components of a circuit board as shown in Figure 6.62. This defect can affect an ITk Pixel module in various ways,

Figure 6.61: A scratched wirebond pad on the flex observed under the VHX-7000 microscope.

depending on the type, source, and amount of contamination. Some of the effects are reduced signal quality and resolution and distorted response.

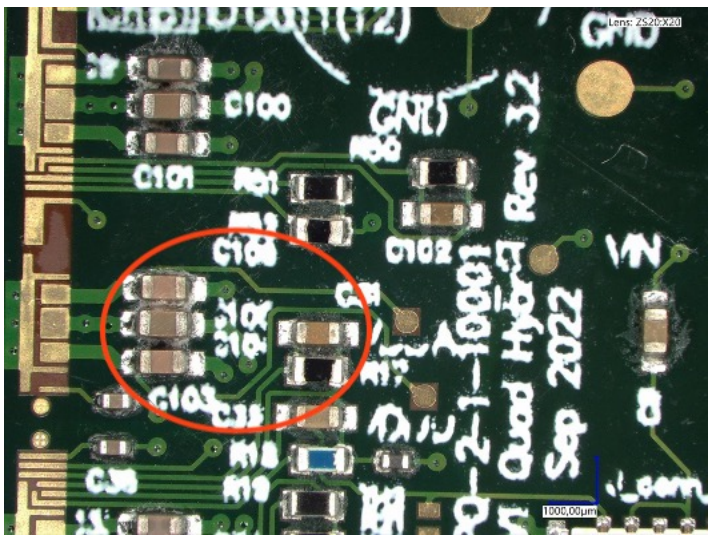

Figure 6.62: The contaminated area surrounding the capacitors on the flex as observed under the VHX-7000 microscope.

6.7.4 Visual Inspection of the Assembled ITk Pixel Modules

The assembled modules were inspected for glue seepage through the HV hole or on the wirebond pads. An example of glue seepage on the wirebond is shown in Figure 6.63.

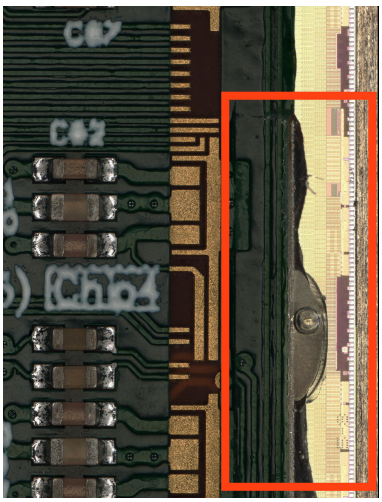

Figure 6.63: Glue seepage on the wirebonds of an ITK Pixel module as observed under the VHX-7000 microscope. This glue excess prevented the wirebonding of this ITK Pixel module.

6.8 The ITk Production Database

For later tracking in the production phase and during HL-LHC operation, the data from the QA/QC tests of every bare module, flex and assembled module were recorded and stored in the ITk Production Database (PDB) [204]. The ITk Production Database shown in Figure 6.64 is a common tool for both the strip and pixel projects to record all workflows covering approximately 10^7 numbered items. This includes individual components, batches and assemblies. The histories of shipments and detailed results of every single QA/QC test are stored as well. It also works as a means of information and data sharing between institutes participating in the assembly. The ITk PDB will continue to be used for those purposes throughout all of production.

The following results were uploaded to the ITk PDB:

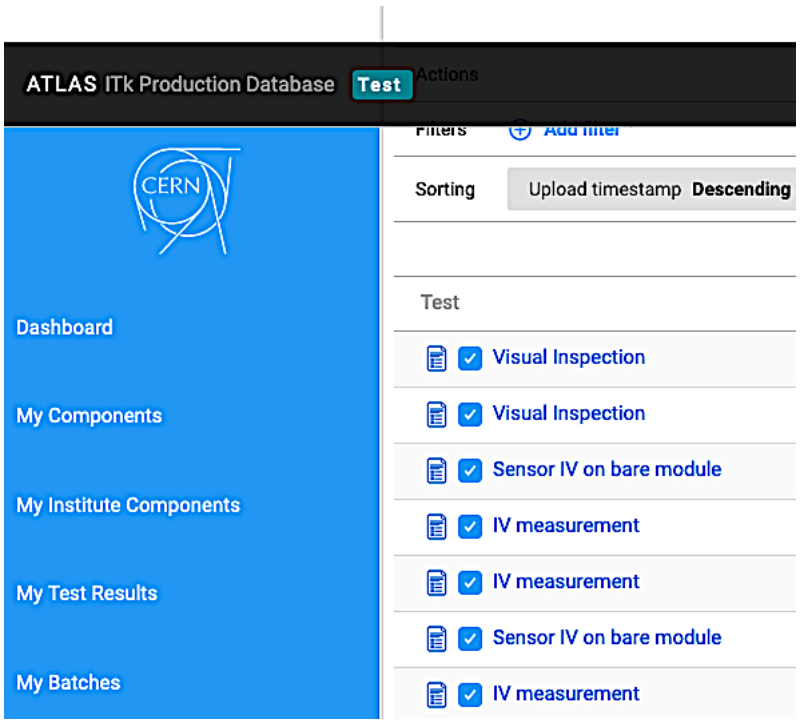

Figure 6.64: Illustration of QA/QC test records in the user interface of the ITk Production Database.

- IV characteristics of 18 bare modules,
- metrology and mass measurements of the bare modules, populated flexes and assembled modules, and
- visual inspection reports of the bare modules, populated flexes and assembled modules.

6.9 Conclusion of ITk Development Research

The pre-production phase has begun as ATLAS prepares for the HL-LHC, which is expected to start in 2028. The assembled modules were sent to LPNHE and

CEA-IRFU, the other ATLAS groups in the Paris Cluster, for further steps such as wire bonding, Parylene coating, thermal cycle tests and long term stability tests. A wirebonded module that was assembled at IJCLab is shown in Figure 6.65. The ITk production will involve a global collaboration of over fifty institutes, which will produce almost 30000 modules within a few years.

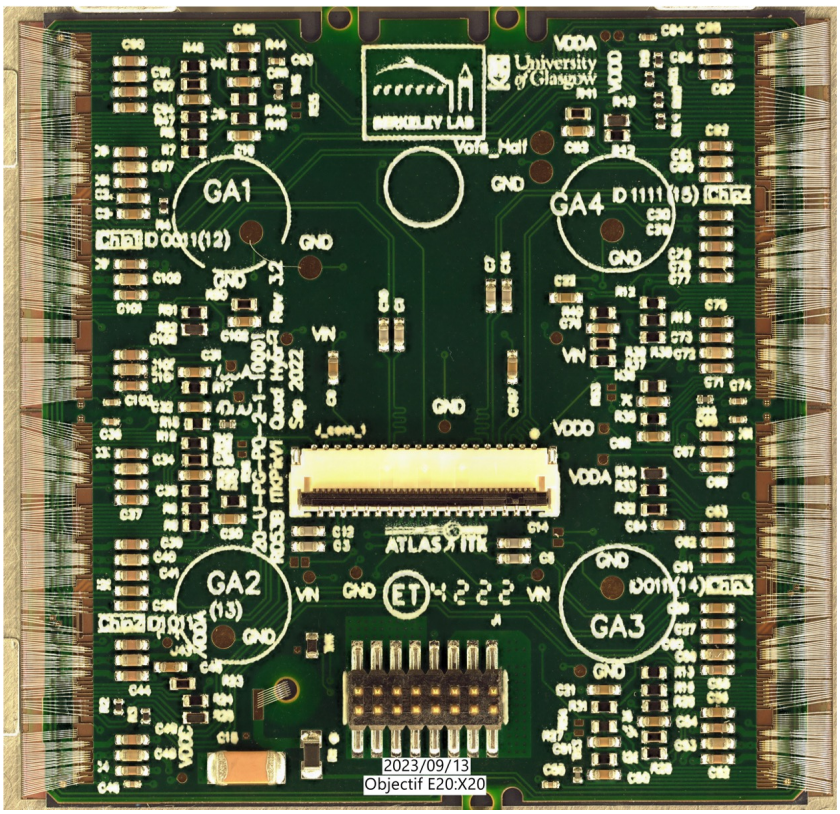

Figure 6.65: An ITK Pixel module that was assembled at IJCLab and was successfully wirebonded.

Chapter 7

Conclusions and Outlook

This dissertation records research in five aspects of the ATLAS experiment. The first one is measurement of the effective lifetime of B^0_{d}-mesons using $B^0_{\mathrm{s}} \to J/\psi K^{*0}$ events reconstructed from a dataset of integrated luminosity 140.1 fb^{-1}. The lifetime measurements allow the ATLAS collaboration to put constraints on the parameters of effective QCD models, which will allow a more precise description of weak decays of heavy hadrons. The measured lifetime of the B^0_{d}-mesons is consistent with the Standard Model predictions. It is more precise than the previous ATLAS measurement, and is statistically 3 times more precise than the experimental average [10] compiled by the Particle Data Group (PDG). The related ratio of average decay widths of the B^0_{s} and B^0_{d}, $\Gamma_{\mathrm{d}}/\Gamma_{\mathrm{s}}$, shows a tension at the level of 3σ with the theoretical predictions and experimental averages, driven by the tension of Γ_{s}.

The second topic is the measurement of CP-violating parameters arising in the interference of $B^0_{\mathrm{s}} - \bar{B}^0_{\mathrm{s}}$ mixing and B^0_{s} decays. The CP-violating phase ϕ_{s} is an excellent observable to search for contributions of New Physics beyond the Standard

Model. The measurements were performed using the decay channel $B_s^0 \to J/\psi\phi$ with a pair of oppositely charged muons in the final state reconstructed from a dataset of 158 fb^{-1} collected by the ATLAS Detector. The measured CP-violating phase ϕ_s is consistent with the Standard Model prediction, and it improves on the precision of previous ATLAS measurements.

The third topic is the implementation of high level dimuon triggers for B-Physics in AthenaMT, an upgraded ATLAS software framework in which the algorithms are optimized for multi-threaded CPUs and efficient memory usage. The decay topologies of $B_s^0 \to J/\psi\phi$, $B_d^0 \to J/\psi K^{*0}$ and $B^+ \to J/\psi K^+$, which are presented in this dissertation, were used to validate the triggers. All the implemented triggers are very efficient and can select events that can improve the precision of the above mentioned measurements in Run 3.

The fourth topic is the study of the evolution of radiation induced effects on the ATLAS Pixel detectors, both current and upgraded, through the leakage current and depletion voltage, which are two powerful probes to study the damage in the sensor bulk. The leakage currents and depletion voltages were predicted for several operational scenarios using the Hamburg Model which is based on a set of equations that describe the evolution of the effective doping concentration with time and accumulated fluence. The Hamburg Model was fitted to the depletion voltages measured in Run 2 and early Run 3 to extract introduction rates for the two innermost layers of the ATLAS Pixel Detector. These parameters can be projected to higher fluences and used during the design of future particle physics detectors such as the ATLAS ITk, whose innermost layer will need to cope with at least 10 times more fluence than the IBL will receive by the end of Run 3.

The last aspect of this dissertation is the contribution to quality control in the production of the ITk Pixel quad modules carried out at the IJCLab in France during the pre-production phase. The comprehensive quality control performed includes all steps from reception, inspection, testing of the bare components, assembly of the modules, their characterization, and communication about validated and good modules to the collaborating researchers at CERN, Marseille, Grenoble and Annecy. The elementary units of the ITK Pixel modules, namely the bare modules, underwent measurements of leakage current versus bias voltage, followed by metrology and visual inspection, before they were glued together to form the ITk Pixel modules using common tooling to ensure module uniformity among all labs participating in ITk production. The assembled modules underwent another round of metrology tests and visual inspection before they were sent to other labs in the Paris cluster for wirebonding. The measurements from all the tests were recorded in a common database.

The measurements of the effective lifetime of the B^0_{d}-mesons and the CP-violating parameters in the B^0_{s} decays benefit from the high statistics collected by the ATLAS Detector. However, the prospect of observing a significant contribution of New Physics is still hampered by the current statistics. Using Run 3 data, the statistical precision of the lifetime measurement of the B^0_{d}-mesons is expected to improve by a factor of 1.3 compared to the Run 2 measurement, and that of the CP-violating phase in the B^0_{s} decays by a factor of 1.2 times compared to the combined Run 1 and 2 measurement. The thoroughly upgraded detector for the HL-LHC phase, the ATLAS ITk, is being developed and is expected to start data collection in 2029. With Runs 4 and 5 data only, the lifetime measurement of the B^0_{d}-mesons will achieve

a 3.8-fold improvement over Run 3, and the CP-violating phase in the B_s^0 decays will achieve a 3.5-fold improvement over Runs 1 and 2 combined. Further, the ITk will have improved granularity and coverage, which will enhance the resolution and identification of B-mesons. The MS, which will be upgraded with new chambers and electronics, will provide better momentum measurement and trigger capabilities for muons from B-meson decays. The High Granularity Timing Detector (HGTD), which will be installed in front of the end cap calorimeters, will measure the time-of-flight of particles from B-meson decays with a resolution of about 30 ps [205], which will help to mitigate the pile-up effects and improve the signal-to-background ratio. These improvements will significantly reduce the systematic uncertainty of the measurements beyond what is reported in this dissertation. Additionally, continuous monitoring and mitigation of the radiation damage effects on the ATLAS ITk using predictions of leakage current and depletion voltage through the improved Hamburg Model, and combined with the methods developed for quality control during the pre-production phase of the ATLAS ITk modules, could potentially lead to the discovery of New Physics using the statistics collected by the upgraded ATLAS Detector.

The Future Circular Collider (FCC) [206], operating as a hadron collider, is conceived as the successor to the LHC, has the potential to redefine the landscape of particle physics research. With its unprecedented collision energy levels of 100 TeV, nearly eight times that of the LHC, the FCC will delve deeper into the realm of B-meson dynamics. Harnessing its superior luminosity and energy, the FCC is anticipated to significantly enhance the precision of measurements pertaining to B-meson lifetimes and the observation of CP-violation in B-mesons, thereby contributing to a richer understanding of these fundamental particles. In light of the anticipated

increase in particle fluence near the beam by a factor of a thousand compared to the levels at the HL-LHC, the imperative for simulating radiation-induced damage effects in silicon sensors and the development of radiation-resistant silicon sensors is underscored. This marks a new frontier in our quest to unravel the mysteries of the universe.

Appendix A

Lifetimes of $B^0_{\rm d}$ and $B^{\pm}$ Mesons

A.1 Time Efficiencies

A number of studies were performed to understand how time efficiency functions for triggers and selection cuts impact the lifetimes. The following time efficiencies were obtained for each year:

- correction for the condition "inclusiveTrueBd==1" only; this condition ensures that the selected candidates have four tracks,
- correction for selection cuts and "inclusiveTrueBd==1",
- correction for trigger selection and "inclusiveTrueBd==1", and
- correction for all of the above.

The above were obtained by using ratios of the following candidates to the true signal candidates, for

- all candidates; or
- best χ^2 candidates.

The time efficiencies were then used for lifetime fits to the best χ^2 candidates. Lifetimes for each case mentioned above are shown in Figures A.1, A.2 and A.3 for 2015-16, 2017, and 2018, respectively.

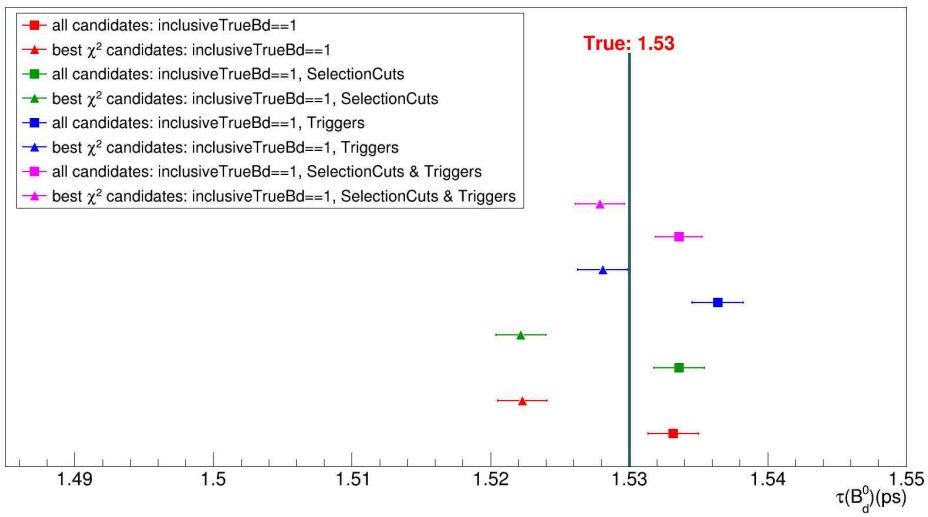

Figure A.1: A comparison of B^0_d lifetime measurement results using the 2015-16 MC.

From the figures, it can be seen that the results were pushed towards the right of the true lifetime which is 1.53 ps for both the best χ^2 candidates and all candidates if time efficiency functions for triggers were used. However, there was no impact due to time efficiencies for selection cuts. For the remainder of the study, the time efficiencies for "inclusiveTrudeBd==1", selection cuts, and triggers were used for each year.

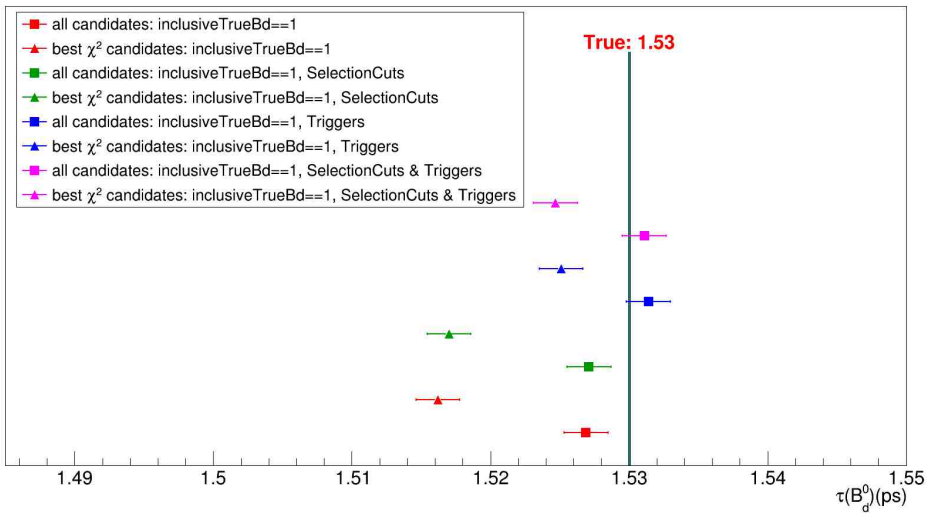

Figure A.2: A comparison of B^0_d lifetime measurement results using the 2017 MC.

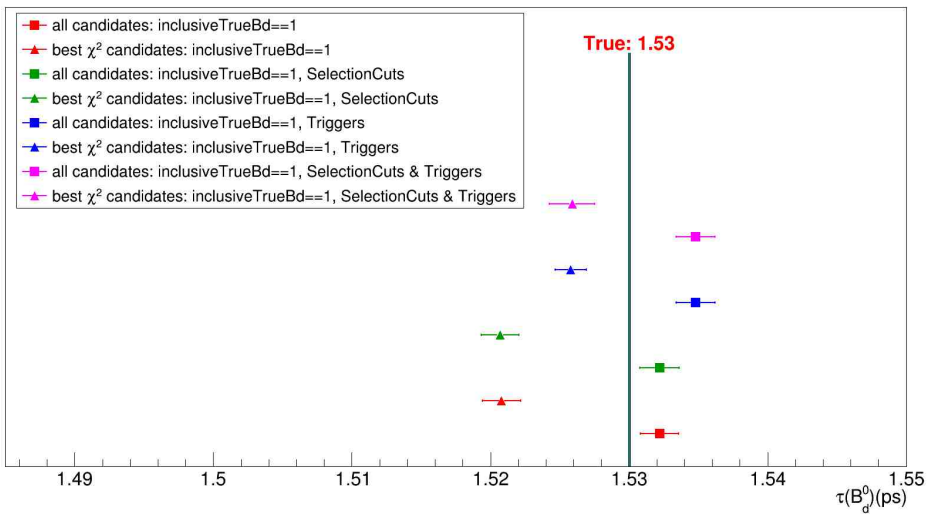

Figure A.3: A comparison of B^0_d lifetime measurement results using the 2018 MC.

Appendix B

CP-violation in $B_{\rm S}^0 \to J/\psi\phi$ Decays

B.1 Time-dependent Amplitudes and Angular Functions

The final time-dependent amplitudes and the additional S-wave terms are shown in Table B.2. The amplitudes for $k = (1 \to 6)$ correspond to P-wave states. Accounting for the S-wave contribution introduces four additional amplitudes: the S-wave amplitude for $k = 7$ and interference terms between the S-wave and P-wave decays for $k = (8, 9, 10)$. To each amplitude $\mathcal{O}^{(k)}(t)$ corresponds an angular function $g^{(k)}(\theta_{\rm T}, \psi_{\rm T}, \phi_{\rm T})$. The summary of angular functions is shown in Table B.1.

k	$g^{(k)}(\theta_T, \psi_T, \phi_T)$
1	$2\cos^2\psi_T(1-\sin^2\theta_T\cos^2\phi_T)$
2	$\sin^2\psi_T(1-\sin^2\theta_T\sin^2\phi_T)$
3	$\sin^2\psi_T\sin^2\theta_T$
4	$\frac{1}{\sqrt{2}}\sin 2\psi_T\sin^2\theta_T\sin 2\phi_T$
5	$-\sin^2\psi_T\sin 2\theta_T\sin\phi_T$
6	$\frac{1}{\sqrt{2}}\sin 2\psi_T\sin 2\theta_T\cos\phi_T$
7	$\frac{2}{3}(1-\sin^2\theta_T\cos^2\phi_T)$
8	$\frac{1}{3}\sqrt{6}\sin\psi_T\sin^2\theta_T\sin 2\phi_T$
9	$\frac{1}{3}\sqrt{6}\sin\psi_T\sin 2\theta_T\cos\phi_T$
10	$\frac{4}{3}\sqrt{3}\cos\psi_T(1-\sin^2\theta_T\cos^2\phi_T)$

Table B.1: The angular functions $g^{(k)}(\theta_T, \psi_T, \phi_T)$ for the $B_s^0 \to J/\psi\phi$ decay including the S-wave contribution.

k	$g^{(k)}(\theta_T, \psi_T, \phi_T)$
1	$\frac{1}{2}\lvert A_0(0)\rvert^2 \Big[(1+\cos\phi_s)e^{-\Gamma_L^{(s)}t} + (1-\cos\phi_s)e^{-\Gamma_H^{(s)}t} \pm 2e^{-\Gamma_s t}\sin(\Delta m_s t)\sin\phi_s\Big]$
2	$\frac{1}{2}\lvert A_\parallel(0)\rvert^2 \Big[(1+\cos\phi_s)e^{-\Gamma_L^{(s)}t} + (1-\cos\phi_s)e^{-\Gamma_H^{(s)}t} \pm 2e^{-\Gamma_s t}\sin(\Delta m_s t)\sin\phi_s\Big]$
3	$\frac{1}{2}\lvert A_\perp(0)\rvert^2 \Big[(1-\cos\phi_s)e^{-\Gamma_L^{(s)}t} + (1+\cos\phi_s)e^{-\Gamma_H^{(s)}t} \mp 2e^{-\Gamma_s t}\sin(\Delta m_s t)\sin\phi_s\Big]$
4	$\frac{1}{2}\lvert A_0(0)\rvert\lvert A_\parallel(0)\rvert\cos\delta_\parallel \Big[(1+\cos\phi_s)e^{-\Gamma_L^{(s)}t} + (1-\cos\phi_s)e^{-\Gamma_H^{(s)}t} \pm 2e^{-\Gamma_s t}\sin(\Delta m_s t)\sin\phi_s\Big]$
5	$\lvert A_\parallel(0)\rvert\lvert A_\perp(0)\rvert \Big[\frac{1}{2}(e^{-\Gamma_L^{(s)}t} - e^{-\Gamma_H^{(s)}t})\cos(\delta_\perp - \delta_\parallel)\sin\phi_s \pm e^{-\Gamma_s t}(\sin(\delta_\perp - \delta_\parallel)\cos(\Delta m_s t) - \cos(\delta_\perp - \delta_\parallel)\cos\phi_s\sin(\Delta m_s t))\Big]$
6	$\lvert A_0(0)\rvert\lvert A_\perp(0)\rvert \Big[\frac{1}{2}(e^{-\Gamma_L^{(s)}t} - e^{-\Gamma_H^{(s)}t})\cos\delta_\perp\sin\phi_s \pm e^{-\Gamma_s t}(\sin\delta_\perp\cos(\Delta m_s t) - \cos\delta_\perp\cos\phi_s\sin(\Delta m_s t))\Big]$
7	$\frac{1}{2}\lvert A_S(0)\rvert^2 \Big[(1-\cos\phi_s)e^{-\Gamma_L^{(s)}t} + (1+\cos\phi_s)e^{-\Gamma_H^{(s)}t} \mp 2e^{-\Gamma_s t}\sin(\Delta m_s t)\sin\phi_s\Big]$
8	$\alpha\lvert A_S(0)\rvert\lvert A_\parallel(0)\rvert \Big[\frac{1}{2}(e^{-\Gamma_L^{(s)}t} - e^{-\Gamma_H^{(s)}t})\sin(\delta_\parallel - \delta_S)\sin\phi_s \pm e^{-\Gamma_s t}(\cos(\delta_\parallel - \delta_S)\cos(\Delta m_s t) - \sin(\delta_\parallel - \delta_S)\cos\phi_s\sin(\Delta m_s t))\Big]$
9	$\frac{1}{2}\lvert A_S(0)\rvert\lvert A_\perp S(0)\rvert\sin(\delta_\perp - \delta_S) \Big[(1-\cos\phi_s)e^{-\Gamma_L^{(s)}t} + (1+\cos\phi_s)e^{-\Gamma_H^{(s)}t} \mp 2e^{-\Gamma_s t}\sin(\Delta m_s t)\sin\phi_s\Big]$
10	$\alpha\lvert A_0(0)\rvert\lvert A_S(0)\rvert \Big[\frac{1}{2}(e^{-\Gamma_H^{(s)}t} - e^{-\Gamma_L^{(s)}t})\sin\delta_S\sin\phi_s \pm e^{-\Gamma_s t}(\cos\delta_S\cos(\Delta m_s t) - \sin\delta_S\cos\phi_s\sin(\Delta m_s t))\Big]$

Table B.2: The time dependent amplitudes $\mathcal{O}^{(k)}(t)$ for the $B_s^0 \to J/\psi\phi$ decay including the S-wave contribution.

Appendix C

Quality Assurance of the Next Generation ATLAS Detector

C.1 Metrology and Mass Measurements

A total of 28 flexes were measured using the Vertex-261 instrument and the results are shown in Table C.1.

Flex ID	Mass (g)	X (mm)	Y (mm)	AVG GA thickness (mm)	STD DEV GA (mm)	AVG thickness - Power Connector (mm)	AVG thickness - HV Capacitor (mm)
0046	1.580	39.605	40.566	0.208	0.001	1.519	1.803
0492	1.558	39.562	40.562	0.204	0.004	1.585	1.848
0353	1.576	39.586	40.575	0.207	0.002	1.603	1.846
0354	1.584	39.590	40.573	0.207	0.002	1.569	1.950
0355	1.579	39.587	40.576	0.207	0.002	1.552	1.823
0356	1.591	39.634	40.571	0.207	0.002	1.583	1.914
0440	1.590	39.582	40.554	0.211	0.001	1.592	1.979
0066	1.587	39.573	40.562	0.208	0.005	1.538	1.935
0458	1.572	39.561	40.559	0.209	0.002	1.525	1.965
0170	1.592	39.575	40.553	0.210	0.002	1.523	1.924
0564	1.599	39.579	40.552	0.209	0.004	1.527	1.931
0440	1.596	39.595	40.564	0.205	0.005	1.561	1.913
0061	1.592	39.588	40.564	0.208	0.005	1.540	1.930
0014	1.585	39.595	40.562	0.207	0.003	1.531	1.892
0015	1.583	39.567	40.556	0.208	0.004	1.537	1.915
0173	1.588	39.592	40.563	0.208	0.003	1.517	1.949
0016	1.587	39.573	40.553	0.207	0.003	1.545	1.907
0460	1.578	39.585	40.557	0.212	0.002	1.518	1.913
0013	1.584	39.571	40.562	0.200	0.004	1.543	1.929
0074	1.586	39.591	40.567	0.208	0.003	1.551	1.905
0175	1.581	39.565	40.563	0.207	0.003	1.590	1.915
0176	1.590	39.571	40.560	0.210	0.004	1.534	1.929
0437	1.590	39.573	40.562	0.209	0.002	1.557	1.921
0457	1.575	39.570	40.570	0.206	0.003	1.522	1.907
0459	1.575	39.562	40.564	0.212	0.004	1.521	1.939
0466	1.584	39.591	40.557	0.204	0.002	1.530	1.895
0554	1.600	39.598	40.567	0.204	0.005	1.540	1.916
0563	1.593	39.567	40.554	0.212	0.002	1.560	1.934
AVG	1.585	39.582	40.562	0.208	0.003	1.547	1.912

Table C.1: Metrology and mass measurements of 28 ITk Pixel flexes.

Bibliography

[1] O. S. Brüning et al. *LHC Design Report*. CERN Yellow Reports: Monographs. Geneva: CERN, 2004. URL: https://cds.cern.ch/record/782076 (cit. on pp. 1, 4).

[2] ATLAS Collaboration. "The ATLAS Experiment at the CERN Large Hadron Collider." *JINST* 3.08 (Aug. 2008), S08003. URL: https://dx.doi.org/10.1088/1748-0221/3/08/S08003 (cit. on pp. 1, 5, 11, 13, 15, 18, 19, 22, 181).

[3] F. Englert and R. Brout. "Broken Symmetry and the Mass of Gauge Vector Mesons." *Phys. Rev. Lett.* 13 (9 Aug. 1964), pp. 321–323. URL: https://link.aps.org/doi/10.1103/PhysRevLett.13.321 (cit. on p. 3).

[4] Sheldon L. Glashow. "Partial-symmetries of weak interactions." *Nuclear Physics* 22.4 (1961), pp. 579–588. URL: https://www.sciencedirect.com/science/article/pii/0029558261904692 (cit. on p. 3).

[5] G. S. Guralnik, C. R. Hagen, and T. W. B. Kibble. "Global Conservation Laws and Massless Particles." *Phys. Rev. Lett.* 13 (20 Nov. 1964), pp. 585–587. URL: https://link.aps.org/doi/10.1103/PhysRevLett.13.585 (cit. on p. 3).

[6] Peter W. Higgs. "Broken Symmetries and the Masses of Gauge Bosons." *Phys. Rev. Lett.* 13 (16 Oct. 1964), pp. 508–509. URL: https://link.aps.org/doi/10.1103/PhysRevLett.13.508 (cit. on p. 3).

[7] Abdus Salam. "Gauge unification of fundamental forces." *Rev. Mod. Phys.* 52 (3 July 1980), pp. 525–538. URL: https://link.aps.org/doi/10.1103/RevModPhys.52.525 (cit. on p. 3).

[8] Steven Weinberg. "A Model of Leptons." *Phys. Rev. Lett.* 19 (21 Nov. 1967), pp. 1264–1266. URL: https://link.aps.org/doi/10.1103/PhysRevLett.19.1264 (cit. on p. 3).

[9] C. N. Yang and R. L. Mills. "Conservation of Isotopic Spin and Isotopic Gauge Invariance." *Phys. Rev.* 96 (1 Oct. 1954), pp. 191–195. URL: https://link.aps.org/doi/10.1103/PhysRev.96.191 (cit. on p. 3).

[10] Particle Data Group et al. "Review of Particle Physics." *Progress of Theoretical and Experimental Physics* 2020.8 (Aug. 2020). 083C01. URL: https://doi.org/10.1093/ptep/ptaa104 (cit. on pp. 4, 42, 46, 47, 65, 69, 77, 78, 81, 88, 89, 98, 101–103, 109, 138, 142, 143, 147, 277).

[11] M. B. Gavela et al. "Standard Model *CP*-violation and Baryon Asymmetry." *Mod. Phys. Lett. A* 09.09 (Mar. 1994), pp. 795–809. URL: https://doi.org/10.1142/S0217732394000629 (cit. on p. 4).

[12] Patrick Huet and Eric Sather. "Electroweak baryogenesis and standard model CP violation." *Phys. Rev. D* 51 (1995), pp. 379–394 (cit. on p. 4).

[13] K. C. Freeman. "On the Disks of Spiral and S0 Galaxies." *The Astrophysical Journal* 160 (June 1970), p. 811 (cit. on p. 4).

[14] Vera C. Rubin and W. Kent Ford Jr. "Rotation of the Andromeda Nebula from a Spectroscopic Survey of Emission Regions." *The Astrophysical Journal* 159 (Feb. 1970), p. 379 (cit. on p. 4).

[15] F. Zwicky. "On the Masses of Nebulae and of Clusters of Nebulae." *The Astrophysical Journal* 86 (Oct. 1937), p. 217 (cit. on p. 4).

[16] S. Perlmutter et al. "Measurements of Ω and Λ from 42 High-Redshift Supernovae." *The Astrophysical Journal* 517.2 (June 1999), p. 565. URL: https://dx.doi.org/10.1086/307221 (cit. on p. 4).

[17] A. G. Riess et al. "Observational Evidence from Supernovae for an Accelerating Universe and a Cosmological Constant." *The Astronomical Journal* 116.3 (Sept. 1998), p. 1009. URL: https://dx.doi.org/10.1086/300499 (cit. on p. 4).

[18] K. S. Babu and Christopher Kolda. "Higgs-Mediated $B^0 \to \mu^+\mu^-$ in Minimal Supersymmetry." *Phys. Rev. Lett.* 84 (2 Jan. 2000), pp. 228–231. URL: https://link.aps.org/doi/10.1103/PhysRevLett.84.228 (cit. on p. 4).

[19] S. R. Choudhury et al. "Signatures Of New Physics In Dileptonic B-decays." *Int. J. Mod. Phys. A* 21.12 (2006), pp. 2617–2634. URL: https://doi.org/10.1142/S0217751X06029491 (cit. on p. 4).

[20] S. Rai Choudhury and Naveen Gaur. "Dileptonic decay of B_s meson in SUSY models with large $\tan\beta$." *Phys. Lett. B* 451.1 (1999), pp. 86–92. URL: https://www.sciencedirect.com/science/article/pii/S0370269399002038 (cit. on p. 4).

[21] C. Hamzaoui, M. Pospelov, and M. Toharia. "Higgs-boson-mediated FCNC in supersymmetric models with large $\tan\beta$." *Phys. Rev. D* 59 (9 Apr. 1999),

p. 095005. URL: https://link.aps.org/doi/10.1103/PhysRevD.59.095005 (cit. on p. 4).

[22] Chao-Shang Huang, Wei Liao, and Qi-Shu Yan. "Promising process to distinguish supersymmetric models with large $\tan\beta$ from the standard model: $B \to X_s\mu^+\mu^-$." *Phys. Rev. D* 59 (1 Nov. 1998), p. 011701. URL: https://link.aps.org/doi/10.1103/PhysRevD.59.011701 (cit. on p. 4).

[23] Andrzej J. Buras. "Relations between $\Delta M_{s,d}$ and $B_{s,d} \to \mu\overline{\mu}$ in models with minimal flavour violation." *Phys. Lett. B* 566.1 (2003), pp. 115–119. URL: https://www.sciencedirect.com/science/article/pii/S0370269303005616 (cit. on p. 4).

[24] G. D'Ambrosio et al. "Minimal flavour violation: an effective field theory approach." *Nucl. Phys. B* 645.1 (2002), pp. 155–187. URL: https://www.sciencedirect.com/science/article/pii/S0550321302008362 (cit. on p. 4).

[25] Sacha Davidson and Sébastien Descotes-Genon. "Minimal Flavour Violation for leptoquarks." *JHEP* 2010.11 (Nov. 2010). URL: https://doi.org/10.48550/arXiv.1009.1998 (cit. on p. 4).

[26] D. Guadagnoli and G. Isidori. "$\mathcal{B}(B \to \mu^+\mu^-)$ as an electroweak precision test." *Phys. Lett. B* 724.1 (2013), pp. 63–67. URL: https://www.sciencedirect.com/science/article/pii/S037026931300436X (cit. on p. 4).

[27] CMS Collaboration. "The CMS experiment at the CERN LHC." *JINST* 3.08 (Aug. 2008), S08004. URL: https://dx.doi.org/10.1088/1748-0221/3/08/S08004 (cit. on p. 5).

[28] LHCb Collaboration. "The LHCb Detector at the LHC." *JINST* 3.08 (Aug. 2008), S08005. URL: https://dx.doi.org/10.1088/1748-0221/3/08/S08005 (cit. on p. 5).

[29] ALICE Collaboration. "The ALICE experiment at the CERN LHC." *JINST* 3.08 (Aug. 2008), S08002. URL: https://dx.doi.org/10.1088/1748-0221/3/08/S08002 (cit. on pp. 5, 11).

[30] Ewa Lopienska. "The CERN accelerator complex, layout in 2022" (2022). General Photo. URL: https://cds.cern.ch/record/2800984 (cit. on p. 5).

[31] W. Herr and B. Muratori. "Concept of luminosity" (2006). URL: https://cds.cern.ch/record/941318 (cit. on pp. 7, 8).

[32] F. Halzen and A. D. Martin. *Quarks and Leptons: An introductory course in modern particle physics*. Wiley, 1984 (cit. on p. 7).

[33] S. Mandelstam. "Determination of the Pion-Nucleon Scattering Amplitude from Dispersion Relations and Unitarity: General Theory." *Phys. Rev.* 112 (4 Nov. 1958), pp. 1344–1360. URL: https://link.aps.org/doi/10.1103/PhysRev.112.1344 (cit. on p. 7).

[34] ATLAS Collaboration. "Luminosity determination in pp collisions at $\sqrt{s} =$ 13 TeV using the ATLAS detector at the LHC" (2019). URL: https://cds.cern.ch/record/2677054 (cit. on p. 9).

[35] ATLAS Collaboration. *"ATLAS Luminosity Public Results in Run 2"*. URL: https://twiki.cern.ch/twiki/bin/view/AtlasPublic/LuminosityPublicResultsRun2 (cit. on p. 10).

[36] URL: http://lhc-commissioning.web.cern.ch/schedule/LHC-long-term.htm (cit. on pp. 9, 188).

[37] B. Abbott et al. "Production and integration of the ATLAS Insertable B-Layer." *JINST* 13.05 (May 2018), T05008. URL: https://dx.doi.org/10.1088/1748-0221/13/05/T05008 (cit. on p. 16).

[38] G. Aad et al. "ATLAS pixel detector electronics and sensors." *JINST* 3.07 (July 2008), P07007. URL: https://dx.doi.org/10.1088/1748-0221/3/07/P07007 (cit. on p. 16).

[39] ATLAS Collaboration. *A Leakage Current-based Measurement of the Radiation Damage in the ATLAS Pixel Detector*. Tech. rep. Geneva: CERN, 2014. URL: https://cds.cern.ch/record/1752122 (cit. on p. 16).

[40] ATLAS Collaboration. *Technical Design Report for the ATLAS Inner Tracker Pixel Detector*. Tech. rep. Geneva: CERN, 2017. URL: https://cds.cern.ch/record/2285585 (cit. on pp. 16, 152, 189, 190, 212).

[41] C. Da Viá et al. "3D silicon sensors: Design, large area production and quality assurance for the ATLAS IBL pixel detector upgrade." *Nucl. Instrum. and Meth. A* 694 (2012), pp. 321–330. URL: https://www.sciencedirect.com/science/article/pii/S0168900212008509 (cit. on p. 17).

[42] ATLAS Collaboration. "Operation and performance of the ATLAS semiconductor tracker." *JINST* 9.08 (Aug. 2014), P08009–P08009. URL: https://doi.org/10.48550/arXiv.1404.7473 (cit. on p. 17).

[43] ATLAS TRT Collaboration et al. "The ATLAS Transition Radiation Tracker (TRT) proportional drift tube: design and performance." *JINST* 3.02 (Feb.

2008), P02013. URL: https://dx.doi.org/10.1088/1748-0221/3/02/P02013 (cit. on p. 18).

[44] ATLAS Collaboration. "ATLAS Forward Detectors." General Photo. 2018. URL: https://cds.cern.ch/record/2627582 (cit. on p. 25).

[45] G. Aad et al. "Luminosity Determination in *pp* Collisions at $\sqrt{s} = 7$ TeV Using the ATLAS Detector at the LHC." *Eur. Phys. J. C* 71 (2011), p. 1630 (cit. on p. 26).

[46] G. Avoni et al. "The new LUCID-2 detector for luminosity measurement and monitoring in ATLAS." *JINST* 13.07 (July 2018), P07017. URL: https://dx.doi.org/10.1088/1748-0221/13/07/P07017 (cit. on pp. 27, 44).

[47] M. Leite. "Performance of the ATLAS Zero Degree Calorimeter" (2013). URL: https://cds.cern.ch/record/1613233 (cit. on p. 27).

[48] J. Lange et al. "Beam tests of an integrated prototype of the ATLAS Forward Proton detector." *JINST* 11.09 (Sept. 2016). URL: https://dx.doi.org/10.1088/1748-0221/11/09/P09005 (cit. on p. 27).

[49] Maciej Trzebinski, Rafal Staszewski, and Janusz Chwastowski. "LHC High β^* Runs: Transport and Unfolding Methods." *ISRN High Energy Phys.* 2012 (2012), p. 491460 (cit. on p. 28).

[50] G. Aad et al. "Measurement of the total cross section from elastic scattering in *pp* collisions at $\sqrt{s} = 7$ TeV with the ATLAS detector." *Nucl. Phys. B* 889 (2014), pp. 486–548. URL: https://www.sciencedirect.com/science/article/pii/S0550321314003253 (cit. on p. 28).

[51] URL: https://atlassoftwaredocs.web.cern.ch/athena/ (cit. on p. 28).

[52] A. Buckley et al. "The HepMC3 event record library for Monte Carlo event generators." *Comput. Phys. Commun.* 260 (2021), p. 107310. URL: https://www.sciencedirect.com/science/article/pii/S0010465520301181 (cit. on p. 29).

[53] S. Agostinelli et al. "GEANT4–a simulation toolkit." *Nucl. Instr. and Meth. A* 506 (2003), pp. 250–303 (cit. on pp. 29, 155).

[54] I. Antcheva et al. "ROOT: A C++ framework for petabyte data storage, statistical analysis and visualization." *Comput. Phys. Commun.* 180 (2009), pp. 2499–2512 (cit. on p. 29).

[55] W. Verkerke and D. Kirkby. *RooFit Users Manual v2.91*. URL: https://root.cern.ch/download/doc/RooFit_Users_Manual_2.91-33.pdf (cit. on p. 29).

[56] L. Moneta et al. "The RooStats Project." *PoS* ACAT2010 (2010). Ed. by T. Speer et al., p. 057 (cit. on p. 29).

[57] P. Mato. *GAUDI-Architecture design document*. Tech. rep. Geneva: CERN, 1998. URL: https://cds.cern.ch/record/691746 (cit. on p. 29).

[58] G. A. Stewart et al. "Multi-threaded software framework development for the ATLAS experiment." *Journal of Physics: Conference Series* 762.1 (Oct. 2016), p. 012024. URL: https://dx.doi.org/10.1088/1742-6596/762/1/012024 (cit. on p. 29).

[59] URL: https://root.cern/doc/v620/release-notes.html#release-6.2006 (cit. on p. 30).

[60] P. J. Laycock et al. "Derived Physics Data Production in ATLAS: Experience with Run 1 and Looking Ahead." *Journal of Physics: Conference Series* 513.3 (June 2014), p. 032052. URL: https://dx.doi.org/10.1088/1742-6596/513/3/032052 (cit. on p. 31).

[61] D. Adams et al. "Dual-use tools and systematics-aware analysis workflows in the ATLAS Run-2 analysis model." *Journal of Physics: Conference Series* 664.3 (Dec. 2015), p. 032007. URL: https://dx.doi.org/10.1088/1742-6596/664/3/032007 (cit. on pp. 31, 32).

[62] Torbjörn Sjöstrand, Stephen Mrenna, and Peter Skands. "A brief introduction to PYTHIA 8.1." *Comput. Phys. Commun.* 178.11 (2008), pp. 852–867. URL: https://www.sciencedirect.com/science/article/pii/S0010465508000441 (cit. on pp. 33, 34).

[63] G. Marchesini et al. "HERWIG: A Monte Carlo event generator for simulating hadron emission reactions with interfering gluons. Version 5.1 - April 1991." *Comput. Phys. Commun.* 67 (1992), pp. 465–508 (cit. on p. 33).

[64] M. Smizanska. *PythiaB an interface to Pythia6 dedicated to simulation of beauty events*. Tech. rep. Geneva: CERN, 2003. URL: https://cds.cern.ch/record/681440 (cit. on pp. 33, 34).

[65] D. J. Lange. "The EvtGen particle decay simulation package." *Nucl. Instrum. Meth. A* 462 (2001). Ed. by S. Erhan, P. Schlein, and Y. Rozen, pp. 152–155 (cit. on p. 33).

[66] ATLAS Collaboration. *ATLAS Level-1 Trigger: Technical Design Report*. CERN, 1998. URL: http://cds.cern.ch/record/381429 (cit. on p. 35).

[67] P. Jenni et al. *ATLAS high-level trigger, data-acquisition and controls: Technical Design Report*. Geneva: CERN, 2003. URL: http://cds.cern.ch/record/616089 (cit. on p. 36).

[68] Moritz Backes. "The ATLAS Trigger System: Ready for Run-2." *PoS* Lepton-Photon 2015 (2016), p. 045 (cit. on p. 36).

[69] ATLAS Collaboration. *Technical Design Report for the Phase-I Upgrade of the ATLAS TDAQ System*. Tech. rep. Final version presented to December 2013 LHCC. 2013. URL: https://cds.cern.ch/record/1602235 (cit. on p. 36).

[70] R. Achenbach et al. "The ATLAS Level-1 Calorimeter Trigger." *JINST* 3.03 (Mar. 2008), P03001. URL: https://dx.doi.org/10.1088/1748-0221/3/03/P03001 (cit. on p. 36).

[71] G. Aad et al. "Performance of the ATLAS muon triggers in Run 2." *JINST* 15.09 (2020), P09015 (cit. on p. 37).

[72] Rosa Simoniello. "The ATLAS Level-1 Topological Processor: from design to routine usage in Run-2." *2018 IEEE Nuclear Science Symposium and Medical Imaging Conference Proceedings (NSS/MIC)*. 2018, pp. 1–4 (cit. on p. 37).

[73] M. Elsing et al. "The ATLAS Tier-0: Overview and operational experience." *Journal of Physics: Conference Series* 219.7 (Apr. 2010), p. 072011. URL: https://dx.doi.org/10.1088/1742-6596/219/7/072011 (cit. on p. 38).

[74] V. A. Khoze and M. A. Shifman. "Heavy quarks." *Phys. Usp.* 26.5 (May 1983), p. 387. URL: https://dx.doi.org/10.1070/PU1983v026n05ABEH004398 (cit. on p. 42).

[75] I. I. Bigi. *The QCD Perspective on Lifetimes of Heavy-Flavour Hadrons*. 1995. URL: https://arxiv.org/pdf/hep-ph/9508408.pdf (cit. on p. 42).

[76] I. I. Y. Bigi et al. *Nonleptonic decays of beauty hadrons: From phenomenology to theory*. Jan. 1994. URL: https://arxiv.org/pdf/hep-ph/9401298.pdf (cit. on p. 42).

[77] N. Uraltsev. "Heavy quark expansion in beauty and its decays." *Proc. Int. Sch. Phys. Fermi* 137 (1998). Ed. by I. I. Y. Bigi and L. Moroni, pp. 329–409 (cit. on p. 42).

[78] M. Neubert. "B decays and the heavy quark expansion." *Adv. Ser. Direct. High Energy Phys.* 15 (1998). Ed. by A. J. Buras and M. Lindner, pp. 239–293 (cit. on p. 42).

[79] I. I Bigi and N.G. Uraltsev. "Gluonic enhancements in non-spectator beauty decays—an inclusive mirage though an exclusive possibility." *Phys. Lett. B* 280.3 (1992), pp. 271–280. URL: https://www.sciencedirect.com/science/article/pii/037026939290066D (cit. on p. 42).

[80] I. I. Bigi, N.G. Uraltsev, and A.I. Vainshtein. "Nonperturbative corrections to inclusive beauty and charm decays. QCD versus phenomenological models." *Phys. Lett. B* 293.3 (1992), pp. 430–436. URL: https://www.sciencedirect.com/science/article/pii/037026939290908M (cit. on p. 42).

[81] Gerhard Buchalla, Andrzej J. Buras, and Markus E. Lautenbacher. "Weak decays beyond leading logarithms." *Rev. Mod. Phys.* 68 (4 Oct. 1996), pp. 1125–1244. URL: https://link.aps.org/doi/10.1103/RevModPhys.68.1125 (cit. on p. 42).

[82] M. Kirk, A. Lenz, and T. Rauh. "Dimension-six matrix elements for meson mixing and lifetimes from sum rules." *JHEP* 12 (2017). [Erratum: JHEP 06, 162 (2020)], p. 068 (cit. on p. 43).

[83] M.A. Shifman, A.I. Vainshtein, and V.I. Zakharov. "QCD and resonance physics. theoretical foundations." *Nuclear Physics B* 147.5 (1979), pp. 385–447. URL: https://www.sciencedirect.com/science/article/pii/0550321379900221 (cit. on p. 43).

[84] M.A. Shifman, A.I. Vainshtein, and V.I. Zakharov. "QCD and resonance physics. applications." *Nuclear Physics B* 147.5 (1979), pp. 448–518. URL: https://www.sciencedirect.com/science/article/pii/0550321379900233 (cit. on p. 43).

[85] Howard Georgi. "An effective field theory for heavy quarks at low energies." *Phys. Lett. B* 240.3 (1990), pp. 447–450. URL: https://www.sciencedirect.com/science/article/pii/037026939091128X (cit. on pp. 43, 44).

[86] R. Aaij et al. "Measurements of the B^+, B^0, B_s^0 meson and Λ_b^0 baryon lifetimes." *JHEP* 04 (2014), p. 114 (cit. on p. 44).

[87] R. Aaij et al. "Effective lifetime measurements in the $B_s^0 \to K^+K^-$, $B^0 \to K^+\pi^-$ and $B_s^0 \to \pi^+K^-$ decays." *Phys. Lett. B* 736 (2014), pp. 446–454 (cit. on p. 44).

[88] ATLAS Collaboration. "Measurement of the B_{d}^0 and B_{s}^0 lifetimes in the decay modes $B_{\mathrm{d}}^0 \to J/\psi K^{*0}$ and $B_{\mathrm{s}}^0 \to J/\psi\phi$ in ATLAS" (July 2011) (cit. on p. 44).

[89] G. Aad et al. "Measurement of the Λ_b^0 lifetime and mass in the ATLAS experiment." *Phys. Rev. D* 87.3 (2013), p. 032002 (cit. on p. 44).

[90] A. M. Sirunyan et al. "Measurement of b hadron lifetimes in pp collisions at $\sqrt{s} = 8$ TeV." *Eur. Phys. J. C* 78.6 (2018). [Erratum: Eur.Phys.J.C 78, 561 (2018)], p. 457 (cit. on p. 44).

[91] G. Aad et al. "Luminosity determination in *pp* collisions at $\sqrt{s} = 13$ TeV using the ATLAS detector at the LHC." *Eur. Phys. J. C* 83.10 (2023), p. 982 (cit. on p. 44).

[92] T. Sjöstrand et al. "An introduction to PYTHIA 8.2." *Comput. Phys. Commun.* 191 (2015), pp. 159–177 (cit. on pp. 44, 156).

[93] *ATLAS Pythia 8 tunes to 7 TeV data*. Tech. rep. Geneva: CERN, 2014. URL: https://cds.cern.ch/record/1966419 (cit. on p. 45).

[94] J. Pumplin et al. "New generation of parton distributions with uncertainties from global QCD analysis." *JHEP* 07 (2002), p. 012 (cit. on p. 45).

[95] G. Aad et al. "The ATLAS Simulation Infrastructure." *Eur. Phys. J. C* 70 (2010), pp. 823–874 (cit. on p. 45).

[96] S. Agostinelli et al. "Geant4—a simulation toolkit." *Nucl. Instr. and Meth. A* 506.3 (2003), pp. 250–303. URL: https://www.sciencedirect.com/science/article/pii/S0168900203013688 (cit. on p. 45).

[97] G. Aad et al. "Muon reconstruction and identification efficiency in ATLAS using the full Run 2 *pp* collision data set at $\sqrt{s} = 13$ TeV." *Eur. Phys. J. C* 81.7 (2021), p. 578 (cit. on p. 45).

[98] ATLAS collaboration. *Vertex Reconstruction Performance of the ATLAS Detector at* $\sqrt{s} = 13$ *TeV*. Tech. rep. Geneva: CERN, 2015. URL: https://cds.cern.ch/record/2037717 (cit. on p. 47).

[99] N. L. Johnson. "Systems Of Frequency Curves Generated By Methods Of Translation." *Biometrika* 36.1-2 (June 1949), pp. 149–176. URL: https://doi.org/10.1093/biomet/36.1-2.149 (cit. on p. 49).

[100] Muriel Pivk and Francois R. Le Diberder. "SPlot: A statistical tool to unfold data distributions." *Nucl. Instrum. Meth. A* 555 (2005), pp. 356–369 (cit. on p. 51).

[101] R. Fleischer and R. Knegjens. "Effective Lifetimes of B_s Decays and their Constraints on the B_s^0-$\bar{B}_s^0$ Mixing Parameters." *Eur. Phys. J. C* 71 (2011), p. 1789 (cit. on p. 51).

[102] Y. S. Amhis et al. "Averages of b-hadron, c-hadron, and τ-lepton properties as of 2018." *Eur. Phys. J. C* 81.3 (2021), p. 226 (cit. on pp. 52, 105).

[103] Amol S. Dighe, Isard Dunietz, and Robert Fleischer. "Extracting CKM phases and $B_s - \bar{B}_s$ mixing parameters from angular distributions of nonleptonic B decays." *Eur. Phys. J. C* 6 (1999), pp. 647–662 (cit. on pp. 52, 119).

[104] Y. S. Amhis et al. "Averages of b-hadron, c-hadron, and τ-lepton properties as of 2021." *Phys. Rev. D* 107.5 (2023), p. 052008 (cit. on pp. 52, 84).

[105] URL: https://root.cern.ch/doc/master/classTRandom3.html (cit. on p. 66).

[106] G. Aad et al. "Alignment of the ATLAS Inner Detector in Run-2." *Eur. Phys. J. C* 80.12 (2020), p. 1194 (cit. on p. 79).

[107] J.E. Gaiser. "Charmonium Spectroscopy From Radiative Decays of the J/ψ and ψ'." Ph.D. thesis. Aug. 1982 (cit. on p. 80).

[108] Y. S. Amhis et al. "Averages of b-hadron, c-hadron, and τ-lepton properties as of 2021." *Phys. Rev. D* 107 (2023), p. 052008 (cit. on pp. 81, 118).

[109] Alexander Lenz, Maria Laura Piscopo, and Aleksey V. Rusov. "Disintegration of beauty: a precision study." *JHEP* 01 (2023), p. 004 (cit. on pp. 83, 84).

[110] Damir Becirevic. "Theoretical progress in describing the B meson lifetimes." *PoS* HEP2001 (2001). Ed. by Dezsõ Horváth, Péter Lévai, and András Patkós, p. 098 (cit. on pp. 83, 84).

[111] G. Aad et al. "Measurement of the CP-violating phase ϕ_s in $B_s^0 \to J/\psi\phi$ decays in ATLAS at 13 TeV." *Eur. Phys. J. C* 81.4 (2021), p. 342 (cit. on pp. 83, 84, 118, 124, 130, 133).

[112] E. Noether. "Invariante Variationsprobleme." ger. *Nachr. d. König. Gesellsch. d. Wiss. zu Göttingen, Math-phys. Klasse, Seite 235-157* 1918 (1918), pp. 235–257. URL: http://eudml.org/doc/59024 (cit. on p. 90).

[113] URL: https://en.wikipedia.org/wiki/Chirality_physics (cit. on p. 92).

[114] C. S. Wu et al. "Experimental Test of Parity Conservation in Beta Decay." *Phys. Rev.* 105 (4 Feb. 1957), pp. 1413–1415. URL: https://link.aps.org/doi/10.1103/PhysRev.105.1413 (cit. on p. 94).

[115] URL: https://upload.wikimedia.org/wikipedia/commons/4/41/Parity_violation_principle_Wu_experiment_(English).jpg (cit. on p. 95).

[116] M. Goldhaber, L. Grodzins, and A. W. Sunyar. "Helicity of Neutrinos." *Phys. Rev.* 109 (1958), pp. 1015–1017 (cit. on p. 95).

[117] URL: https://universe-review.ca/R02-14-CPviolation.htm (cit. on p. 96).

[118] J. H. Christenson et al. "Evidence for the 2π Decay of the K_2^0 Meson." *Phys. Rev. Lett.* 13 (4 July 1964), pp. 138–140. URL: https://link.aps.org/doi/10.1103/PhysRevLett.13.138 (cit. on p. 97).

[119] Makoto Kobayashi and Toshihide Maskawa. "CP Violation in the Renormalizable Theory of Weak Interaction." *Prog. Theor. Phys.* 49 (1973), pp. 652–657 (cit. on p. 99).

[120] Nicola Cabibbo. "Unitary Symmetry and Leptonic Decays." *Phys. Rev. Lett.* 10 (12 June 1963), pp. 531–533. URL: https://link.aps.org/doi/10.1103/PhysRevLett.10.531 (cit. on p. 99).

[121] S. L. Glashow, J. Iliopoulos, and L. Maiani. "Weak Interactions with Lepton-Hadron Symmetry." *Phys. Rev. D* 2 (7 Oct. 1970), pp. 1285–1292. URL: https://link.aps.org/doi/10.1103/PhysRevD.2.1285 (cit. on p. 99).

[122] P. Dita. "Parametrisation of unitary matrices." *Journal of Physics A: Mathematical and General* 15.11 (Nov. 1982), p. 3465. URL: https://dx.doi.org/10.1088/0305-4470/15/11/023 (cit. on p. 100).

[123] Ling-Lie Chau and Wai-Yee Keung. "Comments on the Parametrization of the Kobayashi-Maskawa Matrix." *Phys. Rev. Lett.* 53 (1984), p. 1802 (cit. on p. 100).

[124] Lincoln Wolfenstein. "Parametrization of the Kobayashi-Maskawa Matrix." *Phys. Rev. Lett.* 51 (1983), p. 1945 (cit. on p. 101).

[125] C. Jarlskog. "Commutator of the Quark Mass Matrices in the Standard Electroweak Model and a Measure of Maximal CP Nonconservation." *Phys. Rev. Lett.* 55 (1985), p. 1039 (cit. on p. 102).

[126] J. Charles et al. "CP violation and the CKM matrix: assessing the impact of the asymmetric B factories." *E.P.J.C* 41.1 (May 2005), pp. 1–131. URL: https://doi.org/10.1140/epjc/s2005-02169-1 (cit. on pp. 104–106, 117, 119, 120).

[127] B. Aubert et al. "Measurement of time-dependent CP asymmetry in $B^0 \to c\bar{c}K^{(*)0}$ decays." *Phys. Rev. D* 79 (7 Apr. 2009), p. 072009. URL: https://link.aps.org/doi/10.1103/PhysRevD.79.072009 (cit. on pp. 104, 105).

[128] I. Adachi et al. "Precise Measurement of the CP Violation Parameter sin2ϕ_1 in $B^0 \to (c\bar{c})K^0$ Decays." *Phys. Rev. Lett.* 108 (17 Apr. 2012), p. 171802. URL: https://link.aps.org/doi/10.1103/PhysRevLett.108.171802 (cit. on pp. 104, 105).

[129] R. Aaij et al. "Measurement of CP Violation in $B^0 \to J/\psi K^0_S$ Decays." *Phys. Rev. Lett.* 115 (3 July 2015), p. 031601. URL: https://link.aps.org/doi/10.1103/PhysRevLett.115.031601 (cit. on pp. 105, 115).

[130] G. Aad et al. "Flavor tagged time-dependent angular analysis of the $B_s \to J/\psi\phi$ decay and extraction of $\Delta\Gamma$s and the weak phase ϕ_s in ATLAS." *Phys. Rev. D* 90.5 (2014), p. 052007 (cit. on p. 105).

[131] G. Aad et al. "Measurement of the CP-violating phase ϕ_s and the B^0_s meson decay width difference with $B^0_s \to J/\psi\phi$ decays in ATLAS." *JHEP* 08 (2016), p. 147 (cit. on pp. 105, 118).

[132] D. Boutigny et al. *The BABAR physics book: Physics at an asymmetric B factory*. Oct. 1998 (cit. on p. 105).

[133] K. Anikeev et al. *B Physics at the Tevatron: Run II and Beyond*. 2002. URL: https://arxiv.org/abs/hep-ph/0201071 (cit. on p. 105).

[134] Ian C. Brock and Thomas Schörner-Sadenius, eds. *Physics at the Terascale*. 2011 (cit. on p. 105).

[135] Gerhart Lüders. "Proof of the TCP theorem." *Annals of Physics* 2.1 (1957), pp. 1–15. URL: https://www.sciencedirect.com/science/article/pii/0003491657900325 (cit. on pp. 108, 112).

[136] R. Aaij et al. "Measurement of the semileptonic CP asymmetry in $B^0 - \overline{B}^0$ mixing." *Phys. Rev. Lett.* 114 (2015), p. 041601 (cit. on p. 114).

[137] R. Aaij et al. "Measurement of the CP asymmetry in $B_s^0 - \overline{B}_s^0$ mixing." *Phys. Rev. Lett.* 117.6 (2016). [Addendum: Phys. Rev. Lett. 118, 129903 (2017)], p. 061803 (cit. on p. 114).

[138] M. Bona et al. "The Unitarity Triangle Fit in the Standard Model and Hadronic Parameters from Lattice QCD: A Reappraisal after the Measurements of $\Delta m_{\rm s}$ and $BR(B \to \tau\nu_\tau)$." *JHEP* 10 (2006), p. 081 (cit. on p. 117).

[139] Marina Artuso, Guennadi Borissov, and Alexander Lenz. "CP violation in the B_s^0 system." *Rev. Mod. Phys.* 88 (4 Oct. 2016), p. 045002. URL: https://link.aps.org/doi/10.1103/RevModPhys.88.045002 (cit. on pp. 117, 119, 120).

[140] C. T. H. Davies et al. "Lattice QCD Matrix Elements for the $B_s^0 - \overline{B}_s^0$ Width Difference beyond Leading Order." *Phys. Rev. Lett.* 124 (8 Feb. 2020), p. 082001. URL: https://link.aps.org/doi/10.1103/PhysRevLett.124.082001 (cit. on p. 117).

[141] T. Aaltonen et al. "Measurement of the CP-Violating Phase $\beta_s^{J/\psi\phi}$ in $B_s^0 \to J/\psi\phi$ Decays with the CDF II Detector." *Phys. Rev. D* 85 (2012), p. 072002 (cit. on p. 118).

[142] V. M. Abazov et al. "Measurement of the CP-violating phase $\phi_s^{J/\psi\phi}$ using the flavor-tagged decay $B_s^0 \to J/\psi\phi$ in 8 fb^{-1} of $p\bar{p}$ collisions." *Phys. Rev. D* 85 (2012), p. 032006 (cit. on p. 118).

[143] A. M. Sirunyan et al. "Measurement of the CP-violating phase ϕ_s in the $B_s^0 \to J/\psi\phi(1020) \to \mu^+\mu^-K^+K^-$ channel in proton-proton collisions at $\sqrt{s} =$ 13 TeV." *Phys. Lett. B* 816 (2021), p. 136188 (cit. on p. 118).

[144] R. Aaij et al. "Updated measurement of time-dependent CP-violating observables in $B_s^0 \to J/\psi K^+K^-$ decays." *Eur. Phys. J. C* 79.8 (2019). [Erratum: Eur. Phys. J. C 80, 601 (2020)], p. 706 (cit. on p. 118).

[145] R. Aaij et al. "Measurement of the CP-violating phase ϕ_s from $B_s^0 \to J/\psi\pi^+\pi^-$ decays in 13 TeV pp collisions." *Phys. Lett. B* 797 (2019), p. 134789 (cit. on p. 118).

[146] R. Aaij et al. "First study of the CP-violating phase and decay-width difference in $B_s^0 \to \psi(2S)\phi$ decays." *Phys. Lett. B* 762 (2016), pp. 253–262 (cit. on p. 118).

[147] A. S. Dighe et al. "Angular distributions and lifetime differences in $B_s \to J/\psi\phi$ decays." *Phys. Lett. B* 369 (1996), pp. 144–150 (cit. on p. 119).

[148] R. Aaij et al. "Measurement of CP violation and the B_s^0 meson decay width difference with $B_s^0 \to J/\psi K^+K^-$ and $B_s^0 \to J/\psi\pi^+\pi^-$ decays." *Phys. Rev. D* 87.11 (2013), p. 112010 (cit. on pp. 121, 123).

[149] Michael Moll. "Radiation damage in silicon particle detectors: Microscopic defects and macroscopic properties." Ph.D. thesis. Hamburg U., 1999 (cit. on pp. 152, 154, 159, 167, 188, 191).

[150] G. Lindstrőm. "Radiation damage in silicon detectors." *Nucl. Instrum. Meth. A* 512 (2003). Ed. by P. Holl et al., pp. 30–43 (cit. on p. 153).

[151] A Chilingarov. "Temperature dependence of the current generated in Si bulk." *JINST* 8.10 (Oct. 2013), P10003. URL: https://dx.doi.org/10.1088/1748-0221/8/10/P10003 (cit. on p. 153).

[152] R. Wunstorf et al. "Investigations of donor and acceptor removal and long term annealing in silicon with different boron/phosphorus ratios." *Nucl. Instrum. Meth. A* 377 (1996), pp. 228–233 (cit. on pp. 154, 191).

[153] S. Baranov et al. *Estimation of Radiation Background, Impact on Detectors, Activation and Shielding Optimization in ATLAS*. Tech. rep. Geneva: CERN, 2005. URL: https://cds.cern.ch/record/814823 (cit. on pp. 155, 156).

[154] G. Battistoni et al. "Overview of the FLUKA code." *Annals Nucl. Energy* 82 (2015), pp. 10–18 (cit. on p. 155).

[155] J. Allison et al. "Geant4 developments and applications." *IEEE Trans. Nucl. Sci.* 53.1 (2006), pp. 270–278 (cit. on p. 155).

[156] J. Allison et al. "Recent developments in Geant4." *Nucl. Instrum. Meth. A* 835 (2016), pp. 186–225 (cit. on p. 155).

[157] G. Battistoni et al. "The FLUKA code: description and benchmarking." *AIP Conference Proceedings* 896.1 (Mar. 2007), pp. 31–49. URL: https://doi.org/10.1063/1.2720455 (cit. on p. 155).

[158] A. Ferrari et al. *FLUKA: A multi-particle transport code (program version 2005)*. CERN Yellow Reports: Monographs. Geneva: CERN, 2005. URL: https://cds.cern.ch/record/898301 (cit. on p. 155).

[159] A. D. Martin et al. "Parton distributions for the LHC." *Eur. Phys. J. C* 63 (2009), pp. 189–285 (cit. on p. 156).

[160] ATLAS Collaboration. *The Pythia 8 A3 tune description of ATLAS minimum bias and inelastic measurements incorporating the Donnachie-Landshoff diffractive model*. Tech. rep. Geneva: CERN, 2016. URL: https://cds.cern.ch/record/2206965 (cit. on p. 156).

[161] G.P. Summers et al. "Damage correlations in semiconductors exposed to gamma, electron and proton radiations." *IEEE Transactions on Nuclear Science* 40.6 (1993), pp. 1372–1379 (cit. on pp. 156, 166).

[162] M. Huhtinen and P.A. Aarnio. "Pion induced displacement damage in silicon devices." *Nucl. Instrum. Methods Phys. Res. A: Accelerators, Spectrometers, Detectors and Associated Equipment* 335.3 (1993), pp. 580–582. URL: https://www.sciencedirect.com/science/article/pii/016890029391246J (cit. on pp. 156, 166).

[163] A.Yu. Konobeyev, Yu.A. Korovin, and V.N. Sosnin. "Neutron displacement cross-sections for structural materials below 800 MeV." *J. Nucl. Mater.* 186.2 (1992), pp. 117–130. URL: https://www.sciencedirect.com/science/article/pii/002231159290328I (cit. on pp. 156, 166).

[164] P. J. Griffin et al. "SNL RML recommended dosimetry cross section compendium" (Nov. 1993). URL: https://www.osti.gov/biblio/10115441 (cit. on pp. 156, 166).

[165] Michael Moll. "Displacement Damage in Silicon Detectors for High Energy Physics." *IEEE Transactions on Nuclear Science* 65.8 (2018), pp. 1561–1582 (cit. on p. 156).

[166] A. Vasilescu and G. Lindström. "Displacement damage in silicon." *online compilation* (2000). URL: https://rd50.web.cern.ch/NIEL/ (cit. on pp. 156, 166).

[167] G. Aad et al. *Measurement of Radiation Damage through Leakage Current Monitoring of the ATLAS Pixel Detector*. Tech. rep. Geneva: CERN, 2019. URL: https://cds.cern.ch/record/2699903 (cit. on pp. 157, 160–162, 165).

[168] G. Aad et al. "Measurements of sensor radiation damage in the ATLAS inner detector using leakage currents." *JINST* 16 (2021), P08025 (cit. on pp. 158, 171).

[169] M. Moll, E. Fretwurst, and G. Lindström. "Leakage current of hadron irradiated silicon detectors – material dependence." *Nucl. Instr. and Meth. A* 426.1 (1999), pp. 87–93. URL: https://www.sciencedirect.com/science/article/pii/S0168900298014752 (cit. on p. 161).

[170] ATLAS Collaboration. *Hamburg Model Simulation Code*. 2019. URL: https://gitlab.cern.ch/atlas/athena/-/tree/main/InnerDetector/InDetCalibAlgs/PixelCalibAlgs/RadDamage/HamburgModel (cit. on p. 161).

[171] D. Aitree et al. *The Evaporative Cooling System for the ATLAS Inner Detector*. Tech. rep. Geneva: CERN, 2008. URL: https://cds.cern.ch/record/1100863 (cit. on p. 162).

[172] F. Lemeilleur, G. Lindström, and S. Watts. "Third RD48 status report" (Dec. 1999) (cit. on pp. 167, 182, 184, 186).

[173] G. Aad et al. "Operation and performance of the ATLAS semiconductor tracker in LHC Run 2." *JINST* 17.01 (2022), P01013 (cit. on pp. 167, 177, 178, 208).

[174] M. Capeans et al. *ATLAS Insertable B-Layer Technical Design Report*. Tech. rep. 2010. URL: https://cds.cern.ch/record/1291633 (cit. on pp. 169, 172, 174, 181).

[175] G. Lindström, S. Watts, and F. Lemeilleur. *3rd RD48 status report*. Tech. rep. Geneva: CERN, 1999. URL: https://cds.cern.ch/record/421210 (cit. on p. 176).

[176] M. Aaboud et al. "Modelling radiation damage to pixel sensors in the ATLAS detector." *JINST* 14.06 (2019), P06012 (cit. on pp. 176, 182, 184, 186).

[177] Fred James and Matthias Winkler. "MINUIT User's Guide" (June 2004) (cit. on p. 183).

[178] M. Battaglia et al. *Measurement of the Planar IBL Sensor Depletion Voltage as a function of Particle Fluence with Run 2 and 3 Collision Data*. Tech. rep. Geneva: CERN, 2023. URL: https://cds.cern.ch/record/2875608 (cit. on p. 184).

[179] M. Battaglia, Marco Bomben, and Marcello Bindi. *private communication* (cit. on p. 185).

[180] O. Aberle et al. *High-Luminosity Large Hadron Collider (HL-LHC): Technical design report*. CERN Yellow Reports: Monographs. Geneva: CERN, 2020. URL: https://cds.cern.ch/record/2749422 (cit. on p. 188).

[181] ATLAS Collaboration. *Expected tracking and related performance with the updated ATLAS Inner Tracker layout at the High-Luminosity LHC*. Tech. rep. Geneva: CERN, 2021. URL: http://cds.cern.ch/record/2776651 (cit. on p. 190).

[182] J. Lange et al. "Radiation hardness of small-pitch 3D pixel sensors up to a fluence of 3×10^{16} n_{eq}/cm^2." *JINST* 13.09 (Sept. 2018), P09009–P09009. URL: https://doi.org/10.1088/1748-0221/13/09/P09009 (cit. on p. 190).

[183] R. Garcia Alia. *Annual HL-LHC performance parameters for the R2E radiation level specification document*. Tech. rep. 2020. URL: https://edms.cern.ch/document/2364638/1.2 (cit. on p. 191).

[184] J. Beyer. *Measurements and Simulations of the Depletion Voltage for the ATLAS Pixel Detector*. URL: https://indico.cern.ch/event/695271/contributions/2958674/attachments/1637640/ (cit. on p. 191).

[185] V. Cindro et al. "Radiation damage in p-type silicon irradiated with neutrons and protons." *Nucl. Instrum. Meth. A* 599 (2009), pp. 60–65 (cit. on p. 191).

[186] URL: https://atlas-service-radsim.web.cern.ch (cit. on pp. 191, 208).

[187] Claudia Gemme. *private communication* (cit. on p. 192).

[188] Maurice Garcia-Sciveres. *The RD53A Integrated Circuit*. Tech. rep. Geneva: CERN, 2017. URL: https://cds.cern.ch/record/2287593 (cit. on p. 213).

[189] Maurice Garcia-Sciveres, Flavio Loddo, and Jorgen Christiansen. *RD53B Manual*. Tech. rep. Geneva: CERN, 2019. URL: https://cds.cern.ch/record/2665301 (cit. on p. 213).

[190] J. Pater. *The ATLAS Pixel Detector Upgrade at the HL-LHC*. Tech. rep. Geneva: CERN, 2020. URL: https://cds.cern.ch/record/2709133 (cit. on p. 214).

[191] S. Möbius and on behalf of the ATLAS ITk Group. "Module development for the ATLAS ITk pixel detector." *Journal of Instrumentation* 17.03 (Mar. 2022), p. C03042. URL: https://dx.doi.org/10.1088/1748-0221/17/03/C03042 (cit. on pp. 215, 247).

[192] K. Lantzsch et al. "The ATLAS Detector Control System." *Journal of Physics: Conference Series* 396.1 (Dec. 2012), p. 012028. URL: https://dx.doi.org/10.1088/1742-6596/396/1/012028 (cit. on p. 215).

[193] URL: https://www.microvu.com/machines/vertex (cit. on p. 217).

[194] URL: https://www.wasserman.eu/en/p/precision-balance-with-blow-cabinet-sbs-lw-300a-lcd-0001g-to-300g-338546 (cit. on p. 221).

[195] URL: https://twiki.cern.ch/twiki/bin/viewauth/Atlas/ITKPixelModuleAssemblyITkPixV1 (cit. on pp. 236, 256).

[196] URL: https://signatone.com/wl-350-le-300mm-semi-automatic-rf-dc-probe-system-with-local-enclosure/ (cit. on p. 237).

[197] URL: https://www.att-systems.com/products/#chucks (cit. on p. 238).

[198] URL: https://download.tek.com/datasheet/1KW-60780-61KW-60780-6_4200A-SCS_Parameter_Analyzer_Datasheet_061523.pdf (cit. on p. 238).

[199] URL: https://download.tek.com/datasheet/1KW-60780-61KW-60780-6_4200A-SCS_Parameter_Analyzer_Datasheet_061523.pdf (cit. on p. 238).

[200] URL: https://download.tek.com/datasheet/1KW-60906-0_Series_2600BDatasheet_112718.pdf (cit. on p. 238).

[201] URL: https://www.thinkymixer.com/en-gl/planetary-centrifugal-system/ (cit. on p. 251).

[202] Helge Christoph Beck. *Module development for the HL-LHC ATLAS ITk Pixel upgrade*. Tech. rep. 12. Geneva: CERN, 2019. URL: https://cds.cern.ch/record/2693063 (cit. on p. 261).

[203] URL: https://www.keyence.com/products/microscope/digital-microscope/vhx-7000/ (cit. on p. 267).

[204] M. Sykora et al. "Monitoring System of the ATLAS ITk Laboratory." *Journal of Physics: Conference Series* 2374.1 (Nov. 2022), p. 012098. URL: https://dx.doi.org/10.1088/1742-6596/2374/1/012098 (cit. on p. 274).

[205] *Technical Design Report: A High-Granularity Timing Detector for the ATLAS Phase-II Upgrade*. Tech. rep. Geneva: CERN, 2020. URL: https://cds.cern.ch/record/2719855 (cit. on p. 280).

[206] A. Abada et al. "FCC Physics Opportunities: Future Circular Collider Conceptual Design Report Volume 1." *Eur. Phys. J. C* 79.6 (2019), p. 474 (cit. on p. 280).